

**Theoretical Studies of a Single 3d
Transition Metal Doped Simple and Noble Metal Clusters
using Density Functional theory**

By

Vikas Chauhan

PHYS08200804005

Harish-Chandra Research Institute, Allahabad

*A thesis submitted to the
Board of Studies in Physical Sciences*

*In partial fulfillment of requirements
For the degree of*

DOCTOR OF PHILOSOPHY

of

HOMI BHABHA NATIONAL INSTITUTE



September, 2014

Homi Bhabha National Institute

Recommendations of the Viva Voce Board

As members of the Viva Voce Committee, we certify that we have read the dissertation prepared by *Vikas Chauhan* entitled “Theoretical Studies of a Single *3d* Transition Metal Doped Simple and Noble Metal Clusters using Density Functional theory” and recommend that it may be accepted as fulfilling the thesis requirement for the award of Degree of Doctor of Philosophy.

_____ **Date:**
Chairman - Prof. Jayanta K. Bhattacharjee

_____ **Date:**
Guide / Convener - Prof. Prasenjit Sen

_____ **Date:**
Member 1 - Prof. Sumathi Rao

_____ **Date:**
Member 2 - Prof. Anirban Basu

Final approval and acceptance of this thesis is contingent upon the candidate's submission of the final copies of the thesis to HBNI.

I hereby certify that I have read this dissertation prepared under my direction and recommend that it may be accepted as fulfilling the thesis requirement.

Date:

Place:

Guide

STATEMENT BY AUTHOR

This dissertation has been submitted in partial fulfillment of requirements for an advanced degree at Homi Bhabha National Institute (HBNI) and is deposited in the Library to be made available to borrowers under rules of the HBNI.

Brief quotations from this dissertation are allowable without special permission, provided that accurate acknowledgement of source is made. Requests for permission for extended quotation from or reproduction of this manuscript in whole or in part may be granted by the Competent Authority of HBNI when in his or her judgment the proposed use of the material is in the interests of scholarship. In all other instances, however, permission must be obtained from the author.

Date:

Vikas Chauhan
(Ph.d Candidate)

DECLARATION

I, hereby declare that the investigation presented in the thesis has been carried out by me. The work is original and has not been submitted earlier as a whole or in part for a degree/diploma at this or any other Institution/University.

Date:

Vikas Chauhan
(Ph.d Candidate)

Certificate

This is to certify that the Ph.D. thesis titled “Theoretical Studies of a Single $3d$ Transition Metal Doped Simple and Noble Metal Clusters using Density Functional theory” by Vikas Chauhan is a record of bonafide research work done under my supervision. It is further certified that the thesis represents independent and original work by the candidate.

Guide:

Prof. Prasenjit Sen

Date:

List of Publications arising from the thesis

Journal

1. Hund's rule in superatoms with transition metal impurities, V. M. Medel, J. U. Reveles, S. N. Khanna, V. Chauhan, P. Sen, and A. W. Castleman, Jr., Proc. Natl. Acad. Sci. U.S.A. **2011**, 108, 10062-10066.
2. Shell magnetism in transition metal doped calcium superatom, V. Chauhan, V. M. Medel, J. U. Reveles, S. N. Khanna, and P. Sen, Chem. Phys. Lett. **2012**, 528, 39-43.
3. Electronic and magnetic properties of 3d transition metal-doped strontium clusters: Prospective magnetic superatoms, V. Chauhan and P. Sen, Chem. Phys. **2013**, 417, 37-44.
4. Structural, electronic and magnetic properties of binary transition metal aluminum clusters: absence of electronic shell structure, V. Chauhan, A. Singh, C. Majumder, and P. Sen, J. Phys.; Condens. Matter, **2014**, 26, 015006-015013.
5. Nature of Valence Transition and Spin Moment in Ag_nV^+ Clusters, V. M. Medel, A. C. Reber, V. Chauhan, P. Sen, A. M. Köster, P. Calaminici, and S. N. Khanna, J. Am. Chem. Soc. **2014**, 136, 8229-8236.

Others

1. Ab-initio and anion photoelectron studies of Rh_n ($n = 19$) clusters, M. R. Beltran, F. B Zamudio, V. Chauhan, P. Sen, H. Wang, Y. J. Ko, and K. Bowen, Eur. Phys. J. D, **2013**, 67, 63-70.

To
My Grandparents
&
Parents

Acknowledgments

I would like to take this opportunity to express my gratitude towards my advisor Prof. Prasenjit Sen for his continuous support during my Ph.d. His guidance, patience, motivation, enthusiasm, and immense knowledge helped me in course of my research and in writing of this thesis. I am sincerely grateful to my advisor for sharing his illuminating views on a number of problems related to this thesis and having faith in me.

Besides my advisor, I would like to thank Prof. Pinaki Majumdar, Prof. Sumathi Rao, Prof. T. P. Pareek, and Prof. G. V. Pai for their continuous encouragement. I am thankful to the members of my thesis advisory committee for their support to continue my research without any obstructions. I would like to thank Prof. A. Raychaudhuri and Prof. J. K. Bhattacharjee for giving me an opportunity to work at HRI. I express my deep gratitude to Prof. Ashoke Sen, Prof. Rajesh Gopakumar, Prof. Sudhakar Panda, Prof. L. Sriram Kumar, Prof. V. Ravindran, and Prof. Ashesh Krishna Datta for giving me unparallel courses on basic physics.

I would never forget all the beautiful moments which I shared with my friends at HRI. I would like to acknowledge Shailesh, Sanjay Amrutiya, Bhavin, Kalpataru, Anamitra, Jaban, Siddharth, Priyanka, Trilochan, Sanjoy, Subrat, Abhinav, Roji, Uttam, Tripathi, Abhishek, Saikat, Karam Deo, Pradeep (Rai and Mishra), Shishir, Ramesh, Jai, Kasi, Senthil, Akhilesh, Sourabh, Saurav, Arunabha, Ujjal, Ashutosh, Rishu, Anitha, Ankit, Suchitra, other senior and junior fellows in physics and mathematics. I would like to express my gratitude to Akansha, Pooja, Sabyasachi, Saurabh Pradhan, Nyayabanta, and Ajanta with whom I had wonderful discussions during my Ph.d days. Those discussions helped me a lot to give my best.

My acknowledgement will never be complete without mentioning Rajarshi (Khali-har) and Ramlal (Rawan). They are not only my friends but also biggest and ruthless critics of mine both in academics and social context. They have been a source of valuable moral support to me and have extended their helping hands in difficult moments. I am even more thankful to their better halves (Priyanka and Minakshi) for being their critics.

I am immensely thankful to the administration of HRI, for their help and support. I specially thank to Ravindra Singh, Yashpal Bhadauriya, Ajay Srivastava, Umakant Dwivedi, Dharmendra Malhotra, Amit Roy, Raj Gulati, Archana Tandon, Seema Agrawal, Amit Khulve, Pradeep, and Saadhu for their helping nature and support

during my stay at HRI. I am thankful for the HPC clusters at HRI, on which all the numerical calculations relevant to this thesis were done.

Outside HRI, I express my heart-felt gratitude to Prof. K. S. Singh, Kamal deep, Vipin, Pawan, and Deepti for their continuous moral support. I would like to express my gratitude to my childhood friends Sachin (Dhama and Kumar), Suresh, and Kamal with whom I spent unique, magical and cheerful moments.

Finally, I would like to express my gratitude and love from the deepest of corner of my heart for those people which mean the world to me, my parents, my brother, bhabhi, my nephew, and niece. Without you my life would be meaningless. Thank you very much for all the support that I needed in order to constantly push myself to succeed. Without your unconditional love and support, I wouldn't be here today !

Contents

SYNOPSIS	v
LIST OF FIGURES	x
LIST OF TABLES	xvi
1 Introduction	1
1.1 Atomic clusters	1
1.2 Metal clusters	2
1.2.1 Simple metal clusters	2
1.2.2 Noble metal clusters	2
1.2.3 Transition metal clusters	2
1.2.4 Mixed clusters	3
1.3 Electronic shell structure and shell models	3
1.3.1 Spherical Shell Models	4
1.3.2 Clemenger-Nilsson shell model	6
1.3.3 Jellium model	8
1.4 Monovalent (group-IA and-IB) clusters	9
1.4.1 IP's and shell effects	9
1.5 Shell effects in other metal clusters	12
1.5.1 Divalent (group-IIA) metal clusters (Mg_N , Ca_N , Sr_N)	12
1.5.2 Trivalent metal clusters (Al_N clusters)	16
1.6 Experimental status of shell model : Angle resolved PES	19
1.7 Superatoms	22
1.7.1 Cluster assembled materials (CAM)	24

1.8	Shell effects in bimetallic clusters	26
1.8.1	TM doped noble metal clusters	26
1.8.2	TM doped alkali metal clusters : Magnetic superatom	28
1.8.3	TM doped Mg clusters	32
1.8.4	TM doped aluminium clusters	34
1.9	Aromaticity and all-metal clusters	35
1.10	Goals of this thesis	36
2	Methodology	39
2.1	Introduction	39
2.1.1	Density functional theory	39
2.1.2	The Kohn-Sham method	42
2.1.3	Exchange-correlation functional	44
2.2	Kohn-Sham equations: Introduction of basis sets	46
2.2.1	Kohn-Sham equations in localized basis	46
2.2.2	Kohn-Sham equations in plane wave basis	52
2.2.3	Forces and local structure optimization	55
2.3	Evolutionary algorithm	56
2.3.1	Initialization	56
2.3.2	Variation operators	56
2.3.3	Halting criteria	57
3	TM doped calcium clusters	58
3.1	Introduction	58
3.2	Computational details	58
3.3	Study of TMCa_8 clusters	60
3.3.1	Motivation	60
3.3.2	Ground state structures	60
3.3.3	Relative Stabilities	61
3.3.4	Stability of FeCa_8 cluster	65
3.3.5	Local moments on TM dopants	67
3.4	Study of FeCa_N ($N=5-12$) clusters	68
3.4.1	Ground state structures	68
3.4.2	Relative stabilities	69
3.4.3	Magnetic properties	69
3.5	FeCa_8 as a magnetic superatom	73
3.6	Role of Hund's coupling and Crystal field effect	75

3.7	Conclusions	80
4	TM doped strontium clusters	81
4.1	Introduction	81
4.2	Computational details	81
4.3	Ground State Structures of TMSr ₈	81
4.3.1	Relative stabilities	82
4.3.2	Local moments on TM dopants	86
4.3.3	Interplay of Crystal field effect and Hund's coupling	87
4.3.4	Conclusions	91
5	Cr and Mn doped strontium clusters	93
5.1	Introduction	93
5.2	Computational details	94
5.3	Study of CrSr _N (<i>N</i> =4-12) clusters	94
5.3.1	Ground state structures	94
5.3.2	Relative stabilities	95
5.3.3	Stability of CrSr ₉	96
5.3.4	Magnetic properties of CrSr _N clusters	98
5.4	Study of MnSr _N (<i>N</i> =4-12) clusters	101
5.4.1	Ground state structures	101
5.4.2	Relative stabilities	101
5.4.3	Stability of MnSr ₁₀	102
5.4.4	Magnetic properties of MnSr _N clusters	104
5.4.5	CrSr ₉ and MnSr ₁₀ clusters as magnetic superatoms	105
5.4.6	Conclusions	106
6	TM doped aluminium clusters	107
6.1	Introduction	107
6.2	Computational details	108
6.3	Study of TM-Al clusters (TM=Cr, Mn and Fe)	108
6.3.1	Ground state structures	108
6.3.2	Relative stabilities	108
6.4	Study of TMA ₄ and TMA ₃ (TM=Cr-Ni) clusters	113
6.5	Shell model and electronic structure of TM-Al clusters	117
6.5.1	Stability of FeAl ₄ and CoAl ₃ clusters and shell models	117
6.5.2	Applicability of shell models at larger sizes	119

6.5.3	<i>s-p</i> hybridization	120
6.6	Origin of stability: Aromaticity	121
6.6.1	Conclusions	122
7	V doped silver clusters	124
7.1	Introduction	124
7.2	Computational details	124
7.3	Ground State structures	125
7.4	Relative stabilities	126
7.5	Origin of the stability of VAg_5^+ and VAg_7^+	129
7.6	Conclusions	132
8	Future prospects	133
8.1	Introduction	133
8.2	Reactivity with Oxygen	133
8.3	Magnetic superatoms at finite temperature	134
8.4	Magnetic superatoms on substrates	134
8.5	Applicability of shell models	135
	APPENDIX	136
A	TM doped calcium clusters	136
B	TM doped strontium clusters	139
C	Cr and Mn doped strontium clusters	141
D	TM doped aluminium clusters	146
E	V doped silver clusters	150

Synopsis

Atomic clusters are aggregates of atoms consisting of a few to a few hundred atoms. Because of the wide range of their possible sizes, compositions and charge states, atomic clusters constitute virtually a new ‘phase’ of matter with properties distinct from those of an atom and the corresponding bulk. Difference in properties with respect to the bulk arises primarily because of two reasons: first, unlike bulk, the number of atoms on the surface of a cluster is a substantial fraction of the total number of atoms; second, the arrangement of atoms in a cluster is generally very different from that in the corresponding bulk. The most extraordinary feature of atomic clusters is an extreme size-dependence of their structural, electronic, magnetic, chemical, and optical properties. Addition or removal of even one atom or an electron can substantially alter their physical and chemical properties [1].

For an ease of analysis and understanding, atomic clusters can be classified in various ways. Clusters can be classified as small, medium-sized and large depending on the number of constituent atoms. Another convenient classification is based on the types of the constituent atoms and the nature of bonding between them. One talks about (i) semiconductor clusters such as Ge_N , Si_N , (ii) ionic clusters, such as $[\text{Na}_N\text{Cl}_M]^{(N-M)+}$, (iii) rare gas clusters, e.g., Ar_N , (iv) metal clusters with metallic bonding such as Na_N and Au_N , (v) molecular clusters, e.g., $(\text{CO})_N$.

During the last three decades, metal clusters have been the most extensively explored class of clusters by experimental and theoretical means. Metal clusters can be further subdivided into simple metal, noble metal, transition metal (TM), and mixed or alloy clusters. We term clusters composed of group-IA (alkali), group-II and group-IIIA metal elements as simple metal clusters [1–3]. Clusters of group-IB elements are termed noble metal clusters. Although they share many properties of the simple metal clusters, there can be significant differences also, most notably in case of Au clusters. A characteristic feature of simple metal clusters is a greater stability of clusters having certain specific number of valence electrons compared to their neighbors. In 1984, Knight *et al* measured the mass abundance spectrum of Na_N clusters which showed strongly size-dependent abundance [4]. Particularly sharp drops in intensity were observed just after $N = 8, 20, 40, 58$ and 92 . In the mass abundance spectrum of gas phase clusters peaks of higher intensity indicate higher stability of these clusters with respect to their neighbors. Thus Na_N clusters at $N = 8, 20, 40, 58$ and 92 were more stable. These clusters are termed magic clusters. Magic clusters were also observed in other experiments on various simple metal and noble metal clusters [1]. In order to explain the enhanced stability of

metal clusters of specific sizes, several simple quantum mechanical models have been invoked. These models are known as shell models [1,5]. The underlying assumption of all these models is that the valence electrons of all the metal atoms are confined within a finite region of space defined by the ‘volume’ of the cluster. Using spherically symmetric confining potentials, such as the 3D harmonic oscillator potential, one obtains the following sequence of one electron orbitals $1S^2$, $1P^6$, $(1D^{10} 2S^2)$, $(1F^{14} 2P^6)$, $(1G^{18} 2D^{10} 3S^2)$, $(1H^{22} 2F^{14} 3P^6)$ One-electron orbitals within parentheses are degenerate in energy. Completely filled electronic shells will result when there are 2, 8, 20, 40, 70, 112 . . . electrons in the cluster. If the confining potential is of hard-wall form, magic clusters occur for valence electron counts of 18, 34, 58, 68, 92 *etc.* in addition to 2, 8, 20, 40 and 70 [1]. We know that atoms with filled electronic shells exhibit enhanced stability. Similarly, it was argued that stability of magic clusters is due to their closed electronic shells. Experiments were performed to measure other properties directly related to the electronic structure, e.g., ionization potential, electron affinity and polarizability. Sharp drops in the ionization potential have been observed at sizes just after the magic sizes. Also, low values of electron affinity were seen at the magic sizes. All these experimental observations indicate that stability of magic clusters is an electronic feature [1,6].

The existence of the electronic shells in simple metal clusters and their dominating role in governing stability provides a very exciting possibility that clusters may exhibit electronic and chemical features similar to elemental atoms. Leuchtner *et al* studied reactivity of Al_n^- clusters with oxygen [7]. All the anionic clusters reacted with O_2 except for Al_{13}^- , Al_{23}^- and Al_{37}^- . With three valence electrons per Al atom, Al_{13}^- , Al_{23}^- and Al_{37}^- have 40, 70 and 112 valence electrons respectively. Therefore their non-reactive behavior can be understood in terms of closed electronic shells. This experiment demonstrated that the electronic shell structure plays a decisive role in determining the reactivity of simple metal clusters. Since non-reactive behaviour is also well known for inert gas atoms due to their closed shells, Al_{13}^- can be regarded as an analogue of those atoms. This led to the idea of ‘superatoms’. The most recent definition of superatoms as given by the proponents Castleman and Khanna is as follows. A superatom is a cluster not only mimicking some properties of an elemental atom but a motif that is stable in chemical assembly and may also demonstrate new chemical features beyond the analogue atom [8]. Various combined theoretical and experimental studies revealed that Al_{13} and Al_{14} behave as a halogen and an alkaline earth element respectively [9–12]. Al_7^- was shown to behave as a multi valence superatom in a way similar to a C atom [13]. Thus, simple

quantum mechanical shell models provide us with an elegant electron counting rule through which we can understand the electronic and chemical properties of simple metal clusters. Electronic properties of noble metal clusters, particularly Cu and Ag, are also understood within shell models [6]. Recently, it has been shown that the conventional shell sequence in spherical metal clusters as discussed so far can be modified by structural distortions which can lead to species with enhanced stability at unconventional electron counts. For example, CuAl_{22}^- with 68 valence electrons was shown to have reduced reactivity against O_2 [14]. In the spherical shell model, 68 electrons correspond to a closed 2D^{10} shell, with an empty 3S^2 . However, the origin of the enhanced stability of CuAl_{22}^- was shown to be due to splitting of the 2D^{10} shell because of a structural distortion of the cluster. This deformation can be understood in terms of a crystal field like splitting of degenerate shells into subshells.

Recently, the idea of superatoms has been extended to ‘magnetic superatoms’. VCs_8 is the first example of a magnetic superatom in which atomic d electrons localized on the V atom provide a moment of $5 \mu_B$ whereas delocalized electrons from the s -valence states of the Cs and V atoms form a filled shell of $1\text{S}^2 1\text{P}^6$. This provides stability to the cluster [15]. It has been shown that two and three units of VCs_8 do not coalesce when they are brought in contact. They are found to retain their structural identity, magnetic moment and form a stable dimers and trimers.

Despite having great success, there are cases where shell models cannot explain the properties of all-metal clusters as observed in various experimental and theoretical studies [16, 17]. There are other simple electron counting rules in chemistry like the Hückel rule and Wade-Mingos rules which account for stability of electronic systems. According to the Hückel rule, planar and cyclic hydrocarbons having $(4n+2)\pi$ electrons have enhanced stability. These hydrocarbons are known as aromatic compounds. Benzene, i.e., C_6H_6 is one of the classic examples. Recently, Li *et al* [16] have shown that the concept of aromaticity can be used in explaining the enhanced stability of bimetallic LiAl_4^- , NaAl_4^- , and CuAl_4^- clusters. After that, numerous studies have been devoted to finding stable cluster motifs using aromaticity as a guiding principle. Although aromaticity is a widely used term, a precise quantitative and well-accepted definition of this quantity is still missing. For quantitative estimation of aromaticity, different criteria have been proposed by different authors [17]. These can be based on structural, energetic, reactivity, electronic or magnetic properties. The most popular criterion used to identify an aromatic cluster is perhaps the nucleus independent chemical shift (NICS), a magnetic measure. Clusters with negative values of NICS are classified as aromatic. while clusters with positive values of NICS

are classified as anti-aromatic [18, 19].

Motivated by the interesting concept of superatom, a major part of my thesis is devoted to identifying stable clusters which behave as magnetic superatoms. The detailed study of structural, electronic and magnetic properties of a single 3d TM doped alkaline earth and aluminum clusters using first-principles approach based on density functional theory forms a major part of this thesis. In addition, I have studied V doped silver clusters using first-principle calculations. This work is motivated by recent experiments performed by Janssens *et al* on these clusters [20]. This thesis is organized as follows.

Chapter 1 This chapter is an introduction to the topic of atomic clusters and superatoms. In this I review the literatures on atomic clusters, various shell models, and shell effects in simple metal and noble metal clusters. In addition, the concepts of superatom, magnetic superatom, cluster assembled materials (CAM's), and aromaticity in all-metal clusters are reviewed.

Chapter 2 is about the underlying theory and techniques of calculations used in this thesis. Density functional theory is reviewed. Techniques for solving the Kohn-Sham equations using both localized and plane wave basis sets, and the concept of pseudopotential are discussed. An evolutionary algorithm for finding the global minima of clusters is also discussed.

Chapter 3 In this chapter the electronic and magnetic properties of 3d TM doped calcium clusters are presented. We have found TiCa_8 and FeCa_8 to have enhanced stability as indicated by large gaps between the highest occupied and lowest unoccupied molecular orbitals (HL gap), hardness (η) and adiabatic spin excitation energy (ΔE_{spin}). In addition, FeCa_8 is found to have a magnetic moment of $4 \mu_B$. The stability of TiCa_8 is understood from the fact that it has 20 valence electrons, a magic number. Most striking feature of this chapter is the stability of FeCa_8 at an unconventional electron count of 24. We have shown that the origin of this stability is an interplay between crystal field effect and Hund's coupling. FeCa_8 is identified as a magnetic superatom in the same spirit as VCs_8 [21].

Chapter 4 extends our search for magnetic superatoms by investigating the electronic and magnetic properties of the TMSr_8 clusters. TiSr_8 and CoSr_8 are found to have enhanced stability within the TMSr_8 clusters. The enhanced stability of TiSr_8 is understood in a way similar to TiCa_8 . Because of the low magnetic moment

of $1 \mu_B$, CoSr_8 is not found to be an attractive candidate for magnetic superatom. Most strikingly, FeSr_8 does not emerge as a cluster with enhanced stability. We have discussed the reasons behind this. Furthermore, we have shown that the ground state electronic configuration of a TMSr_8 cluster is also determined by the combined effect of Hund's coupling and crystal field effect [22].

Chapter 5 explores the possibility of finding clusters with enhanced stability and finite magnetic moment within the CrSr_N and MnSr_N ($N=4-12$) series. Motivation for studying these clusters originated from the study of TMSr_8 clusters. We found that CrSr_9 and MnSr_{10} have enhanced stability as indicated by their hardness, second order energy difference ($\Delta_2(N)$) and ΔE_{spin} . CrSr_9 and MnSr_{10} are found to have magnetic moments of $4\mu_B$ and $5\mu_B$ respectively. Again, the origin of stability and magnetic moment in CrSr_9 and MnSr_{10} clusters is the combined effect of crystal field and Hund's coupling. CrSr_9 and MnSr_{10} are also found to behave as magnetic superatoms [22].

Chapter 6 focuses on the electronic and magnetic properties of a single Cr, Mn, Fe, Co and Ni doped Al clusters in search of magnetic superatoms. While we have not been able to identify any possible candidates for magnetic superatoms in these series, we have found some very interesting properties in them. We have found that FeAl_4 , and CoAl_3 clusters have enhanced stability as indicated by their second order energy difference, hardness and adiabatic spin excitation energy. However, they have no net magnetic moment. Most importantly we found that spherical shell models cannot describe the electronic structure of TM doped aluminum clusters, in contrast to binary TM doped alkali and alkaline earth clusters. In fact we have shown that stability of FeAl_4 , and CoAl_3 can be associated with their aromatic behaviour as revealed by their negative NICS values [23].

Chapter 7 investigates the evolution in the atomic structure, bonding characteristics, stability, and the spin magnetic moment of neutral and cationic VAg_N clusters. This work is motivated by the experimental study of the VAg_N^+ clusters in which VAg_5^+ and VAg_7^+ were found to be stable [20]. We found that VAg_5^+ and VAg_7^+ have enhanced stability in agreement with the experiments, indicated by their large HL gap and $\Delta_2(N)$. In addition we show that the stability of VAg_5^+ and VAg_7^+ can be explained in terms of exchange splitting within the 1D shell orbitals of these clusters [24].

List of Figures

1.1	Mass abundance spectrum of Na_N clusters [4].	3
1.2	Energy level occupation for (a) spherical three dimensional harmonic, (b) intermediate (Woods-Saxon), and (c) square-well potentials [1].	5
1.3	Total electronic energy curves as functions of η for the 3D harmonic potential. Open circles denote the optimal values for the valence electron counts given next to the circles [1,5].	7
1.4	(A) Change in the electronic energy difference, $\Delta(N + 1) - \Delta(N)$ vs N . [4] (B) Second order energy difference for Na_N clusters using harmonic oscillator potential with spheroidal distortions [5].	8
1.5	(Left) Ionization potentials of sodium and potassium clusters as function of their size [1]. (Right) Theoretical results derived from the Clemenger-Nilsson ellipsoidal model. Open squares show experimental IP's [35].	10
1.6	Open squares show experimentally measured EA's of $\text{K}_{N=5-22}$ clusters [40], Top panel : The spherical model compared to experimental data. Middle panel : The spheroidal model compared to experimental data. Lower panel : The ellipsoidal model compared to experimental data [35].	11
1.7	Experimentally measured ionization potentials of Al_N clusters [74].	16
1.8	Schematic angle-resolved spectrum of three hypothetical electronic states exhibiting perpendicular, isotropic, and parallel distributions (β parameters -1 , 0 , and $+2$ respectively). The angular distributions are visualized as three-dimensional polar plots above [83].	20

1.9	Angle-resolved photoelectron spectrum of Na_{40}^- , measured at threshold photon energy of 500 nm. In the upper panel, the angle-integrated spectrum is shown, in the lower panel, the spectra are plotted as a function of the emission angle with respect to the light polarization [83].	21
1.10	Charge density map of the HOMO for Al_{13}I^- [11]. Blue spheres are Al atoms while the red sphere represents an I atom.	22
1.11	(Left)BE of Al_7M^- , (Right) HL gap of Al_7M^- clusters, M is an atom of the second, third, and fourth row of the periodic table [13].	24
1.12	Density of states of CAM based on Al_{13}K clusters. Fermi energy level was set to zero [87].	25
1.13	Geometrical structure of various cluster assembled materials made of As7 combined with K, Cs. or cryptated K atoms. The calculated band gaps of the resulting solids are also marked. Adoped from ref [90].	26
1.14	One-electron energy levels and molecular orbital isosurfaces for VNa_8 (left) and VCs_8 (right). Majority and minority levels are shown. Continuous lines correspond to the filled levels and the dotted lines correspond to the unfilled states. For each level, the degeneracy is marked. Upper-case letters stand for delocalized 1S and 1P shells, and lower-case letters for localized 3d atomic orbitals [15].	29
1.15	Lowest-energy structures of (a) V_2Na_{16} and (b) $(\text{VCs}_8)_2$ dimer starting from free clusters. The arrows indicate the direction of the vanadium local spin moments. The superscripts indicate spin multiplicity [15].	30
1.16	Photoelectron spectra at 355 nm for VNa_N^- clusters ($N = 7, 8$). The calculated absorption spectra of neutral VNa_8 is marked in red. The calculated vertical detachment energies are marked with blue lines [104].	32
1.17	One electron energy levels and orbital wavefunction isosurfaces in the FeMg_8 cluster [105].	33
2.1	Flowchart of a typical evolutionary algorithm [158].	57
3.1	Ground state structure and multiplicity ($M=2S + 1$)of TMCa_8 clusters. Point group symmetry of TMCa_8 are also given. $r_{\text{TM-Ca}}$ and $r_{\text{Ca-Ca}}$ are average TM-Ca and Ca-Ca bond lengths in Å.	60
3.2	Variation of η and ΔE_{spin} with respect to TM atom.	62

3.3	Molecular orbital energy levels and orbital wave-function isosurfaces of (a) ScCa ₈ and (b) TiCa ₈ . Continuous lines correspond to the filled levels while the dotted lines correspond to the unfilled states. Degeneracies are also marked.	63
3.4	Variation of the magnetic moments (μ_B) with the TM atom and the nature of frontier orbitals.	64
3.5	(a) Molecular orbital energy levels and orbital wave-function isosurfaces of FeCa ₈ . Red and green arrows showing the exchange splitting of the 1D and 2D orbitals respectively. (b) One electron energy levels and atomic orbitals of Fe atom. Blue arrow shows the exchange splitting of <i>d</i> orbitals of Fe atom.	65
3.6	Ground state structure and multiplicity (2S+1) of FeCa _N clusters. $r_{\text{Fe-Ca}}$ and $r_{\text{Ca-Ca}}$ are average Fe-Ca and Ca-Ca bond lengths.	68
3.7	Energetic and magnetic trends of FeCa _N ($N=5-12$) clusters. (a) Variation of η and ΔE_{spin} vs the number of Ca atoms, (b) variation of the second order energy difference ($\Delta_2(N)$) for FeCa _N series.	69
3.8	Evolution of magnetic moment as a function of the number of Ca atoms in the FeCa _N clusters.	70
3.9	Molecular orbital energy levels and orbital wave-function isosurfaces of (a) FeCa ₆ and (b) FeCa ₇	71
3.10	Molecular orbital energy levels and orbital wave-function isosurfaces of (a) FeCa ₉ and (b) FeCa ₁₀	72
3.11	Relative energy (eV) of (FeCa ₈) ₂ as a function of magnetic moment.	74
3.12	Evolution of the magnetic moments in the FeCa _N and FeMg _N clusters [105].	76
3.13	Molecular orbital energy levels and orbital wave-function isosurfaces of (a) VCa ₈ and (b) CrCa ₈	77
3.14	Molecular orbital energy levels and orbital wave-function isosurfaces of MnCa ₈	78
3.15	(a)Molecular orbital energy levels and orbital wave-function isosurfaces of CoCa ₈ and (b) NiCa ₈	79
4.1	Ground state structures and spin multiplicities of TMSr ₈ clusters. $r_{\text{TM-Sr}}$ and $r_{\text{Sr-Sr}}$ are the average TM-Sr and Sr-Sr bond lengths.	82
4.2	The hardness (η) and adiabatic spin excitation energies of all the TMSr ₈ clusters.	83

4.3	Molecular orbital energy levels and orbital wave-function isosurfaces of (a) ScSr ₈ (b) TiSr ₈	84
4.4	MO energy level diagrams and isosurface plots for the (a) ³ FeSr ₈ and (b) ⁵ FeSr ₈ . MO's that cannot be identified to have definite angular momentum character are marked with '?'.	85
4.5	MO energy level diagrams and isosurface plots for the (a) VCa ₈ and (b) VSr ₈	89
4.6	MO energy level diagrams and isosurface plots for the (a) CrCa ₈ and (b) CrSr ₈	90
4.7	MO energy level diagrams and isosurface plots for the (a) MnCa ₈ and (b) MnSr ₈	91
5.1	Variation of the magnetic moments (μ_B) with the TM atom and the nature of frontier orbitals upto TM=Sc-Mn.	93
5.2	Ground state structure and multiplicity of CrSr _N clusters. $r_{\text{Cr-Sr}}$ and $r_{\text{Sr-Sr}}$ are the average Cr-Sr and Sr-Sr bond lengths. r_z is the extent of the cluster perpendicular to the square planes.	95
5.3	(a) Hardness (η), ΔE_{spin} and (b) the second order energy difference ($\Delta_2(N)$) for the CrSr _N as a function of the number of Sr atoms N	96
5.4	MO energy level diagrams and isosurface plots for the ⁵ CrSr ₉	97
5.5	Variation of the magnetic moment of CrSr _N clusters.	98
5.6	Ground state structures and spin multiplicities of MnSr _N clusters. $r_{\text{Mn-Sr}}$ and $r_{\text{Sr-Sr}}$ are the average Mn-Sr and Sr-Sr bond lengths. r_z is the extent of the cluster perpendicular to the square planes.	101
5.7	(a) Hardness, ΔE_{spin} (b) second order energy difference ($\Delta_2(N)$) for the MnSr _N clusters as a function of the number of Sr atoms N	102
5.8	MO energy level diagrams and isosurface plots for the (a) ⁶ MnSr ₉ and (b) ⁶ MnSr ₁₀ clusters.	103
5.9	Variation of magnetic moment of MnSr _N clusters.	104
5.10	Optimized structures for dimers of CrSr ₉ with parallel (FM) and anti-parallel (AFM) alignments of the TM spins. ΔE is the energy difference between the two situations.	105
5.11	Optimized structures for dimer of MnSr ₁₀ with parallel (FM) and anti-parallel (AFM) alignments of the TM spins.	106
6.1	Ground state structures and spin multiplicities of Cr-, Mn- and FeAl _N clusters for $N=2-12$	109

6.2	(a) HL gap and ΔE_{spin} (b) second order energy difference ($\Delta_2(N)$) of CrAl_N clusters as a function of number of Al atoms.	110
6.3	(a) HL gap and ΔE_{spin} (b) second order energy difference ($\Delta_2(N)$) of MnAl_N clusters as a function of number of Al atoms.	111
6.4	(a) HL gap and ΔE_{spin} (b) second order energy difference ($\Delta_2(N)$) of FeAl_N clusters as a function of number of Al atoms.	112
6.5	Ground state structures and spin multiplicities of TAl_4 clusters. . .	113
6.6	The HL gap and ΔE_{spin} of TAl_4 clusters.	114
6.7	Ground state structures and spin multiplicities of CoAl_N ($N=2-6$) clusters.	114
6.8	(a) The HL gap, $\Delta_2(N)$ and (b) spin excitation energy (ΔE_{spin}) of CoAl_N clusters.	115
6.9	Ground state structures and spin multiplicities of TAl_3 clusters. . .	116
6.10	The HL gap and ΔE_{spin} of TAl_3 clusters.	116
6.11	MO energy level diagrams and isosurface plots for (a) $^1\text{FeAl}_4$ and (b) $^1\text{CoAl}_3$	117
6.12	MO energy level diagrams and isosurface plots of $^2\text{NiAl}_3$	118
6.13	MO energy level diagrams and isosurface plots of (a) $^1\text{Al}_{13}^-$ and (b) $^5\text{MnAl}_{11}$	119
6.14	Bond lengths in Å of the CoAl_3 and FeAl_4 clusters.	122
7.1	Ground state structures and spin multiplicities of (a) VAg_N^+ and (b) VAg_N clusters.	125
7.2	(a) The HL gap and (b) $\Delta_2(N)$ of $\text{VAg}_N^{+/0}$ clusters.	126
7.3	ΔE_{Ag} , i.e., Ag addition energy of $\text{VAg}_N^{+/0}$ clusters.	127
7.4	Variation of AIP and VIP of VAg_N clusters as a function of number of Ag atoms.	128
7.5	Variation of the fragmentation energy of VAg_N^+ clusters.	129
7.6	MO energy level diagrams and isosurface plot of (a) VAg_5^+ (b) VAg_7^+ clusters. Blue arrow shows exchange splitting in 1D orbitals.	130
A.1	Higher energy isomers of TMCa_8 clusters.	136
A.2	Higher energy isomers of FeCa_N ($N=5-12$) clusters.	137
A.3	MO energy level diagrams and isosurface plot of (a) $^5\text{FeCa}_{11}$ and (b) $^5\text{FeCa}_{12}$	138
B.1	Higher energy isomers of TMSr_8 clusters.	139

B.2	MO energy level diagrams and isosurface plot of (a) ${}^2\text{CoSr}_8$ and (b) ${}^3\text{NiSr}_8$	140
C.1	Higher energy isomers of $\text{CrSr}_N (N=4-12)$ clusters.	141
C.2	One electron energy levels and atomic orbitals of Cr atom. Arrow shows the exchange splitting in $3d$ orbitals of Cr atom.	142
C.3	MO energy level diagrams and isosurface plot of (a) ${}^3\text{CrSr}_6$ (b) ${}^3\text{CrSr}_7$	143
C.4	MO energy level diagrams and isosurface plot of ${}^5\text{CrSr}_{10}$	144
C.5	Higher energy isomers of $\text{MnSr}_N (N=4-12)$ clusters.	145
D.1	Higher energy isomers of $\text{CrAl}_N (N=2-12)$ clusters.	146
D.2	Higher energy isomers of $\text{MnAl}_N (N=2-12)$ clusters.	147
D.3	Higher energy isomers of $\text{FeAl}_N (N=2-12)$ clusters.	148
D.4	Higher energy isomers of Co-, and Ni- doped Al_N clusters.	148
D.5	(a) HL gap, ΔE_{spin} and (b) $\Delta_2(N)$ for NiAl_N clusters.	149
E.1	Higher energy isomers of $\text{VAg}_N^+ (N=3-10)$ clusters.	150
E.2	Higher energy isomers of $\text{VAg}_N (N=3-10)$ clusters.	151
E.3	One electron energy level and atomic orbital plots of V.	152
E.4	MO energy level diagrams and isosurface plot of ${}^4\text{VAg}_9^+$	153

List of Tables

1.1	List of works reported for Mg_N clusters. Abbreviations : n=Neutral, a=Anion, c=Cation, QC=Quantum chemistry methods, Freq=Frequency, BE=Binding energy, FE=Fragmentation energy, and AE=Atomization energy.	13
1.2	Summary of theoretical works on Ca_N clusters. Abbreviations : GO=Global optimization, CI=Configuration interaction, TB=Tight binding model. Rest of the abbreviations are given in Table 1.1.	14
1.3	Summary of theoretical works on Sr_N clusters.	15
1.4	Expected electronic shell closings and the corresponding closed shell neutral, anionic and cationic clusters of trivalent Al.	17
1.5	List of theoretical works on Al_N clusters. Abbreviation : APES= Angle resolved PES.	18
1.6	Observed Shell features in $Au_N X^+$. n_v is the number of delocalized electrons coming from the TM and n_e is the total number of delocalized electrons corresponding to closed electronic shells [95].	27
3.1	HL gap, hardness (η) and ΔE_{spin} of the $TMCa_8$ clusters.	62
3.2	Atomic spins in $TMCa_8$ (TM=Sc, V, Cr, Mn, Fe and Co) clusters using Mulliken population analysis.	67
3.3	HL gap, adiabatic spin excitation (ΔE_{spin}), hardness (η) and $\Delta_2(N)$ of $FeCa_N$ clusters. All the values are given in eV.	70
3.4	Atomic spins in $FeCa_N$ clusters using Mulliken population analysis.	73
3.5	TM-AE, r_h and r_v bond lengths and ground state electronic configurations of $TMAE_8$ clusters. All the bond lengths are given in Å.	76

4.1	The HL gap, ΔE_{spin} and hardness (η) of TMSr_8 clusters.	83
4.2	Atomic spins in TMSr_8 clusters obtained by Mulliken population analysis.	87
4.3	The average TM-AE (AE=Ca,Sr), r_h bond lengths and the ground state electronic configurations of $\text{TM}(\text{AE})_8$ clusters. Here AE are Ca and Sr. r_h is distance between AE-AE atoms within a plane, while distance between the two planes is given by r_v . All the bond lengths are given in Å.	88
5.1	The HL gap, η , ΔE_{spin} , and $\Delta_2(N)$ of CrSr_N clusters. All the values are given in eV.	96
5.2	Atomic spins in the CrSr_N clusters using Mulliken population analysis. 100	
5.3	The HL gap, adiabatic spin excitation (ΔE_{spin}), hardness (η) and $\Delta_2(N)$ of MnSr_N clusters. All the values are given in eV.	102
5.4	Atomic spins in the MnSr_N clusters obtained by Mulliken population analysis.	104
6.1	HL gap, adiabatic spin excitation (ΔE_{spin}), hardness (η) and $\Delta_2(N)$ of CrAl_N clusters.	110
6.2	HL gap, adiabatic spin excitation (ΔE_{spin}), hardness (η) and $\Delta_2(N)$ of MnAl_N clusters.	111
6.3	The HL gap, adiabatic spin excitation energy (ΔE_{spin}), hardness (η) and $\Delta_2(N)$ of FeAl_N clusters.	112
6.4	The HL gap, hardness (η) and ΔE_{spin} of TMAI_4 clusters. All values are given in eV.	114
6.5	The HL gap, adiabatic spin excitation (ΔE_{spin}), hardness (η) and $\Delta_2(N)$ of CoAl_N clusters. All values are given in eV.	115
6.6	The HL gap, hardness (η) and ΔE_{spin} of TMAI_3 clusters. All values are given in eV.	116
6.7	Contribution of the TM and Al atomic orbitals to the frontier orbitals in the TMAI_3 clusters. Also contributions of the d orbitals of the TM atoms and sp atomic orbitals of Al atoms are given.	120

6.8	Contribution of the TM and Al atomic orbitals to the frontier orbitals in the TMAI_4 clusters. Also contributions of the d orbitals of the TM atoms and sp atomic orbitals of Al atoms are given.	120
6.9	Multiplicity ($M=2S+1$) and NICS values for TMAI_3 and TMAI_4 clusters.	121
6.10	Multiplicity ($M=2S+1$) and NICS values for FeAl_N and CoAl_N clusters.	122
7.1	The HL gap and $\Delta_2(N)$ values of VAg_N^+ and VAg_N clusters. All the values are given in eV.	127
7.2	ΔE_{Ag} values of VAg_N^+ and VAg_N clusters. All the values are given in eV.	127
7.3	Adiabatic and vertical ionization potential of VAg_N clusters.	128
7.4	Fragmentation energies of VAg_N^+ clusters. All values are given in eV. .	129
D.1	HL gap, Adiabatic spin excitation (ΔE_{spin}), Hardness (η) and $\Delta_2(N)$ of NiAl_N clusters.	149

Introduction

1.1 Atomic clusters

Atomic clusters are aggregates of atoms consisting of a few to a few hundred atoms. Because of the wide range of their possible sizes, compositions and charge states, atomic clusters constitute virtually a new ‘phase’ of matter with properties distinct from those of an atom and the corresponding bulk. Difference in properties with respect to the bulk arises primarily because of two reasons: first, unlike bulk, the number of atoms on the surface of a cluster is a substantial fraction of the total number of atoms; second, the arrangement of atoms in a cluster is generally very different from that in the corresponding bulk. Clusters are also distinct from molecules. For instance, molecules are typically formed by either covalent or ionic bonds between the atoms, while bonding within clusters could be metallic, covalent, van der Waals or ionic. Molecules are very stable against coalescing, whereas clusters are metastable objects. The most striking feature of atomic clusters is an extreme size-dependence of electronic, magnetic, chemical and optical properties. Addition or removal of even one atom or one electron can induce dramatic changes in these properties [1].

For an ease of analysis and understanding, atomic clusters can be classified in various ways. One convenient classification is based on the types of the constituent atoms and the nature of bonding between them. One talks about (i) semiconductor clusters such as Ge_N , Si_N , (ii) ionic clusters, such as $(\text{NaCl})_N$ (iii) rare gas clusters, such as Ar_N , (iv) metal clusters with metallic bonding such as Na_N and Au_N . In this thesis we will focus only on the metal clusters.

1.2 Metal clusters

During the last three decades, metal clusters have been the most extensively explored class of clusters by experimental and theoretical means. Clusters formed by atoms that form metallic systems in the bulk are termed metal clusters. Metal clusters can be further subdivided into simple metal, noble metal, transition metal (TM), and mixed or alloy clusters.

1.2.1 Simple metal clusters

We term clusters composed of group-IA (alkali), group-II, and group-IIIA metal elements as simple metal clusters. Bonding between the atoms in these clusters is largely through the delocalized outermost s and p orbitals. A characteristic feature of simple metal clusters is a greater stability of clusters having certain specific number of valence electrons compared to their neighbors [1, 3, 4]. This stability has been explained in terms of simple quantum mechanical models which are known as shell models.

1.2.2 Noble metal clusters

Clusters of group-IB elements (Cu, Ag and Au) are termed noble metal clusters. Because of ns^1 electronic configuration of these atoms, they also share many properties of the alkali clusters [25]. However due to the presence of $(n-1)d^{10}$ electrons, structural evolution of noble metal clusters is found to be different from that of alkali clusters. For example, Cu_N clusters having more than 3 atoms assume 3D structures [26, 27], while alkali metal clusters adopt 3D structures when they have more than 6 atoms [2].

1.2.3 Transition metal clusters

TM elements of $3d$, $4d$, and $5d$ series form TM clusters. In contrast to simple metal and noble metal clusters, presence of partially filled d orbitals leads to completely different and irregular variation in the electronic and geometric properties as the cluster size increases. Generally, instead of having electronic shells (discussed in next subsection), TM clusters form compact atomic arrangements like icosahedral or cuboctahedral structures. The most exciting feature of these clusters is the size evolution of magnetic properties. For example, Fe_N and Co_N clusters have higher magnetic moments compared to the corresponding ferromagnetic bulk [28].

1.2.4 Mixed clusters

Mixed or heteroatomic metal clusters can be thought of miniature versions of metallic alloys [10, 29]. An interesting class of mixed clusters is TM doped simple and noble metal clusters which are suitable candidates to understand the effects of non-magnetic environment on the localized magnetic moment of a TM atom. Apart from that, one can study how the geometric and electronic evolution of pure metal clusters are affected by an impurity atom [6].

1.3 Electronic shell structure and shell models

In 1984, Knight *et al* [4] measured the mass abundance spectrum of Na_N clusters which showed a non-monotonic behaviour with respect to the size (N) of the clusters. Particularly sharp drops in the intensity were observed just after $N=8, 20, 40,$ and 58 as shown in Figure 1.1. In the mass abundance spectrum of gas phase clusters, peaks of higher intensity indicate greater stability of those clusters with respect to their neighbors. Thus Na_N clusters at $N=8, 20, 40, 58$ are more stable. These

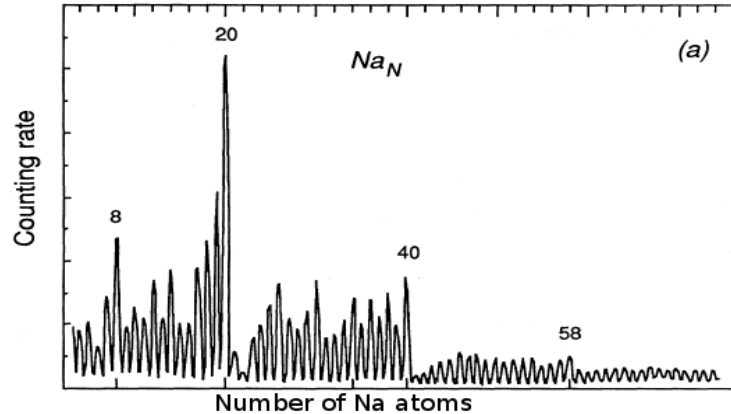


Figure 1.1: Mass abundance spectrum of Na_N clusters [4].

clusters are termed magic clusters. Magic clusters were also observed in experiments on various other simple metal and noble metal clusters [1].

Origin of this enhanced stability at certain sizes can be understood in terms of simple quantum mechanical models. The common assumption of all these models is that the valence electrons of all the metal atoms move freely within a finite region of space defined by the ‘volume’ of the cluster. Depending on the symmetry of the confining potential, quantum confinement leads to discrete electronic energy levels with degeneracies. These simple quantum mechanical shell models provide us with

an elegant electron counting rule through which we can understand the electronic and chemical properties of simple metal clusters. Electronic properties of noble metal clusters, particularly Cu_N and Ag_N , are also understood within shell models [1]. I now briefly describe different shell models proposed and used in the literature.

1.3.1 Spherical Shell Models

In the spherical shell models, as the name suggests, the potential confining the valence electrons is assumed to be spherically symmetric. The radius of the confining sphere R_0 is taken as

$$R_0 = xN^{1/3}r_s \quad (1.1)$$

where r_s is the Wigner-Seitz radius in the corresponding bulk and x is the valence of the metal atom. In the simplest of these models, the valence electrons experience a potential $V(\vec{r})$ which is given by

$$\begin{aligned} V(\vec{r}) &= 0 ; r < R_0 \\ &= \infty ; r \geq R_0 \end{aligned} \quad (1.2)$$

Since the valence electrons feel an infinite potential at the boundary, this model can be termed as the ‘hard sphere’ model. By solving the Schrödinger’s equation, one can obtain the one-electron energy levels E_{nl} of this model :

$$E_{nl} = \frac{\hbar^2 \beta_{nl}^2}{2mR_0^2} \quad (1.3)$$

where β_{nl} is the n^{th} order zero of the spherical Bessel function j_l . Since the potential has spherical symmetry, energy eigenstates are also angular momentum eigenstates and possess $2(2l+1)$ fold degeneracies. These energy eigenstates form the electronic shells (n, l) which are arranged in increasing energy as $1\text{S}^2, 1\text{P}^6, 1\text{D}^{10}, 2\text{S}^2, 1\text{F}^{14}, 2\text{P}^6, 1\text{G}^{18}$... as shown in Figure 1.2(c). Thus electronic shells will be completely filled when there are 2, 8, 18, 20, 34, 40, 58, ... electrons in the cluster. As filled electronic shells lead to greater stability in atoms, filled shell clusters are expected to be more stable. Therefore Na_N clusters with $N=8, 20, 40, 58, \dots$ electrons will be more stable. Note that this model also predicts stable clusters at $N=18, 34,$ and 68 which were not found with high intensity in the spectrum (see Figure 1.1).

One may choose softer boundaries for the confining potential. One such widely

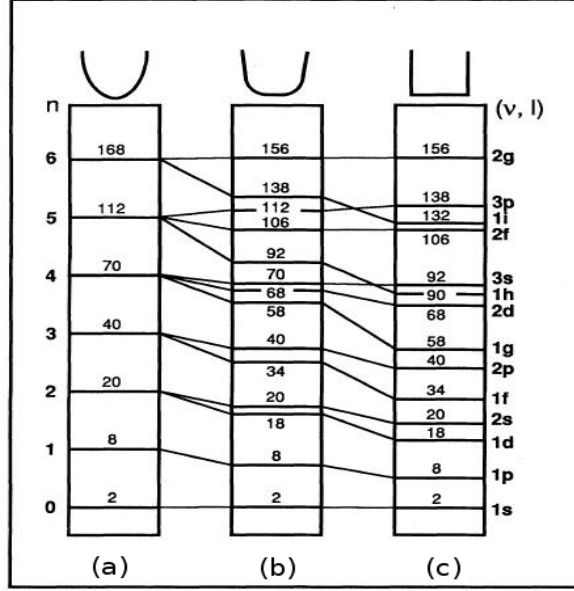


Figure 1.2: Energy level occupation for (a) spherical three dimensional harmonic, (b) intermediate (Woods-Saxon), and (c) square-well potentials [1].

used model is the spherical harmonic potential $V(\vec{r}) = \frac{1}{2}m\omega_0^2r^2$. ω_0 is the harmonic oscillator frequency. Energy eigenvalues for this potential are well known and are given by

$$E_n = \hbar\omega_0(n + 3/2) \quad (1.4)$$

where n is quantum number given by $(2\nu+l-2)$ with $\nu=1, 2, 3 \dots$, and l is the angular momentum quantum number. Figure 1.2(a) shows that energy eigenstates having the same value of $(2\nu + l - 2)$ are degenerate. Hence energy eigenstates are in the following order-1S, 1P, (1D,2S), (1F,2P), (1G,2D,3S), (1H,2F,3P), ... Eigenstates within parentheses are degenerate in energy. Completely filled electronic shells will result when there are 2, 8, 20, 40, 70, 112 ... electrons in the cluster.

Figure 1.2(b) shows energy states for the Woods-Saxon potential given by

$$V(\vec{r}) = -\frac{U_0}{e^{(r-R_0)/\lambda} + 1} \quad (1.5)$$

where U_0 is taken equal to the sum of the Fermi energy and the work function of the bulk [4]. λ controls the variation of the potential near the boundary. Since the potential is spherically symmetric, the energy eigenstates are again $2(2l+1)$ -fold degenerate. We can see from Figure 1.2(b) that magic clusters again occur for valence electron counts of 18, 34, 58, 68, 92 etc. in addition to 2, 8, 20, 40 and 70. One

may notice that the shell model with harmonic potential does not predict the magic numbers 58 and 92 at which stable clusters were found in the Figure 1.1.

1.3.2 Clemenger-Nilsson shell model

Though the shell models discussed in the previous section were quite successful in explaining the relative stability of magic clusters, they were not able to capture the fine structure of the mass abundance spectrum. This is a consequence of the assumed spherical shape of the clusters. Indeed shape of an open shell cluster does not need to be spherical. To explain the fine structure of the mass spectrum, Clemenger [5] proposed a model based on the ideas of Nilsson model. This model is known as Clemenger-Nilsson shell model. The basic idea is to introduce spheroidal deformations in a 3D harmonic oscillator confining potential. In spheroidal deformations, two semi-axes (R_x) and (R_y) were taken equal and the third (R_z) could be different, with the constraint that the volume of the cluster remains unchanged. This constraint is imposed through the condition

$$R_x R_y R_z = R_0^3 \quad (1.6)$$

The distortion parameter for a spheroidal deformation was defined as

$$\eta = 2 \frac{R_z - R_x}{R_z + R_x} \quad (1.7)$$

Based on the whether R_z is greater or smaller in comparison to R_x , clusters will have prolate or oblate shape respectively. Figure 1.3 shows the optimal values of the distortion parameter η that minimize the total energy of the cluster at different numbers of valence electrons. The basic idea in this model is that for a given number of electrons, the cluster's shape adjusts itself keeping the volume constant to minimize the total electronic energy. We can see that closed shell clusters, i.e., clusters with 2, 8, 20 electrons are spherical ($\eta=0$), while open shell clusters are either prolate or oblate spheroids. For instance, η has positive values for clusters with 3 and 4 electrons, thus they have prolate shapes. Clusters with 5, 6, and 7 electrons are oblate as indicated by the negative values of η . Also one should notice that in the spheroidal model, clusters with 18 and 34 electrons turn out to be non-spherical.

To see the stability of a cluster with N atoms with respect to adjacent clusters, Knight *et al* [4] and Clemenger [5] calculated the second order energy differences ($\Delta_2(N)$) for Na_N clusters with total energies (E) obtained from spherical and

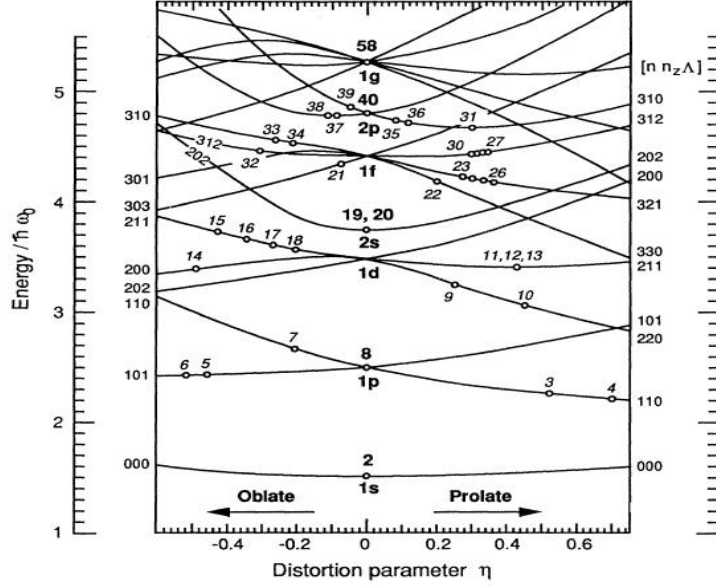


Figure 1.3: Total electronic energy curves as functions of η for the 3D harmonic potential. Open circles denote the optimal values for the valence electron counts given next to the circles [1, 5].

spheroidal shell models respectively. $\Delta_2(N)$ is defined as

$$\begin{aligned}
 \Delta_2(N) &= E(N+1) + E(N-1) - 2E(N) \\
 &= [E(N+1) - E(N)] + [E(N-1) - E(N)] \\
 &= \Delta(N+1) - \Delta(N)
 \end{aligned} \tag{1.8}$$

where $\Delta(N)$ is the first order energy difference and given by $\Delta(N) = E(N) - E(N-1)$. $\Delta_2(N)$ represents the relative stability of a cluster with N atoms with respect to clusters with $N+1$ and $N-1$ atoms. Peaks in $\Delta_2(N)$ vs N will occur whenever an electronic energy level is exactly filled at specific N and next higher energy orbital is occupied for a cluster with $N+1$ atoms. Results of $\Delta_2(N)$ obtained by Knight *et al* and Clemenger [5] for the Woods-Saxon and deformable harmonic oscillator potentials are shown in the panels (A) and (B) of Figure 1.4 respectively. We can see from the Figure 1.4(B) that the spheroidal model not only captures the stability of the closed shell clusters but also produces the observed fine structure at $N=6, 12, 14, 18, 26, 30, 34, 50, 54$, etc. On the other hand, only stability of the closed shell clusters appeared in the Figure 1.4(A).

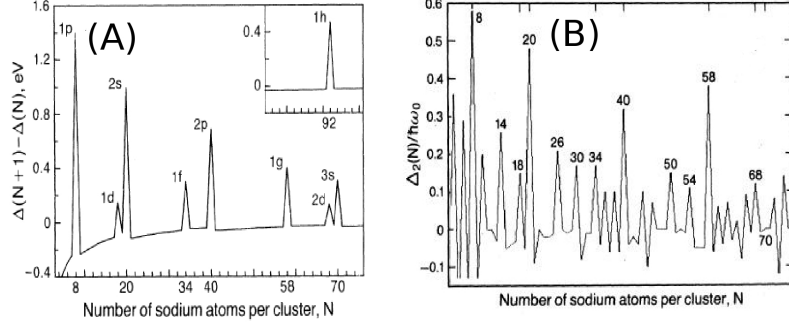


Figure 1.4: (A) Change in the electronic energy difference, $\Delta(N+1)-\Delta(N)$ vs N . [4] (B) Second order energy difference for Na_N clusters using harmonic oscillator potential with spheroidal distortions [5].

1.3.3 Jellium model

Jellium model is a more realistic model compared to shell models discussed so far as it includes the Coulomb interaction between the valence electrons. However, the discrete nature of the ionic cores are neglected and the entire positive charge is uniformly distributed over the spherical shape of a cluster of radius R_0 as a static background having density $n_+(\vec{r})$. Positive charge density $n_+(\vec{r})$ is given by

$$n_+(\vec{r}) = n_+^0 \theta(R_0 - r) \quad (1.9)$$

while $\theta(R_0 - r)$ is the step function, and has value 1 for $r \leq R_0$ and 0 for $r > R_0$. The radius of the cluster is given by Eqn. 1.1. Uniform positive charge density of the background yields an attractive potential for valence electrons

$$V(\vec{r}) = - \int \frac{n_+(\vec{r}')}{|\vec{r} - \vec{r}'|} d^3\vec{r}' \quad (1.10)$$

Chou *et al* [30] used density functional theory (DFT) within the local density approximation (LDA) to calculate the ground state of interacting electrons subject to this potential. They obtained closed electronic shell for the Na_{40} cluster with electronic configuration $1S^2 1P^6 1D^{10} 2S^2 1F^{14} 2P^6$ as obtained in the shell models. Similar to shell models, jellium model is very successful in explaining the magic numbers of simple metal clusters, but it does not explain the fine structure of the mass abundance spectrum. However, one can relax the constraint of spherical shape of the background charge distribution and allow deformations as done in the Clemenger-Nilsson model. Then the fine structure in the mass abundance spectrum is captured [31, 32].

1.4 Monovalent (group-IA and-IB) clusters

We have seen that electronic shell structures control the stability of the Na_N clusters. Other alkali metal (K_N , Cs_N) clusters were also found to have enhanced stability at $N=2, 8, 20, 40$ [33, 34]. Similarly, mass abundance spectrum of Ag_N^+ , Au_N^+ , and Cu_N^+ clusters showed large peaks at $N=3, 9, 21, 35, 41, 59, 93, 139$. Spherical shell models easily explain the stability of these clusters [25]. We know that ionization potential (IP) and electron affinity (EA) reveal the electronic shell effects in atoms. For example, alkali atoms are known to have low IP's because they have only a single valence electron in the outermost shells, while halogens possess high EA's as they are just one electron short of filled shell configuration. Thus it is expected that IP's and EA's of these metal clusters will provide a glimpse of their underlying electronic shell structures.

1.4.1 IP's and shell effects

Ionization potential of a cluster is defined as

$$\text{IP} = E_N^+ - E_N \quad (1.11)$$

It is the energy required for extracting an electron from the neutral cluster. The corresponding quantity for the bulk is known as the work function. IP's are measured in photo-ionization experiment in which clusters are ionized by a laser of tunable frequency. In photo-ionization experiment cluster ions (cations) relax into their ground state structures which are generally different from those of the corresponding neutral clusters. However, according to Frank-Condon principle, structural transitions are much slower than electronic transitions. Therefore removal of an electron leaves the ionized cluster with instantaneously negligible structural changes. Consequently one can define two ionization potentials, the vertical ionization potential (VIP), and the adiabatic ionization potential (AIP). VIP is defined as the energy difference between the neutral and cation clusters, both at the structure of the neutral. The AIP is the difference in the ground state energies of the neutral and the cation clusters. Generally, difference between the AIP and VIP is large for small clusters where structural changes are large, while for large size clusters, this difference is small. Left panel in the Figure 1.5 shows the IP's of Na_N and K_N clusters measured in photo-ionization experiments. In addition to odd-even oscillations, there are sharp drops in IP's at $N=9, 19, 21, 41, 59, \text{ and } 93$ for Na_N clusters. Similar features are also observed

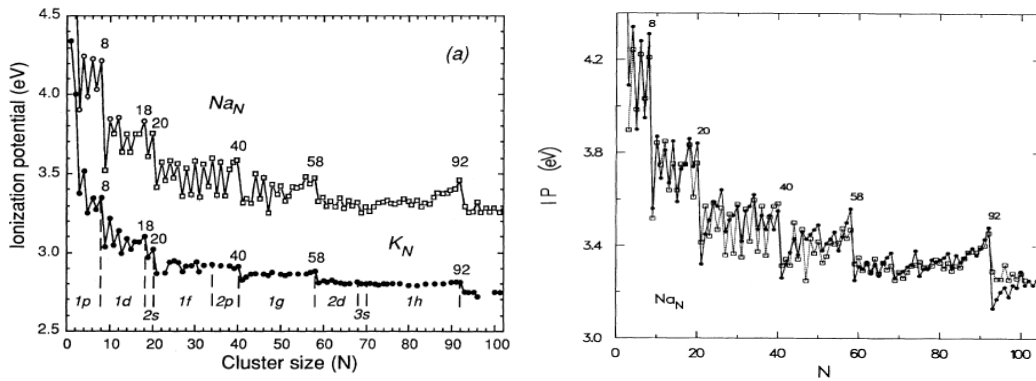


Figure 1.5: (Left) Ionization potentials of sodium and potassium clusters as function of their size [1]. (Right) Theoretical results derived from the Clemenger-Nilsson ellipsoidal model. Open squares show experimental IP's [35].

in the K_N clusters. Sharp drops in IP's just after $N=8, 18, 20, 40$ can be easily understood from the fact that the energy required to remove the single electron in the outermost shells is much lower compared to the energy required to remove an electron from a filled shell. Yannouleas *et al* [35] calculated the IP's for Na_N clusters using the Clemenger-Nilsson ellipsoidal model as shown in the right panel of Figure 1.5. This model not only shows high IP's for magic clusters, but also produces the odd-even effect. This critical observation demonstrates the applicability of the ellipsoidal shell model for monovalent clusters. Similar shell effects were observed in the experimental measured IP's of Li_N [36] and noble metal clusters (Cu_N, Ag_N) [37, 38].

1.4.1.1 EA's and shell effects

Just like a halogen atom which has a high EA in order to complete its electronic shell, clusters with one electron short of closed electron shells are expected to have high EA's. The electron affinity of a cluster is defined as the energy difference between the neutral and anionic cluster.

$$EA = E_N - E_N^- \quad (1.12)$$

Experimentally it is extracted from photoelectron spectroscopy (PES) in which an anionic cluster is irradiated with a photon of fixed frequency. The kinetic energy of the ejected photoelectron is measured subsequently. The kinetic energy (KE) of the

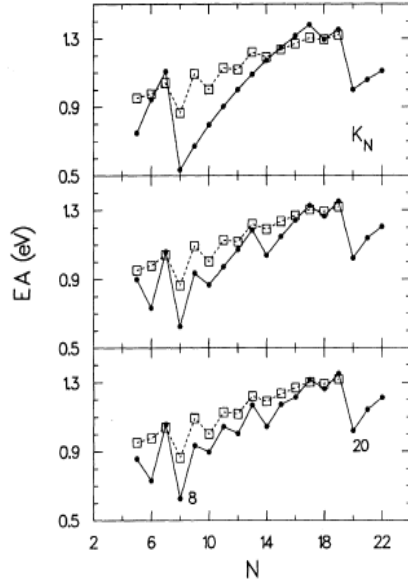


Figure 1.6: Open squares show experimentally measured EA's of $K_{N=5-22}$ clusters [40], Top panel : The spherical model compared to experimental data. Middle panel : The spheroidal model compared to experimental data. Lower panel : The ellipsoidal model compared to experimental data [35].

emitted electron is given by

$$KE = h\nu - EBE \quad (1.13)$$

where ν is photon frequency and EBE is the electron binding energy of the photoemitted electron in the cluster. It is the EBE of an electron in the highest molecular orbital (HOMO) of the anion cluster which gives the EA of the corresponding neutral cluster within Koopmans' theorem [39]. One can define adiabatic electron affinity (AEA) and vertical detachment energy (VDE) in a way similar to IP's. AEA is defined as the energy difference between the ground states of the anion and the neutral clusters, and VDE of a given anion cluster is the energy difference between the anion and the neutral both at the anion geometry. AEA is also equivalent to adiabatic detachment energy (ADE) of the anion clusters. Top, middle and lower panels of Figure 1.6 demonstrate the applicability of spherical, spheroidal and ellipsoidal shell models by comparing the theoretically calculated EA's of K_N , $N=5-22$ with measured EA's [40]. We can easily see that high EA's are indicated by peaks at $N=7, 17, 19$ while low EA's are associated with the magic clusters in all three models. However with the spheroidal and ellipsoidal models, a significantly better agreement (odd-even oscillations) between the theory and experiment was achieved. Similarly,

drops in EA's after $N=7, 17, 19, 33,$ and 39 of Cu_N and Ag_N clusters were measured by Pettiette *et al* [41] and Ganteför *et al* [42,43].

Apart from the EA's, anion PES also provides the energy gap between the highest occupied molecular orbital (HOMO) and lowest unoccupied molecular orbital (LUMO) of the neutral cluster. This gap is known as HOMO-LUMO (HL) gap. A large HL gap is an indicator of its chemical stability as clusters will resist both donating and accepting electrons. If HOMO of the neutral cluster is fully occupied, then it is the EBE difference of the first two peaks in the low binding energy end of PES of its anion which provides the HL gap of the neutral cluster.

1.5 Shell effects in other metal clusters

1.5.1 Divalent (group-IIA) metal clusters ($\text{Mg}_N, \text{Ca}_N, \text{Sr}_N$)

Since shell models account for the electronic shell closure of the monovalent clusters at $n_e=2, 8, 18, 20, 34, 40, 58, 68, 90, 92,$ etc., where n_e is the number of valence electrons, divalent clusters with enhanced stability are expected to appear at $N = n_e/2$. In this section we will particularly focus on the applicability of shell models to $\text{Mg}_N, \text{Ca}_N,$ and Sr_N clusters. Apart from the validity of shell models, the most interesting feature of these clusters is the nature of bonding between the atoms which evolves as the cluster size increases. Because of the closed electronic (ns^2) shells of these atoms, the dimers are bound by van der Waals forces, while in the bulk they have metallic characteristics due to complete overlap of the s and p bands which originate from the s and p atomic orbitals. To study the emergence of metallic behaviour in these clusters, one can monitor the gap between the s and p bands with respect to size N . In general this s - p band gap tends to decrease as the cluster size increases and eventually both bands merge at a critical size. Therefore many studies have been dedicated to finding the critical size at which 'insulator to metal transition' (IMT) occurs.

1.5.1.1 Mg_N clusters

Diederich *et al* [44] obtained the mass abundance spectrum of bare Mg_N clusters upto $N=80$ by the pickup of atoms in helium nanodroplets. By examining the spectrum, stable clusters were observed at $N=5, 10, 15, 18, 20, 25, 26, 28, 30, 35, 40, 46, 47, 56, 59, 62, 69,$ and 74 . Also exceptionally pronounced minima were found at $N=22, 37, 57,$ and 71 . Assuming each Mg atom gives 2 valence electrons, stability of the clusters

at $N=10, 15, 20, 25, 35,$ and 46 can be easily interpreted in terms of the spheroidal model (Figure 1.4B). To explain the stability of clusters at $N=26, 30, 40, 56, 59, 62, 69,$ and 74 Diederich *et al* introduced an energy level crossing mechanism between the high angular-momentum (l) and low angular-momentum quantum states within the spherical shell model. However, stability of clusters at $N=5, 18,$ and 47 was not clear. Also, there were no signs of shell-closing at $N=4$ and 9 in the spectrum.

Thomas *et al* [45] measured the mass abundance spectrum of $\text{Mg}_{N=3-30}^-$ clusters in which intense peaks were seen at $N=4, 9, 19, 34, 46, 55,$ and 69 . These authors explained the stability of $\text{Mg}_9^-, \text{Mg}_{19}^-, \text{Mg}_{34}^-$ via closed electronic shells. For example, these clusters are just one electron short of having closed electronic shells with $20, 40,$ and 70 electrons respectively. However continuing this argument, stability of Mg_4^- was not clear. Furthermore, by examining PES of $\text{Mg}_{N=3-30}^-$, Thomas *et al* observed a gradual decrease in the sp band gap with local peaks at $N=4, 10,$ and 20 . These local peaks could be attributed to closed electronic shell with $8, 20,$ and 40 valence electrons.

Authors	Element	Charge	Range	Methods	Properties studied
Lee <i>et al</i> [46]	Mg	n	≤ 4	QC	BE and Freq
Klopper <i>et al</i> [47]	Mg	n	≤ 4	QC	BE
Bauschlicher <i>et al</i> [48]	Mg	n	4	QC	AE
Reuse <i>et al</i> [49]	Mg	n, a, c	≤ 6	DFT	EA
Reuse <i>et al</i> [50]	Mg	n, a, c	≤ 7	DFT	AE, IMT, FE, and EA
Acioli <i>et al</i> [51]	Mg	a	2-22	DFT	BE, HL gap, IMT
Jellinek <i>et al</i> [52]	Mg	n,a	2-22	DFT	BE, HL gap, $\Delta_2(N)$, and VIP
Kumar <i>et al</i> [53]	Mg	n	2-13	MD	$\Delta_2(N)$, HL gap, and IMT
Delaly <i>et al</i> [54]	Mg	n	≤ 20	DFT	BE
Akola <i>et al</i> [55]	Mg	n	≤ 13	DFT	$\Delta_2(N)$, HL gap, and IMT
Serra <i>et al</i> [56]	Mg	n	≤ 50	DFT	
Köhn <i>et al</i> [57]	Mg	n	2-22	DFT	BE and $\Delta_2(N)$
Lyalin <i>et al</i> [58]	Mg	n,c	2-21	DFT	BE, $\Delta_2(N)$, IP, and HL gap

Table 1.1: List of works reported for Mg_N clusters. Abbreviations : n=Neutral, a=Anion, c=Cation, QC=Quantum chemistry methods, Freq=Frequency, BE=Binding energy, FE=Fragmentation energy, and AE=Atomization energy.

Table 1.1 gives a summary of theoretical studies of $\text{Mg}_N^{0/+/-}$ clusters reported in the literature. The equilibrium geometries and electronic properties of Mg_N clusters having less than 7 atoms were explored with ab-initio and DFT methods [46–50]. Acioli *et al* [51] and Jellinek *et al* [52] provided theoretical support to the observations made in Ref [45] by performing density functional calculations of the neutral and anion Mg_N ($N=2-22$) clusters. Local peaks in the HL gap and $\Delta_2(N)$ were observed at $N=4, 7, 10, 15,$ and 20 . Greater stability of these clusters was understood via

the spheroidal shell model. Similar findings were obtained by Kumar *et al* [53] in the density functional molecular dynamics simulations for $\text{Mg}_{N=2-13}$ clusters. The peaks in $\Delta_2(N)$ showed stability for Mg_4 , Mg_7 , Mg_9 , and Mg_{10} clusters. Recently, Lyalin *et al* [58] has reported extensive density functional calculations for neutral and cation $\text{Mg}_{N=2-21}$ clusters. These authors found stable clusters at $N=4, 7, 10, 13, 15, 17$, and 20 as indicated by the $\Delta_2(N)$ and HL gap. Again these stabilities were explained in terms of the spheroidal shell model.

1.5.1.2 Ca_N clusters

Unfortunately there are no mass abundance spectra available for Ca_N clusters focusing on the small sizes. But mass abundance spectrum for Ca_N ($N=1-5000$) clusters was reported by Martin *et al* [59,60]. Because of the poor resolution of mass abundance spectrum, any feature of the electronic shell structure within the size range $N=1-100$ was not resolved. Nevertheless these studies revealed the fact that growth sequence of the clusters was determined by the closed geometric shells rather than closed electronic shells.

Table 1.2 shows a short summary of various theoretical studies which were dedicated to investigating the electronic and geometric properties of Ca_N clusters.

Authors	Element	Charge	Range	Methods	Properties studied.
Hearn <i>et al</i> [61]	Ca,Sr	n	≤ 20	GO	BE and $\Delta_2(N)$
Mirick <i>et al</i> [62]	Ca	n	3-13	DFT	IMT and HL Freq and $\Delta_2(N)$
Dai <i>et al</i> [63]	Ca	n, a	2-19	DFT	EA and Freq
Pacchioni <i>et al</i> [64]	Ca	n	≤ 5	QC(CI)	IMT, IP
Dong <i>et al</i> [65]	Ca	n, c	6-13, 32-84	TB	Freq, HL, and $\Delta_2(N)$
Blaisten-Barojas <i>et al</i> [66]	Ca	c	≤ 8	DFT	Frag.

Table 1.2: Summary of theoretical works on Ca_N clusters. Abbreviations : GO=Global optimization, CI=Configuration interaction, TB=Tight binding model. Rest of the abbreviations are given in Table 1.1.

Hearn *et al* [61] optimized structures of Ca_N clusters with the empirical potential of Murrell and Mottram (MM) which has two- and three-body interactions. In their study icosahedral growth was preferred over the truncated decahedral, cuboctahedral, and rhombic dodecahedral growth. $\Delta_2(N)$ was shown with local peaks at $N=4, 7, 13$, and 19 . The stability of clusters at $N=4, 7, 13$, and 19 can be described by the spheroidal shell model. Local maxima at $N=13$ and 19 can be interpreted in terms of close packing structures which act as building blocks for icosahedral growth [1].

On the contrary, first-principles studies by Mirick *et al* [62] and Dai *et al* [63] showed peaks in $\Delta_2(N)$ for Ca_{10} alongwith Ca_4 , Ca_7 [62,63], Ca_{13} , and Ca_{17} [63]. The HL gap was shown to decrease as the cluster size increases but there were local peaks at $N=4, 7$, and 10 [62]. Again the spheroidal shell model was invoked to explain the peaks in $\Delta_2(N)$ and HL gap for Ca_4 , Ca_7 , and Ca_{10} . Dai *et al* [63] calculated the EA's of the neutral clusters which show a sharp dip at $N=10$. This sharp dip in EA was understood in terms of the closed electronic shell with 20 valence electrons.

1.5.1.3 Sr_N clusters

Unlike Ca_N clusters, strontium clusters have been explored in more detail, specifically at lower sizes. Dugourd *et al* [67] observed Sr_3 and Sr_4 clusters with prominent peaks in the mass abundance spectrum. The measured IP (4.73 eV) of Sr_2 was in excellent agreement with the classical conducting sphere model [1]. Therefore these authors argued that small Sr_N clusters can be approximated by a metallic sphere. Bréchnignac *et al* [68] measured the mass abundance spectrum of photoionized singly charged Sr_N^+ clusters. Local peaks were found at $N=11, 19, 23, 34, 43, 52, 61$, and 81 . While the stability at $N=34$ can be understood in terms of the spheroidal model, observed sequence of the peaks was found to be different from that observed in other alkaline earth metal clusters [69]. In particular, peaks at $N=13$ and 55 characterizing the icosahedral compact structure were absent.

Authors	Element	Charge	Range	Methods	Properties studied.
Wang <i>et al</i> [70]	Sr	n	≤ 63	DFT, GO	Freq and $\Delta_2(N)$
Kumar <i>et al</i> [71]	Sr	n	2-35 55 & 147	MD	HL and $\Delta_2(N)$
Wang <i>et al</i> [72]	Sr	n	2-13	QC	IP, EA, HL, and Freq
Lyalin <i>et al</i> [73]	Sr	n, c	2-14	DFT	HL and $\Delta_2(N)$

Table 1.3: Summary of theoretical works on Sr_N clusters.

Wang *et al* [70] measured the fine mass abundance spectrum for Sr_N clusters containing up to 96 atoms. Intense mass peaks were observed at $N=34$ and 61 . Even though Sr_{34} and Sr_{61} have 68 and 112 valence electrons corresponding to closing of electronic shells, their stability was argued in terms of their compact structures.

Similar to Ca_N , structures and stability of Sr_N up to 20 atoms had been investigated with the empirical potential of MM [61]. Local maxima in $\Delta_2(N)$ were found at the same sizes as for Ca_N [61]. The evolution of electronic states and multi-shell relaxation in Sr_N , $N=2-35, 55$, and 147 was studied by ab-initio molecular dynamics

with plane wave basis and ultra-soft pseudopotential [71]. The HL gap was shown to have local maxima at $N=4, 7, 13, 19, 23, 26, 29,$ and 33 . The spheroidal shell model can explain the stability of these clusters except for $N=26$. Recently, density functional calculations of Sr_N ($N=2-14$) clusters have been carried out by Lyalin *et al* [73]. An interplay between the electronic and geometric shell closure was shown to control the size evolution of their electronic and structural properties. Also HL gap and $\Delta_2(N)$ were found to have local maxima at $N=4, 7, 10,$ and 13 in agreement with the spheroidal shell model [73]. Table 1.3 summarizes various theoretical studies of Sr_N clusters.

In summary, there are differences (local peaks at different sizes) in the mass abundance spectrum of group-IIA metal clusters. There are also common electronic shell features, specially at $N=4, 7, 10,$ and 20 for $\text{Mg}_N, \text{Ca}_N,$ and Sr_N clusters. In addition, geometric effects also play an important part in stabilities of these clusters at large sizes.

1.5.2 Trivalent metal clusters (Al_N clusters)

Aluminium clusters are one of the most extensively studied class of clusters. In the bulk, Al ($[\text{Ne}]3s^23p^1$) shows the characteristics of a metal because of a complete hybridization of the $3s$ and $3p$ bands originating from the atomic $3s$ and $3p$ orbitals. Therefore electronic shell effects, a common feature of the alkali and noble metal clusters were expected for Al_N clusters. Table 1.4 shows the possible electronic shell closings for the neutral and singly charged Al_N clusters by assuming that each Al atom provides three valence electrons.

Schrivier *et al* [74] measured the IP's of Al_N clusters as shown in the Figure 1.7. IP's show a sharp rise up to $N=4$ (in fact higher than atomic IP 5.98 eV), and drops

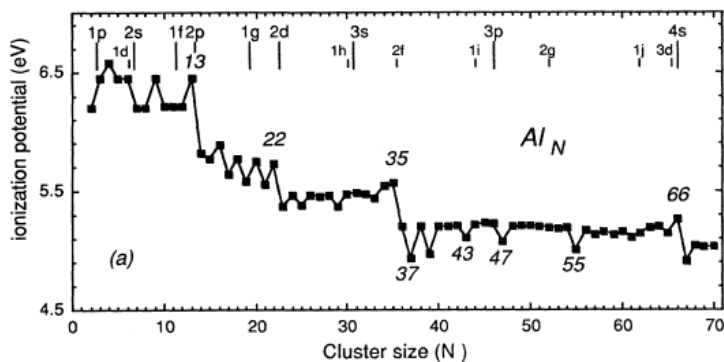


Figure 1.7: Experimentally measured ionization potentials of Al_N clusters [74].

Table 1.4: Expected electronic shell closings and the corresponding closed shell neutral, anionic and cationic clusters of trivalent Al.

Orbital	Number of valence electrons	$\text{Al}_N^{0/-,+}$
$3F^{14}$	234	Al_{78}
$2H^{22}$	220	Al_{73}^-
$1J^{30}$	198	Al_{66}
$4S^2$	168	Al_{56}
$3D^{10}$	166	Al_{55}^-
$2G^{18}$	156	Al_{52}
$1I^{26}$	138	Al_{46}
$3P^6$	112	Al_{37}^-
$2F^{14}$	106	Al_{35}^-
$1H^{22}$	92	
$3S^2$	70	Al_{23}^-
$2D^{10}$	68	
$1G^{18}$	58	Al_{19}^-
$2P^6$	40	Al_{13}^-
$1F^{14}$	34	Al_{11}^-
$2S^2$	20	Al_7^+
$1D^{10}$	18	Al_6
$1P^6$	8	
$1S^2$	2	

at $N=7, 14, 17, 23, 29, 37, 39, 43, 47, 55,$ and 67 . Drops in IP's at $N=7$ and 14 can be understood from shell closings for 20 and 40 valence electrons. However, expected drops after Al_{19}^- , Al_{23}^- , and Al_{37}^- were not seen. Upton calculated the IP's of the Al_N clusters by incorporating the effect of atomic nuclei as a perturbation in the jellium model and found a similar rise in IP's upto $N=4$, and a low value of IP at $N=5$ [75]. Usually, IP's of metal clusters are found to decrease as the cluster size increases. This can be understood within a classical conducting sphere model [1]. Therefore the initial rise in the IP's of the Al_N clusters was rather surprising. A qualitative argument for this initial rise in IP's was given by Upton [75]. In an Al atom $3s$ and $3p$ orbitals are separated by 3.6 eV [76]. As the cluster size increases, $3s$ and $3p$ orbitals on different atoms hybridize and form their own $3s$ and $3p$ bonding and anti-bonding states respectively. These $3p$ occupied bonding states are deeper in energy compared to the atomic $3p$ state, and therefore it requires more energy to ionize the clusters than an Al atom. Also due to the lack of $3s$ and $3p$ hybridization, an Al atom

behaves effectively as a monovalent atom and it was believed that electronic shell structures will not emerge until Al behaves as a trivalent atom within the cluster. The transition from monovalent to trivalent character is thus associated with the overlap of $3s$ and $3p$ derived states.

Schrifer *et al* [74] identified the onset of s - p hybridization with the abrupt leveling of IP's of the Al_N clusters near $N=5$. In other works, $3s$ and $3p$ derived bands were claimed to overlap at $N=8$ by analyzing the evolution of the photoelectron spectra (PES) of Al_N^- clusters [77, 78]. PES study of Al_N^- ($N=1-162$) clusters was reported by Li *et al* [79]. These authors observed the onset of the s - p hybridization at $N=9$. Assuming 3 valence electrons per Al atom, Li *et al* identified the closure of electronic shells for Al_{11}^- , Al_{13}^- , Al_{19}^- , Al_{23}^- , Al_{35}^- , Al_{37}^- , Al_{46} etc. From the above experimental findings, it is clear that different experiments have different answers regarding s - p hybridization. Furthermore, Leuchtner *et al* studied reactivity of Al_N^- clusters with oxygen [7]. All the anionic clusters reacted with O_2 except for Al_{13}^- , Al_{23}^- and Al_{37}^- . With 3 valence electrons per Al atom, Al_{13}^- , Al_{23}^- and Al_{37}^- have 40, 70 and 112 valence electrons respectively. Therefore their non-reactive behavior can be understood in terms of closed electronic shells.

Table 1.5 represents a short summary of the theoretical works on Al clusters which have been reported. Rao *et al* [80] performed density functional calculations for the neutral and ionized Al_N ($N=1-15$) clusters. Al_7^+ , Al_{11}^- , and Al_{13}^- were identified with greater stability as indicated by their HL gap and binding energies. Their stability was explained in terms of closed electronic shells. To monitor s - p hybridization these

Authors	Element	Charge	Range	Methods	Properties studied.
T. H. Upton [75]	Al	n	2-6		s - p hybridization, IP
Rao et al. [80]	Al	n,a,c	≤ 13	DFT	s - p hybridization,HL, IP,EA
Akola et al. [81]	Al	n	2-23	DFT	s - p hybridization,IP
Melko et al. [82]	Al	a	3-6	APES + DFT	s - p hybridization

Table 1.5: List of theoretical works on Al_N clusters. Abbreviation : APES= Angle resolved PES.

authors calculated the s and p orbital contributions in the HOMO's of the clusters and found s - p hybridization in the range $5 \leq N \leq 7$. This result was consistent with the interpretations of the experimental findings [77, 78]. A density functional study for Al_N ($N=2-23$) was reported by Akola *et al* [81]. Their calculated AIP's were

found to be in excellent agreement with the experimentally measured IP's, especially high IP's at $N=6$ and 13 [74]. By projecting each occupied molecular orbital (MO) of Al_4 onto spherical harmonics, these authors found that $3s$ and $3p$ orbitals overlap substantially in most of the MO's. This result was clearly in contradiction with the experimental observation of Li *et al* [77–79]. In a recent work, Melko *et al* [82] performed angle-resolved PES (subsection 1.6) and *ab-initio* study for Al_N^- , ($N=3-6$) clusters. These authors have argued that $s-p$ hybridization is present in clusters as small as Al_3 , calling into question interpretations of earlier PES experiments. Most importantly, they have shown that $s-p$ hybridization does not suddenly appear at a critical cluster size, but exhibits an oscillatory behavior as Al atoms are added one by one.

From the above discussion, it is fair to say that there are some inconsistencies between the experimental and theoretical works regarding $s-p$ hybridization. However one can see some evidence of shell feature in Al_N^- (e.g., at $N=11, 13,$ and 19) and in Al_7^+ with the assumption that Al acts as a trivalent atom.

1.6 Experimental status of shell model : Angle resolved PES

We have seen that shell models are very successful in explaining many properties of metal clusters such as their relative stability, IP's, EA's etc. However one may ask whether the electrons really occupy discrete shells with $2(2l+1)$ -fold degeneracy, and whether these states can be identified to have an angular momentum quantum number l . Answers to these questions are partly obtained from the anion PES of experiments. Typically in PES, electronic shells are broadened into band of sub-shells [1]. Broadening of energy shells into sub-shells is caused by the interaction of valence electrons with the ionic background which is completely ignored in the shell models. Thus strictly speaking l will not remain a good quantum number. Recently, the angular momentum character of the valence orbitals of Na_N^- clusters has been investigated by angle-resolved PES [83]. In angle-resolved PES, one obtains the angular distribution ($I(\theta)$) of the photo-detached electrons (PAD). $I(\theta)$ is given by the expression

$$I(\theta) \propto 1 + \beta \left(\frac{3}{2} \cos^2 \theta - 1 \right) \quad (1.14)$$

where θ is the electron emission angle with respect to the electric field vector of the linearly polarized laser light and β is the so-called anisotropy parameter given by

$$\beta = \frac{l(l-1)R_-^2 + (l+1)(l+2)R_+^2 - 6l(l+1)R_+R_- \cos(\delta)}{(2l+1)(lR_-^2 + (l+1)R_+^2)} \quad (1.15)$$

Here

$$R_{\pm} = \int \psi_f^{\pm}(r)\psi_i(r)r^3 dr \quad (1.16)$$

are the radial dipole matrix elements between the final state $\psi_f^{\pm}(r)$ with angular momenta $l \pm 1$ and initial state $\psi_i(r)$ of the electron that has an angular momentum l . $\delta = \delta_+ - \delta_-$ is the difference of the Coulomb phase shifts of the final state wave functions $\psi_f^{\pm}(r)$. Using Eqn. 1.15, β takes values between -1 and 2 corresponding to perpendicular and parallel distributions respectively as shown in the Figure 1.8. For spherical systems bound and continuum states have well-defined angular mo-

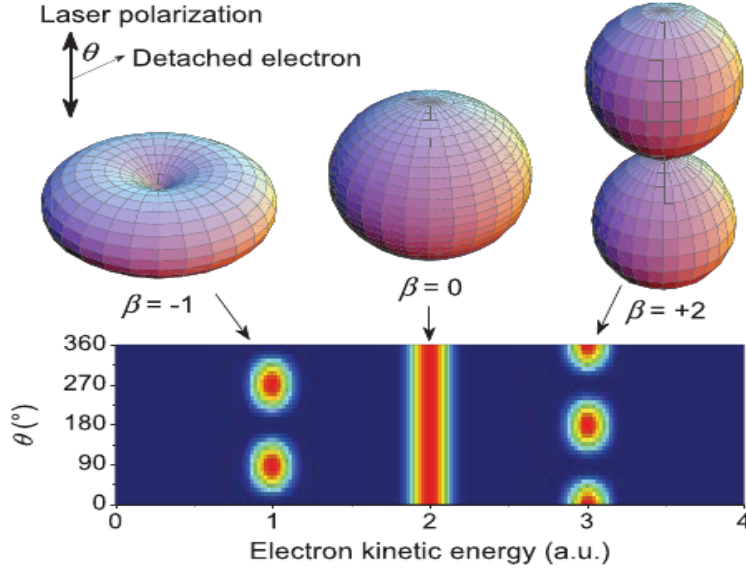


Figure 1.8: Schematic angle-resolved spectrum of three hypothetical electronic states exhibiting perpendicular, isotropic, and parallel distributions (β parameters -1 , 0 , and $+2$ respectively). The angular distributions are visualized as three-dimensional polar plots above [83].

mentum l , and for linearly polarized light the transition selection rules are given by $\Delta l = \pm 1$ and $\Delta m = 0$. If the incident photon causes emission of an electron from the s orbital ($l = 0$), then according to selection rule it will result in an outgoing wave with $l' = 1$ and $m = 0$, and $\beta = 2$. In all other cases, it gives rise to

two partial waves with $l' = l \pm 1$ corresponding to two peaks in the direction of the light polarization. Also interference of these two outgoing waves may give any value of β between -1 and 2 . Most importantly it is the angular momentum (l) of the initial state of photoemitted electron which determines its angular distribution. This fact was shown by Bethe [84] and Cooper *et al* [85] for one- and many-electron systems respectively. In Figure 1.9, the top panel shows the photoelectrons spec-

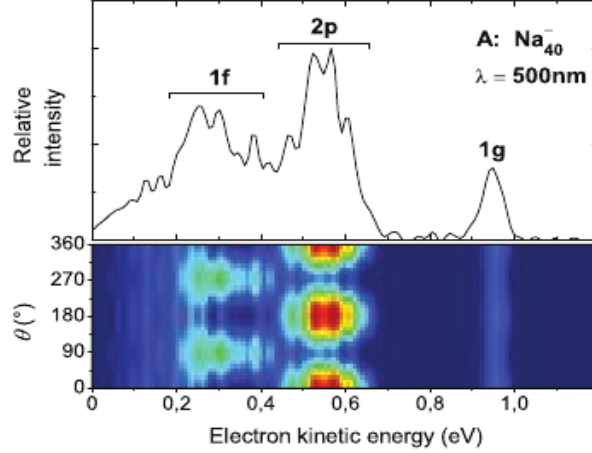


Figure 1.9: Angle-resolved photoelectron spectrum of Na_{40}^- , measured at threshold photon energy of 500 nm. In the upper panel, the angle-integrated spectrum is shown, in the lower panel, the spectra are plotted as a function of the emission angle with respect to the light polarization [83].

trum of Na_{40}^- cluster with the identification of shell model quantum numbers, while the lower panel shows corresponding PAD. Na_{40}^- has the following electronic configuration $1S^2 1P^6 1D^{10} 2S^2 1F^{14} 2P^6 1G^1$. Given the photon energy, top panel shows the spectrum of three uppermost electronic shells: 1F, 2P, and 1G. These shells have broadened due to the interaction with the ionic background. For example, 2P shell has a width of 0.2 eV. However the corresponding PAD in the lower panel shows a simple picture for the Na_{40}^- cluster. PAD for electrons emitted from subshells of 2P shell has parallel distribution ($\beta = +2$), isotropic for 1G shell ($\beta = 0$) and perpendicular for 1F shell ($\beta = -1$). Therefore all the subshells of a given shell show similar behaviour in the PAD, whereas different shells demonstrate different PAD's. In conclusion, the ionic background was shown to lift the degeneracies of the shells, but not enough to destroy the angular character of those shells. More details are given in Ref [83].

1.7 Superatoms

We have seen that stability of magic clusters was argued in terms of their closed electronic shells. Experiments were performed to measure other properties directly related to the electronic structure, e.g., IP's and EA's. Sharp drops in the IP's have been observed at sizes just after the magic sizes. Also, low values of EA's were seen at the magic sizes. All these experimental observations indicate that stability of magic clusters is an electronic feature. The existence of the electronic shells in simple metal clusters and their dominating role in governing stability provides a very exciting possibility that clusters may exhibit electronic and chemical features similar to elemental atoms.

In section 1.5, reduced reactivity of Al_{13}^- , Al_{23}^- and Al_{37}^- against oxygen was mentioned, which was explained in terms of the electronic shell closures with 40, 70, and 112 electrons [7]. This experiment demonstrated that the electronic shell structure plays a decisive role in determining the reactivity of simple metal clusters. Since non-reactive behaviour is also well known for inert gas atoms due to their closed shells, Al_{13}^- can be regarded as an analogue of those atoms. This led to the idea of 'superatoms'. The most recent definition of superatoms as given by the proponents Castleman and Khanna is as follows. A superatom is a cluster not only mimicking some properties of an elemental atom but a motif that is stable in chemical assembly and may also demonstrate new chemical features beyond the analogue atom [8]. For example, Al_{13} is one electron short of a closed electronic shell, and it was expected to behave similar to a halogen atom. In fact density functional calculations performed by Khanna *et al* [9] showed that EA of 3.7 eV of Al_{13} is comparable to that of a Cl atom (3.6 eV).

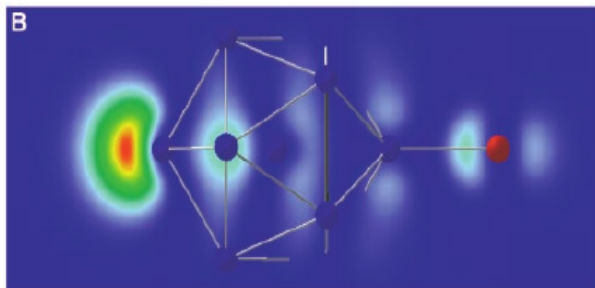


Figure 1.10: Charge density map of the HOMO for Al_{13}I^- [11]. Blue spheres are Al atoms while the red sphere represents an I atom.

Experimental evidence for this was also seen [11, 12, 79]. By analyzing the anion PES of $\text{Al}_{N=1-162}^-$ clusters, Li *et al* [79] showed that EA (3.62 eV) of Al_{13} was close

to that of a Cl atom. Bergeron *et al* [11] investigated the reaction of Al_N^- clusters with HI gas in which a stable species Al_{13}I^- was identified. The VDE and AEA values of Al_{13} obtained from DFT calculations were found to be 3.56 eV and 3.34 eV respectively which are higher than the EA (3.05 eV) of an I atom. This indicates that Al_{13} has more halogen character than iodine. It was justified by the charge density map of the HOMO of Al_{13}I^- as shown in Figure 1.10. An extra electron was found to be localized on the vertex of Al_{13} opposite to an I atom. These results suggested that Al_{13} has characteristics analogous to a halogen atom and hence it was termed ‘superhalogen’

Later on, Bergeron *et al* [12] provided more insight into the halogen characteristic of Al_{13} . These authors studied the reactivity of the Al_N^- clusters with I_2 . Mass spectrum was shown to consist of two series of stable clusters $\text{Al}_{13}\text{I}_{x=2,4,6,\dots}^-$, and $\text{Al}_{14}\text{I}_{x=3,5,7,\dots}^-$. In particular, stability of $\text{Al}_{13}\text{I}_2^-$ revealed the well known polyhalide nature of the halogens such as BrI_2 or ClI_2 . Also Bergeron *et al* shown that Al_{13} retains its icosahedral structure in the reaction with I_2 . On the other hand, stability of $\text{Al}_{14}\text{I}_3^-$ was quite interesting. A careful analysis of the ground state geometry and Mulliken charges in $\text{Al}_{14}\text{I}_3^-$ in their DFT calculations showed that Al_{14}^{+2} ($n_e=40$) core was energetically stabilized in the presence of three I atoms and results first stable product $\text{Al}_{14}\text{I}_3^-$ of the series. Thus Al_{14} can be thought of as a cluster that mimics an alkaline earth metal. This also demonstrates that adding just one more atom to previous size of the cluster can change the chemical behaviour completely.

In periodic table many elements are known to have multiple valence. For example, a C atom exhibits both divalent and tetravalent character and strongly binds with O and Si atoms to form CO and SiC. The idea of superatoms was put on a firmer ground when it was shown that some clusters behave as ‘multiple valence superatoms’. Reveles *et al* measured the mass abundance spectrum of Al_NC_x^- clusters [13]. Intense peaks were found at Al_7C^- along with Al_{13}^- . Their DFT calculations identified Al_7C^- as a stable cluster after examining the variation in HL gap and energy gain by adding one Al atom at a time. Al_7C^- also emerged with greater stability against the formation of AlO_2 , AlO_2^- , and Al_2O_2 in the presence of O_2 molecules [13]. Reveles *et al* found that Al_7^- binds more strongly to tetravalent atoms, e.g., C and divalent atoms, e.g., O compared to trivalent atoms as shown in the left panel of Figure 1.11. Also, calculated HL gaps of the Al_7M^- clusters were shown to have local peaks whenever M was a divalent or a tetravalent atom (right panel of Figure 1.11). These findings were rationalized in terms of the spherical shell model. Since Al_7^- is a 22 electron system with an electronic configuration $1\text{S}^21\text{P}^61\text{D}^{10}2\text{S}^21\text{F}^2$, it would

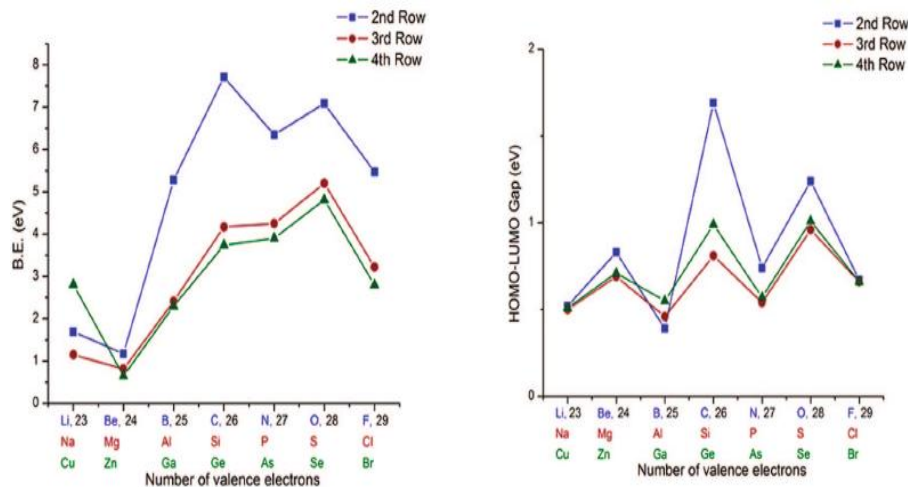


Figure 1.11: (Left) BE of Al_7M^- , (Right) HL gap of Al_7M^- clusters, M is an atom of the second, third, and fourth row of the periodic table [13].

like to bind more strongly to atoms that need 2 or 4 electrons to fill their outermost shells. This also means that Al_7^- tends to have electronic shell closure of 18 or 20 electrons. Thus experiments combined with theoretical calculations showed that Al_7^- behaves as multiple valence superatom.

In summary, while the Al_{13} and Al_{14} were the first superatoms which showed an analogy between the elemental atoms and superatoms, Al_7^- showed multiple valence feature. Most importantly, their electronic and chemical properties can be rationalized in terms of the shell models.

1.7.1 Cluster assembled materials (CAM)

We have seen that Al_N clusters with specific size and charge mimic electronic and chemical properties of elemental atoms. Since atoms are the fundamental building blocks of materials, it is natural to ask whether it is possible to build solids by assembling these clusters. Various theoretical studies explored this exciting possibility [86–92]. Such materials are known as cluster assembled materials (CAM).

Al_{12}C and Al_{13}K were identified as suitable motifs for CAM in theoretical calculations [9, 93, 94]. These clusters were found to have binding energy (BE) per atom comparable to Al_{13}^- . For example, BE of Al_{13}^- was found to be 3.11 eV per atom, while it was 3.16 eV and 3.04 eV per atom for Al_{12}C and Al_{13}K respectively. It is interesting to note that even though both clusters have the same number of valence electrons, i.e., 40 electrons, the origins of their stability are of completely different nature. While the stability of Al_{13}K is due to ionic bonding between Al_{13} and the

K atom, Al_{12}C attains its stability due to closure of both electronic and geometric shells. To find the nature of hypothetical fcc solid based on Al_{12}C , band structure calculations were carried out by Manninen *et al* [86]. Particularly, the energy-band structure of the CAM at a lattice constant of 11.64 Å showed that fermi energy lies between the $2p$ and $1g$ bands derived from the $2P$ and $1G$ orbitals (of Al_{12}C) respectively. The magnitude of the band gap was found to be 0.5 eV that showed a semiconductor nature of the proposed CAM. However, the lattice constant was not optimized in these calculations. Liu *et al* reported first-principles calculations for the crystalline phase of KAl_{13} [87]. Ionic molecules are known to form ionic solids having either face centered (e.g., NaCl) or body centered cubic (bcc) lattice (e.g., CsCl). Therefore these authors considered both lattice structures for the CAM in their calculations. By optimizing the total energy with respect to lattice constant, the bcc structure was found to be more stable. By examining the density of states (DOS), Liu *et al* found metallic nature of the CAM as shown in Figure 1.12.

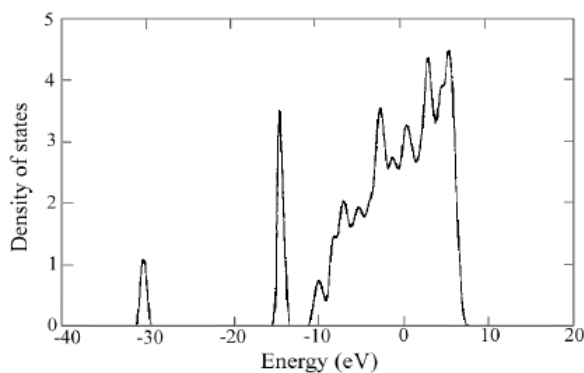


Figure 1.12: Density of states of CAM based on Al_{13}K clusters. Fermi energy level was set to zero [87].

Recently, Castleman *et al* [89] have introduced a protocol in which one can synthesize cluster assemblies by finding suitable candidates. This approach involves three steps : (i) identification of the potential building blocks through experiments on size selected clusters in the gas phase, (ii) investigation of the energetics and chemical stability of the cluster motifs via first principles calculations, (iii) synthetic chemical approaches designed to assemble desired motifs using the information obtained in steps (i) and (ii).

Following this protocol, these authors found As_7K_3 , and As_{11}K_3 as suitable motifs for CAM after analyzing the mass abundance spectrum of As_NK_M^+ and the variation of HL gap, fragmentation energy (FE) of the clusters [89]. In particular, Castleman *et al* claimed that As_7K_3 can be regarded as As_7^{-3} units bonded by three K^+ ions. Since

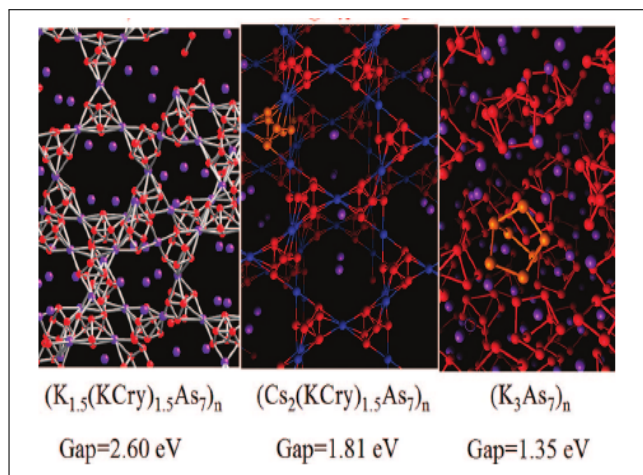


Figure 1.13: Geometrical structure of various cluster assembled materials made of As_7 combined with K, Cs, or cryptated K atoms. The calculated band gaps of the resulting solids are also marked. Adopted from ref [90].

then a number of CAM's have been synthesized using As_7^{-3} units in combination with different bare and cryptated alkali atoms¹ which act as linkers between the cluster units [89]. Most importantly, theoretical calculations showed that the band gap of the assembled material can be tuned by changing the cation linkers (Figure 1.13). Also, cluster assemblies with As_7^{-3} and As_{11}^{-3} motifs have been synthesized in one and two dimensions [91, 92].

1.8 Shell effects in bimetallic clusters

In previous sections, we have seen that many properties of simple metal clusters reveal electronic shell effects. These are not the only clusters where size evolution of the properties is governed by shell effects. There are numerous studies on bimetallic clusters which showed that electronic shell models are good guiding tools to understand their properties. In particular, we discuss in TM doped noble metal (Au_N , Ag_N), and simple metal (Na_N , Cs_N , Mg_N , and Al_N) clusters.

1.8.1 TM doped noble metal clusters

Neukermans *et al* [95] studied the mass abundance spectrum of photo-fragmented $3d$ TM doped Au_N^+ clusters (TM=Sc, Ti, V, Cr, Mn, Fe, Co, and Ni). They rationalized the stability of the doped clusters in terms of shell models. Table 1.6 shows the

¹Cryptated alkali atom has a lower IP than bare alkali atom.

observed shell features in these clusters. For example, clusters with greater stability in Au_NSc^+ series were found at $N=6, 16,$ and 32 . A Sc atom has $3d^14s^2$ electronic configuration. Assuming all the 3 electrons of Sc are delocalized, these clusters will have 8, 18, and 34 valence electrons respectively. Therefore enhanced stability of these clusters can be understood in terms of the shell models. Similar features were also observed for Ti doped Au clusters. Au_N^+ clusters doped with Cr, Mn, Fe, and Co emerged with greater stability at $N=1, 5, 7, 17, 19,$ and 33 . By considering only the 2 electrons from the 4s orbitals of TM atoms as itinerant electrons, the origin of their stability were explained via closure of the electronic shells with $n_e=2, 6, 8, 18, 20,$ and 34 number of valence electrons. Enhanced stabilities of $\text{Au}_5\text{V}^+, \text{Au}_5\text{Cr}^+,$

Table 1.6: Observed Shell features in Au_NX^+ . n_v is the number of delocalized electrons coming from the TM and n_e is the total number of delocalized electrons corresponding to closed electronic shells [95].

X	Valence	Enhanced stability at (N)	n_v	n_e
Sc	$3d^14s^2$	6, 16, 32	3	8, 18, 34
Ti	$3d^24s^2$	5, 15, (27)	4	8, 18, 30
V	$3d^34s^2$	5, 7	2	6, 8
Cr	$3d^54s^1$	1, 5, 7, 17, (19) 33	2	2, 6, 8, 18, (20), 34
Mn	$3d^54s^2$	1, 5, 7, 17, (19) 33	2	2, 6, 8, 18, (20), 34
Fe	$3d^64s^2$	1, 5, 7, 17, (19) 33	2	2, 6, 8, 18, (20), 34
Co	$3d^74s^2$	1, 5, 7, 17, (19) 33	2	2, 6, 8, 18, (20), 34
Ni	$3d^84s^2$	2, 8, 18	1	2, 8, 18

$\text{Au}_5\text{Mn}^+,$ and Au_5Co^+ were of particular interest. All these clusters have 6 electrons that lead to a closed electronic shell configuration $1S^21P^4$ in the two dimensional shell model [96]. Later on density functional calculations for Au_5X^+ ($\text{X}=\text{Sc}, \text{Ti}, \text{Cr},$ and Fe) clusters were reported by Janssens *et al* [97]. Local magnetic moments on the TM elements within these clusters were shown to be reduced in comparison to their bare atomic magnetic moments.

Li *et al* [98] presented PES study combined with density functional calculations for MAu_6^- ($\text{M}=\text{Ti}, \text{V},$ and Cr) clusters. These authors found that TM atoms retain their bare atomic magnetic moments within these clusters. Torres *et al* [99] reported first-principles study of $\text{Au}_{N\leq 9}\text{M}^+$ ($\text{M} = \text{Sc}, \text{Ti}, \text{V}, \text{Cr}, \text{Mn},$ and Fe) clusters. Based on $\Delta_2(N)$, HL gap, and fragmentation energies, these authors identified stable clusters at $N=6$ for Sc, $N=5$ for Ti, and $N=5,7$ for V, Cr, Mn and Fe. A

noteworthy result of this work was odd-even oscillations of the magnetic moments of TM atoms as a function of cluster size. In addition, moments of the dopant atoms were found to decrease as the cluster size increases. A combined theoretical (DFT) and photo-fragmentation study of $\text{MAg}_{N \leq 30}^+$ (M=Sc, Ti, V, Fe, Co, and Ni) clusters was reported by Janssens *et al* [20]. These authors observed pronounced peaks for $\text{Ag}_{16}\text{Sc}^+$, $\text{Ag}_{15}\text{Ti}^+$, Ag_{14}V^+ , $\text{Ag}_{11}\text{Fe}^+$, $\text{Ag}_{10}\text{Co}^+$, and Ag_9Ni^+ in the mass abundance spectrum. Assuming TM impurities provide all the $3d$ and $4s$ electrons, stabilities of these clusters were attributed to a closed electronic shell with 18 electrons. Their DFT calculations for $\text{Ag}_{10}\text{Co}^+$ also verified the above assumption. In addition, due to closed electronic shell, these clusters do not have any net magnetic moment.

1.8.2 TM doped alkali metal clusters : Magnetic superatom

1.8.2.1 Theoretical proposals

Pradhan *et al* [100] studied electronic, magnetic and structural properties of Sc, Ti, and V doped Na_N ($N=4-6$) clusters. Oscillations in the magnetic moments of these clusters were observed as the cluster size increases. Particularly, VNa_4 , VNa_5 , and VNa_6 were shown to have magnetic moments of $6\mu_B$, $5\mu_B$, and $6\mu_B$ respectively, while moments of TiNa_5 and TiNa_6 were found to be $3\mu_B$, and $4\mu_B$ respectively. Interestingly, magnetic moments of these clusters are higher than those of bare V and Ti atoms. These observations are different from the results obtained in Ref [99] where the magnetic moment of TM atoms decreased as the cluster size increased. By examining the MO's of these clusters, these authors claimed transfer of $3s$ electrons of Na to the partially filled $3d$ atomic orbitals of TM atoms in the α channel² due to smaller (Pauling) electronegativity of Na compared to the TM atoms. Therefore one obtains higher than atomic moments in these clusters. Later on, Pradhan *et al* [101] reported first-principles calculations of late TM doped Na_N ($N=4-7$) clusters, where TM=Cr-Ni. Interestingly, Mulliken atomic spins within Cr, Mn, Fe and Co doped Na_N clusters showed ferro or anti-ferro magnetic coupling between the local moments of the TM atoms and those of Na host atoms that cause odd-even oscillations in the magnetic moments. However, no odd-even oscillations were observed for Ni doped clusters over the size range studied. Also HL gaps of these clusters were shown to have size-dependent behaviour.

A detailed density functional study of V doped Na_N and Cs_N ($N=1-12$) clusters was carried out by Reveles *et al* [15]. These authors identified VNa_8 and VCs_8 as

²Majority and minority spin channels are called up (α) and down (β).

stable clusters (with a magnetic moment of $5\mu_B$) indicated by large alkali addition energy (ΔE_N^3) and adiabatic spin excitation energy (ΔE_{spin}). Adiabatic spin excitation energy (ΔE_{spin}) of a cluster is defined as the energy difference between its ground state and the next higher energy spin multiplicity in their respective lowest energy structures. It indicates the stability of the ground state of a cluster against spin excitation. Counting all $3d$ and $4s$ electrons of V atom ($3d^34s^2$), VNa_8 and

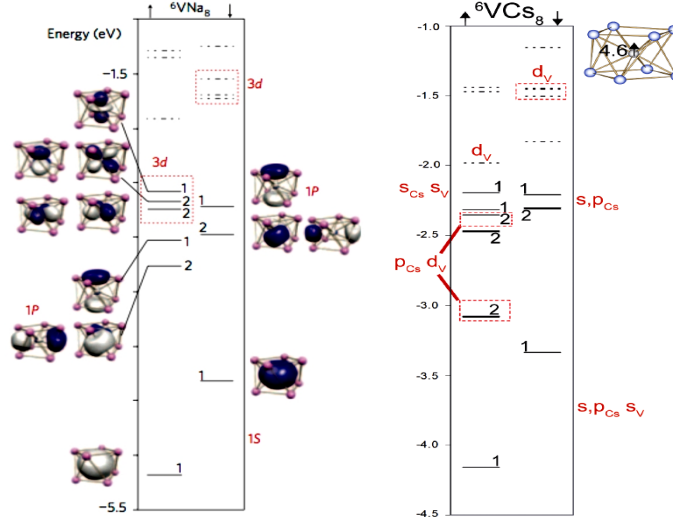


Figure 1.14: One-electron energy levels and molecular orbital isosurfaces for VNa_8 (left) and VCs_8 (right). Majority and minority levels are shown. Continuous lines correspond to the filled levels and the dotted lines correspond to the unfilled states. For each level, the degeneracy is marked. Upper-case letters stand for delocalized $1S$ and $1P$ shells, and lower-case letters for localized $3d$ atomic orbitals [15].

VCs_8 have 13 electrons that do not correspond to any magic number. Therefore their stability was quite surprising. To explain this intriguing phenomenon, Reveles *et al* showed that 8 electrons out of 13 occupy the delocalized $1S^21P^6$ shell orbitals and spread over the entire cluster as shown in the left panel of Figure 1.14. The remaining five electrons are localized. These localized orbitals were found to have d angular character with major contributions from V $3d$ orbitals. Therefore both clusters acquire enhanced stability due to a filled shell configuration ($1S^21P^6$), and atomic d electrons localized on the V atom provide a moment of $5\mu_B$. VNa_8 and VCs_8 resemble the electronic configuration of a Mn atom having a half filled $3d$ and filled $4s$ states. However, according to the definition of a superatom, these clusters should retain their structural identity and associated magnetic properties when assembled to form molecules or larger clusters. To test this two units of these

³ $\Delta E_N = E(A) + E(\text{VA}_{N-1}) - E(\text{VA}_N)$; A is Na or Cs

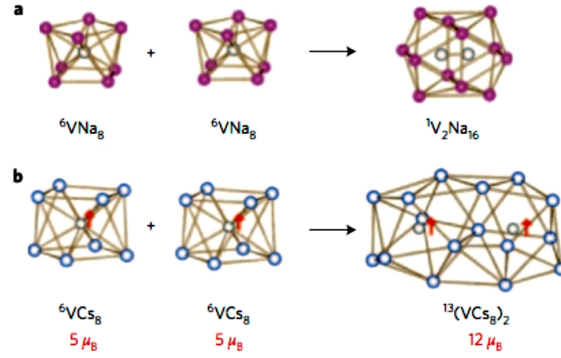


Figure 1.15: Lowest-energy structures of (a) V_2Na_{16} and (b) $(VCs_8)_2$ dimer starting from free clusters. The arrows indicate the direction of the vanadium local spin moments. The superscripts indicate spin multiplicity [15].

clusters were brought close to each other from different directions and orientations. Figure 1.15(a) shows that two units of VNa_8 coalesce together rather than making a $(VNa_8)_2$ dimer. However, VCs_8 prefers to make $(VCs_8)_2$ dimer as shown in Figure 1.15(b). Also V spins in $(VCs_8)_2$ dimer were found to be aligned parallel to each other providing a high magnetic moment of $12 \mu_B$. Anti-ferromagnetic coupled state in a $(VCs_8)_2$ dimer was found to be ~ 0.1 eV higher in energy relative to its ground state. Therefore Reveles *et al* concluded that VNa_8 does not satisfy the necessary criteria of being a superatom, while VCs_8 can be regarded as a superatom with a magnetic moment of $5 \mu_B$. It was termed a “magnetic superatom”.

Inspired by the proposal of magnetic superatoms, various theoretical studies have been carried out to identify possible candidates for magnetic superatoms [102, 103]. Reveles *et al* performed density functional calculations for neutral and anionic $TiNa_N$ ($N=1-13$) clusters [102]. By examining the variation of HL gap and ΔE_{Na} ,⁴ $TiNa_5$, $TiNa_7$, and $TiNa_9$ were identified as stable clusters with magnetic moments of $3 \mu_B$, $3 \mu_B$, and $5 \mu_B$ respectively. Treating all $3d$ and $4s$ electrons of Ti ($3d^24s^2$) atom as delocalized electrons, $TiNa_5$ has 9 valence electrons. It was shown that stability of $TiNa_5$ was because of a closed electronic shell ($1S^21P^4$) within the two dimensional shell model. Remaining 3 electrons were found to be localized on Ti in the majority spin channel providing a magnetic moment of $3 \mu_B$. For $TiNa_7$ and $TiNa_9$, enhanced stability was attributed to a closed shell configuration $1S^21P^6$. Particularly, $TiNa_9$ was the first candidate in which all five $3d$ orbitals on Ti in the majority spin channel were filled in a way similar to VCs_8 . Thus $TiNa_9$ was identified as a possible candidate for magnetic superatom. In addition, $TiNa_{12}$ was also found with enhanced

⁴ $\Delta E_{Na} = E(Na) + E(TiNa_{N-1}) - E(TiNa_N)$

stability indicated by ΔE_{Na} . This is because of its highly symmetric and compact icosahedral ground state structure.

Later on, first-principles calculations of ScNa_N ($N=1-12$) clusters were carried out by Pradhan *et al* [103]. By analyzing ΔE_{Na} and ΔE_{spin} , ScNa_{12} was found to have enhanced stability with a magnetic moment of $3\mu_B$. Its stability was attributed to its compact icosahedral structure. By examining the molecular orbital isosurface plots, it was shown that change of the alkali atoms provides the control over the relative position of 1S, 1P, and 3d states which could lead to larger magnetic moments. ScK_{12} and ScCs_{12} were found to have magnetic moments of $5\mu_B$ in which the 3d orbitals of Sc adopt a half-filled configuration, while the clusters were stabilized by a filled $1S^21P^62S^2$ configuration. Therefore these authors argued that ScK_{12} and ScCs_{12} with magnetic moment of $5\mu_B$ could be possible candidates for magnetic superatoms.

In summary, the idea of superatom is extended to a new class of superatoms, i.e., magnetic superatoms which not only have enhanced stability but also possess finite magnetic moments. VCs_8 was the first example of a magnetic superatom. TiNa_9 , ScK_{12} and ScCs_{12} were possible members of the magnetic superatom family. However, the questions whether they retain their structural identity and associated magnetic properties while making assemblies were not addressed.

1.8.2.2 Experimental status of magnetic superatoms

In last section, we saw that various theoretical studies have put forward the interesting idea of magnetic superatoms. Experimental evidence for these came recently. Zhang *et al* [104] measured the mass abundance spectrum of $\text{V}_{1,2}\text{Na}_N^-$ clusters. Particularly intense peaks were observed for VNa_N^- at $N=6, 7, 8,$ and 9 . Subsequently, these authors performed anion PES for the VNa_N^- ($N=6, 7, 8,$ and 9) clusters. Since anion PES involves the transition from the ground state of the anion to the ground and excited states of the neutral, shape of PES corresponds to the absorption spectra of the neutral clusters. Thus these authors have calculated theoretical absorption spectra of VNa_N^- ($N=6, 7, 8,$ and 9) clusters using time dependent DFT to obtain more insight into photoelectron spectra.

Figure 1.16 shows the experimental PES of VNa_7^- and VNa_8^- and the corresponding theoretical absorption spectra. AEA is marked as the onset of the first peak in the PES, while VDE is identified by the position of first peak. First two peaks of both experimental and theoretical spectra were in excellent agreement with each other as shown in Figure 1.16. For example, theoretically calculated first and second VDE of VNa_7^- with a magnetic moment of $5\mu_B$ were 1.00 eV and 1.23 eV respec-

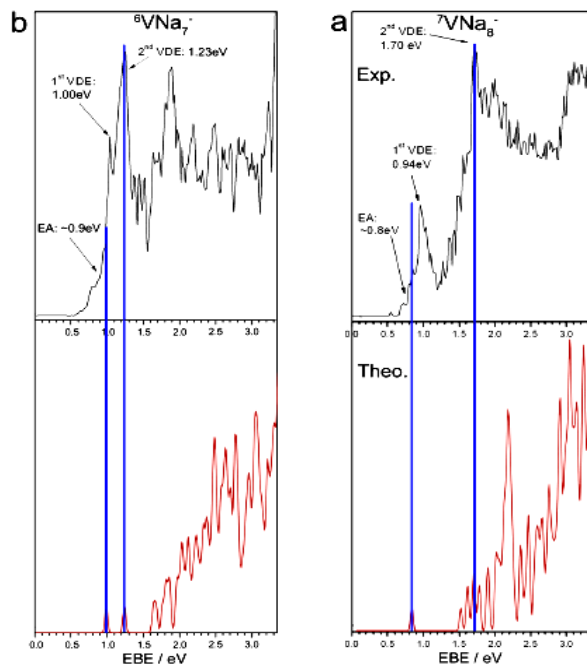


Figure 1.16: Photoelectron spectra at 355 nm for VNa_N^- clusters ($N = 7, 8$). The calculated absorption spectra of neutral VNa_8 is marked in red. The calculated vertical detachment energies are marked with blue lines [104].

tively, consistent with the corresponding experimental values of 0.9 eV and 1.23 eV. Similar agreement was observed for VNa_8^- . The AEA (0.81 eV) of VNa_8 was also found to be the lowest, consistent with a closed shell $1S^21P^6$ configuration. Peak at VNa_7^- in the mass abundance spectrum can be understood from the fact that VNa_7^- is isoelectronic to VNa_8 . In fact, VNa_7^- was shown to have an electronic configuration $1S^21P^63d_\alpha^5$ similar to VNa_8 [15]. Therefore, by comparing the experimental photoelectron spectrum with theoretical transitions, these authors concluded that VNa_7^- possess electronic and magnetic properties similar to VNa_8 .

1.8.3 TM doped Mg clusters

Recently, Medel *et al* [105] carried out density functional calculations for 3d TM doped Mg_N ($N=1-12$) clusters. FeMg_8 with a magnetic moment of $4\mu_B$ was found to have enhanced stability as indicated by its large HL gap, Mg addition energy (ΔE_{Mg}), and ΔE_{spin} . Treating all 3d and 4s electrons of the Fe atom ($3d^64s^2$) as valence electrons, FeMg_8 has 24 valence electrons which do not correspond to any shell closing. Thus enhanced stability of FeMg_8 at the unconventional electron count of 24 was quite intriguing. These authors showed that the origin of this stability

1.8.4 TM doped aluminium clusters

So far we have seen that electronic and magnetic features of a single TM doped noble metal, alkali metal, and Mg clusters can be explained in terms of shell models. Here we will briefly review the literature for a single TM doped Al clusters. Even though various studies are available for non-transition metal (e.g., Mg, Na, Li, K, and Cu) doped Al_N clusters [106–116], very few studies have been done for TM doped Al_N clusters. Harms *et al* [117] studied the reactivity of NbAl_N^- and VAl_N^- clusters with oxygen. Particularly, NbAl_4^- and VAl_6^- were found to have reduced reactivity. They argued that closure of electronic shells within shell models can account for their reduced reactivity. Treating all the $4d$ and $5s$ electrons of Nb ($4d^45s^1$) as valence electrons, NbAl_4^- has 18 valence electrons, a magic number. On the other hand if every valence electron of V ($3d^34s^2$) is counted, VAl_6^- will have 24 electrons which is not a predicted shell closing. However, Harms *et al* suggested that if one of the $4s$ electrons of V atom is promoted to the partially filled $3d$ atomic orbitals, then V will provide only one free $4s$ electron. Therefore VAl_6^- becomes a 20 electron magic cluster. However, there is no theoretical justification of this from first-principles calculations.

Using laser photoionization mass spectroscopy, Menezes *et al* [118] measured IP's of Al_NCo_M ($N=0-35$, $M=0-7$) clusters. Within the Al_NCo series, local minima in IP's were seen at $N=7$, and 14, consistent with new shell openings at $n_e=22$ and 43. These authors argued for the closing of an electronic shell by 40 electrons for Al_{13}Co with the assumption that Co contributes only one $4s$ electron. Pramann *et al* [119] obtained ADE's of the CoAl_N^- ($N=8-17$) clusters. Particularly, a significant drop in ADE's at $N=12$ was observed. With 3 valence electrons per Al atom and an oxidation state of +3 of Co atom ($3d^74s^2$), Pramann *et al* claimed that $\text{Al}_{12}\text{Co}^-$ has 40 electrons leading to a closed electronic shell. Therefore $\text{Al}_{12}\text{Co}^-$ was expected to show a minimum in ADE. Recently, Lang *et al* [120] reported structural information of V, Cr and Ti doped Al_N^+ ($N=5-35$) clusters using Ar physisorption experiments. These authors concluded that Al_{16}^+ is the smallest cage that can enclose V and Cr atoms, while Ti atom is encapsulated between $N=19$ and 21.

On the theoretical side, Gong *et al* [121] carried out density functional calculations to investigate the relative stabilities of TMAl_{12} clusters. These authors considered only the icosahedral structure for this series, where the TM was encapsulated in an Al_{12} cage. They identified CrAl_{12} and MnAl_{12} as stable clusters by examining their binding energies. Recently, density functional study for TMAl_N (TM=Cr, Mn, Fe, Co, Ni ; $N=1-7,12$) clusters have been reported by Wang *et al* [122]. Based on

$\Delta_2(N)$ and fragmentation energy, all TMAI_3 clusters were claimed to have enhanced stability. In addition, calculated HL gap also showed local peaks for all the TMAI_3 clusters except FeAl_3 . The magnetic moments of the TMAI_3 and TMAI_4 clusters were found to be 3, 2, 1, 0, 1 μ_B , and 0, 1, 2, 1, 2 μ_B respectively. To explain magnetic moments of these clusters Wang *et al* invoked the shell models. For example, treating all 3d and 4s electrons of Co and Cr atoms as itinerant electrons, CoAl_3 and CrAl_4 have 18 and 20 electrons respectively that lead to closed electronic shells. Thus CoAl_3 and CrAl_4 were found to be non-magnetic.

In summary, above studies claimed the existence of electronic shell effects which govern the electronic and magnetic properties of TM doped Al clusters.

1.9 Aromaticity and all-metal clusters

Despite having great successes, there are cases where shell models cannot explain the properties of all-metal clusters as observed in various experimental and theoretical studies [16,17,123]. There are other simple electron counting rules in chemistry like the Hückel rule and the Wade-Mingos rules [124,125] which account for stability of electronic systems. According to the Hückel rule, planar and cyclic hydrocarbons having $(4n+2)$ π -electrons have enhanced stability. These hydrocarbons are known as aromatic compounds. Benzene, i.e, C_6H_6 is the prototypical example of an aromatic compound having 6 π -electrons, and satisfies the Hückel rule. On the other hand, systems having $4n$ π -electrons are known as anti-aromatic compounds.

Recently, the idea of aromaticity has been extended to all-metal clusters. In this section we will briefly discuss aromaticity in Al-based bimetallic clusters only. A combined experimental (anion PES), and theoretical study reported by Li *et al* [16] showed the crucial role of aromaticity in stabilizing the MAl_4^- ($\text{M} = \text{Li}, \text{Na}, \text{and Cu}$) clusters. These authors showed a doubly degenerate HOMO of MAl_4^- occupied by two delocalized π electrons that is consistent with the Hückel rule for $n=0$. Later on, it was argued that aromaticity in the MAl_4^- clusters originated due to σ electrons rather than π electrons [126]. Xi *et al* [127] reported experimental and theoretical studies for mixed valence MAl_3^- ($\text{M}=\text{Si}, \text{Ge}, \text{Sn}, \text{or Pb}$) aromatic clusters which were iso-electronic to Al_4^{-2} . After that, numerous studies have been devoted to finding stable cluster motifs using aromaticity as a guiding principle [128,129].

Although aromaticity is a widely used term, a precise, quantitative and well-accepted definition of this quantity is still missing. For quantitative estimation of aromaticity, different criteria have been proposed by different authors [17]. These can

be based on structural, energetic, reactivity, electronic or magnetic properties. The most popular criterion used to identify an aromatic cluster is perhaps the nucleus independent chemical shift (NICS), a magnetic measure. The NICS value is the negative of the trace of the nuclear magnetic shielding tensor at the nucleus of an inert probe atom. Clusters with negative values of NICS are classified as aromatic, while clusters with positive values of NICS are classified as anti-aromatic [18, 19].

A joint experimental and theoretical study of anionic and neutral Al_NBi^- ($N=1-5$) clusters was done by Jones *et al* [128]. Al_3Bi and Al_5Bi were identified with greater stability as shown by their large values of IP's and HL gaps. Interestingly, the origins of their enhanced stability turned out to be very different. Jones *et al* argued that Al_3Bi was an aromatic cluster because of the presence of 6 π -electrons, consistent with the Hückel rule for $n=1$. A negative value of NICS (-32.19 ppm⁵) also verified its aromatic character. While assuming 3 electrons per Al atom, the stability of Al_5Bi was attributed to closing of an electronic shell with 20 electrons. Therefore this work presents an interesting scenario in which stability of the clusters can be explained with two different rules as the number of atoms and valence change. Melko *et al* [129] reported anion PES and first-principles calculations for Al_NX ($N=1-6$; $\text{X}=\text{As}$ and Sb) clusters. By inspecting the variation of HL gaps, these authors found Al_3X and Al_5X clusters with enhanced stability. Enhanced stabilities of Al_3As and Al_3Sb were explained in terms of aromaticity as indicated by the negative values of their NICS. On the other hand, a closed electronic shell configuration ($1\text{S}^21\text{P}^61\text{D}^{10}2\text{S}^2$) accounted for the enhanced stability of Al_5As and Al_5Sb . Besides these works, there are numerous studies on aromaticity in all-metal clusters. A review of these are given in ref. [123, 130–132].

1.10 Goals of this thesis

Motivated by the interesting concept of superatom, a major part of my thesis is devoted to identifying stable clusters which behave as magnetic superatoms. Detailed study of structural, electronic and magnetic properties of a single $3d$ TM doped alkaline earth and aluminum clusters is performed using first-principles approach based on density functional theory. It forms a major part of this thesis. In addition, I have studied V doped silver clusters using first-principle calculations. This work is motivated by the experiments performed by Janssens *et al* on these clusters [20]. The remaining chapters of this thesis are organized as follows.

⁵Unit of NICS is given in terms of parts per million (ppm).

Chapter 2 is about the underlying theory and techniques of calculations used in this thesis. Density functional theory is reviewed. Techniques for solving the Kohn-Sham equations using both localized and plane wave basis sets, and the concept of effective core potentials, Mulliken population analysis are discussed. An evolutionary algorithm for finding the global minima of clusters is also discussed.

Chapter 3 In this chapter the electronic and magnetic properties of 3d TM doped calcium clusters are presented. We have found TiCa_8 and FeCa_8 to have enhanced stability as indicated by large HL gaps, hardness (η) and adiabatic spin excitation energy (ΔE_{spin}). In addition, FeCa_8 is found to have a magnetic moment of $4 \mu_B$. The stability of TiCa_8 is understood from the fact that it has 20 valence electrons, a magic number. FeCa_8 is identified as a magnetic superatom in the same spirit as VCs_8 [21].

Chapter 4 extends our search for magnetic superatoms by investigating the electronic and magnetic properties of the TMSr_8 clusters. TiSr_8 and CoSr_8 are found to have enhanced stability within the TMSr_8 clusters. The enhanced stability of TiSr_8 is understood in a way similar to TiCa_8 . Most strikingly, FeSr_8 does not emerge as a cluster with enhanced stability. We have discussed the reasons behind this. Furthermore, we have shown that the ground state electronic configuration of a TMSr_8 cluster is also determined by the combined effect of Hund's coupling and crystal field effect [22].

Chapter 5 explores the possibility of finding clusters with enhanced stability and finite magnetic moment within the CrSr_N and MnSr_N ($N=4-12$) series. Motivation for studying these clusters originated from the study of TMSr_8 clusters. We found that CrSr_9 and MnSr_{10} have enhanced stability as indicated by their hardness, second order energy difference ($\Delta_2(N)$) and ΔE_{spin} . CrSr_9 and MnSr_{10} are found to have magnetic moments of $4\mu_B$ and $5\mu_B$ respectively. Again, the origin of stability and magnetic moment in CrSr_9 and MnSr_{10} clusters is the combined effect of crystal field and Hund's coupling. CrSr_9 and MnSr_{10} are also found to behave as magnetic superatoms [22].

Chapter 6 focuses on the electronic and magnetic properties of a single Cr, Mn, Fe, Co and Ni doped Al clusters in search of magnetic superatoms. While we have not been able to identify any possible candidates for magnetic superatoms in these series, we have found some very interesting properties in them. We have found that FeAl_4 ,

and CoAl_3 clusters have enhanced stability as indicated by their $\Delta_2(N)$, hardness and ΔE_{spin} . However, they have no net magnetic moment. Most importantly we found that spherical shell models cannot describe the electronic structure of TM doped aluminum clusters, in contrast to binary TM doped alkali and alkaline earth clusters. In fact we have shown that stability of FeAl_4 , and CoAl_3 can be associated with their aromatic behaviour [23].

Chapter 7 investigates the evolution in the atomic structure, bonding characteristics, stability, and the spin magnetic moment of neutral and cationic VAg_N clusters. This work is motivated by the experimental study on the VAg_N^+ clusters in which VAg_5^+ and VAg_7^+ were found to be stable [20]. We found that VAg_5^+ and VAg_7^+ have enhanced stability in agreement with the experiments, indicated by their large HL gap and $\Delta_2(N)$. We showed that the energy gap between the occupied and unoccupied $3d$ orbitals of a bare V atom leads to greater stability of VAg_5^+ . An effective exchange splitting in $1D$ orbitals can account for enhanced stability of VAg_7^+ [24].

Chapter 8 briefly discusses the scope of various further works based on our studies.

Methodology

2.1 Introduction

In the Born-Oppenheimer approximation, Schrödinger equation ¹ for an N -electron atomic system is given by

$$\left[\sum_{i=1}^N \frac{-\nabla_i^2}{2} + \sum_{i=1}^N \hat{V}_{ext}(r_i) + \sum_{i=1}^N \sum_{j>i}^N \hat{V}_{ee}(r_i, r_j) \right] \Psi = E\Psi \quad (2.1)$$

where the first term in the bracket is the kinetic energy operator. Second and third terms are the nucleus-electron interaction potential and the repulsive electron-electron interaction potential operators respectively. Ψ represents the N -electron wavefunction. One can solve Eqn. 2.1 within the Hartee-Fock (HF) approximation in which the N -electron wavefunction is approximated by a Slater determinant. Density functional theory (DFT) provides an alternative approach to solve this N -electron problem. In this chapter we will discuss the basic ideas of DFT. Tools for solving the so-called Kohn-Sham equations using localized and plane wave basis sets will be briefly discussed. The concept of effective core potentials (ECP's), Mulliken population analysis and an evolutionary algorithm for finding the global minima of clusters are also discussed.

2.1.1 Density functional theory

Two theorems given by Hohenberg and Kohn [133] form the foundation of the density functional theory.

¹Hartee atomic units is taken in which $\hbar=m_e=c=1$.

2.1.1.1 First Hohenberg-Kohn theorem

First theorem states that the ground state electron density $\rho(\vec{r})$ of an electronic system uniquely determines the external potential acting on the electrons up to an additive constant.

Proof : We first assume opposite of the theorem to be true. It means the existence of two external potentials V_{ext} and V'_{ext} differing by more than an additive constant for a given $\rho(\vec{r})$ of an N -electron system. Two different external potentials V_{ext} and V'_{ext} lead to two different Hamiltonians \hat{H} and \hat{H}' respectively. Let the ground state wavefunctions of \hat{H} and \hat{H}' be Ψ and Ψ' having energies E and E' respectively. Note that $\hat{H} - \hat{H}'$ is equivalent to $\hat{V}_{ext} - \hat{V}'_{ext}$. Hence using variational principle, we will have

$$\begin{aligned} \langle \Psi' | \hat{H} | \Psi' \rangle &> E \\ \langle \Psi' | \hat{H}' + (\hat{H} - \hat{H}') | \Psi' \rangle &> E \\ E' + \int (V_{ext} - V'_{ext}) \rho(\vec{r}) d\vec{r} &> E. \end{aligned} \quad (2.2)$$

Similarly, $\langle \Psi | \hat{H}' | \Psi \rangle > E'$ will lead to

$$E + \int (V'_{ext} - V_{ext}) \rho(\vec{r}) d\vec{r} > E'. \quad (2.3)$$

From the Eqn. 2.2 and Eqn. 2.3, we obtain $E + E' > E + E'$ which is a contradiction. Therefore we conclude that the same ground state electron density cannot correspond to two different external potentials. This theorem establishes a one to one correspondence between the ground state electron density and the external potential. The ground state electron density determines the total number of electrons N through

$$\int \rho(\vec{r}) d\vec{r} = N. \quad (2.4)$$

Hence $\rho(\vec{r})$ uniquely determines the Hamiltonian via N and V_{ext} .

2.1.1.2 Second Hohenberg-Kohn theorem

Once the Hamiltonian is known, in principle, one can obtain the wavefunction of any state by solving the Schrödinger equation. Consequently, the ground state wavefunction and all the ground state properties such as kinetic and potential energies are

uniquely determined by the ground state electron density $\rho(\vec{r})$. Thus for a given V_{ext} , the total energy becomes a functional of $\rho(\vec{r})$ as follows :

$$\begin{aligned} E[\rho] &= T[\rho] + V_{ee}[\rho] + \int \rho(\vec{r})V_{ext}d\vec{r} \\ &= F_{HK}[\rho] + \int \rho(\vec{r})V_{ext}d\vec{r} \end{aligned} \quad (2.5)$$

where $F_{HK}[\rho]=T[\rho] + V_{ee}[\rho]$ is called the Hohenberg-Kohn functional and is defined for the ground state of an N -electron system. Also, it is independent of the external potential V_{ext} and is a universal functional of $\rho(\vec{r})$. $T[\rho]$ is the kinetic energy functional.

The second Hohenberg-Kohn theorem provides a variational principle for $E[\rho]$ with $\rho(\vec{r})$ as the basic variable. It says that for a given trial density $\rho'(\vec{r})$ with constraints $\int \rho'(\vec{r})d\vec{r} = N$ and $\rho'(\vec{r}) \geq 0$, total energy functional (Eqn 2.5) will be given by

$$E[\rho'] \geq E[\rho]. \quad (2.6)$$

Proof : From the first Hohenberg-Kohn theorem, we know that the trial density $\rho'(\vec{r})$ uniquely determines its Hamiltonian \hat{H}' and hence its own ground state wavefunction Ψ' . Using Ψ' as a trial wavefunction for the Hamiltonian \hat{H} corresponding to the problem of interest :

$$\langle \Psi' | \hat{H} | \Psi' \rangle = \int \rho'(\vec{r})V_{ext}(\vec{r})d\vec{r} + F_{HK}[\rho'] \geq \langle \Psi | \hat{H} | \Psi \rangle.$$

Using Eqn 2.5 we obtain $E[\rho'] \geq E[\rho]$ which proves the theorem.

The electron density which minimizes $E[\rho]$ is obtained via stationary principle :

$$\delta \left[E[\rho] - \mu \left\{ \int \rho(\vec{r})d\vec{r} - N \right\} \right] = 0 \quad (2.7)$$

where μ is the Lagrange multiplier for the constraint $\int \rho(\vec{r})d\vec{r} = N$. Eqn. 2.7 yields the value of μ at the minimum for a constrained minimization

$$\mu = V_{ext} + \frac{\delta F_{HK}[\rho]}{\delta \rho(\vec{r})}. \quad (2.8)$$

μ is known as the chemical potential of the N -electron system.

2.1.2 The Kohn-Sham method

From the Hohenberg-Kohn theorems, we learn about the possibility of calculating ground state properties by knowing the ground state electron density. However, they do not provide any computational scheme to calculate $\rho(\vec{r})$ because the functional form of F_{HK} is unknown. The Kohn-Sham formalism provides a set of equations known as the Kohn-Sham equations. These equations are solved self-consistently to obtain $\rho(\vec{r})$ that minimizes $E[\rho]$ [134].

For a given N -electron interacting system, Kohn and Sham assumed the existence of a non-interacting reference system. The only constraint is that the fictitious reference system should have same electron density $\rho(\vec{r})$ in the ground state as the interacting system of interest [134]. For such a non-interacting N -electron system, we can write the Hamiltonian as follows

$$\begin{aligned}\hat{H} &= -\sum_{i=1}^N \frac{\nabla_i^2}{2} + \sum_{i=1}^N v_s(\vec{r}_i) \\ &= \sum_{i=1}^N \hat{h}_i\end{aligned}\tag{2.9}$$

where \hat{h}_i is single-electron Hamiltonian and $v_s(\vec{r}_i)$ is single-electron potential which is unknown. For this system, the ground state wave function will be given by a Slater determinant of the N lowest energy states. Its kinetic energy can be calculated exactly and is given by

$$\begin{aligned}T_{KS}[\rho] &= -\langle \Psi_s | \sum_{i=1}^N \frac{\nabla_i^2}{2} | \Psi_s \rangle \\ &= -\sum_{i=1}^N \langle \psi_i | \frac{\nabla^2}{2} | \psi_i \rangle\end{aligned}\tag{2.10}$$

where ψ_i 's represent the single electron orbitals and are the eigenstates of one-electron Hamiltonian \hat{h}_i .

The idea behind the proposal of a non-interacting system is as follows. As electron-electron interactions are absent, the kinetic energy functional ($T_{KS}[\rho]$) of the reference system is not equal to $T[\rho]$ of the interacting system. Kohn and Sham wrote $E[\rho]$ in the following form :

$$E[\rho] = T_{KS}[\rho] + J[\rho] + E_{xc}[\rho] + \int \rho(\vec{r}) V_{ext} d\vec{r}\tag{2.11}$$

Here $J[\rho]=\frac{1}{2} \int \int \rho(\vec{r}_1) \frac{1}{r_{12}} \rho(\vec{r}_2) d\vec{r}_1 d\vec{r}_2$ is the classical electron-electron repulsion energy and $E_{xc}[\rho]$ is given by,

$$E_{xc}[\rho] = T[\rho] - T_{KS}[\rho] + V_{ee}[\rho] - J[\rho]. \quad (2.12)$$

Difference of the two kinetic energies, i.e., $T[\rho] - T_{KS}[\rho]$ along with non-classical part of $V_{ee}[\rho]$ is clubbed into a functional known as the exchange-correlation functional $E_{xc}[\rho]$.

Using stationary principle (Eqn. 2.7), a condition on $\rho(\vec{r})$ that minimizes $E[\rho]$ is given by

$$\mu = V_{ext} + \frac{\delta J[\rho]}{\delta \rho(r)} + \frac{\delta E_{xc}[\rho]}{\delta \rho(r)} + \frac{\delta T_{KS}[\rho]}{\delta \rho(\vec{r})} \quad (2.13)$$

Now comparison of Eqn 2.13 with the chemical potential of the reference system, i.e., $\mu = v_s + \frac{\delta T_{KS}[\rho]}{\delta \rho(\vec{r})}$ provides,

$$\begin{aligned} v_s &= V_{ext} + \frac{\delta J[\rho]}{\delta \rho(r)} + \frac{\delta E_{xc}[\rho]}{\delta \rho(r)} \\ &= V_{ext} + \int \frac{\rho(\vec{r}')}{|\vec{r} - \vec{r}'|} d\vec{r}' + V_{xc} . \end{aligned} \quad (2.14)$$

where we have defined the exchange-correlation potential as follows :

$$V_{xc}[\rho] = \frac{\delta E_{xc}[\rho]}{\delta \rho(\vec{r})} . \quad (2.15)$$

Thus we can see that problem of interacting N -electron system under V_{ext} is mapped into a problem of non-interacting electrons moving under an effective potential $V_{eff}(\vec{r})=v_s(\vec{r})$. Thus set of the N single-electron equations is given by,

$$\left[\frac{-\nabla_i^2}{2} + \hat{V}_{eff}(\vec{r}_i) \right] \psi_i = \varepsilon_i \psi_i . \quad (2.16)$$

These N single-electron equations are known as Kohn-Sham equations. The ground state electron density and single-electron or Kohn-Sham orbitals, i.e., ψ_i 's are related as follows:

$$\rho(\vec{r}) = \sum_{i=1}^N |\psi_i(\vec{r})|^2 \quad (2.17)$$

Now Eqn. 2.16 and Eqn. 2.14 are solved self-consistently to obtain the Kohn-Sham orbitals ψ_i 's under the constraint Eqn. 2.17. Within the Kohn-Sham formalism, total energy can be rewritten as

$$\begin{aligned}
E[\rho] &= \sum_{i=1}^N \langle \psi_i | \frac{-\nabla^2}{2} | \psi_i \rangle + \int \frac{\rho(\vec{r}_1)\rho(\vec{r}_2)}{|\vec{r}_1 - \vec{r}_2|} d\vec{r}_1 d\vec{r}_2 + E_{xc}[\rho] + \int \rho(\vec{r}) V_{ext} d\vec{r} \\
\text{Or} \\
&= \sum_{i=1}^N \varepsilon_i - \frac{1}{2} \int \frac{\rho(\vec{r}_1)\rho(\vec{r}_2)}{|\vec{r}_1 - \vec{r}_2|} d\vec{r}_1 d\vec{r}_2 + E_{xc}[\rho] - \int \rho(\vec{r}) V_{xc} d\vec{r} \quad (2.18)
\end{aligned}$$

where $\sum_{i=1}^N \varepsilon_i = \sum_{i=1}^N \langle \psi_i | \frac{-\nabla^2}{2} + \hat{V}_{eff}(\vec{r}_i) | \psi_i \rangle$.

The meaning of self-consistency in practice is as follows. In order to solve the single electron coupled equations, i.e., Eqn. 2.16, one must know V_{eff} , thereby $\rho(\vec{r})$. It means that we should know the occupied set of the Kohn-Sham orbitals ψ_i 's. We start with some trial charge density and generate V_{eff} . Then we solve the Kohn-Sham equations to get ψ_i 's and calculate $\rho(\vec{r})$. This process is repeated till the output charge density is the same as the input charge density, or equivalently the energy of the system does not change any more.

2.1.3 Exchange-correlation functional

The key difference between the HF and DFT is that DFT contains no approximation as we can see from its formalism. All we need to know is a functional expression for E_{xc} . Unfortunately, an explicit form of E_{xc} is unknown. Various approximations for E_{xc} have been suggested which are discussed briefly below.

2.1.3.1 The Local density Approximation (LDA)

The simplest approximation for E_{xc} is given by the so-called local density approximation (LDA). In LDA [134], one writes

$$E_{xc}^{LDA}[\rho] = \int \rho(\vec{r}) \varepsilon_{xc}(\rho(\vec{r})) d\vec{r} \quad (2.19)$$

where $\varepsilon_{xc}(\rho)$ denotes the exchange-correlation energy per particle of a uniform electron gas of density ρ . Further, $\varepsilon_{xc}(\rho)$ can be divided into exchange and correlation

contributions

$$\varepsilon_{xc}(\rho) = \varepsilon_x(\rho) + \varepsilon_c(\rho). \quad (2.20)$$

The exchange energy per particle for a uniform electron gas is provided by Dirac's expression

$$\varepsilon_x(\rho) = -\frac{3}{4} \left(\frac{3}{\pi} \right)^{1/3} \rho(\vec{r})^{1/3}. \quad (2.21)$$

Unfortunately, there is no such explicit expression for $\varepsilon_c(\rho)$. However, accurate numerical results for the homogeneous electron gas were given by Ceperly *et al* [135] using quantum Monte-Carlo. Based on these results, various authors have presented analytical expressions of $\varepsilon_c(\rho)$ using interpolation schemes. The most widely used representations of $\varepsilon_c(\rho)$ are the ones developed by Vosko *et al* [136] and Perdew *et al* [137].

The extension of LDA for spin-polarized system is provided by local spin density approximation (LSDA). In LSDA, the exchange energy is provided by following expression :

$$E_x^{LSDA} = -\frac{3}{2} \left(\frac{3}{4\pi} \right)^{1/3} \int [\rho_\uparrow(\vec{r})^{4/3} + \rho_\downarrow(\vec{r})^{4/3}] d\vec{r}. \quad (2.22)$$

Here we have used two spin density $\rho_\uparrow(\vec{r})$ and $\rho_\downarrow(\vec{r})$ corresponding to up-spin (\uparrow) and down-spin (\downarrow) electrons respectively. Total electron density is given by

$$\rho_\uparrow(\vec{r}) + \rho_\downarrow(\vec{r}) = \rho(\vec{r}). \quad (2.23)$$

The general form of the correlation part is given by

$$E_c^{LSDA}[\rho_\uparrow, \rho_\downarrow] = \int \rho(\vec{r}) \epsilon_c(\rho_\uparrow(\vec{r}), \rho_\downarrow(\vec{r})) d\vec{r} \quad (2.24)$$

where $\epsilon_c(\rho_\uparrow(\vec{r}), \rho_\downarrow(\vec{r}))$ is the correlation energy per electron in a homogeneous electron gas. LDA has been reasonably successful in reproducing various properties for example structural properties of materials [138].

2.1.3.2 Generalized gradient approximation (GGA)

Along with remarkable successes of LDA, there are some well-known drawbacks. For example, overestimation of binding energies, underestimating band gaps are the

failure of this approximation. Also it does not properly describe strongly correlated systems, such as transition-metal oxides [139]. An obvious logical step to improve upon LDA is to include, in addition to the $\rho(\vec{r})$, its spatial variations in order to account for the non-homogeneity of the electron density. This provides a new class of functionals, known as generalized gradient approximations (GGA's). Most general form of the GGA functionals is given by

$$E_{xc}^{GGA}[\rho_{\uparrow}, \rho_{\downarrow}] = \int f\left(\rho_{\uparrow}(\vec{r}), \rho_{\downarrow}(\vec{r}), \nabla\rho_{\uparrow}(\vec{r}), \nabla\rho_{\downarrow}(\vec{r})\right) d\vec{r} \quad (2.25)$$

There are a large number of distinct GGA functionals depending on the form of the function f . Two of the most widely used functionals in the literature are the Perdew-Wang functional (PW91) [140] and the Perdew-Burke-Ernzerhof functional (PBE) [141]. An excellent review of the exchange-correlation functionals is given by Kohn [142].

2.2 Kohn-Sham equations: Introduction of basis sets

2.2.1 Kohn-Sham equations in localized basis

In the previous section, we have obtained a set of N single-particle Kohn-Sham equations. In order to solve these equations, Kohn-Sham orbitals are expressed in terms of a linear combination of Gaussian-type orbitals (LCGTO) as follows :

$$\psi_i(\vec{r}) = \sum_{\mu} C_{\mu i} \mu(\vec{r}) \quad (2.26)$$

where $\mu(\vec{r})$ is an atom centered basis function. From Eqn 2.26, the problem of finding the Kohn-Sham orbitals reduces to the problem of calculating the set of expansion coefficients $C_{\mu i}$'s that minimizes energy. These basis functions are further a linear combination of a fixed set of primitive cartesian Gaussian functions,

$$\mu(\vec{r}) = \sum_{p=1}^M d_p \phi_p^{GF}(x, y, z; \xi_p, i, j, k) \quad (2.27)$$

where M is the contraction length, d_p 's are the contraction coefficients. ξ_p 's are the orbital exponents which are always positive. The contraction length (M), contraction

coefficients (d_p 's) and ξ_p 's are optimized to mimic the Slater-type orbitals (STO's). In cartesian coordinates, ϕ_p^{GF} 's are given in the following form:

$$\phi_p(x, y, z; \xi_p, i, j, k) = \left(\frac{2\xi_p}{\pi}\right)^{\frac{3}{4}} \left[\frac{(8\xi_p)^{i+j+k} i! j! k!}{(2i!)(2j!)(2k!)}\right]^{\frac{1}{2}} x^i y^j z^k e^{-\xi_p(x^2+y^2+z^2)} \quad (2.28)$$

where (i, j, k) are non-negative integers. Their sum determines the angular character of a basis function. For example, when all three indices are zero, the GTO is an s -type orbital. A p -type GTO is obtained when one of the indices is equal to one. When the sum of the indices is equal to two, the orbital will be a d -type GTO. However, there can be six cartesian d -type functions $x^2, y^2, z^2, xy, xz, yz$. Sometimes these are transformed into five spherical d orbitals and one additional s -type orbital $(x^2+y^2+z^2)$. There are various kind of basis sets available. For example, minimal basis sets such as STO-3G and spilt valence basis sets such as 4-31G (double zeta basis), 6-31G etc. Details about localized basis sets are given in the books by Szabo and Ostlund [143], and Cramer [144].

Using Eqn. 2.26, $\rho(\vec{r})$ is given by

$$\begin{aligned} \rho(\vec{r}) &= \sum_{i=1}^N |\psi_i(\vec{r})|^2 \\ &= \sum_{\mu\nu} P_{\mu\nu} \mu(\vec{r}) \nu(\vec{r}) \end{aligned} \quad (2.29)$$

where the sum is over the occupied Kohn-Sham orbitals and \mathbf{P} is a matrix whose matrix elements are

$$P_{\mu\nu} = \sum_{i=1}^N C_{\mu i} C_{\nu i} . \quad (2.30)$$

\mathbf{P} is called the density matrix. With the help of Eqn. 2.29, the total energy E (Eqn 2.11) can be rewritten as follows :

$$E = \sum_{\mu\nu} P_{\mu\nu} H_{\mu\nu} + \frac{1}{2} \sum_{\mu\nu} \sum_{\sigma\tau} P_{\mu\nu} P_{\sigma\tau} \langle \mu\nu || \sigma\tau \rangle + E_{xc}[\rho] \quad (2.31)$$

where the symbol $||$ represents the $\frac{1}{|\vec{r}_1 - \vec{r}_2|}$ operator and

$$H_{\mu\nu} = \langle \mu | \frac{-\nabla^2}{2} | \nu \rangle + \sum_A \langle \mu | \frac{-Z_A}{|\vec{r} - \vec{R}_A|} | \nu \rangle \quad (2.32)$$

are defined as the elements of core Hamiltonian matrix. Here Z_A is the nuclear charge of an atom A and \vec{R}_A represents its position vector. Computational cost of $H_{\mu\nu}$ is of the order of N_b^2 , where N_b is the number of basis functions. The Coulomb term in Eqn. 2.31 has a formal N_b^4 scaling. Computation of $E_{xc}[\rho]$ given in Eqn. 2.19 requires a 3D numerical integration which scales as N_b^2 times g , where g denotes the number of grid points in the numerical integration. Therefore Coulomb repulsion energy is the computationally most expensive part. To reduce the computational time, variational approximation of Coulomb potential has been suggested [145, 146]. This approximation reduces its scaling from N_b^4 to N_b^2 times M , where M is the number of auxiliary functions in terms of which the electronic density is approximated by,

$$\rho(\vec{r}) \approx \tilde{\rho}(\vec{r}) = \sum_{\tilde{k}} x_{\tilde{k}}(\vec{r}) \tilde{k}(\vec{r}) \quad (2.33)$$

where $x_{\tilde{k}}$ are auxiliary expansion coefficients, and $\tilde{k}(\vec{r})$'s are the primitive Hermite Gaussian auxiliary functions centered on an atom and are given by

$$\begin{aligned} \tilde{k}(\vec{r}) &= \left(\frac{\partial}{\partial R_x} \right)^{\tilde{k}_x} \left(\frac{\partial}{\partial R_y} \right)^{\tilde{k}_y} \left(\frac{\partial}{\partial R_z} \right)^{\tilde{k}_z} \\ &\times e^{-\zeta_{\tilde{k}}(\vec{r}-\vec{R})^2} \end{aligned} \quad (2.34)$$

where $(\tilde{k}_x, \tilde{k}_y, \tilde{k}_z)$ determines the angular character of Hermite functions. $R_i (i=x,y,z)$ represent the components of \vec{R} of an atom. We have used deMon2k code for first-principles calculations in which variational approximation of the Coulomb potential is based on the minimization of error in the classical electron-electron interaction term with respect to auxiliary expansion coefficient. The error is given by

$$\varepsilon_2 = \frac{1}{2} \int \int \frac{[\rho(\vec{r}) - \tilde{\rho}(\vec{r})][\rho(\vec{r}') - \tilde{\rho}(\vec{r}')]d\vec{r}d\vec{r}'}{|\vec{r} - \vec{r}'|} \quad (2.35)$$

and it is positive, i.e.,

$$\varepsilon_2 \geq 0. \quad (2.36)$$

Using $\rho(\vec{r})$ and its auxiliary version ($\tilde{\rho}(\vec{r})$), Eqn. 2.35 will take following form :

$$\begin{aligned} \varepsilon_2 &= \frac{1}{2} \sum_{\mu\nu} \sum_{\sigma\tau} P_{\mu\nu} P_{\sigma\tau} \langle \mu\nu || \sigma\tau \rangle - \sum_{\mu\nu} \sum_{\tilde{k}} P_{\mu\nu} \langle \mu\nu || \tilde{k} \rangle x_{\tilde{k}} \\ &+ \frac{1}{2} \sum_{\tilde{k}\tilde{l}} x_{\tilde{k}} x_{\tilde{l}} \langle \tilde{k} || \tilde{l} \rangle \end{aligned} \quad (2.37)$$

where $\langle \tilde{k} | \tilde{l} \rangle = \int \int \frac{\tilde{k}(\vec{r})\tilde{l}(\vec{r}')}{|\vec{r}-\vec{r}'|} d\vec{r}d\vec{r}'$ and $\langle \mu\nu | \tilde{k} \rangle = \int \int \frac{\mu(\vec{r})\nu(\vec{r}')\tilde{k}(\vec{r}')}{|\vec{r}-\vec{r}'|} d\vec{r}d\vec{r}'$. The expansion coefficients of $\tilde{\rho}(\vec{r})$ which minimize ε_2 are given by $\frac{\partial \varepsilon_2}{\partial x_{\tilde{m}}} = 0$. It leads to following set of equations :

$$\sum_{\tilde{k}} x_{\tilde{k}} \langle \tilde{k} | \tilde{m} \rangle = \sum_{\mu\nu} P_{\mu\nu} \langle \mu\nu | \tilde{m} \rangle \quad \forall \tilde{m} \quad (2.38)$$

Finally total energy (Eqn. 2.31) is approximated with the help of Eqn 2.36 and 2.37,

$$\begin{aligned} E &= \sum_{\mu\nu} \sum_i C_{\mu i} C_{\nu i} H_{\mu\nu} + \sum_{\tilde{k}} \sum_{\mu\nu} \sum_i C_{\mu i} C_{\nu i} \langle \mu\nu | \tilde{k} \rangle x_{\tilde{k}} \\ &\quad - \frac{1}{2} \sum_{\tilde{k}\tilde{l}} x_{\tilde{k}} x_{\tilde{l}} \langle \tilde{k} | \tilde{l} \rangle + E_{xc}[\rho]. \end{aligned} \quad (2.39)$$

We demand that Kohn-Sham orbitals should be orthonormal, i.e.,

$$\begin{aligned} \langle \psi_i | \psi_j \rangle &= \delta_{ij} \\ \sum_{\mu\nu} C_{\mu\nu} C_{\nu j} S_{\mu\nu} &= \delta_{ij} \end{aligned} \quad (2.40)$$

where $S_{\mu\nu} = \langle \mu | \nu \rangle$ are the elements of overlap matrix \mathbf{S} . Now minimization of E with respect to $C_{\mu i}$ i.e., $\frac{\partial E}{\partial C_{\mu i}} = 0$ gives

$$K_{\mu\nu} C_{\nu i} = \sum_{\nu} \sum_j S_{\mu\nu} C_{\nu j} \epsilon_{ij} \quad \forall \mu, i \quad (2.41)$$

where $K_{\mu\nu}$ represent the elements of the Kohn-Sham matrix \mathbf{K} and are given by

$$K_{\mu\nu} = H_{\mu\nu} + \sum_{\tilde{k}} \langle \mu\nu | \tilde{k} \rangle x_{\tilde{k}} + \langle \mu | V_{xc}[\rho] | \nu \rangle. \quad (2.42)$$

ϵ_{ij} are the undetermined Lagrange multipliers corresponding to Eqn 2.40. With the help of unitary transformations of the occupied ψ_i 's, one obtains canonical Kohn-Sham equations :

$$\mathbf{KC} = \epsilon \mathbf{SC} \quad (2.43)$$

where \mathbf{C} is the molecular orbital coefficient matrix, and ϵ forms the diagonal matrix of the Lagrange multipliers, i.e., the Kohn-Sham orbital energies. Note that \mathbf{S} is not

a unit matrix due to non-orthogonal basis set. Therefore Eqn 2.43 is not in the form of usual matrix eigenvalue equation. In order to obtain matrix eigenvalue equation, one can introduce a new coefficient matrix \mathbf{C}' such that

$$\mathbf{C}' = \mathbf{X}^{-1}\mathbf{C} \quad (2.44)$$

where \mathbf{X} is a matrix which transforms \mathbf{S} into a unit matrix, i.e., $\mathbf{X}^{-1}\mathbf{S}\mathbf{X} = \mathbf{1}$. Substituting $\mathbf{C} = \mathbf{X}\mathbf{C}'$ into Eqn 2.43 leads to a matrix eigenvalue equation,

$$\mathbf{K}'\mathbf{C}' = \epsilon\mathbf{C}' \quad (2.45)$$

where $\mathbf{K}' = \mathbf{X}^\dagger\mathbf{K}\mathbf{X}$ represents the transformed Kohn-Sham matrix. This equation is solved for \mathbf{C}' by diagonalizing \mathbf{K}' .

This method can be summarized as follows. Starting from the given trial density, the expansion coefficients of approximated density $\tilde{\rho}(\vec{r})$ are obtained by solving the Eqn 2.38. Subsequently, Kohn-Sham matrix \mathbf{K}' is constructed with the help of Eqn. 2.42. Then a new set of molecular orbital coefficients are obtained by the diagonalization of the Kohn-Sham matrix. This new set of molecular orbital coefficients is used in the construction of density matrix, i.e., Eqn 2.30 and subsequently in a new $\tilde{\rho}(\vec{r})$. This self consistent (SCF) cycle is continued until self-consistency in energy is achieved. Further details are given in the Ref. [147, 148].

2.2.1.1 Effective Core Potentials

Core states of atoms are known to change very little when atoms aggregate to form either molecules or solids. They are highly localized and not involved in the chemical bonding. Hence core states play a minor role in determining the electronic and chemical properties. On the other hand, valence states are extended and are responsible for chemical bonding between the atoms. To reduce the computational cost, it will be of great help if we do not treat the core electrons explicitly and replace their effect by an effective core potential (ECP) or pseudopotential (PP's) to which valence electrons respond. By introducing ECP's and PP's, true valence orbitals are replaced by pseudo orbitals that match the true valence orbitals outside a core region. Inside the core region, pseudo orbitals are smooth and nodeless. Another important criterion is that true valence and pseudo orbitals inside the core region should have same norm so that one have the correct charge density outside the core region. This condition is called norm-conserving condition [149, 150].

Furthermore, it is known that relativistic effects are very important for core electrons in heavy atoms. One way to include relativistic effects is to generate the relativistic ECP (RECP). The generation of RECP's involves the numerical valence orbitals obtained from the self-consistent relativistic Hartee-Fock (HF) calculations. Then numerical ECP's are derived from these numerical pseudo orbitals and are fit to an analytic form with Gaussian functions. The numerical valence orbitals are also fit to Gaussian functions to obtain the corresponding basis sets. This approach has been used by Hay *et al* [151] to obtain RECP's. Lee *et al* generate the relativistic ECP's using two-component atomic Dirac-HF wave functions [152]. Such relativistic ECP's are usually known as quasi-relativistic ECP's (QECP's). We have used Stuttgart-Dresden QECP's in some of our first-principles calculations. For instance, (QECP19|SD) for Ag atom is taken where 19 specifies the number of valence electrons.

Since the rapid oscillations of true valence orbitals near nuclei are not taken in pseudopotential calculations, one can use a different method known as projector augmented wave (PAW) method to obtain all electron properties. In this method true valence orbitals with all nodes are obtained while ion-electron interactions are described by PAW pseudopotentials. This approach is used in solving Kohn-Sham equations within the plane wave formalism [153,154].

2.2.1.2 Mulliken population analysis

Study of charge distribution within molecules allows us to understand the chemical behaviour of constituent atoms. By knowing the charges on atoms, a qualitative information about the nature of bonding between them is obtained. Population analysis methods provide effective charges on the atoms within molecules. These methods use the atomic basis functions to estimate the total number of electrons associated with an atom. There are two methods available, namely Mulliken and Löwdin population analysis. Here we will briefly discuss Mulliken population approach.

Total number of electrons N in the system is obtained by integrating the electrons

density given in Eqn 2.29,

$$\begin{aligned}
N &= \int \rho(\vec{r}) d\vec{r} = \int \sum_{\mu\nu} P_{\mu\nu} \mu(\vec{r}) \nu(\vec{r}) d\vec{r} \\
&= \sum_{\mu\nu} P_{\mu\nu} S_{\nu\mu} \\
&= \text{Tr}[\mathbf{PS}].
\end{aligned} \tag{2.46}$$

In Mulliken population analysis $(\mathbf{PS})_{\mu\mu}$ is defined as the number of electrons associated with the atomic orbital μ . Now total electrons associated with an atom A is obtained by summing up the contributions from all the atomic basis functions centered on the atom A ,

$$q_A = \sum_{\mu \in A} (\mathbf{PS})_{\mu\mu}. \tag{2.47}$$

Mulliken charge on atom A is given by the sum of the nuclear and electronic contributions,

$$Q_A = Z_A - q_A. \tag{2.48}$$

One can also defined density matrices for \uparrow and \downarrow spin electrons separately in a manner similar to Eqn 2.30. For example, density matrix $P_{\mu\nu}^\uparrow$ for \uparrow spin electrons (N_\uparrow) is given by

$$P_{\mu\nu}^\uparrow = \sum_{i=1}^{N_\uparrow} C_{\mu i}^\uparrow C_{\nu i}^\uparrow. \tag{2.49}$$

Thus using Eqn's 2.47, 2.48 and 2.49, one can get Q_A^\uparrow and Q_A^\downarrow . Their sum and difference provide the net Mulliken charge and spin respectively.

2.2.2 Kohn-Sham equations in plane wave basis

For a periodic solid, a convenient expansion of the Kohn-Sham orbitals is given in terms of plane waves as follows :

$$\psi_{n,\vec{k}}(\vec{r}) = \sum_{\vec{G}} C_{n,\vec{k}+\vec{G}} e^{i(\vec{k}+\vec{G})\cdot\vec{r}}. \tag{2.50}$$

where \vec{k} and \vec{G} are the wave and reciprocal lattice vectors respectively. The Fourier components are given by $C_{n,\vec{k}+\vec{G}}$, where n represents the band index. These wave functions are known as Bloch wave functions. A disadvantage of using plane waves is that fast oscillations of wave functions near the nuclei require a large number of plane waves. However, plane waves are used in conjunction with PP's which reduce the number of plane waves significantly as the pseudo-valence functions are smooth in the core region. One can use the plane waves as basis sets even for finite systems such as atoms, molecules and clusters. Desired finite system is placed inside a large cubic unit cell. This introduces enough empty space between the periodic images of the finite system so that the interactions between them are negligible. The Kohn-Sham equations in the real space is given by

$$\left[-\frac{\nabla^2}{2} + \hat{V}_{eff}(\vec{r}) \right] \psi_{n,\vec{k}}(\vec{r}) = \varepsilon_{n,\vec{k}} \psi_{n,\vec{k}}(\vec{r}) \quad (2.51)$$

where

$$\hat{V}_{eff}(\vec{r}) = \sum_{\vec{R},i} \hat{V}_i^{ps}(\vec{r} - \vec{R} - \vec{t}_i) + \int \frac{\rho(\vec{r}')}{|\vec{r} - \vec{r}'|} d\vec{r}' + \hat{V}_{xc}(\vec{r}) \quad (2.52)$$

Using the pseudopotential approximation, the external potential is the sum of the pseudopotentials of all the atoms in the system. Vectors \vec{R} are the Bravais-lattice vectors, while the position of an atom within the unit cell is given by \vec{t}_i . $\varepsilon_{n,\vec{k}}$'s denote the Kohn-Sham band energies. \vec{k} values are restricted to within the first Brillouin Zone (BZ) of the reciprocal space. With the help of Eqn. 2.50, the Fourier transform of Eqn. 2.51 will yield a set of linear equations for the Fourier components $C_{n,\vec{k}+\vec{G}}$,

$$\sum_{\vec{G}'} \left[|\vec{k} + \vec{G}|^2 \delta_{\vec{G}\vec{G}'} + V_{eff}(\vec{k} + \vec{G}, \vec{k} + \vec{G}') \right] C_{n,\vec{k}+\vec{G}'} = \varepsilon_{n,\vec{k}} C_{n,\vec{k}+\vec{G}} \quad (2.53)$$

where $V_{eff}(\vec{k} + \vec{G}, \vec{k} + \vec{G}') = \int e^{-i(\vec{k}+\vec{G})\vec{r}} \hat{V}_{eff}(\vec{r}) e^{i(\vec{k}+\vec{G}')\vec{r}} d\vec{r}$ and has the following three contributions,

$$\begin{aligned} V_{eff}(\vec{k} + \vec{G}, \vec{k} + \vec{G}') &= V^{ps}(\vec{k} + \vec{G}, \vec{k} + \vec{G}') + V_{ee}(\vec{G} - \vec{G}') \\ &+ V_{xc}(\vec{G} - \vec{G}'). \end{aligned} \quad (2.54)$$

Three terms are the Fourier transforms of the pseudopotential, classical electron-electron, and exchange-correlation potential respectively. Eqn 2.53 can be viewed as

matrix eigenvalue equation and is diagonalized to obtain the $C_{n,\vec{k}+\vec{G}}$'s. One major advantage of using plane wave is that fast Fourier transform (FFT) technique can be invoked to evaluate matrix elements.

In principle, an exact solution (Eqn. 2.50) of the Kohn-Sham equations requires an infinite number of \vec{G} . However, in practice, the contribution from higher Fourier coefficients decreases with increasing $|\vec{k} + \vec{G}|$. Therefore we truncate the expansion at some value of $|\vec{k} + \vec{G}|$. To do this, only the plane waves with kinetic energy lower than the chosen energy cutoff E_{cut} are included in Eqn. 2.50 :

$$\frac{1}{2}|\vec{k} + \vec{G}|^2 \leq E_{cut}. \quad (2.55)$$

Total energy will be a sum of E and inter-nuclei interaction energy E_{II} .

$$E_{total} = E + E_{II} \quad (2.56)$$

where E can be given by Eqn 2.18 with ε_i 's replaced by $\varepsilon_{n,\vec{k}}$ and summation is taken over \vec{k} for all occupied bands and $E_{II} = \sum_i \sum_{j>i} \frac{Z_i Z_j}{|\vec{R}_i - \vec{R}_j|}$. E_{II} is evaluated within periodic boundary conditions using Ewald summation techniques [155]. We have used in our calculations are PAW pseudopotentials in our calculations. These pseudopotentials are constructed within PAW method. In this method a linear transformation of pseudo valence orbitals leads to true valence orbitals with the help of projector functions. PAW transformation modifies the pseudo orbitals to have all the nodes only within the atom-centered augmentation sphere. As a result true valence orbital decomposes into a smoother orbital outside the augmentation sphere and a contribution coming from the augmentation sphere. A detail discussion of DFT in plane wave formalism is given in ref [156].

This method can be summarized as follows: An initial guess for trial electron density and trial set of occupied $\psi_{n,\vec{k}}(\vec{r})$ is taken. Now we calculate the V^{ps} , V_{ee} , and V_{xc} potentials in the Fourier space. Subsequently, we diagonalize Eqn 2.53 to obtain the Kohn-Sham energy eigenstates which generate different electron density. Then again new V_{ee} and V_{xc} potentials are constructed which are used in diagonalizing Eqn 2.53. This process is repeated until the self-consistency in density or total energy is achieved. Once the self-consistency is obtained, one can calculate forces on atoms etc. These forces can be used in local structure optimization of a given atomic system.

2.2.3 Forces and local structure optimization

In order to find a local minima on a potential energy surface², one needs to know the forces on the constituent atoms (ions) of the given system. These forces can be easily calculated using Hellmann-Feynman theorem [157]. The ions are moved in the direction of the forces until the calculated forces are smaller than a pre-set cutoff value. For a given ionic configuration, Hamiltonian \hat{H} is a function of $\vec{R} = (\vec{R}_1, \vec{R}_2, \vec{R}_3 \dots)$, where $\vec{R}_{i=1,2,3\dots}$ are the position vectors of the ions. The Hellman-Feynman force on an ion A is given by

$$\begin{aligned}
 \vec{F}_A &= -\frac{dE_{total}}{d\vec{R}_A} = -\frac{d}{d\vec{R}_A}(E + E_{II}) \\
 &= -\frac{d}{d\vec{R}_A} \left[\langle \Psi_s(\vec{R}) | \hat{H}(\vec{R}) | \Psi_s(\vec{R}) \rangle + E_{II}(\vec{R}) \right] \\
 &= -\langle \Psi_s(\vec{R}) | \frac{\partial \hat{H}(\vec{R})}{\partial \vec{R}_A} | \Psi_s(\vec{R}) \rangle - \langle \frac{\partial \Psi_s(\vec{R})}{\partial \vec{R}_A} | \hat{H}(\vec{R}) | \Psi_s(\vec{R}) \rangle - \langle \Psi_s(\vec{R}) | \hat{H}(\vec{R}) | \frac{\partial \Psi_s(\vec{R})}{\partial \vec{R}_A} \rangle \\
 &\quad - \frac{\partial E_{II}(\vec{R})}{\partial \vec{R}_A}
 \end{aligned} \tag{2.57}$$

where \vec{R}_A is the position of an ion A . When the self consistency is achieved as discussed previously, $|\Psi_s\rangle$ will be the ground state eigenfunction of Hamiltonian \hat{H} , i.e., $\hat{H}|\Psi_s\rangle = E|\Psi_s\rangle$. Then Eqn 2.57 will take the following form :

$$\vec{F}_A = -\langle \Psi_s(\vec{R}) | \frac{\partial \hat{H}(\vec{R})}{\partial \vec{R}_A} | \Psi_s(\vec{R}) \rangle - E \frac{\partial \langle \Psi_s | \Psi_s \rangle}{\partial \vec{R}_A} - \frac{\partial E_{II}(\vec{R})}{\partial \vec{R}_A} \tag{2.58}$$

Using $\langle \Psi_s | \Psi_s \rangle = 1$, we will have

$$\vec{F}_A = -\langle \Psi_s(\vec{R}) | \frac{\partial \hat{H}(\vec{R})}{\partial \vec{R}_A} | \Psi_s(\vec{R}) \rangle - \frac{\partial E_{II}(\vec{R})}{\partial \vec{R}_A} \tag{2.59}$$

where we have used $\langle \Psi_s | \Psi_s \rangle = 1$. When a localized basis set is used to expand $|\Psi_s\rangle$, then middle term in Eqn 2.58 will contribute a finite contributions known as Pulay forces. However when one use plane wave basis sets which are independent of the atomic position, Pulay force will be zero. Clusters can be relaxed to the nearest local minima of the potential energy surface using the Hellmann-Feynman forces and an optimization technique such as conjugate gradient.

²Within the Born-Oppenheimer approximation, the potential energy surface represents a surface in $3N-6$ configurational space.

2.3 Evolutionary algorithm

Predicting the lowest energy structure, i.e., global minimum of a given cluster requires a large number of total energy calculations performed at various cluster geometries. To find the global minimum, one can use intuition to guess various initial structures that are chemically reasonable. However, the number of local minima on the potential energy surface increases exponentially as the cluster size increases. Therefore finding the lowest energy structure of a given cluster is one of the most challenging tasks. Here we have used an evolutionary algorithm which involves genetic algorithm to obtain the global minimum and a number of metastable structures for a given cluster [158, 159]. Figure 2.1 shows a working flowchart of the evolutionary algorithm. The fundamental idea of the algorithm is to start with a set of initial structures and evolve them using heredity and mutation operators. Here we will provide a short summary of the evolutionary algorithm.

2.3.1 Initialization

The evolutionary algorithm starts with providing an initial population. Here it is generated by applying possible point group symmetries for a given size to randomly produced atomic coordinates. After that these initial structures of the cluster are relaxed to their nearest local minimum using a conjugate gradient method. Energies of these structures are calculated using the plane wave PAW method within DFT [153, 154]. The PBE exchange correlation functional is used [141].

2.3.2 Variation operators

The population in the next generation is produced by variational operators which are basically the heredity, soft-mutation and mutation operators. By applying heredity operators, a child structure is created from two or more parents. Particularly, randomly chosen parts of the parent structures are combined into a single child structure. On the other hand, a child structure is obtained from a single parent by applying the mutation operator. In soft-mutation operator, atoms are moved along the eigenvectors of the softest normal mode of vibrations. These low frequency modes are associated with the low curvature of potential energy surface. Consequently, new structures are obtained after crossing such small energy barriers. A child structure is also generated by an atom permutation operator. By an atom permutation operator, chemically different atoms are swapped in randomly selected pairs that may give a

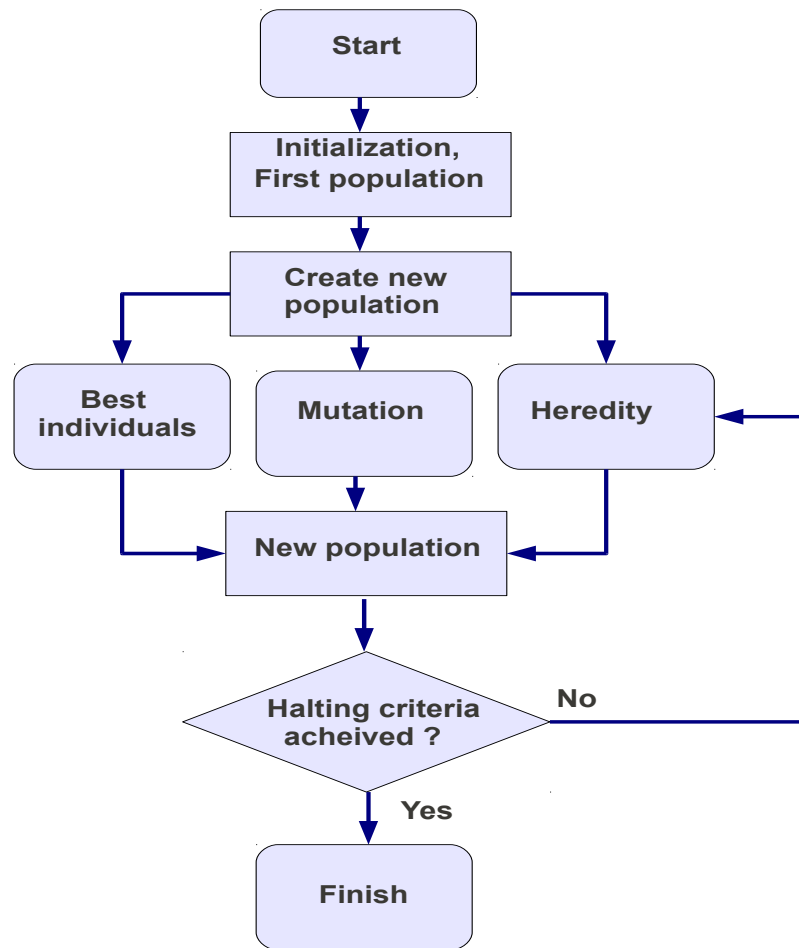


Figure 2.1: Flowchart of a typical evolutionary algorithm [158].

new structure.

2.3.3 Halting criteria

The fitness criterion used for these calculations is the total energy. The calculations are carried out up to a maximum number of generations with the halting criterion that if the energy of the best structure does not change for a certain number of generations then the calculations are stopped.

TM doped calcium clusters

3.1 Introduction

The electronic orbitals in metal clusters, while resembling those in real atoms in shape, do spread over multiple atoms. Generally, filling of electronic shells in these clusters do not follow the Hund's rule of maximizing the spin. Absence of Hund's rule in metal clusters is associated with Jahn-Teller effect. According to Jahn-Teller effect, a cluster with partially filled degenerate electronic shells will undergo geometric distortion and stabilize in a low spin state [160]. Within the shell model framework, it has been proposed that magnetic superatoms with spin moments could be stabilized by inducing exchange splitting within the shell orbitals [105]. The purpose of this chapter is to identify clusters that exhibit magnetic ground states and can possibly behave as magnetic superatoms. We will demonstrate our findings by examining the stability of transition metal doped calcium TMCa_n clusters containing various $3d$ TM atoms and 5-12 Ca atoms. We identify FeCa_8 with 24 valence electrons as a highly stable cluster that has a closed shell of 20 paired electrons and four un-paired electrons occupying the $2D_{xy}$, $2D_{yz}$, $2D_{xz}$, $2D_{x^2-y^2}$ levels, while the $2D_{z^2}$ level is separated by a large energy gap. We show that an interplay of crystal field splitting and Hund's coupling stabilizes this magnetic species. FeCa_8 is also identified as a magnetic superatom.

3.2 Computational details

All our first principles electronic structure calculations are performed within the density functional theory (DFT). Molecular orbitals (MO) are expressed as linear

combinations of Gaussian type orbitals centered on the atomic nuclei. deMon2k code is used for these calculations [161]. Calculation of four-center integrals are avoided by a variational fitting of the Coulomb potential as discussed in chapter 2. The exchange-correlation effects are taken into account using the generalized gradient approximation (GGA) functional proposed by Perdew, Burke and Ernzerhof (PBE) [162]. All electrons on the 3d TM atoms and Ca are treated explicitly using the double- ζ valence plus polarization basis sets optimized for GGA functionals by Calaminici et al. (DZVP-GGA) [163]. The auxiliary density was expanded in primitive Hermite Gaussians using the GEN-A2 auxiliary function set. By using above basis sets and exchange-correlation functional, first and second ionization potentials of Ca are found to be 6.06 eV and 11.98 eV respectively. These potentials are in excellent agreement with experimental values of 6.11 and 11.87 eV respectively [164].

To find the ground state structure of a cluster we have used two approaches. In the first approach, a large number of initial structures are taken for each cluster. These are generated as follows. For TMCa_N cluster, stable isomers of alkali and alkaline earth clusters for size $N+1$ are taken from earlier works and the literature, and different metal atoms are replaced by a TM atom of interest. In addition, possible Ca cage structures encapsulating the TM atom are also taken. Furthermore, we have taken various stable isomers of TMA_N clusters, where A represents an alkali element. For a given TM atom, the alkali atoms of TMA_N are replaced by Ca atoms. We have also taken the structures of TMMg_N reported in Ref [105] and replaced the Mg atoms by Ca. All possible spin states are considered for each initial structure, and all these clusters are fully optimized using a quasi-Newton method in the internal coordinates [165] without any symmetry constraints. We will call this the educated guess approach. To ensure that the optimized structures are local minima, harmonic frequencies are calculated for each one of them. If any structure turns out to have imaginary frequencies, it is re-optimized by distorting it along the unstable vibrational modes.

In the second approach, we perform a direct global search for the minimum energy structure of these clusters based on an evolutionary algorithm. A brief summary of our global structure search is given in chapter 2 of this thesis. Whenever we find a minimum of structure in global search that is different from the lowest energy structure obtained in the educated guess approach, we further relax it in deMon2K and compare the energies of the two structures.

3.3 Study of TMCa_8 clusters

3.3.1 Motivation

The motivation for studying TMCa_8 clusters is the recent study of TMMg_n clusters [105]. Medel *et al* showed FeMg_8 cluster as a magnetic superatom. Since Ca also belongs to the group of alkaline earth elements, a natural choice for finding new members of magnetic superatom family is to study the electronic and magnetic properties of TMCa_8 clusters.

3.3.2 Ground state structures

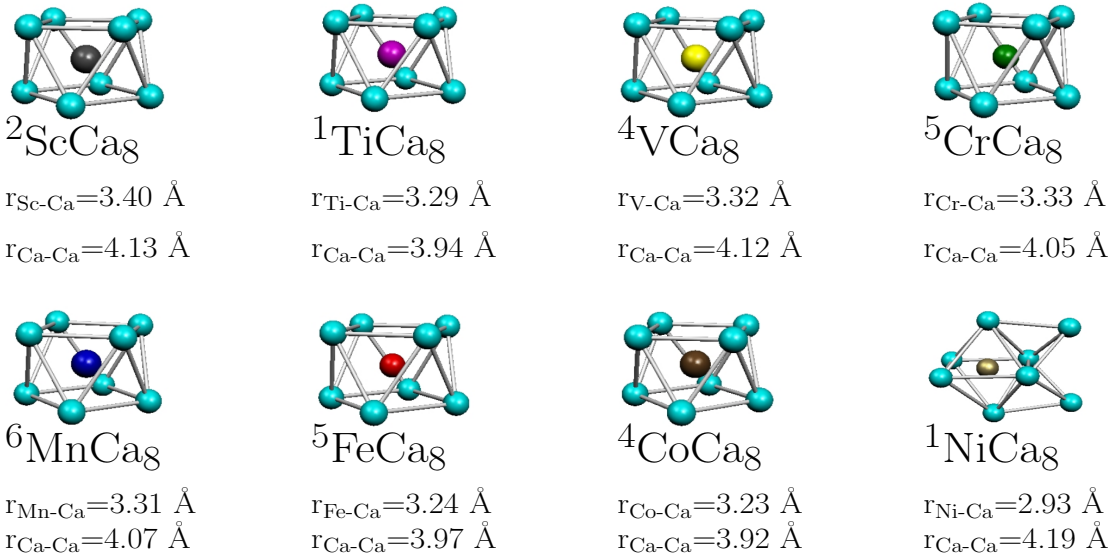


Figure 3.1: Ground state structure and multiplicity ($M=2S + 1$) of TMCa_8 clusters. Point group symmetry of TMCa_8 are also given. $r_{\text{TM-Ca}}$ and $r_{\text{Ca-Ca}}$ are average TM-Ca and Ca-Ca bond lengths in \AA .

Figure 3.1 shows the optimized ground state structures and spin multiplicities of all the TMCa_8 clusters. The ground state structures are found to be square antiprism arrangements of eight Ca atoms with an endohedral TM atom, similar to those previously reported for the TMMg_8 species [105], with the exception of NiCa_8 . NiCa_8 is a singlet with a bi-capped octahedron geometry. We find an isomer nearly degenerate (0.03 eV higher) with the square antiprism structure and a spin magnetic moment of $2\mu_B$ for NiCa_8 . The average Ca-Ca bond length ranges from 4.05 to 4.19

Å, while the average TM-Ca bond length ranges from 2.93 to 3.40 Å in the TMCa₈ series. The next higher energy isomers of all the TMCa₈ clusters are given in the Appendix A.1.

3.3.3 Relative Stabilities

Our primary goal is to identify stable magnetic clusters. Therefore we first proceed to examine (1) the HOMO-LUMO (HL) gap, (2) the adiabatic spin excitation energy (ΔE_{spin}), (3) the magnetic moment of the TMCa₈ clusters. The orbitals of a cluster which participate in bonding with other chemical species are the frontier orbitals. The lower the HOMO, larger is the amount of energy required to take out an electron from the cluster. On the other hand, it is the LUMO of a cluster that accommodates an additional electron. If the energy of the LUMO is high, then occupation of this extra electron is energetically unfavorable. Therefore a cluster with a large HL gap resists both accepting or donating electron and will be chemically more stable [166]. For example, Al₁₃⁻ cluster which has a HL gap of 1.87 eV is found to be non-reactive towards O₂. A measure of the chemical stability is also given by hardness (η). According to the principle of maximum hardness, a molecule tries to maximize its hardness [166, 167]. In conceptual DFT, η is defined as

$$\begin{aligned}\eta &= \frac{1}{2} \left(\frac{\partial \mu}{\partial n_e} \right)_{\nu} \\ &= \frac{1}{2} \left(\frac{\partial^2 E}{\partial n_e^2} \right)_{\nu}\end{aligned}\tag{3.1}$$

where μ is the chemical potential, E is the total energy and n_e is the number of electrons in the cluster. All the derivatives are to be taken at a constant external potential ν . In the finite difference approximation, the hardness can be written as

$$\eta \approx \frac{\text{IP-EA}}{2}\tag{3.2}$$

The IP and EA values can be calculated using Koopmans' theorem. According to Koopmans' theorem, IP and EA are simply equal to the negative of the energies of the HOMO and LUMO respectively. Then Eqn 3.2 becomes

$$\eta = \frac{\text{LUMO-HOMO}}{2}\tag{3.3}$$

Thus hardness becomes half of the HL gap. Consequently, large HL gap of a cluster leads to a large hardness and indicates its chemical stability. A more accurate approach for calculating η is the Δ SCF method. Within this approach, the vertical IP and EA values are obtained by doing self consistent calculations for the cation and the anion cluster respectively at the geometry of the neutral. These values are used in Eqn 3.2 to find η .

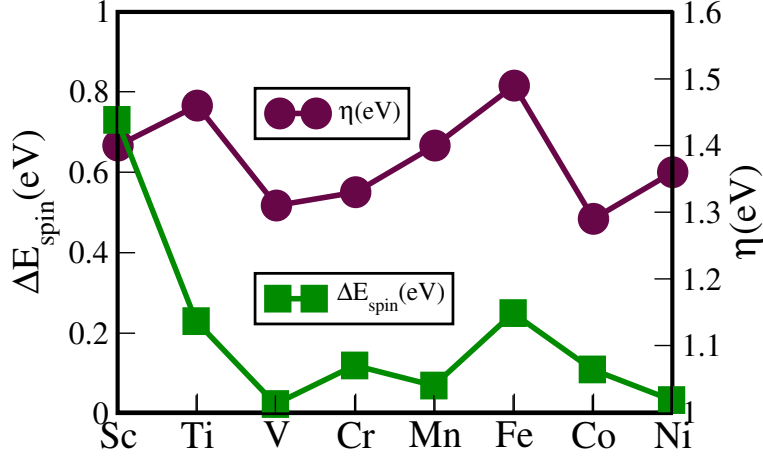


Figure 3.2: Variation of η and ΔE_{spin} with respect to TM atom.

Figure 3.2 shows the variation of η calculated via Δ SCF method and ΔE_{spin} for different TM atoms in the TMCa_8 series. A peak in η indicates enhanced chemical stability of FeCa_8 . Also FeCa_8 shows greater stability against adiabatic spin excitation. In addition, a second maximum in η is observed for TiCa_8 indicating its enhanced chemical stability. Table 3.1 summarizes the values of the HL gap, η and ΔE_{spin} of all the TMCa_8 clusters. TiCa_8 has the largest HL gap of 0.77 eV within the TMCa_8 series.

Cluster	HL(eV)	η (eV)	ΔE_{spin} (eV)
$^2\text{ScCa}_8$	0.41	1.40	0.73
$^1\text{TiCa}_8$	0.77	1.46	0.23
$^4\text{VCa}_8$	0.26	1.31	0.03
$^5\text{CrCa}_8$	0.15	1.33	0.12
$^6\text{MnCa}_8$	0.42	1.40	0.07
$^5\text{FeCa}_8$	0.63	1.49	0.25
$^4\text{CoCa}_8$	0.45	1.29	0.11
$^1\text{NiCa}_8$	0.34	1.36	0.03

Table 3.1: HL gap, hardness (η) and ΔE_{spin} of the TMCa_8 clusters.

Figure 3.3 shows the energies of molecular orbitals (MOs) and their isosurfaces

for ScCa_8 and TiCa_8 . We have identified the angular momentum character of the orbitals by inspection of their global shape and nodes in analogy with the atomic orbitals. We refer to such plots as the MO isosurface plots in this thesis. Majority (up) and minority (down) spin channels will be referred to as α and β respectively. If we count both $3d$ and $4s$ electrons of Ti ($3d^24s^2$) as valence electrons, then TiCa_8 has 20 electrons, a shell closing number within conventional shell models. As expected,

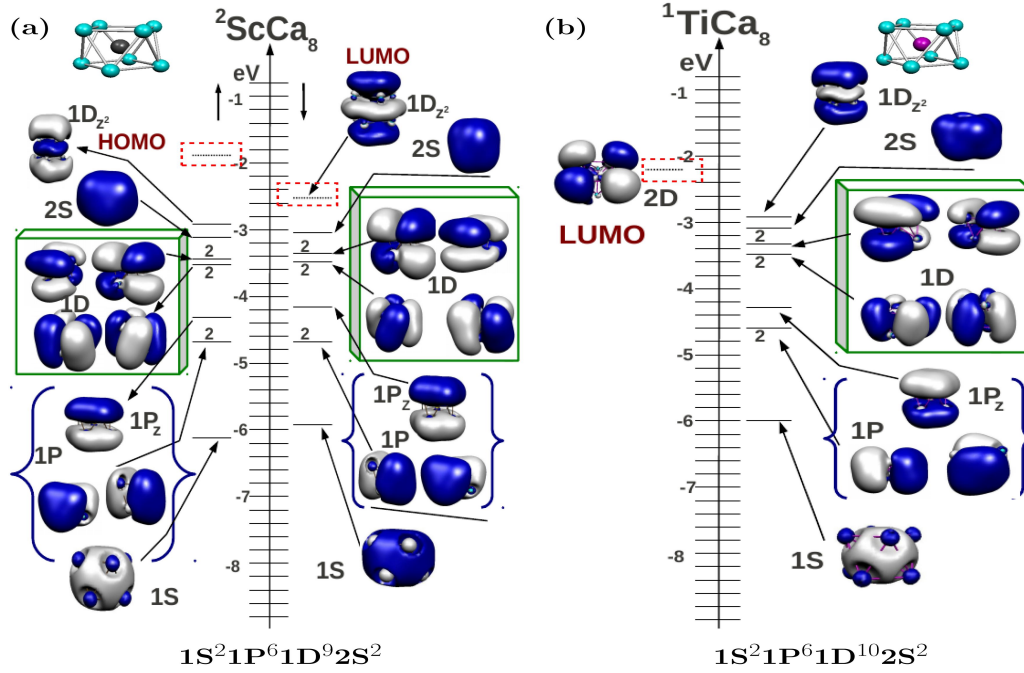


Figure 3.3: Molecular orbital energy levels and orbital wave-function isosurfaces of (a) ScCa_8 and (b) TiCa_8 . Continuous lines correspond to the filled levels while the dotted lines correspond to the unfilled states. Degeneracies are also marked.

TiCa_8 is a singlet with an electronic configuration $1S^2 1P^6 1D^{10} 2S^2$ (Figure 3.3(b)). Usually, a cluster having a large HL gap due to closed electronic shell is accompanied by a large ΔE_{spin} [168]. Surprisingly, the spin excitation energy of TiCa_8 (0.23 eV) is smaller than that of ScCa_8 (0.73 eV). Why ScCa_8 , a 19 electron open shell system, has a larger ΔE_{spin} requires an explanation. Figure 3.3(a) shows that ScCa_8 is a doublet in the ground state with a $1S^2 1P^6 1D^9 2S^2$ configuration. The next higher energy spin state is a quartet. To excite this cluster to a quartet spin state, an electron has to be promoted from the highest occupied orbital, i.e., $2S$ orbital in the β channel to the LUMO in α channel. Let us assume that there are no reorganizations of the MO's during this transition. We will call this the ‘frozen orbital’ approximation. Within

this approximation the energy required for this process is 1.10 eV. On the other hand, to excite TiCa_8 to a triplet state one has to excite one of the electrons from the HOMO to the LUMO. The required energy within the frozen orbital approximation is 0.77 eV only, equal to its HL gap. This argument qualitatively explains why ScCa_8 has a larger ΔE_{spin} . However, the actual ΔE_{spin} values obtained after self-consistent calculations of the spin-excited states are slightly different from these numbers.

The most significant finding of this study is the intriguing stability of FeCa_8 indicated by its large HL gap and ΔE_{spin} values. FeCa_8 contains 24 valence electrons if all the six $3d$ and two $4s$ electrons of the Fe atom ($3d^6 4s^2$) are treated as valence electrons. From the conventional shell model we know that 24 electrons do not correspond to any shell closure. Hence stability at this non-conventional electron count is rather unexpected. Or is it that only the $4s$ electrons act as valence electrons leading to an 18 electron filled shell configuration? Figure 3.4 shows the variation

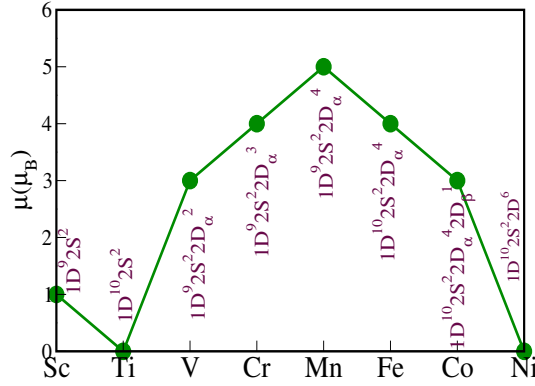


Figure 3.4: Variation of the magnetic moments (μ_B) with the TM atom and the nature of frontier orbitals.

of magnetic moment and nature of the frontier orbitals in the TMCa_8 series. FeCa_8 has a configuration of $1S^2 1P^6 1D^{10} 2S^2 2D_\alpha^4$ and a spin magnetic moment of $4 \mu_B$. Thus FeCa_8 is a unique cluster that has a relatively large hardness (1.49 eV), a large spin excitation energy (0.23 eV), and a spin magnetic moment of $4 \mu_B$. Hence it emerges as a likely candidate for magnetic superatom. Another interesting point is related to the ordering of energy levels in the TMCa_8 clusters. We know that energy ordering of the orbitals in the spherical shell model is $1S|1P|1D|2S|1F|2P|\dots$. However, Figure 3.4 shows the occupation of the $2D$ shell orbitals instead of the $1F$ or $2P$ orbitals from VCa_8 onwards. We shall discuss this point in the context of the FeCa_8 cluster.

3.3.4 Stability of FeCa₈ cluster

To understand the microscopic mechanism underlying its stability and stabilization of the 2D orbitals, we have analyzed the MO plot of FeCa₈ in Figure 3.5(a). The

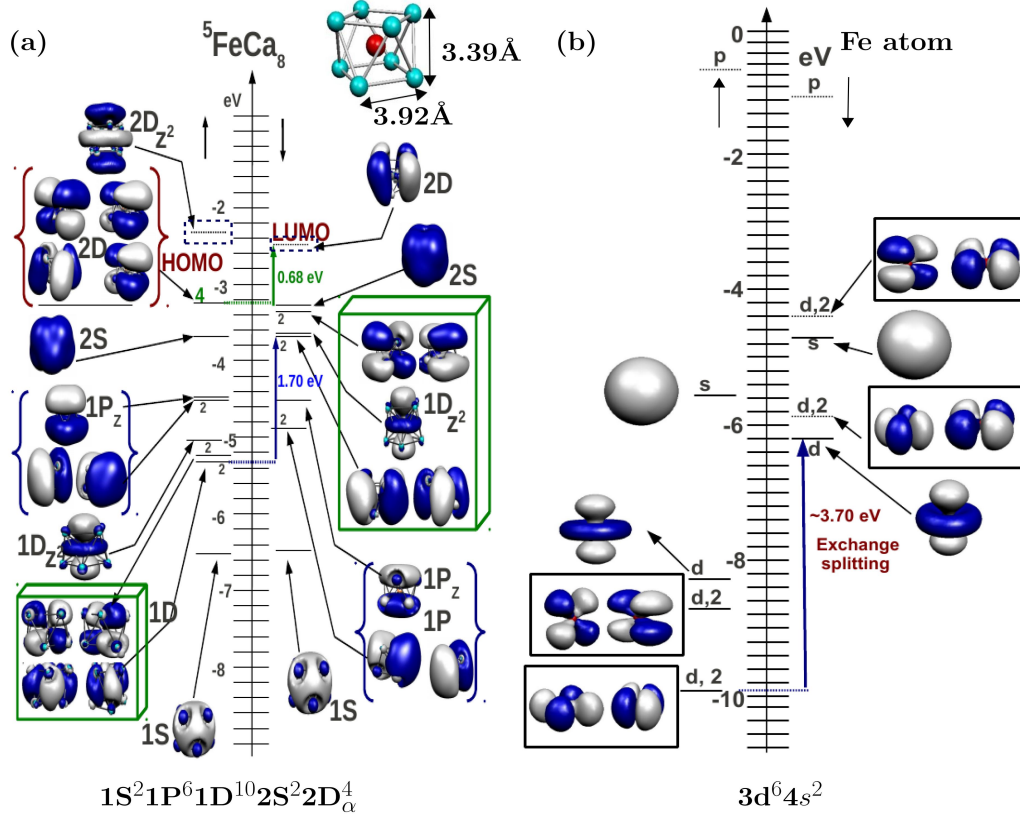


Figure 3.5: (a) Molecular orbital energy levels and orbital wave-function isosurfaces of FeCa₈. Red and green arrows showing the exchange splitting of the 1D and 2D orbitals respectively. (b) One electron energy levels and atomic orbitals of Fe atom. Blue arrow shows the exchange splitting of *d* orbitals of Fe atom.

lowest energy orbitals in both α and β channels have 1S character. The next higher energy orbitals above 1S are of 1D angular character in the α channel, while in the β channel they are of 1P character. In the optimized structure of FeCa₈, distance between the two planes of the antiprism is 3.39 Å, while Ca-Ca distance within a plane is 3.92 Å. Thus the Ca₈ cage in FeCa₈ represents an oblate distortion in the *z*-direction. This oblate shape produces a crystal field that breaks the degeneracy of the 1D orbitals in α channel and pushes the 1D_{*z*²} orbital to a higher energy (0.19 eV) with respect to the other 1D orbitals. Similarly 1P_{*z*} is split off to higher energy in both spin channels. The next set of higher energy orbitals in the α and β channels are

of 1P and 1D angular character respectively. After that the 2S orbitals are occupied in both the spin channels. In this way 1S, 1P, 1D and 2S orbitals in the two spin channels accommodate 20 electrons giving a $1S^21P^61D^{10}2S^2$ configuration. The next higher energy orbitals above 2S in the α channel are four degenerate 2D orbitals occupied by the remaining four electrons. These 2D orbitals form the HOMO of the FeCa_8 cluster. Due to crystal field effect, the $2D_{z^2}$ orbital is 0.95 eV higher in energy relative to HOMO. The LUMO of FeCa_8 is found to be in the β channel and is of 2D angular character. The calculated HL gap (0.68 eV) is higher than the HL gap of all TMCa_8 clusters except TiCa_8 .

According to Hund’s first rule, all the electrons in singly occupied degenerate atomic orbitals have parallel spins in order to maximize the total spin. However, electrons are not found to follow Hund’s rule in the atomic-like shell orbitals of simple metal clusters. Hence simple metal clusters are non-magnetic. In fact, Stern-Gerlach experiments performed by Douglass *et al* could not detect any magnetism in simple metal clusters [169]. Therefore, filling of the degenerate 2D shell orbitals with four electrons in the FeCa_8 cluster is interesting. This clearly demonstrates that electrons follow Hund’s rule in order to maximize the total spin. We will now try to understand the origin of Hund’s coupling in the 2D orbitals in TMCa_8 clusters.

Figure 3.5(b) shows the exchange splitting in the atomic $3d$ orbitals of a bare Fe atom. Here exchange splitting is defined as the energy difference between the lowest energy atomic orbitals of a given angular momentum (l) in the α and β channels. In our calculations, exchange splitting in the $3d$ orbitals of Fe is found to be 3.70 eV. Let us recall that the ground state structure of FeCa_8 is an antiprism in which the Fe atom occupies the central site. Fe atomic $3d$ orbitals are expected to hybridize with D- shell orbitals but not with P- and F- shell orbitals. Indeed, our calculations show that the 1P shell orbitals in both spin channels do not have any contribution from the Fe $3d$ states. 1D orbitals have $\sim 71\%$ contribution from the Fe $3d$ orbitals, while 2D orbital orbitals have $\sim 11\%$ contribution from the Fe $3d$ orbitals. Because of this contribution from the Fe $3d$ orbitals, the 2D orbitals are stabilized more in comparison to the 1F and 2P shell orbitals. In addition, a part of the large exchange splitting in the atomic $3d$ orbitals get transmitted to the D orbitals in the cluster. Figure 3.5(a) shows an exchange splitting of 1.70 eV in the 1D orbitals and 0.68 eV in the 2D orbitals. Thus degenerate $2D_\alpha$ orbitals are lower in energy than the 2D orbitals in the β channel. Consequently, the $2D_\alpha$ orbitals accommodate 4 electrons according to Hund’s rule.

In summary, FeCa_8 cluster emerges as a stable and magnetic species. The origin

of its enhanced stability is associated with the combined role of crystal field effect and exchange splitting. Crystal field breaks the degeneracy of the 2D orbitals and splits them into a group of four degenerate 2D orbitals and a $2D_{z^2}$ orbital. At the same time, presence of the Fe 3d orbitals induces an exchange splitting in the 2D orbitals. As a result, degenerate 2D orbitals are filled with four electrons via Hund's coupling and give a magnetic moment of $4 \mu_B$.

3.3.5 Local moments on TM dopants

It has been known that local moment on a 3d TM element is very sensitive to its environment. For example, early TM atoms (Sc-V) in the $TMNa_n$ clusters are shown to attain spin moments that are higher than their atomic values [100], while late TM atoms (Cr-Ni) are found to retain their atomic moments [101]. Therefore it will be interesting to see the behaviour of local spin moments on the TM dopants in the $TMCa_8$ clusters. Table 3.2 shows the spin moments on the atoms in $TMCa_8$ clusters obtained by carrying out a Mulliken population analysis. Most of the moment in

2ScCa_8	atomic spins	4VCa_8	atomic spins	5CrCa_8	atomic spins
Sc	0.9860	V	3.9310	Cr	4.6989
Ca	-0.0002	Ca	0.0097	Ca	-0.0786
Ca	0.0045	Ca	-0.1764	Ca	-0.0997
Ca	0.0024	Ca	-0.0470	Ca	-0.0907
Ca	-0.0005	Ca	-0.2473	Ca	-0.0983
Ca	0.0016	Ca	0.0140	Ca	-0.0810
Ca	0.0009	Ca	-0.1618	Ca	-0.0874
Ca	0.0026	Ca	-0.2545	Ca	-0.0804
Ca	0.0028	Ca	-0.0678	Ca	-0.0828
6MnCa_8	atomic spins	5FeCa_8	atomic spins	4CoCa_8	atomic spins
Mn	3.955	Fe	2.5144	Co	1.4279
Ca	0.1301	Ca	0.1840	Ca	0.1702
Ca	0.1301	Ca	0.1857	Ca	0.1284
Ca	0.1307	Ca	0.1855	Ca	0.1952
Ca	0.1298	Ca	0.1847	Ca	0.2307
Ca	0.1310	Ca	0.1852	Ca	0.1246
Ca	0.1294	Ca	0.1865	Ca	0.2400
Ca	0.1317	Ca	0.1880	Ca	0.2006
Ca	0.1313	Ca	0.1859	Ca	0.2823

Table 3.2: Atomic spins in $TMCa_8$ (TM=Sc, V, Cr, Mn, Fe and Co) clusters using Mulliken population analysis.

the $TMCa_8$ clusters is on the TM elements. In every case, the presence of a TM polarizes the host, i.e, Ca atoms. In $ScCa_8$, moments on the Sc atom is $0.98 \mu_B$, while moments on most of the Ca atoms are very small. Interestingly, moment

on V is $3.93 \mu_B$ in the VCa_8 cluster, higher than that of a bare V atom. The moments on host atoms except two Ca atoms are polarized in direction opposite to the moment of V. The moment on Cr is found to be $4.69 \mu_B$ in the CrCa_8 cluster. Anti-ferromagnetic coupling between the moments of Cr and host atoms provides a total magnetic moment of $4 \mu_B$. The Mn, Fe and Co doped Ca_8 clusters present a different situation. Moments on the host atoms are aligned parallel to the moments of TM elements. This ferromagnetic coupling provides moments of $5 \mu_B$, $4 \mu_B$ and $3 \mu_B$ respectively for the MnCa_8 , FeCa_8 and CoCa_8 clusters. Thus all TM elements except Ti and Ni polarize the host atoms in Ca_8 cages.

3.4 Study of FeCa_N ($N=5-12$) clusters

In the previous section, we examined the relative stability of TMCa_8 clusters across the $3d$ series. We also would like to investigate whether FeCa_8 is the most stable cluster if we change the number of Ca atoms. Therefore we have performed density functional calculations of FeCa_N cluster in the size range $N=5-12$.

3.4.1 Ground state structures

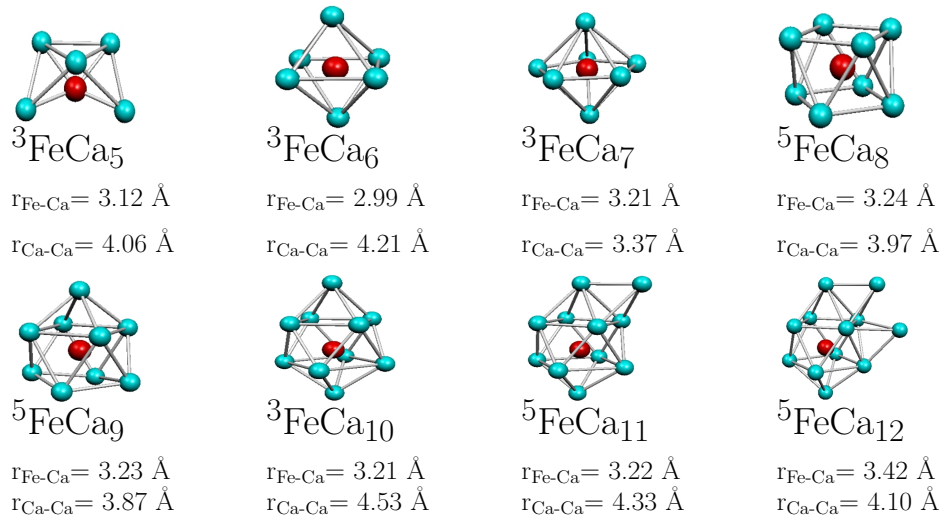


Figure 3.6: Ground state structure and multiplicity ($2S+1$) of FeCa_N clusters. $r_{\text{Fe-Ca}}$ and $r_{\text{Ca-Ca}}$ are average Fe-Ca and Ca-Ca bond lengths.

Figure 3.6 presents the optimized ground state structures of FeCa_N clusters.

FeCa₆ is the first cluster with an endohedral Fe atom at the center of a Ca₆ octahedron. FeCa₇ is found to have a pentagonal bi-pyramid structure in its ground state with Fe at the center. FeCa₉ and FeCa₁₀ are respectively formed by capping one and two square faces of the FeCa₈ cluster. Further addition of Ca on the triangular faces of FeCa₁₀ gives the ground state structures of FeCa₁₁ and FeCa₁₂. The average Ca-Ca bond lengths range from 3.84 to 4.56 Å, while the average Fe-Ca bond lengths range from 2.99 to 3.42 Å in the FeCa_{*n*} clusters. A few higher energy isomers of the FeCa_{*n*} clusters are given in the Appendix A.2

3.4.2 Relative stabilities

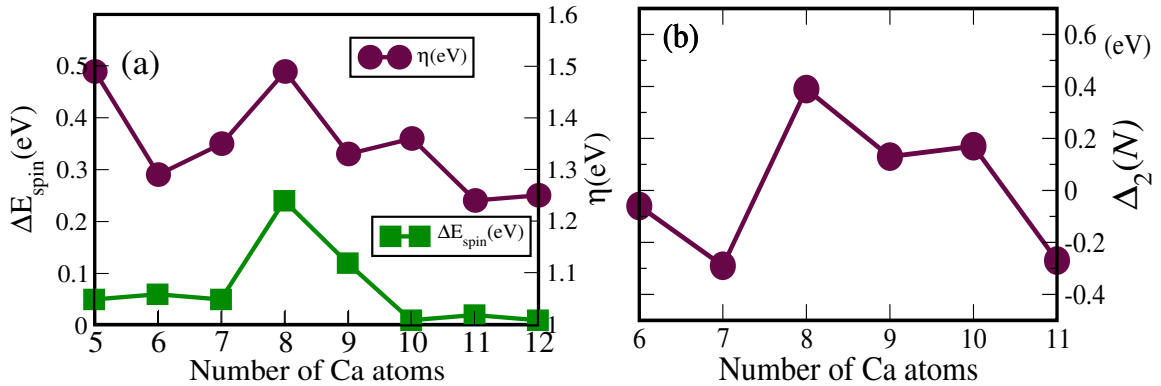


Figure 3.7: Energetic and magnetic trends of FeCa_{*N*} (*N*=5-12) clusters. (a) Variation of η and ΔE_{spin} vs the number of Ca atoms, (b) variation of the second order energy difference ($\Delta_2(N)$) for FeCa_{*N*} series.

In order to probe their chemical and magnetic stability, we have monitored the variations of η calculated via ΔSCF approach and ΔE_{spin} as a function of the number of Ca atoms in the FeCa_{*N*} series. Figure 3.7(a) shows distinct maxima in the hardness and ΔE_{spin} for FeCa₈. Furthermore, we have calculated the second order energy difference ($\Delta_2(N)$) for this series. Figure 3.7(b) also shows a maximum in $\Delta_2(N)$ for FeCa₈ indicating its thermodynamic stability. Values of the HL gap, η , ΔE_{spin} , and $\Delta_2(N)$ of the FeCa_{*N*} clusters are given in the Table 3.3.

3.4.3 Magnetic properties

A bare Fe atom has a moment of 4 μ_B due to its $3d^6 4s^2$ configuration. It will be interesting to understand the evolution of spin magnetic moment as Ca atoms are successively added. Figure 3.8 shows the variation of the spin magnetic moment. Initially, addition of Ca atoms partially quenches the magnetic moment of the Fe

Cluster	HL Gap	η	ΔE_{spin}	$\Delta_2(N)$
${}^3\text{FeCa}_5$	0.39	1.49	0.05	
${}^3\text{FeCa}_6$	0.14	1.29	0.06	-0.06
${}^3\text{FeCa}_7$	0.22	1.35	0.05	-0.29
${}^5\text{FeCa}_8$	0.63	1.49	0.24	0.39
${}^5\text{FeCa}_9$	0.39	1.33	0.12	0.13
${}^3\text{FeCa}_{10}$	0.41	1.36	0.01	0.17
${}^5\text{FeCa}_{11}$	0.30	1.24	0.02	-0.27
${}^5\text{FeCa}_{12}$	0.36	1.25	0.01	

Table 3.3: HL gap, adiabatic spin excitation (ΔE_{spin}), hardness (η) and $\Delta_2(N)$ of FeCa_N clusters. All the values are given in eV.

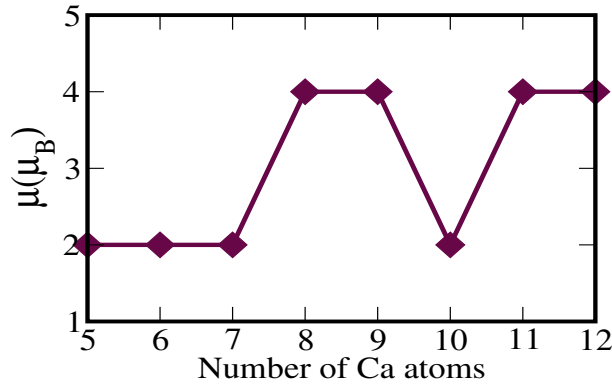


Figure 3.8: Evolution of magnetic moment as a function of the number of Ca atoms in the FeCa_N clusters.

atom. FeCa_N clusters having 5 to 7 Ca atoms show a spin magnetic moment of $2\mu_B$. After that, addition of successive Ca atoms leads to high spin magnetic moment of $4\mu_B$ for FeCa_8 and FeCa_9 . FeCa_{10} cluster again has a magnetic moment of $2\mu_B$ only. To obtain more insight, we have examined the nature of the electronic orbitals in the size range $N=6-10$. Figure 3.9 shows the MO plots of FeCa_6 and FeCa_7 . FeCa_6 is a triplet with a $1S^21P^61D^{10}2S^12D_\alpha^1$ configuration. Surprisingly, though FeCa_6 is a 20 electron cluster, it does not show a closed electronic shell. This is due to the exchange splitting of 0.51 eV in the 2S orbitals because of the presence of Fe 3d states. Thus one of the $2D_\alpha$ orbitals becomes the HOMO, and we have an open shell configuration for FeCa_6 . It should be noticed from Figure 3.9(a) that the two lowest unoccupied MO's in the α and β channels are very close in energy (0.09 eV separation). Two valence electrons provided by the additional Ca atom in FeCa_7 go to these levels as shown in Figure 3.9(b), and give it a $1S^21P^21D^{10}2S^22D_\alpha^2$ configuration. Total spin magnetic moment of $2\mu_B$ of FeCa_7 originates from the two

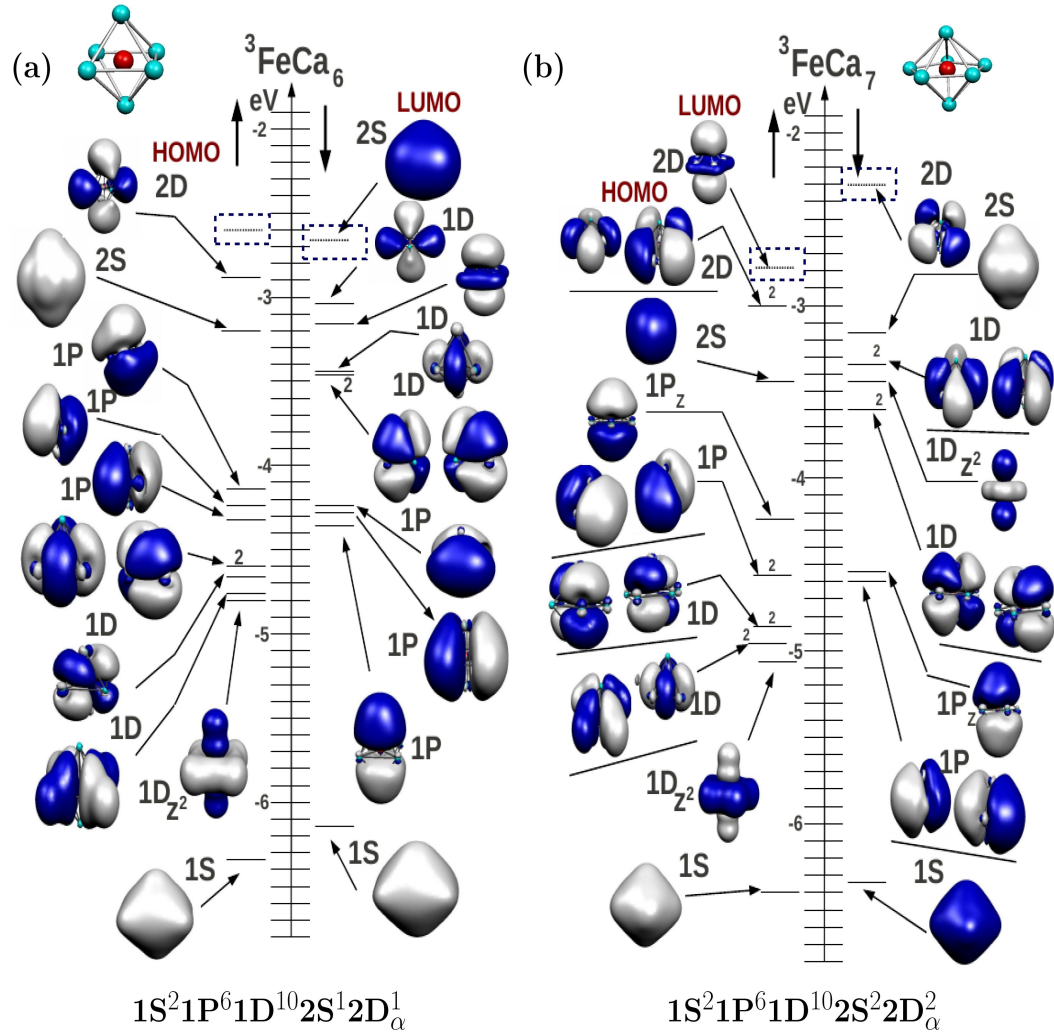


Figure 3.9: Molecular orbital energy levels and orbital wave-function isosurfaces of (a) FeCa₆ and (b) FeCa₇.

unpaired electrons in the $2D_\alpha$ orbitals. Addition of each successive Ca atom gives two electrons. In FeCa₈ cluster, these electrons occupy the $2D_\alpha$ orbitals. Thus we obtain a magnetic moment of $4 \mu_B$ in this case. Spin magnetic moment remains the same for FeCa₉ as two additional electrons occupy the $2D$ orbitals, one each in the α and β channels. This distribution of 26 valence electrons leads to a $1S^2 1P^2 1D^{10} 2S^2 2D_\alpha^5 2D_\beta^1$ configuration as shown in the Figure 3.10(a). Reduced magnetic moment of $2 \mu_B$ for FeCa₁₀ is caused by the occupation of $2P_z$ orbital in the β channel. Figure 3.10(b) shows a $1S^2 1P^2 1D^{10} 2S^1 2D_\alpha^5 2D_\beta^2 2P_\beta^1$ configuration of FeCa₁₀. Underlying origin of stabilization of the $2P_z$ orbital is again crystal field effect. In FeCa₈ we have seen

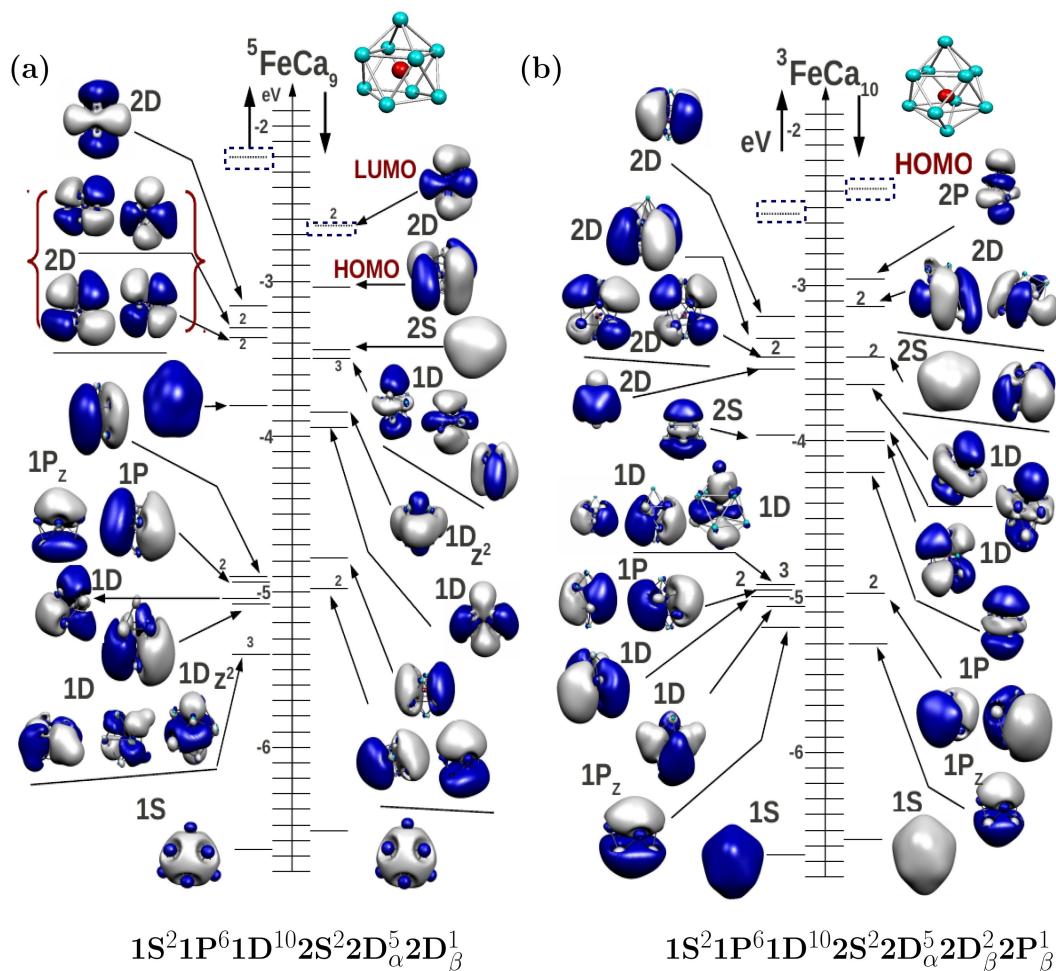


Figure 3.10: Molecular orbital energy levels and orbital wave-function isosurfaces of (a) FeCa₉ and (b) FeCa₁₀.

that the crystal field produced by an oblate shape pushes the $1P_z$ orbitals to a higher energies with respect to the $1P_x$ and $1P_y$ orbitals. The ground state structure of FeCa₁₀ cluster is obtained by the addition two Ca atoms on the square faces of FeCa₈. The distance between the two capping Ca atoms is 8.38 Å. Thus the Ca₁₀ cage can be viewed to have a prolate shape. Hence it is expected that $1P_z$ orbitals will be more stabilized than the $1P_x$ and $1P_y$ orbitals. We can see from the Figure 3.10 that $1P_x$ and $1P_y$ orbitals in both α and β channels are higher in energy than the $1P_z$ orbitals. Same effect is also seen in the 2P orbitals leading to stabilization of the $2P_z$ orbital in the β channel. Further addition of successive Ca atoms leads to less symmetric structures for FeCa₁₁ and FeCa₁₂ clusters. This leads to a poor resemblance of some of their MOs to the shell orbitals. For example, the

HOMO-7 and LUMO-3 MO's of FeCa_{11} do not resemble shell orbitals of any definite angular momentum character as shown in the Appendix A.3. Similarly, the angular character of the fourth MO just above the 1S orbital in the α channel is not clear. Such orbitals are marked with '?'. Therefore we do not attempt to explain their electronic structure and magnetic moment in terms of shell models.

Cluster	Fe	Ca ₁	Ca ₂	Ca ₃	Ca ₄	Ca ₅	Ca ₆	Ca ₇	Ca ₈	Ca ₉	Ca ₁₀	Ca ₁₁	Ca ₁₂
³ FeCa ₅	2.98	-0.16	-0.02	-0.31	-0.30	-0.18							
³ FeCa ₆	2.30	0.20	-0.49	0.20	-0.49	0.14	0.14						
³ FeCa ₇	2.31	-0.54	-0.54	0.15	0.15	0.15	0.15	0.15					
⁵ FeCa ₈	2.51	0.18	0.18	0.18	0.18	0.18	0.18	0.18	0.18				
⁵ FeCa ₉	2.67	0.18	0.18	0.16	0.02	0.11	0.15	0.13	0.17	0.17			
³ FeCa ₁₀	2.71	0.05	-0.006	-0.39	0.04	-0.002	-0.01	-0.08	0.02	-0.33	-0.004		
⁵ FeCa ₁₁	2.76	0.11	-0.04	0.24	0.06	0.34	0.18	0.12	0.11	-0.04	0.06	0.07	
⁵ FeCa ₁₂	2.75	0.19	0.14	0.14	0.03	0.03	0.13	0.02	0.32	0.19	0.07	-0.02	-0.02

Table 3.4: Atomic spins in FeCa_N clusters using Mulliken population analysis.

Table 3.4 shows the spin moments on the atoms in the FeCa_N clusters obtained via Mulliken population analysis. In each cluster, magnetic moment of Fe is always lower than the magnetic moment of a bare Fe atom. However, the presence of a Fe atom polarizes the host atoms significantly. In FeCa_8 and FeCa_9 , total effective moments on the host atoms are found to be $1.49 \mu_B$ and $1.33 \mu_B$ respectively, and are oriented in parallel to the Fe moment. Hence, one gets a total moment of $4 \mu_B$ in these clusters. Similar behaviour of local moments are found in the FeCa_{11} and FeCa_{12} clusters. In FeCa_5 , the spin magnetic moment of Fe is $2.98 \mu_B$, while local moments on all the Ca atoms are oriented opposite to the Fe moment. Hence, a magnetic moment of $2 \mu_B$ is obtained for FeCa_5 . In FeCa_6 and FeCa_7 , mutual anti-parallel alignments of moments of Ca atoms provide the moment of $0.3 \mu_B$ which is oriented opposite to the Fe moment, giving a total moment of $2 \mu_B$.

3.5 FeCa_8 as a magnetic superatom

We have established the stability of FeCa_8 cluster among the TMCa_8 and FeCa_N clusters. Also it has a large spin magnetic moment of $4 \mu_B$. A natural question to ask is whether it behaves as a magnetic superatom. According to the definition of superatoms, a stable and magnetic cluster will be magnetic superatom if it retains its structural identity and associated magnetic properties in assemblies. To test this, we brought two units of FeCa_8 close to each other from different directions and in different orientations. Figure 3.11 shows the ground state of a $(\text{FeCa}_8)_2$ dimer indicated by 'G.S' along with its higher energy spin isomers. In our deMon2k

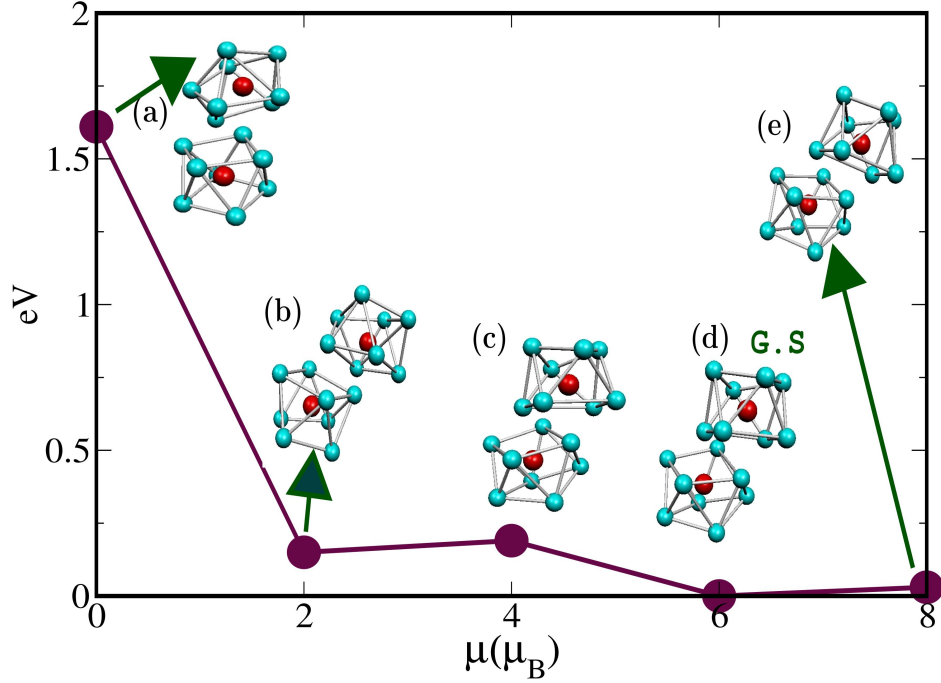


Figure 3.11: Relative energy (eV) of $(\text{FeCa}_8)_2$ as a function of magnetic moment.

calculations, two units of FeCa_8 retain their identity in the ground state of $(\text{FeCa}_8)_2$ and have a total spin magnetic moment of $6 \mu_B$. Mulliken population analysis shows that spin magnetic moment on the two Fe atoms in the dimer are $2.65 \mu_B$ and $2.70 \mu_B$. Therefore Fe spins in the ground state of the dimer are aligned parallel to each other and provide $5.35 \mu_B$ to the total moment. Remaining $0.65 \mu_B$ comes from the Ca atoms which are polarized by the presence of the Fe atoms. Also, binding energy of the dimer in its ground state relative to two isolated FeCa_8 clusters is found to be 2.44 eV . Next higher energy spin isomer (e) with magnetic moment of $8 \mu_B$ is only 0.02 eV less stable with respect to the ground state. Again a ferromagnetic coupling between moments of Fe atoms ($5.48 \mu_B$) and polarized Ca ($2.52 \mu_B$) gives the total spin magnetic moment of $8 \mu_B$. Next isomer (c) with magnetic moment of $4 \mu_B$ is 0.18 eV higher in energy with respect to ground state of $(\text{FeCa}_8)_2$ dimer. A spin moment of $5.36 \mu_B$ is provided by parallel alignment of the Fe spins. A moment of $1.35 \mu_B$ on the Ca atoms is oriented opposite to the Fe moment which leads to a total moment of $4 \mu_B$. The triplet spin state of $(\text{FeCa}_8)_2$, i.e isomer (b) is 0.15 eV higher in energy with respect to the ground state. Interestingly, it presents a different situation in which moments on the Fe atoms are found to be of equal magnitude but anti-parallel to each other. Therefore total spin magnetic moment of

$2\mu_B$ of $(\text{FeCa}_8)_2$ is given by the moments on the Ca atoms.

These results are only indications that FeCa_8 clusters may form assemblies in which each cluster unit retains its identity. The structure and magnetic state of a large number of them are still open an question. It is difficult to address these in a purely first-principles approach.

3.6 Role of Hund’s coupling and Crystal field effect

Though Ca atom belongs to the group of alkaline earth elements, change of the host atoms from Mg to Ca introduces interesting effects in the TM-Ca clusters. Figure 3.12 shows the variation of the spin magnetic moments in FeMg_N and FeCa_N clusters in their respective ground states. Specifically, in the size range $N=5-7$, the magnetic moments of FeCa_N clusters are found to be lower than those of FeMg_N clusters. FeCa_{11} has a magnetic moment of $4 \mu_B$, higher than that of FeMg_{11} . We have already shown that an interplay between crystal field effect and Hund’s coupling determines the ground state spin configurations of the FeCa_N clusters. In this section, we will discuss and compare the ground state spin configurations of TMCa_8 clusters with respect to those of TMMg_8 clusters. Results for the TMMg_8 clusters are taken from Ref [105].

Since the atomic radius of a Ca atom is substantially larger than that of a Mg atom, the size of a Ca_8 cage enclosing the TM will be larger than that of a Mg_8 cage. Also we know that exchange splitting originates from the hybridization between the shell orbitals and TM $3d$ orbitals. Consequently, there will be different relative strengths of crystal field effect and exchange splittings in the TMCa_8 and TMMg_8 clusters. Table 3.5 summaries the electronic configurations of $\text{TM}(\text{AE})_8$ ($\text{AE}=\text{Mg,Ca}$) clusters. TM-AE is the distance between the TM atom and the AE cage atom. r_h represents the average distance between the AE atoms within a horizontal plane of the antiprism, while distance between the two planes is given by r_v . From Table 3.5, it is evident that all the $\text{TM}(\text{AE})_8$ clusters have oblate shapes ($r_h > r_v$). Because of this particular geometric arrangement of the AE atoms, $1P_z$ orbital is higher in energy relative to $1P_x$ and $1P_y$. Similarly $1D_{z^2}$ orbital is pushed to higher energy with respect to the remaining four $1D$ orbitals as shown in Figure 3.3. Since $1S^21P^6$ is common in the electronic configuration of all the clusters, for brevity we will omit this from now on. ScMg_8 cluster has a doublet ground state with a $1D^{10}2S^1$

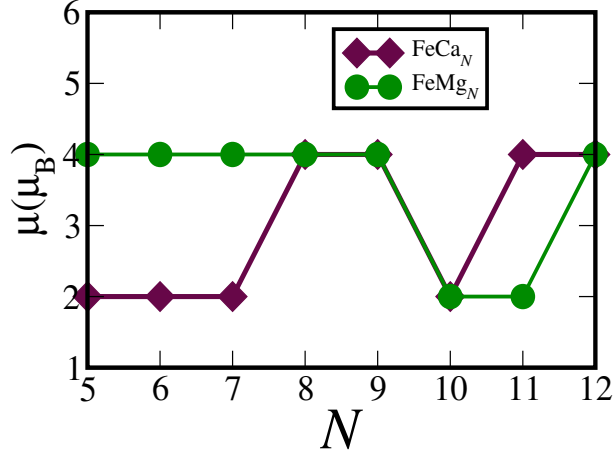


Figure 3.12: Evolution of the magnetic moments in the FeCa_N and FeMg_N clusters [105].

Cluster	TM-AE(Å)	r_h (Å)	r_v (Å)	Electronic configuration
$^2\text{ScMg}_8$	2.79	3.31	3.08	$1S^21P^61D^{10}2S^1$
$^2\text{ScCa}_8$	3.40	4.14	3.54	$1S^21P^61D^92S^2$
$^1\text{TiMg}_8$	2.70	3.22	2.92	$1S^21P^61D^{10}2S^2$
$^1\text{TiCa}_8$	3.28	3.94	3.52	$1S^21P^61D^{10}2S^2$
$^2\text{VMg}_8$	2.66	3.23	2.75	$1S^21P^61D^{10}2S^22D_\alpha^1$
$^4\text{VCa}_8$	3.32	4.12	3.42	$1S^21P^61D^92S^22D_\alpha^2$
$^5\text{CrMg}_8$	2.64	3.13	3.01	$1S^21P^61D^{10}2S^12D_\alpha^3$
$^5\text{CrCa}_8$	3.33	4.05	3.46	$1S^21P^61D^92S^22D_\alpha^3$
$^6\text{MnMg}_8$	2.65	3.20	2.82	$1S^21P^61D^{10}2S^12D_\alpha^4$
$^6\text{MnCa}_8$	3.31	4.07	3.30	$1S^21P^61D^92S^22D_\alpha^4$
$^5\text{FeMg}_8$	2.61	3.17	2.71	$1S^21P^61D^{10}2S^22D_\alpha^4$
$^5\text{FeCa}_8$	3.24	3.92	3.39	$1S^21P^61D^{10}2S^22D_\alpha^4$
$^4\text{CoMg}_8$	2.61	3.22	2.58	$1S^21P^21D^{10}2S^22D_\alpha^42D_\beta^1$
$^4\text{CoCa}_8$	3.24	3.97	3.34	$1S^21P^21D^{10}2S^22D_\alpha^42D_\beta^1$

Table 3.5: TM-AE, r_h and r_v bond lengths and ground state electronic configurations of TMAE_8 clusters. All the bond lengths are given in Å.

electronic configuration. The ground state of ScCa_8 also turns out to be doublet but with a $1D^92S^2$ configuration. To understand this difference, let us have a close look at the interatomic distances in ScMg_8 and ScCa_8 . The Sc-Mg and Sc-Ca distances are 2.79 Å, 3.40 Å respectively. The r_h in Mg_8 and Ca_8 cages are 3.31 Å and 4.14 Å respectively, while r_v are 3.08 Å and 3.54 Å. Thus the size of the cage enclosing the Sc atom increases substantially when the host atoms change from Mg to Ca. A larger size of the Ca_8 cage makes the 2S orbitals to delocalize over a larger volume reducing their energies compared to $1D_{z^2}$ and gives ScCa_8 a $1D^92S^2$ configuration.

Ti(AE)₈ clusters being 20 electron systems prefer to have a closed electronic shell configuration $1S^21P^61D^{10}2S^2$. Small exchange splitting of 2.30 eV in the 3d orbitals of Ti as compared to Fe is not strong enough to induce an exchange splitting in the 1D orbital of the TiCa₈ cluster which gives a non-zero magnetic moment.

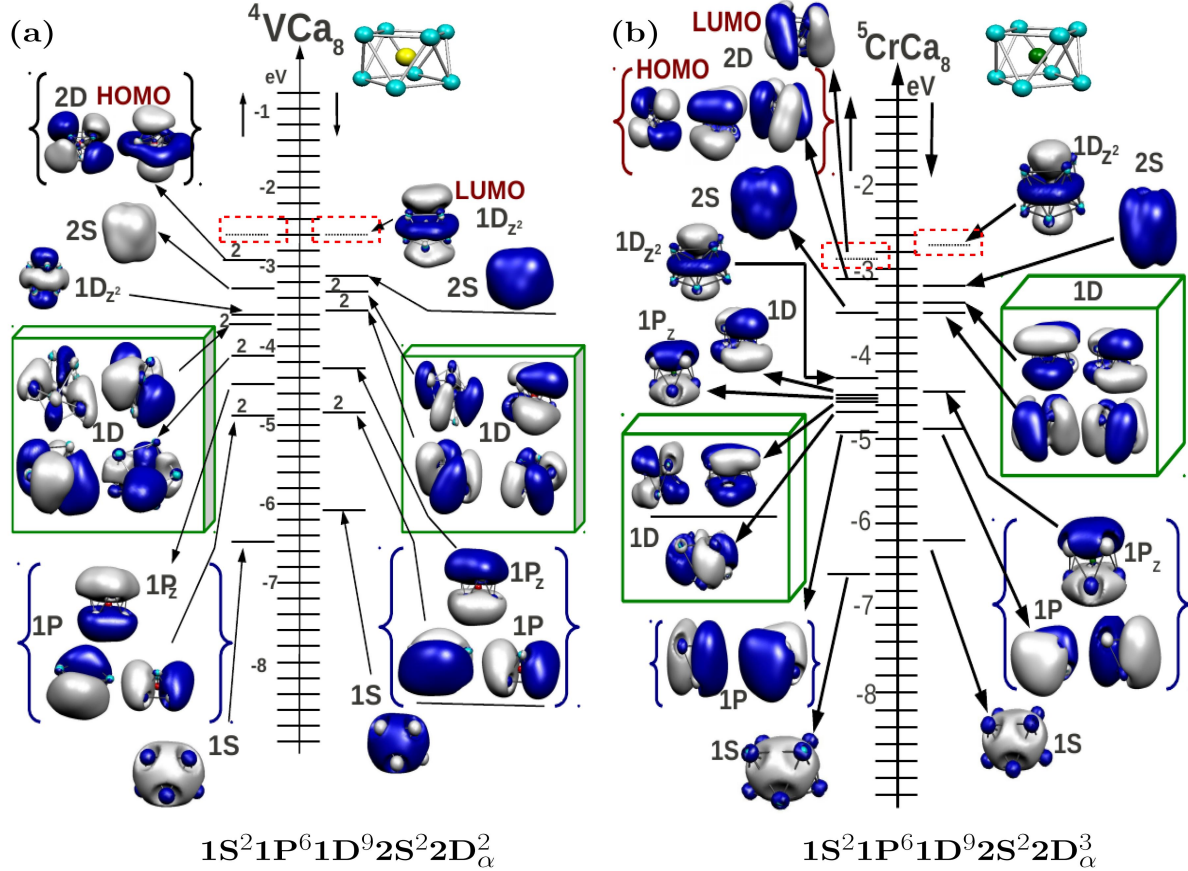


Figure 3.13: Molecular orbital energy levels and orbital wave-function isosurfaces of (a) VCa₈ and (b) CrCa₈.

When the TM changes from Ti to V, Cr and Mn, the situation again turns out to be similar to the case of ScMg₈ and ScCa₈ clusters. Electronic configurations in the ground state of VMg₈, CrMg₈ and MnMg₈ clusters were found to be $1D^{10}2S^22D_\alpha^1$, $1D^{10}2S^12D_\alpha^3$, and $1D^{10}2S^12D_\alpha^4$ respectively [105]. From Table 3.5, we again observe stabilization of the 2S orbital with respect to one of the 1D orbitals for V-Mn doped Ca₈ clusters. So the VCa₈, CrCa₈, and MnCa₈ clusters have $1D^92S^22D_\alpha^2$, $1D^92S^22D_\alpha^3$, and $1D^92S^22D_\alpha^4$ configurations respectively. These can also be understood from the fact that Ca₈ cages in these clusters are larger than Mg₈ cages. MO energy level

diagrams of V-Mn doped Ca_8 clusters are given in the Figures 3.13 and 3.14. Both FeMg_8 and FeCa_8 have a $1\text{D}^{10}2\text{S}^22\text{D}_\alpha^4$ configuration. For the first time, the 2S orbital and the 1D_{z^2} orbital are completely occupied. Therefore change of host atoms from Mg to Ca, does not lead to any difference in the electronic configuration. From Figure 3.5(a), we have seen that the HOMO is a four-fold degenerate state of 2D symmetry in the α channel and Hund's coupling leads to occupation of these degenerate

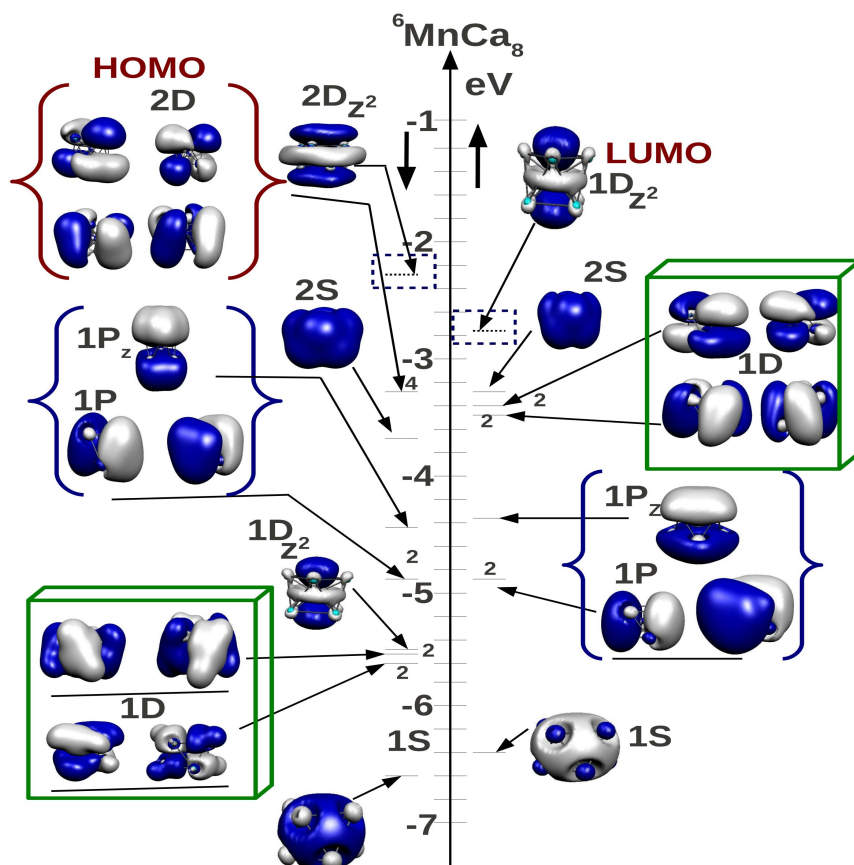


Figure 3.14: Molecular orbital energy levels and orbital wave-function isosurfaces of MnCa_8 .

states by 4 electrons. In fact, it is the Hund's coupling in the 2D orbitals of VCa_8 , CrCa_8 , and MnCa_8 that causes partially filled 2D_α^2 , 2D_α^3 , and 2D_α^4 states respectively. Co doped Ca_8 cluster is found to be a quartet with $1\text{D}^{10}2\text{S}^22\text{D}_\alpha^42\text{D}_\beta^1$ configuration as shown in the Figure 3.15(a). This is also the configuration for CoMg_8 . Again, an interplay of Hund's coupling and crystal field effect can be observed. The 2D_{z^2} levels are split off to higher energies due to crystal field effect. Once four 2D levels are filled

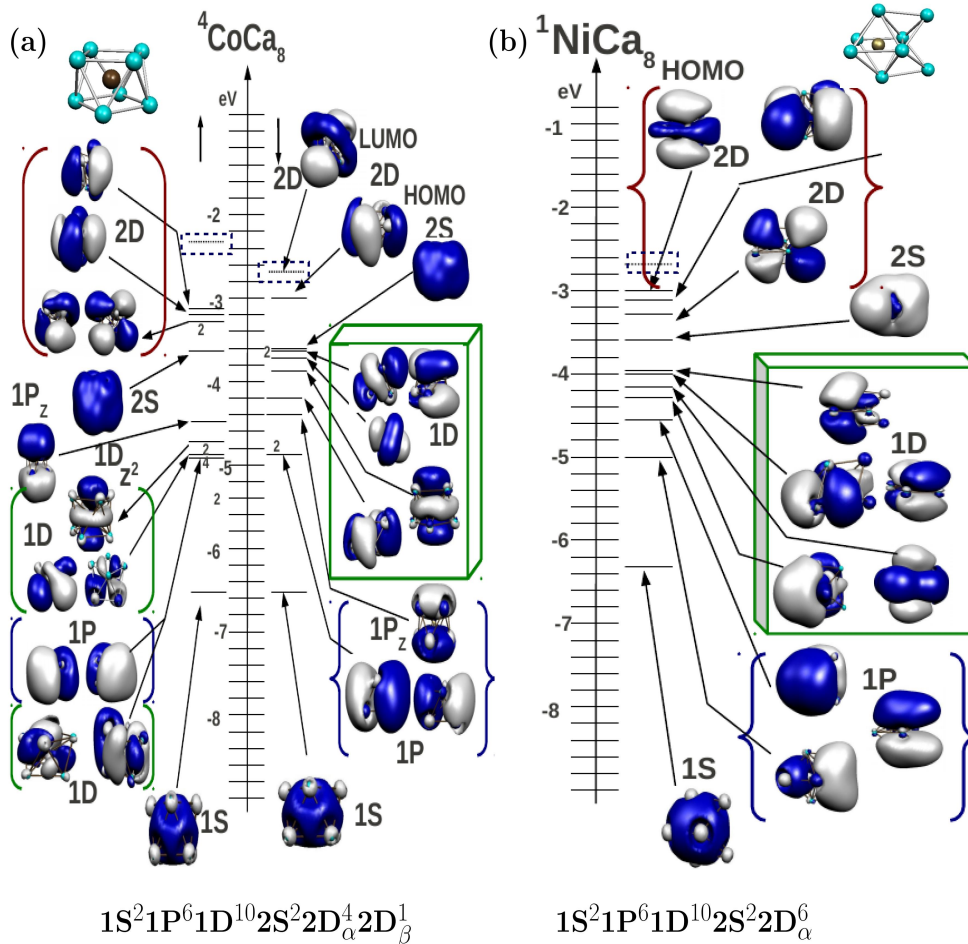


Figure 3.15: (a) Molecular orbital energy levels and orbital wave-function isosurfaces of CoCa_8 and (b) NiCa_8 .

in the α channel in $\text{Fe}(\text{AE})_8$, the next electron occupies a $2D$ level in the β channel in $\text{Co}(\text{AE})_8$. Finally we look at the NiMg_8 and NiCa_8 clusters. Both these clusters are singlets in their ground state structure and have $1S^2 1P^2 1D^{10} 2S^2 2D^6$ configurations. Ground state structure of NiCa_8 is found to be a bi-capped octahedron, while NiMg_8 has an antiprism structure. Figure 3.15(b) shows the MO plot of NiCa_8 . Similar to TiCa_8 , small exchange splitting of 1.12 eV in Ni $3d$ atomic orbitals is not sufficient to induce the exchange splitting in the $1D$ and $2D$ orbitals of the NiCa_8 cluster. Hence NiCa_8 does not have any magnetic moment.

3.7 Conclusions

We have investigated the structural, electronic and magnetic properties of TMCa_8 clusters and FeCa_N ($N=5-12$) clusters. We have identified TiCa_8 and FeCa_8 with enhanced stability. As shown by the analysis of the one electron levels and the associated electronic orbitals, TiCa_8 with 20 valence electrons has a closed shell $1\text{S}^21\text{P}^61\text{D}^{10}2\text{S}^2$ electronic configuration. Replacing Ti by Fe adds four valence electrons and ordinarily should not be a stable species. However, the Fe atom enhances exchange splitting in the 2D_α orbitals leading to a stable FeCa_8 cluster where the filling of 2D_α orbitals results in a spin magnetic moment of $4 \mu_B$. In addition, crystal field effect breaks the degeneracy of the 2D_α orbitals leading to a HL gap of 0.63 eV. Calculations of the $(\text{FeCa}_8)_2$ dimer, starting from two motifs, indicate that the individual clusters do retain their identity and have a ferromagnetic (FM) configuration with a spin magnetic moment of $6 \mu_B$ as the lowest energy state.

TM doped strontium clusters

4.1 Introduction

In this chapter, we will extend our search for possible candidates for magnetic superatoms by studying structural, electronic and magnetic properties of the TM-Sr clusters. Interestingly, we do not find FeSr₈ cluster as a magnetic superatom. The underlying reasons will be discussed in this chapter. We will also compare the magnetic properties of the TMSr₈ clusters with those of TMCa₈ clusters.

4.2 Computational details

All our first-principles electronic structure calculations are performed within the same formalism as described in the previous chapter. For the Sr atom, a quasi-relativistic effective core potential (ECP) (with 28 electrons in the core) and basis set combination from Stuttgart-Dresden (QECP10|SD) distributed with deMon2K is used. This produces the first and second ionization potentials of 5.71 eV and 11.10 eV for a Sr atom, which are in excellent agreement with the experimental values of 5.70 eV and 11.03 eV respectively [170].

4.3 Ground State Structures of TMSr₈

We start our investigations with a single 3d TM doped Sr₈ clusters. One of the reasons behind this choice is our earlier finding that FeCa₈ is a stable cluster that behaves as a magnetic superatom. Figure 4.1 shows the ground state structures, spin multiplicities (2S+1), and bond lengths for all the TMSr₈ clusters. The optimized

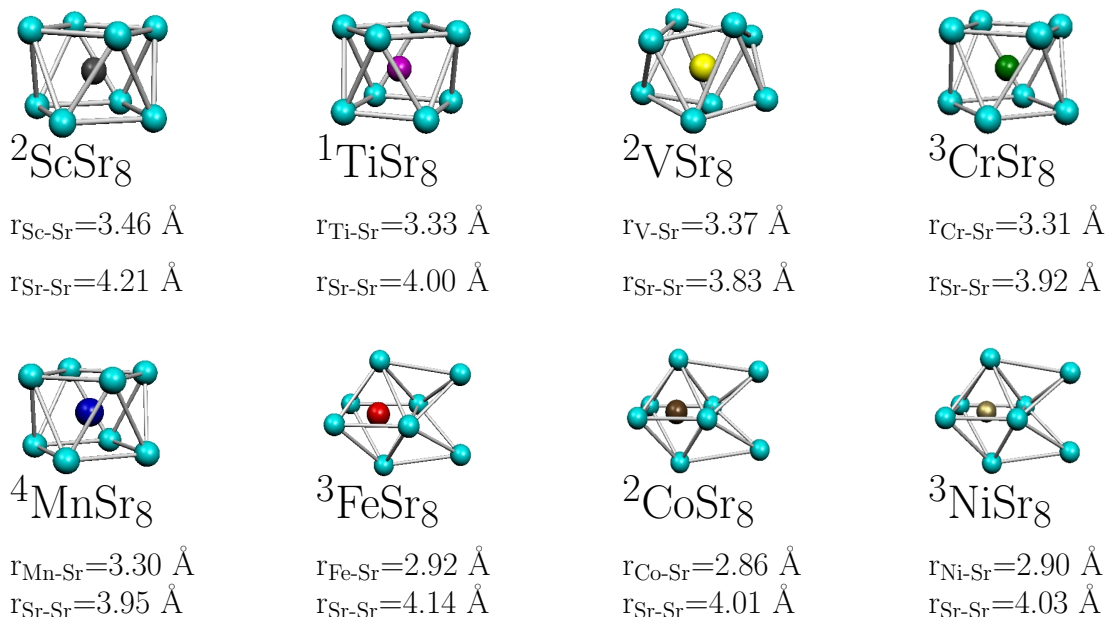


Figure 4.1: Ground state structures and spin multiplicities of TMSr_8 clusters. $r_{\text{TM-Sr}}$ and $r_{\text{Sr-Sr}}$ are the average TM-Sr and Sr-Sr bond lengths.

structures of the TMSr_8 clusters form two families : first, square anti-prism structures for the TMSr_8 (Sc-Mn) clusters ; second, bi-capped octahedron structures of FeSr_8 , CoSr_8 and NiSr_8 as obtained for NiCa_8 . Although the Sr_8 cage is found to be distorted in the case of VSr_8 , its structure still can be viewed as a distorted antiprism. In the first family, the average Sr-Sr bond lengths range from 3.92 to 4.21 \AA , while the average TM-Sr bond lengths range from 3.83 to 4.21 \AA . The Fe, Co, and Ni doped Sr_8 clusters prefer to have bi-capped octahedron structures presumably because of the smaller atomic radii of the late TM atoms compared to the early TM atoms. For example, Fe has an atomic radius of 1.26 \AA , while the atomic radius of Ti is 1.47 \AA . In the second family, the average Sr-Sr bond lengths range from 4.01 to 4.14 \AA , while the average TM-Sr bond lengths range from 2.86 to 2.90 \AA . A few higher energy isomers of the TMSr_8 clusters are given in Appendix B.1.

4.3.1 Relative stabilities

In order to identify clusters with enhanced stability, η and ΔE_{spin} of all the TMSr_8 clusters are plotted in Figure 4.2. Values of η are obtained by using ΔSCF method.

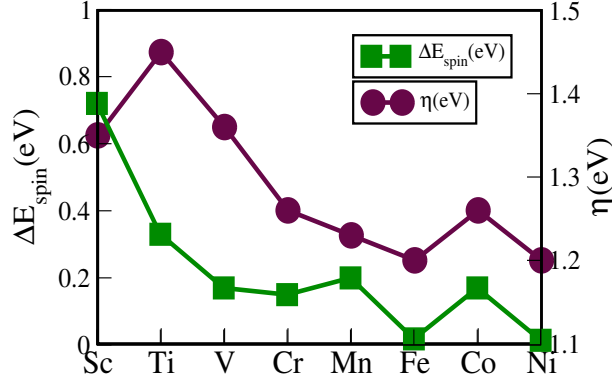


Figure 4.2: The hardness (η) and adiabatic spin excitation energies of all the TMSr₈ clusters.

We have also given the HL gap, η and ΔE_{spin} values of all the TMSr₈ clusters in Table 4.1. Being a 20 electron system, TiSr₈ has the highest HL gap and hardness among all the TMSr₈ clusters. This is not surprising because it has a closed shell configuration $1S^21P^61D^{10}2S^2$ similar to TiCa₈. After showing maximum for TiSr₈,

Cluster	HL(eV)	ΔE_{spin} (eV)	η (eV)
² ScSr ₈	0.40	0.72	1.35
¹ TiSr ₈	0.76	0.33	1.45
² VSr ₈	0.33	0.17	1.36
³ CrSr ₈	0.32	0.15	1.26
⁴ MnSr ₈	0.25	0.20	1.23
³ FeSr ₈	0.10	0.02	1.20
² CoSr ₈	0.28	0.17	1.26
³ NiSr ₈	0.17	0.015	1.20

Table 4.1: The HL gap, ΔE_{spin} and hardness (η) of TMSr₈ clusters.

hardness drops continuously across the 3d series up to FeSr₈. CoSr₈ is found to be a doublet in its ground state and has higher η (1.26 eV) and HL gap (0.28 eV) than those of Fe and Ni doped Sr₈ clusters. In fact, FeSr₈ has the lowest HL gap of 0.10 eV among all the TMSr₈ clusters. After TiSr₈, Sc, V, and Cr doped Sr₈ clusters are found to have next highest HL gaps.

ΔE_{spin} also decreases across the 3d series except for Mn and Co. FeSr₈ has the lowest ΔE_{spin} of 0.02 eV within the TMSr₈ series. Again ScSr₈ has a ΔE_{spin} (0.72 eV) larger than that of TiSr₈ (0.33 eV). This can be explained via ‘frozen orbital’ approximation (discussed later). Though ScSr₈ has the second highest HL gap (0.40 eV) and the largest ΔE_{spin} , it is not considered as a possible candidate of magnetic superatom because of low magnetic moment ($1 \mu_B$). Similar is the case for

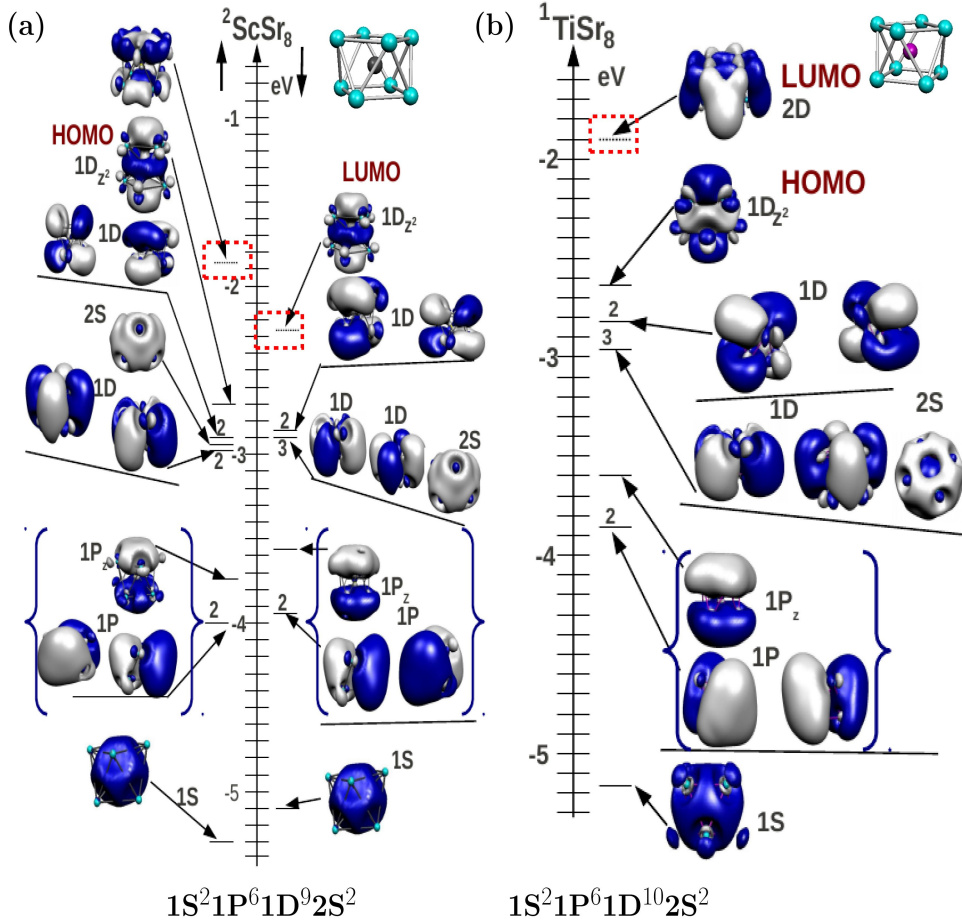


Figure 4.3: Molecular orbital energy levels and orbital wave-function isosurfaces of (a) ScSr₈ (b) TiSr₈.

V, Cr, and Co doped Sr₈ clusters which have low magnetic moments. FeSr₈, MnSr₈ and NiSr₈ are also not identified as potential candidates for magnetic superatoms because of small values of HL gaps and η , though MnSr₈ has a higher value of ΔE_{spin} (0.20 eV) than its neighbors.

Figure 4.3 shows the MO plots of ScSr₈ and TiSr₈. ScSr₈ is a doublet with $1S^2 1P^6 1D^9 2S^2$ configuration. In order to excite it to the next higher energy quartet state, an electron from the highest occupied degenerate 1D orbitals in the β channel to the LUMO in the α spin channel. Amount of energy required for this process is 1 eV within frozen orbital approximation. In order to excite TiSr₈ to a triplet state, one has to excite an electron from the HOMO to the LUMO. The required energy is equal to its HL gap (0.76 eV). Needless to say, these energies will change when we

do self consistent calculations for these spin excited states of the clusters. But the qualitative argument still holds.

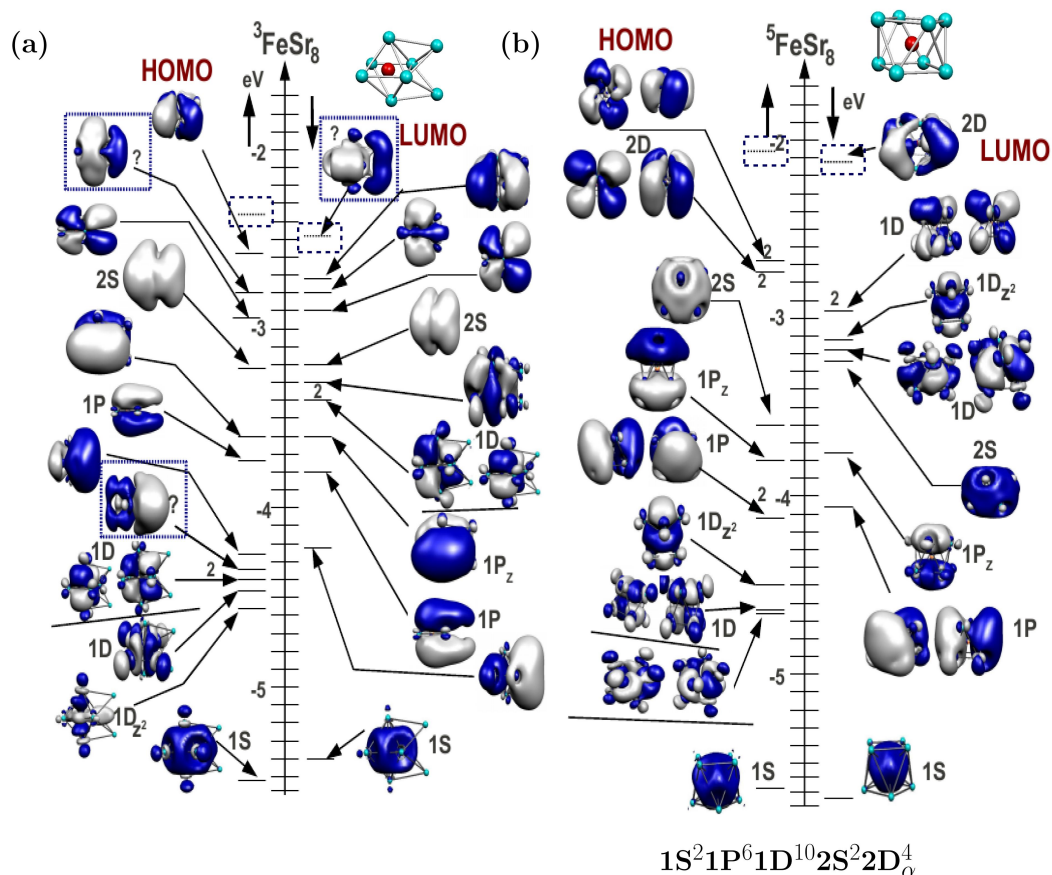


Figure 4.4: MO energy level diagrams and isosurface plots for the (a) ${}^3\text{FeSr}_8$ and (b) ${}^5\text{FeSr}_8$. MO's that cannot be identified to have definite angular momentum character are marked with '?'.

Now let us have a close look at the FeSr_8 cluster. FeSr_8 is a triple with a bi-capped octahedron as the ground state structure. Figure 4.4(a) shows the MO plot of ${}^3\text{FeSr}_8$. Because of less symmetric and non-compact structure of ${}^3\text{FeSr}_8$ compared to an antiprism, interpretation of its MO's in terms of the spherical shell model turns out to be difficult. Some of the frontier MO's of ${}^3\text{FeSr}_8$ do not resemble shell orbitals of any definite angular momentum character. For example, the angular momentum characters of the HOMO-1 in the α channel and the LUMO in the β channel are not clear. Similarly, the angular momentum character of orbital just below the three 1P orbitals in the α channel is not clear. These orbitals are marked with '?'. Our

calculations show that the next spin-excited state is 0.02 eV less stable with respect to the ground state of ${}^3\text{FeSr}_8$. Interestingly, this higher energy spin isomer is a quintet with a square anti-prism structure. Figure 4.4(b) shows the MO plot of the ${}^5\text{FeSr}_8$ cluster. Because it has a compact and symmetric structure, its MO's show a better resemblance to the shell orbitals. In fact, electronic configuration of ${}^5\text{FeSr}_8$ is similar to that of ${}^5\text{FeCa}_8$. Also the HL gap of ${}^5\text{FeSr}_8$ is found to be 0.60 eV due to a crystal field splitting of the 2D shell orbitals, higher than that of ${}^3\text{FeSr}_8$ (0.10 eV).

CoSr_8 and NiSr_8 have the same ground state structures as FeSr_8 . Again lack of compact structures leads to poor resemblance of their MO's to shell orbitals. MO plots of CoSr_8 and NiSr_8 are given in the Appendix B.2.

4.3.2 Local moments on TM dopants

In the previous chapter, we have seen that the TM elements polarize the Ca atoms in the TMCa_8 clusters. Therefore it will be interesting to see the behaviour of local spin moments on the TM dopants in the TMSr_8 clusters. Table 4.2 shows the spin moment on the atoms obtained through Mulliken population analysis.

Most of the total moment is on the TM atoms in the Sc, V, Cr, Mn and Fe doped clusters. The magnetic moments on Sc and V in these clusters are found to be $1.27 \mu_B$ and $3.48 \mu_B$ respectively. These values are higher than their atomic magnetic moments of $1 \mu_B$ and $3 \mu_B$ respectively. In the case of Sc-Mn doped Sr_8 clusters, TM elements polarize the host atoms. Moments on the host atoms have orientation in opposite direction with respect to TM spin. Total magnetic moment on the Sr atoms is $2.48 \mu_B$ in VSr_8 , oriented opposite to the moment of V. In CrSr_8 , the moment on the Cr atom is $3.9 \mu_B$, while each Sr atom has $0.24 \mu_B$. In MnSr_8 , the Mn atom has a moment of $3.46 \mu_B$, while the total moment on the Sr atoms is $0.46 \mu_B$, oriented opposite to the Mn moment. FeSr_8 represents an interesting case in which moment on Fe is $2.0 \mu_B$. Here the presence of Fe also polarizes the Sr atoms, but the moments are effectively cancelled due to their mutual anti-parallel alignment. CoSr_8 and NiSr_8 clusters present a different picture. Most of the moment in these clusters is on the Sr atoms. In CoSr_8 , the moment on the Co atom is only $0.08 \mu_B$, while four of the Sr atoms have $0.17 \mu_B$ each. In NiSr_8 also, the Ni atom has a very small moment of $0.009 \mu_B$, and almost the entire moment is on the Sr atoms. The highest moment on the Sr atoms is $0.32 \mu_B$. Thus all the TM atoms (except Ti) polarize the electron gas spread over the Sr cage in these clusters.

${}^2\text{ScSr}_8$	atomic spins	${}^2\text{VSr}_8$	atomic spins	${}^3\text{CrSr}_8$	atomic spins
Sc	1.2709	V	3.4809	Cr	3.9472
Sr	-0.0323	Sr	-0.3853	Sr	-0.2497
Sr	-0.0376	Sr	-0.3716	Sr	-0.2433
Sr	-0.0360	Sr	-0.2430	Sr	-0.2392
Sr	-0.0338	Sr	-0.2404	Sr	-0.2429
Sr	-0.0345	Sr	-0.3806	Sr	-0.2386
Sr	-0.0285	Sr	-0.2414	Sr	-0.2428
Sr	-0.0360	Sr	-0.3767	Sr	-0.2467
Sr	-0.0322	Sr	-0.2419	Sr	-0.2440
${}^4\text{MnSr}_8$	atomic spins	${}^3\text{FeSr}_8$	atomic spins	${}^2\text{CoSr}_8$	atomic spins
Mn	3.4680	Fe	2.0421	Co	0.00770
Sr	-0.0610	Sr	0.0325	Sr	0.0636
Sr	-0.0594	Sr	0.0276	Sr	0.0659
Sr	-0.0575	Sr	-0.0515	Sr	0.0624
Sr	-0.0588	Sr	-0.0536	Sr	0.0599
Sr	-0.0579	Sr	-0.1413	Sr	0.1634
Sr	-0.0581	Sr	-0.1423	Sr	0.1701
Sr	-0.0577	Sr	0.1436	Sr	0.1652
Sr	-0.0575	Sr	0.1430	Sr	0.1726
${}^3\text{NiSr}_8$	atomic spins				
Ni	-0.0093				
Sr	0.2956				
Sr	0.2937				
Sr	0.3225				
Sr	0.3210				
Sr	0.0896				
Sr	0.0898				
Sr	0.2985				
Sr	0.2986				

Table 4.2: Atomic spins in TMSr_8 clusters obtained by Mulliken population analysis.

4.3.3 Interplay of Crystal field effect and Hund's coupling

Electronic, magnetic and structural properties of several TMSr_8 clusters are found to be different from those of the corresponding TMCa_8 clusters. For example, we find that the ground state structures of FeSr_8 and CoSr_8 are bi-capped octahedra rather than antiprism. Also FeSr_8 does not show any signs of enhanced stability. In addition, magnetic moments of the Cr and Mn doped Sr_8 clusters are found to be $2 \mu_B$ and $3 \mu_B$ respectively which are lower than the magnetic moments ($4 \mu_B$ and $5 \mu_B$) of the CrCa_8 and MnCa_8 clusters. In the study of TMCa_8 clusters, we have seen that the ground state electronic configuration of a cluster is determined by the combined

role of Hund’s coupling and crystal field effect. Therefore, it will be interesting to see how relative strengths of these two effects determine the magnetic state of the TMSr₈ clusters. Table 4.3 shows TM-AE, r_h and r_v distances in the ground state of

Cluster	TM-AE(Å)	r_h (Å)	r_v (Å)	Electronic configuration
² ScCa ₈	3.40	4.13	3.54	1S ² 1P ⁶ 1D ⁹ 2S ²
² ScSr ₈	3.46	4.21	3.64	1S ² 1P ⁶ 1D ⁹ 2S ²
¹ TiCa ₈	3.28	3.94	3.52	1S ² 1P ⁶ 1D ¹⁰ 2S ²
¹ TiSr ₈	3.33	4.00,	3.67	1S ² 1P ⁶ 1D ¹⁰ 2S ²
⁴ VCa ₈	3.22	4.12	3.42	1S ² 1P ⁶ 1D ⁹ 2S ² 2D _α ²
² VSr ₈	3.37	3.83	4.38	1S ² 1P ⁶ 1D ¹⁰ 2S ² 2D _α ¹
⁵ CrCa ₈	3.33	4.05	3.46	1S ² 1P ⁶ 1D ⁹ 2S ² 2D _α ³
³ CrSr ₈	3.33	3.95	3.61	1S ² 1P ⁶ 1D ¹⁰ 2S ² 2D _α ²
⁶ MnCa ₈	3.31	4.07	3.30	1S ² 1P ⁶ 1D ⁹ 2S ² 2D _α ⁴
⁴ MnSr ₈	3.30	3.95	3.53	1S ² 1P ⁶ 1D ¹⁰ 2S ² 2D _α ³

Table 4.3: The average TM-AE (AE=Ca,Sr), r_h bond lengths and the ground state electronic configurations of TM(AE)₈ clusters. Here AE are Ca and Sr. r_h is distance between AE-AE atoms within a plane, while distance between the two planes is given by r_v . All the bond lengths are given in Å.

the TMCa₈ and TMSr₈ clusters along with their electronic configurations. Sc and Ti doped Sr₈ clusters have the same ground state and electronic configurations as observed in the ScCa₈ and TiCa₈ clusters. However, all the interatomic distances in the ScSr₈ and TiSr₈ clusters are larger than those in the ScCa₈ and TiCa₈ clusters. As a result, size of the TM encapsulating Sr₈ cage is larger in comparison to the Ca₈ cage. This leads to a greater stabilization of the 2S orbitals in ScSr₈ and TiSr₈ clusters. This fact is shown in Figure 4.3.

The most interesting are the V, Cr, and Mn doped clusters. VCa₈ is a quartet with a 1D⁹2S²2D_α² configuration. A change of the host atoms from Ca to Sr leads to a doublet spin state for VSr₈ with a 1D¹⁰2S²2D_α¹ configuration. To understand the underlying mechanism, we have examined the MO plots of the VCa₈ and VSr₈ clusters that are given in the Figure 4.5. The HOMO in the α channel of VCa₈ is doubly degenerate and is of 2D symmetry, while the LUMO in the β channel has 1D_{z²} angular character. Changing the host from Ca to Sr leads to a distorted antiprism as the ground state of VSr₈ that lifts the degeneracy of the 2D_α orbitals. One of the 2D_α orbitals goes higher in energy relative to all the 1D orbitals in the β channel. Therefore only one 2D_α orbital is occupied in VSr₈ and it has a 1D¹⁰2S²2D_α¹ configuration.

CrCa₈ is in a quintet spin state with a 1D⁹2S²2D_α³ configuration, while CrSr₈ is

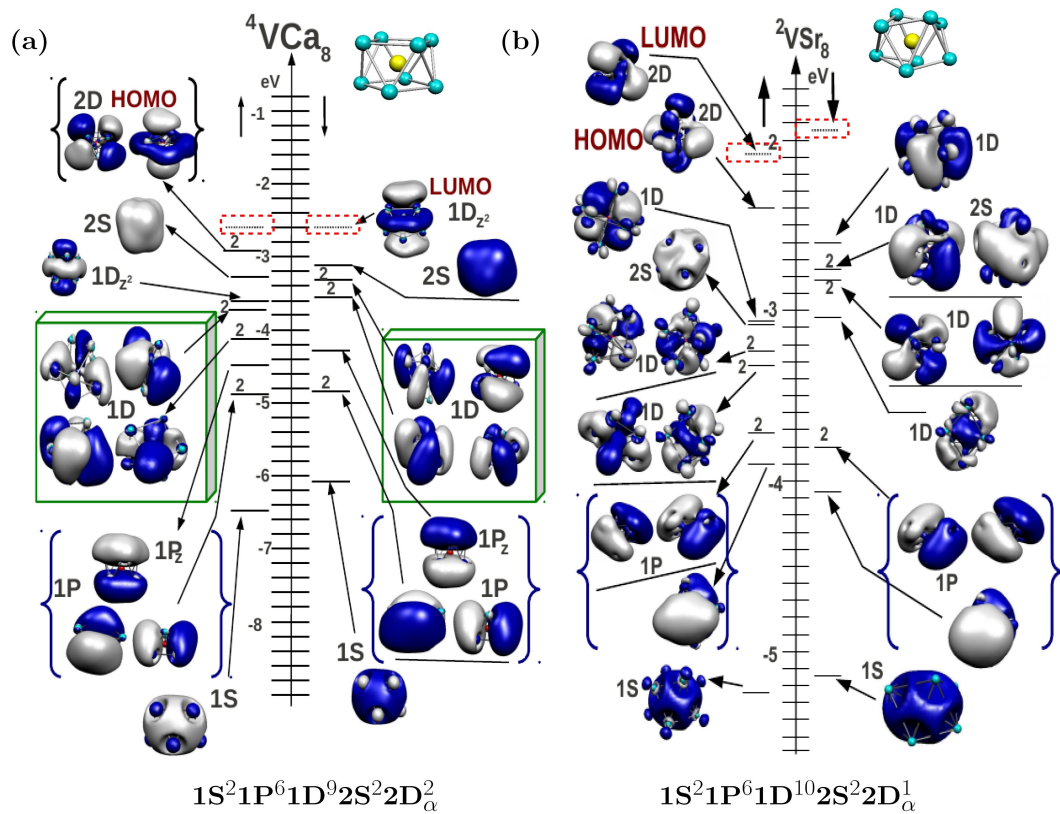


Figure 4.5: MO energy level diagrams and isosurface plots for the (a) VCa_8 and (b) VSr_8 .

found to have a $1\text{D}^{10}2\text{S}^22\text{D}_\alpha^2$ configuration. Both clusters have antiprism structures in their ground states. Hund's coupling is also at play in the 2D states of CrCa_8 and CrSr_8 to give partially filled 2D_α^3 and 2D_α^2 orbitals respectively. However, the reason behind a lower magnetic moment in CrSr_8 is the crystal field effect. The distance between the Sr atoms in the square plane of CrSr_8 turns out to be 3.95 \AA , while the distance between the planes is 3.61 \AA . Thus CrSr_8 still has an oblate shape when host atoms change from Ca to Sr. An oblate shape pushes the 1D_{z^2} and 1P_z orbitals in the two spin channels to higher energies as shown in Figure 4.6(b). However, if we compare r_h and r_v distances of CrCa_8 and CrSr_8 clusters from the Table 4.3, we find a shrink in the lateral extent for the CrSr_8 cluster. From the Figure 4.6(a), we notice that HOMO in the α channel of CrCa_8 is of 2D angular character and has a 3-fold degeneracy. The LUMO is in the β channel and has 1D_{z^2} angular character. The lateral shrink in the Sr_8 cage lifts this 3-fold degeneracy and leads to a 2-fold degenerate 2D_α orbitals at lower energy and a single 2D_α orbital with a higher energy.

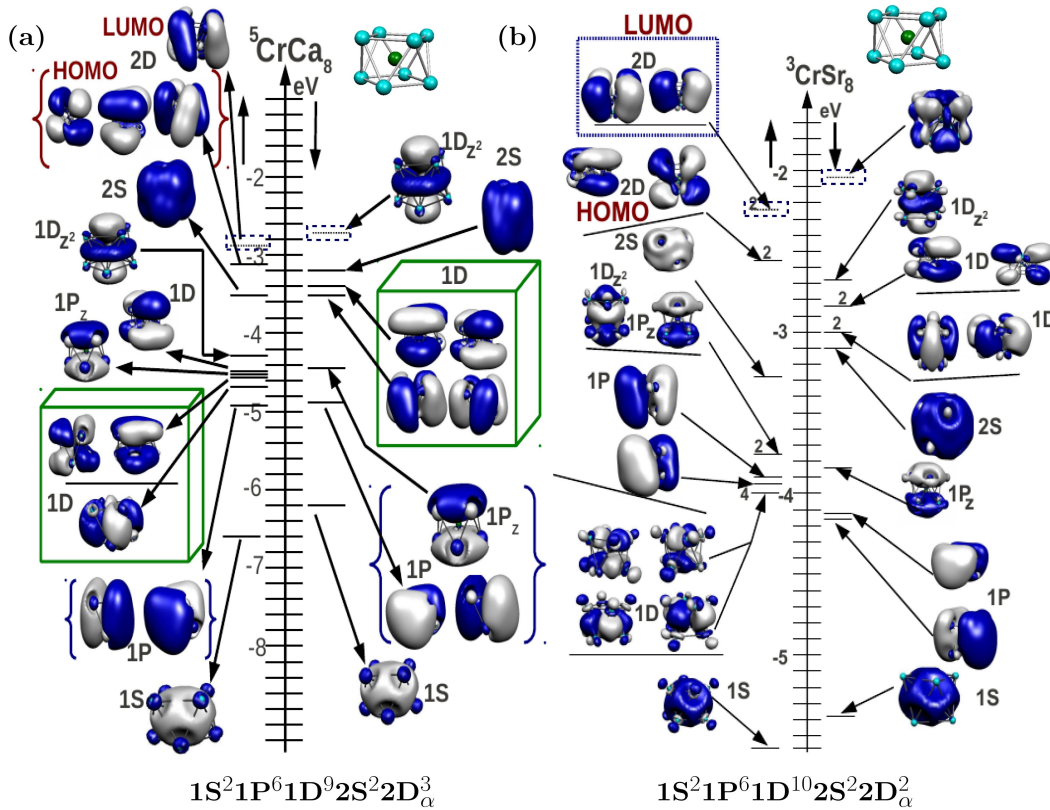


Figure 4.6: MO energy level diagrams and isosurface plots for the (a) CrCa₈ and (b) CrSr₈.

This split-off $2D_\alpha$ orbital is higher in energy with respect to the $1D_{z^2}$ orbital in the β channel, leading to a triplet state with a $1D^{10}2S^2 2D_\alpha^2$ configuration.

Figure 4.7 shows the MO plots of the MnCa₈ and MnSr₈ clusters. MnSr₈ is a quartet with a $1D^{10}2S^2 2D_\alpha^3$ configuration, while $1D^9 2S^2 2D_\alpha^4$ is the configuration for ⁶MnCa₈. Reason behind the lower magnetic moment of MnSr₈ can also be understood by tracing the interatomic distances in the MnSr₈ and MnCa₈. The r_h and r_v distances in these clusters from Table 4.3 again reveal a lateral shrink in MnSr₈ when host atoms change from Ca to Sr. We find that the HOMO of MnCa₈ is 4-fold degenerate. This lateral shrink splits the 4-fold degenerate $2D_\alpha$ in MnSr₈ into three occupied degenerate $2D_\alpha$ orbitals and one unoccupied $2D_\alpha$ orbital. The split-off $2D_\alpha$ orbital being higher in energy than the $1D_{z^2}$ orbital in the β channel, a $1D^{10}2S^2 2D_\alpha^4$ configuration is achieved for MnSr₈.

Since MO plots of Fe, Co and Ni doped Sr₈ clusters show poor resemblance of their MO's to shell orbitals, any explanation of the magnetic states of these clusters

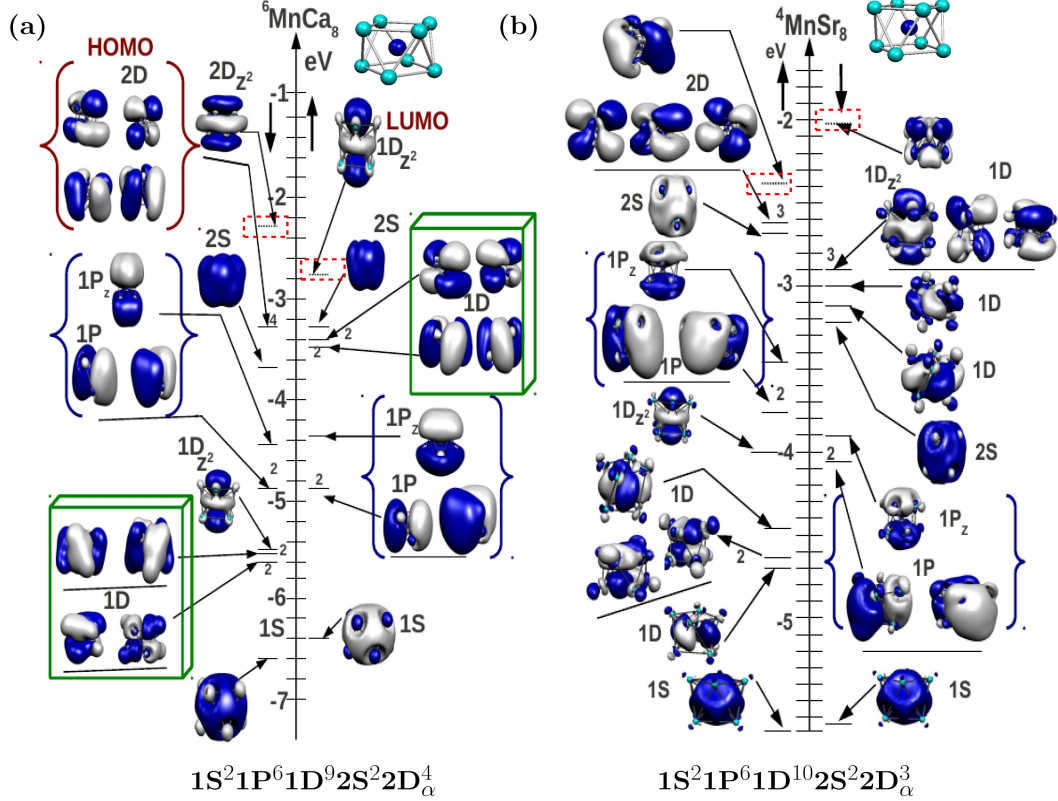


Figure 4.7: MO energy level diagrams and isosurface plots for the (a) MnCa_8 and (b) MnSr_8 .

within the spherical shell models is not attempted.

4.3.4 Conclusions

We have performed a detailed study of TMSr_8 clusters in order to understand their electronic and magnetic properties. By examining the HL gap, η , and ΔE_{spin} of the TMSr_8 clusters, we found TiSr_8 with greater stability. We have not identified any possible candidate for magnetic superatoms either because of low magnetic moments or due to small values of HL gaps, η , and ΔE_{spin} . Due to non-compact and less symmetric ground state structure of Fe, Co, and Ni doped Sr_8 clusters, angular character of the frontier MO's is not identified with any shell orbital of definite angular momentum character. Moreover FeSr_8 , an analog of FeCa_8 and FeMg_8 , is not found to have enhanced stability. Also we have compared the magnetic states of the TMCa_8 and TMSr_8 clusters for $\text{TM}=\text{Sc-Mn}$. The relative strengths of the

crystal field effect and Hund's coupling play a significant role in determining the ground state spin configurations of TMSr_8 clusters. Specifically V, Cr, Mn doped clusters offer a unique opportunity to understand these effects.

Cr and Mn doped strontium clusters

5.1 Introduction

In the study of the TMSr_8 clusters, we have not found any suitable candidate for magnetic superatom. Therefore we ask if there are TM-Sr clusters at other sizes that have enhanced stability and large magnetic moment, and whether they can be candidates for magnetic superatoms. We will particularly focus on Cr and Mn doped Sr clusters. The motivation for studying these clusters comes from Figure 5.1. It

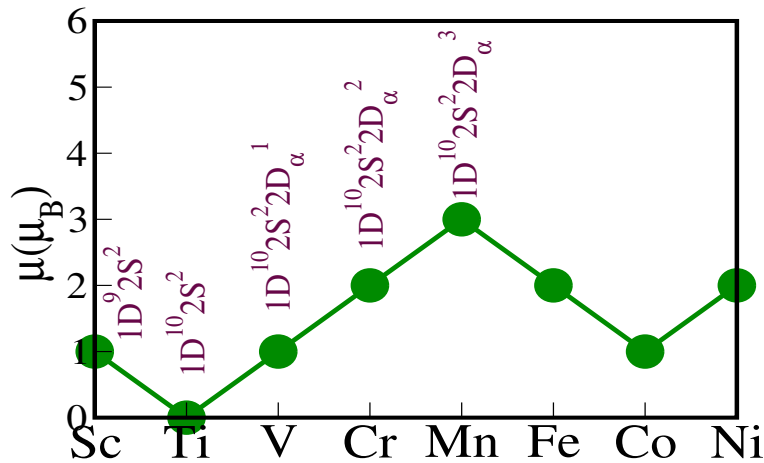


Figure 5.1: Variation of the magnetic moments (μ_B) with the TM atom and the nature of frontier orbitals upto TM=Sc-Mn.

shows the variation of magnetic moments and the nature of the frontier orbitals of the TMSr_8 clusters. Across the TMSr_8 series, total spin magnetic moment increases continuously up to $3 \mu_B$ from Ti to Mn, and then it drops to $1 \mu_B$. Here CrSr_8 and MnSr_8 offer very interesting possibilities. CrSr_8 is a 22-electron system and has

a $1S^21P^61D^{10}2S^22D_\alpha^2$ configuration. Figure 4.6(b) shows that the LUMO of CrSr_8 is a pair of $2D_\alpha$ orbitals. This suggests that if another Sr atom is added, the two valence electrons coming from it are most likely to go to these two $2D_\alpha$ orbitals. This 24-electron cluster may then have a high stability in a way similar to FeCa_8 . On the other hand, MnSr_8 is a quartet with $1S^21P^61D^{10}2S^22D_\alpha^3$ configuration. The occupation of $2D_\alpha$ shell orbitals by two more electrons would lead to a half filled configuration, i.e., $2D_\alpha^5$ for MnSr_9 . An atom with a half-filled d -shell is known to be more stable due to maximum exchange energy. Therefore MnSr_9 with a half-filled $2D$ electronic configuration is expected to acquire greater stability. However, whether these exciting possibilities turn out to be true, can be answered only after doing first-principles calculations. With this motivation we have studied the CrSr_N and MnSr_N ($N=4-12$) clusters.

5.2 Computational details

All our first-principles electronic structure calculations are performed within the same formalism as described in the previous chapter. To check whether stable clusters will behave as magnetic superatoms, VASP code is used [153]. In these calculations, plane wave basis set with an energy cutoff of 350 eV within spin polarized DFT is taken. The PBE-GGA functional is used for the exchange-correlation energy. Brillouin zone integrations are performed using the Γ point only. Ionic potential is represented by Projector Augmented Wave (PAW) potential [154]. The clusters and their dimers are put in periodic boxes of such dimensions that the minimum distance between an atom in the calculation cell and the periodic image of any other atom is 10 Å. All the atoms are completely relaxed till all the force components are less than 0.01 eV/Å.

5.3 Study of CrSr_N ($N=4-12$) clusters

5.3.1 Ground state structures

Figure 5.2 shows the evolution of the ground state structures of the CrSr_N ($N=4-12$) clusters. Ground state spin multiplicities and average bond lengths in all these clusters are also given. The Cr atom is completely encapsulated in the Sr_6 cage. CrSr_6 has an octahedral structure. CrSr_7 is found to have a pentagonal bi-pyramid structure. CrSr_9 and CrSr_{10} clusters are capped and bi-capped square antiprisms.

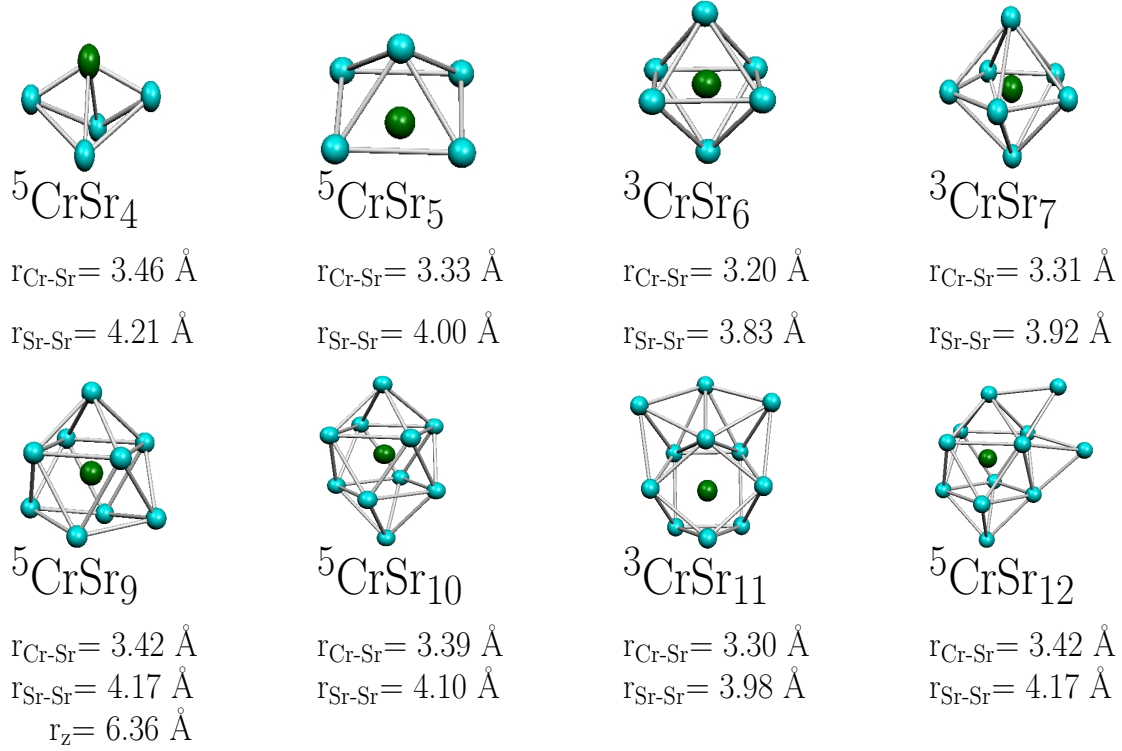


Figure 5.2: Ground state structure and multiplicity of CrSr_N clusters. $r_{\text{Cr-Sr}}$ and $r_{\text{Sr-Sr}}$ are the average Cr-Sr and Sr-Sr bond lengths. r_z is the extent of the cluster perpendicular to the square planes.

Capping of three triangular faces of CrSr_8 cluster provides the ground state structure of CrSr_{11} . CrSr_{12} has a structure which is obtained by decorating two triangular faces of the CrSr_{10} motif. The next higher energy isomers of CrSr_N clusters are given in the Appendix C.1.

5.3.2 Relative stabilities

Hardness (η) calculated using ΔSCF method, and $\Delta_2(N)$ for the CrSr_N clusters are plotted in the Figure 5.3. η is maximum at $N=4$ in the size range studied here. After that η decreases continuously up to $N=7$. $\Delta_2(N)$ shows a large peak at $N=6$ indicating its thermodynamic stability, though there is no peak in the hardness at this size. Clusters having local peaks in $\Delta_2(N)$ and atom addition energy (ΔE_N) without accompanying peaks in the HL gaps are claimed to have greater stability due to their structures [102, 103]. Therefore the likely origin of enhanced stability of CrSr_6 is its compact octahedron geometry. Most importantly, Δ_2 and η both show

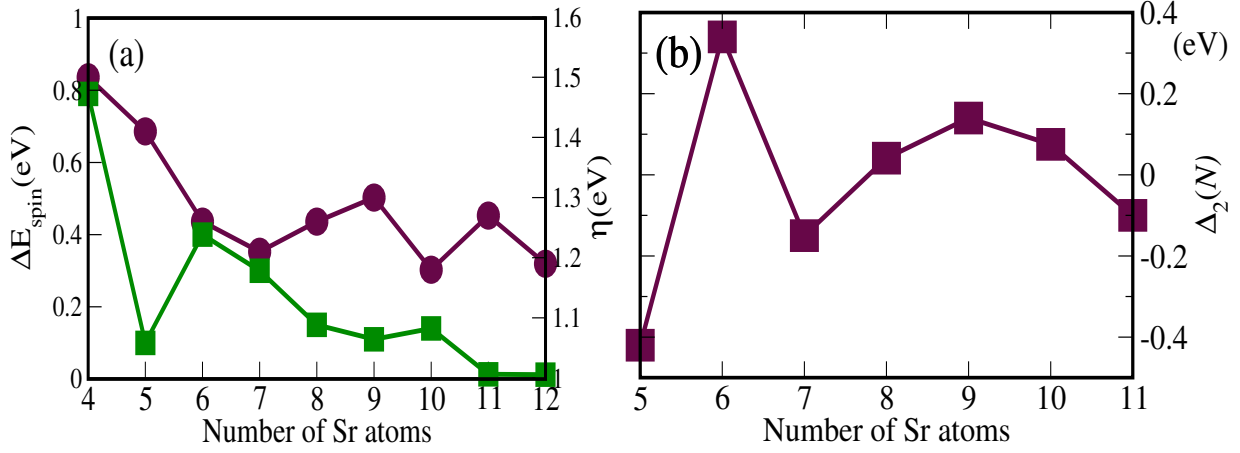


Figure 5.3: (a) Hardness (η), ΔE_{spin} and (b) the second order energy difference ($\Delta_2(N)$) for the CrSr_N as a function of the number of Sr atoms N .

local peaks at $N=9$ which indicate thermodynamic and chemical stability. Therefore the origin of greater stability of CrSr_9 is related to electronic effects. In addition, magnetic moment of the CrSr_9 cluster is found to be $4 \mu_B$. ΔE_{spin} is found to be maximum at $N=4$ and shows a sharp peak at $N=6$. However, CrSr_9 has a slightly lower value of ΔE_{spin} (0.11 eV) compared to its neighbors (Table 5.1). A second maximum in η occurs at $N=11$, however $\Delta_2(N)$ drops continuously from $N=9-11$.

Cluster	HL Gap	η	ΔE_{spin}	$\Delta_2(N)$
${}^5\text{CrSr}_4$	0.41	1.50	0.79	
${}^5\text{CrSr}_5$	0.30	1.41	0.10	-0.42
${}^3\text{CrSr}_6$	0.10	1.26	0.40	0.38
${}^3\text{CrSr}_7$	0.09	1.21	0.30	-0.15
${}^3\text{CrSr}_8$	0.32	1.26	0.15	0.04
${}^5\text{CrSr}_9$	0.46	1.30	0.11	0.15
${}^5\text{CrSr}_{10}$	0.22	1.18	0.14	0.08
${}^3\text{CrSr}_{11}$	0.46	1.27	0.013	-0.10
${}^5\text{CrSr}_{12}$	0.39	1.19	0.012	

Table 5.1: The HL gap, η , ΔE_{spin} , and $\Delta_2(N)$ of CrSr_N clusters. All the values are given in eV.

5.3.3 Stability of CrSr_9

We saw that CrSr_9 turns out to be a unique cluster with enhanced stability as indicated by HL gap, $\Delta_2(N)$, and η . Also it has a magnetic moment of $4 \mu_B$. Therefore we will now focus on CrSr_9 which is the most suitable candidate for a

magnetic superatom. To obtain more insights into the enhanced stability of CrSr_9 , we examine its MO plot shown in Figure 5.4. Interestingly, our anticipation that the two additional electrons from a Sr atom will go into the 2D orbitals in the α channel turns out to be true. CrSr_9 has an electronic configuration $1S^21P^61D^{10}2S^22D_\alpha^4$, same as that of FeCa_8 . Total magnetic moment of $4 \mu_B$ comes from the nearly degenerate $2D_\alpha^4$ orbitals via Hund's coupling. The remaining 2D orbital, i.e., LUMO in the α channel is split-off to a higher energy and gives a HL gap of 0.42 eV. The reason

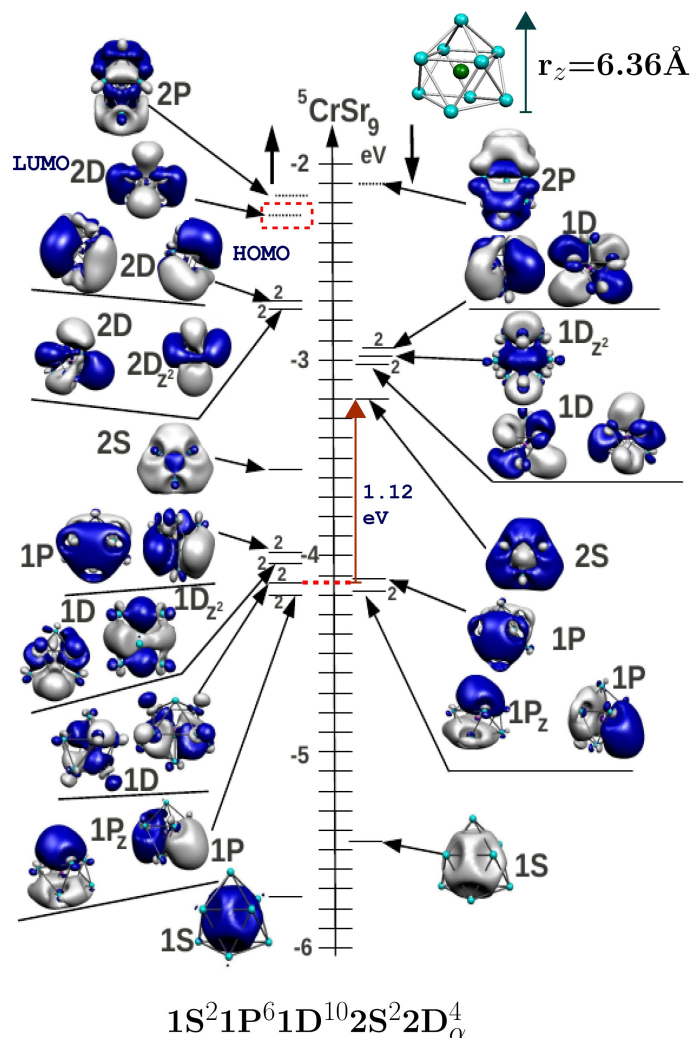


Figure 5.4: MO energy level diagrams and isosurface plots for the $^5\text{CrSr}_9$.

behind the splitting of the $2D_\alpha$ orbitals is again crystal field effect. The addition of one Sr atom to the antiprism structure of CrSr_8 gives a capped antiprism structure for CrSr_9 . It can be described as extension along the z direction and like a prolate structure ($r_z=6.36 \text{ \AA}$) because r_z is greater than the in-plane Sr-Sr distance. As a

consequence, $1D_{z^2}$, $1P_z$, and $2D_{z^2}$ orbitals are relatively more stabilized. In addition, crystal field effect also stabilizes the $2P_z$ orbital compared to the other $2P$ orbitals. We can see from the Figure 5.4 that LUMO+1 in the α channel and LUMO in the β channel are of $2P_z$ character. Note that $2D_\beta$ orbital is the LUMO of FeCa_8 cluster. However we do not find any $2D$ orbital close to $2P_z$ in the β channel. This fact can be understood in terms of the exchange splitting of the $2D$ orbitals. Our calculations show that $2D$ orbitals have $\sim 13\%$ contribution from Cr $3d$ orbitals. Consequently, an exchange splitting of 3.55 eV in the $3d$ atomic orbitals of a bare Cr atom¹ induces a large exchange splitting in the $2D$ orbitals. The lowest $2D_\beta$ orbital is 0.99 eV higher in energy relative to the lowest $2D_\alpha$ orbital.

In summary, CrSr_9 cluster turns out to be a stable and magnetic species. Enhanced stability is due to splitting in the $2D$ shell orbitals caused by the crystal field effect. A total magnetic moment of $4 \mu_B$ arises from the unpaired electrons in the $2D_\alpha$ orbitals.

5.3.4 Magnetic properties of CrSr_N clusters

We will now focus on the magnetic properties of the CrSr_n clusters. Among all the $3d$ TM elements, Cr has a maximum spin magnetic moment of $6 \mu_B$ due to its $3d^5 4s^1$ configuration. Figure 5.5 shows the evolution of magnetic moments of the CrSr_N clusters. For $N=4$ and 5, magnetic moment of the clusters turns out to be $4 \mu_B$.

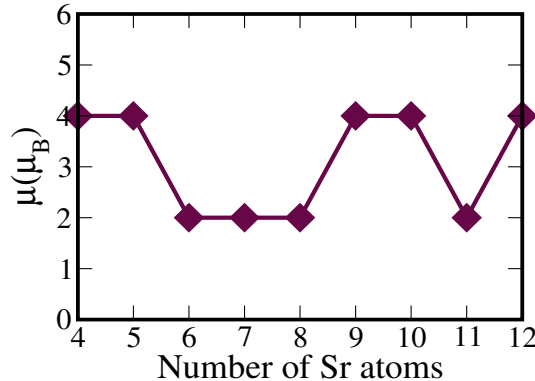


Figure 5.5: Variation of the magnetic moment of CrSr_N clusters.

Further addition of successive Sr atoms up to $N=8$ leads to further quenching in the magnetic moment. CrSr_N ($N=6-8$) clusters are found to have magnetic moment of $2 \mu_B$. Most interestingly, the magnetic moment increases up to $4 \mu_B$ again for $N=9$ and 10.

¹One electron energy levels and atomic orbitals of Cr is given in the Appendix C.2.

To obtain more insight, we have analyzed the MO plots of the CrSr_N ($N=6$ and 7) clusters given in the Appendix C.3. If we count all the $3d$ and $4s$ electrons of a bare Cr atom, CrSr_6 and CrSr_7 will have 18 and 20 electrons which are shell filling numbers in the spherical shell models. Therefore these clusters are expected to have closed shell configurations. However, we found $1S^21P^61D^92S^1$ and $1S^21P^61D^92S^22D_\alpha^1$ configurations for the CrSr_6 and CrSr_7 clusters respectively. Also one of the 1D orbitals in the β channel of both clusters is not occupied. Therefore origin of the open shell configurations of these clusters is inherently related to exchange splitting between the 1D orbitals. The 1D orbitals of the CrSr_6 and CrSr_7 clusters are found to have $\sim 70\%$ and $\sim 85\%$ contributions from the Cr $3d$ orbitals respectively. This leads to an exchange splitting of 0.87 eV and 1.12 eV in the 1D orbitals of these clusters. In CrSr_6 , two unpaired electrons (1D and 1S orbitals) give a magnetic moment of $2 \mu_B$. For CrSr_7 , magnetic moment of $2 \mu_B$ is provided by two unpaired electrons, each coming from the 1D and 2D orbitals of the α channel.

Addition of one Sr atom will give two more electrons which are accommodated in the $2D_\alpha$ orbitals of the CrSr_8 cluster. The electronic configuration of CrSr_8 is shown to be $1S^21P^61D^{10}2S^22D_\alpha^2$ in Figure 4.6(b). Here 1D orbitals in the two spin channels are completely occupied. Note that Hund's coupling leads to partially filled $2D_\alpha^2$ state and gives a magnetic moment of $2 \mu_B$. The MO plot of CrSr_9 in Figure 5.4 shows a $1S^21P^61D^{10}2S^22D_\alpha^4$ configuration. Total magnetic moment of $4 \mu_B$ is given by the partially occupied $2D_\alpha$ orbitals. The ground state structure of CrSr_{10} is a bi-capped antiprism. Further elongation of structure should lead to more stabilization of $2P_z$ orbitals in a way similar to FeCa_{10} . The electronic configuration of CrSr_{10} turns out to be $1S^21P^61D^{10}2S^22D_\alpha^42P_\alpha^12P_\beta^1$ and retains the magnetic moment of $4 \mu_B$ (Appendix C.4). Non-compact structures of the CrSr_{11} and CrSr_{12} clusters lead to poor resemblance of their MO's to the shell orbitals. Therefore we do not attempt to explain their electronic structure and magnetic moments in terms of shell model.

Let us now have a close look at the local moments of the TM elements in the CrSr_N clusters. Table 5.2 shows the atomic spins on the Cr and Sr atoms of the CrSr_N ($N=4-10$) clusters obtained via Mulliken population method. Spin magnetic moment on the Cr atom within the size range studied here varies from $2.14 \mu_B$ to $5.20 \mu_B$ and is always less than that of a bare Cr atom. In addition, the presence of a Cr atom polarizes the host atoms in a way similar to the FeCa_N and TMSr_8 clusters. Net effective moment on Sr atoms is always oriented in the opposite direction to the Cr moment. In CrSr_9 , the spin magnetic moment of Cr is found to be $4.34 \mu_B$. Mutual anti-parallel alignments of Sr moments give a total moment of $0.34 \mu_B$ which

Cluster	Cr	Sr ₁	Sr ₂	Sr ₃	Sr ₄	Sr ₅	Sr ₆	Sr ₇	Sr ₈	Sr ₉	Sr ₁₀	Sr ₁₁	Sr ₁₂
⁵ CrSr ₄	5.08	-0.33	-0.21	-0.20	-0.33								
⁵ CrSr ₅	5.20	-0.27	-0.22	-0.22	-0.23	-0.23							
³ CrSr ₆	2.14	0.11	0.08	-0.26	-0.26	0.08	0.11						
³ CrSr ₇	3.23	0.36	0.36	-0.39	-0.39	-0.39	-0.39	-0.39					
⁵ CrSr ₈	3.93	-0.24	-0.24	-0.23	-0.24	-0.23	-0.24	-0.24	-0.24				
⁵ CrSr ₉	4.34	0.06	-0.10	-0.11	-0.08	-0.09	0.11	0.09	-0.10	-0.11			
³ CrSr ₁₀	4.59	-0.12	-0.12	-0.11	0.10	-0.09	-0.12	-0.12	0.22	-0.12	-0.09		
³ CrSr ₁₁	4.12	0.01	0.01	0.01	-0.32	-0.18	-0.22	-0.33	-0.33	-0.22	-0.33	-0.18	
⁵ CrSr ₁₂	4.64	-0.04	0.03	-0.17	-0.07	-0.17	0.01	0.01	0.15	-0.01	-0.07	-0.14	-0.14

Table 5.2: Atomic spins in the CrSr_N clusters using Mulliken population analysis.

is oriented opposite to the Cr moment. Hence, one gets a total moment of $4 \mu_B$ for the CrSr₉ cluster. Similar is the case for CrSr₁₀ cluster. In case of CrSr₁₁ and CrSr₁₂ clusters, coupling between the moments of Cr impurity and Sr atoms is found to be antiferro and ferro-magnetic respectively. This leads to the magnetic moments of $2 \mu_B$ and $4 \mu_B$ for these clusters.

5.4 Study of MnSr_N ($N=4-12$) clusters

5.4.1 Ground state structures

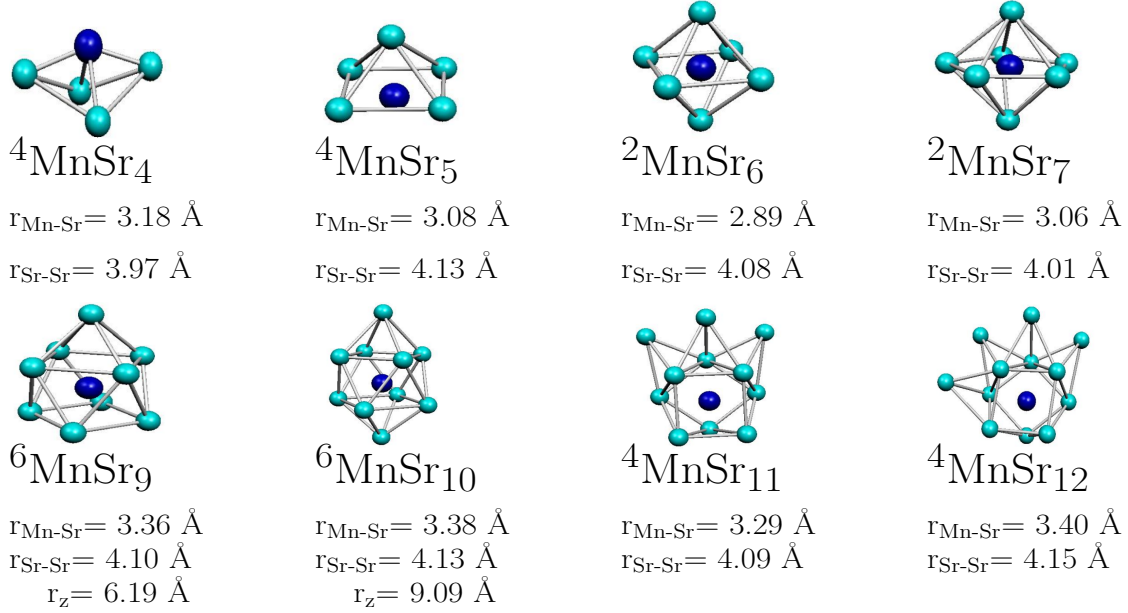


Figure 5.6: Ground state structures and spin multiplicities of MnSr_N clusters. $r_{\text{Mn-Sr}}$ and $r_{\text{Sr-Sr}}$ are the average Mn-Sr and Sr-Sr bond lengths. r_z is the extent of the cluster perpendicular to the square planes.

The optimized ground state structures and spin multiplicities of the MnSr_N ($N=4-12$) clusters are shown in Figure 5.6. All the ground state structures of MnSr_N clusters are very similar to the structures obtained for CrSr_N series, except for MnSr_{12} . The ground state structure of MnSr_{12} is obtained by the capping of four triangular faces of the MnSr_8 motif. A few higher energy isomers of MnSr_N clusters are given in the Appendix C.5.

5.4.2 Relative stabilities

Figure 5.7 shows the results of hardness, ΔE_{spin} and $\Delta_2(N)$ values for the MnSr_N clusters. These clusters show features similar to those of CrSr_N . For example, a continuous drop in hardness from $N=4$ to $N=7$ and a sharp peak in Δ_2 at $N=6$ indicating the thermodynamic stability of MnSr_6 . Surprisingly, MnSr_9 does not emerge as the most stable cluster. Rather, local maxima are found at $N=10$ in η

and Δ_2 which indicate chemical and thermodynamic stability of MnSr_{10} . Also ΔE_{spin} shows a local maximum for MnSr_{10} . In addition, MnSr_{10} has a total spin magnetic moment of $5 \mu_B$. Table 5.3 summarizes the HL gap, η , ΔE_{spin} and $\Delta_2(N)$ values of

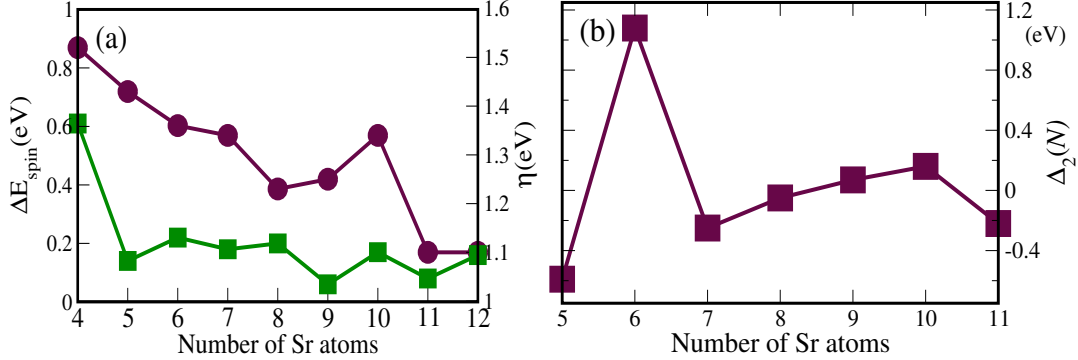


Figure 5.7: (a) Hardness, ΔE_{spin} (b) second order energy difference ($\Delta_2(N)$) for the MnSr_N clusters as a function of the number of Sr atoms N .

Cluster	HL Gap	η	ΔE_{spin}	$\Delta_2(N)$
$^4\text{MnSr}_4$	0.20	1.52	0.61	
$^4\text{MnSr}_5$	0.38	1.43	0.14	-0.59
$^2\text{MnSr}_6$	0.12	1.36	0.22	1.08
$^2\text{MnSr}_7$	0.20	1.34	0.18	-0.26
$^4\text{MnSr}_8$	0.25	1.23	0.20	-0.06
$^6\text{MnSr}_9$	0.32	1.25	0.06	0.07
$^6\text{MnSr}_{10}$	0.45	1.34	0.17	0.16
$^4\text{MnSr}_{11}$	0.23	1.10	0.08	-0.22
$^4\text{MnSr}_{12}$	0.22	1.10	0.16	

Table 5.3: The HL gap, adiabatic spin excitation (ΔE_{spin}), hardness (η) and $\Delta_2(N)$ of MnSr_N clusters. All the values are given in eV.

the MnSr_N clusters.

5.4.3 Stability of MnSr_{10}

To understand the enhanced stability of MnSr_{10} , we examine the MO plots of MnSr_9 and MnSr_{10} which are given in Figure 5.8. MnSr_9 is a capped square anti-prism structure. It is found to have a $1S^21P^61D^{10}2S^22D_\alpha^5$ configuration. Though, it has half filled 2D orbitals, HL gap is 0.32 eV only. Similar to case of CrSr_9 , prolate shape ($r_z=6.19 \text{ \AA}$) of MnSr_9 forces the $2P_z$ orbitals to be lower in energy. In fact, the LUMO in both the spin channels are of $2P_z$ character. However, the LUMO in the β channel is slightly lower in energy (0.12 eV) with respect to the LUMO in the

α channel. As a consequence, the overall gap is 0.32 eV, smaller than the gap in the α channel (0.51 eV). Addition of one more Sr atom to MnSr_9 motif leads to a bi-capped antiprism structure for MnSr_{10} . The distance between the two capping Sr atoms is found to be 9.09 Å. Due to further elongation of the structure along the z direction, $2P_z$ orbitals get more stabilized.

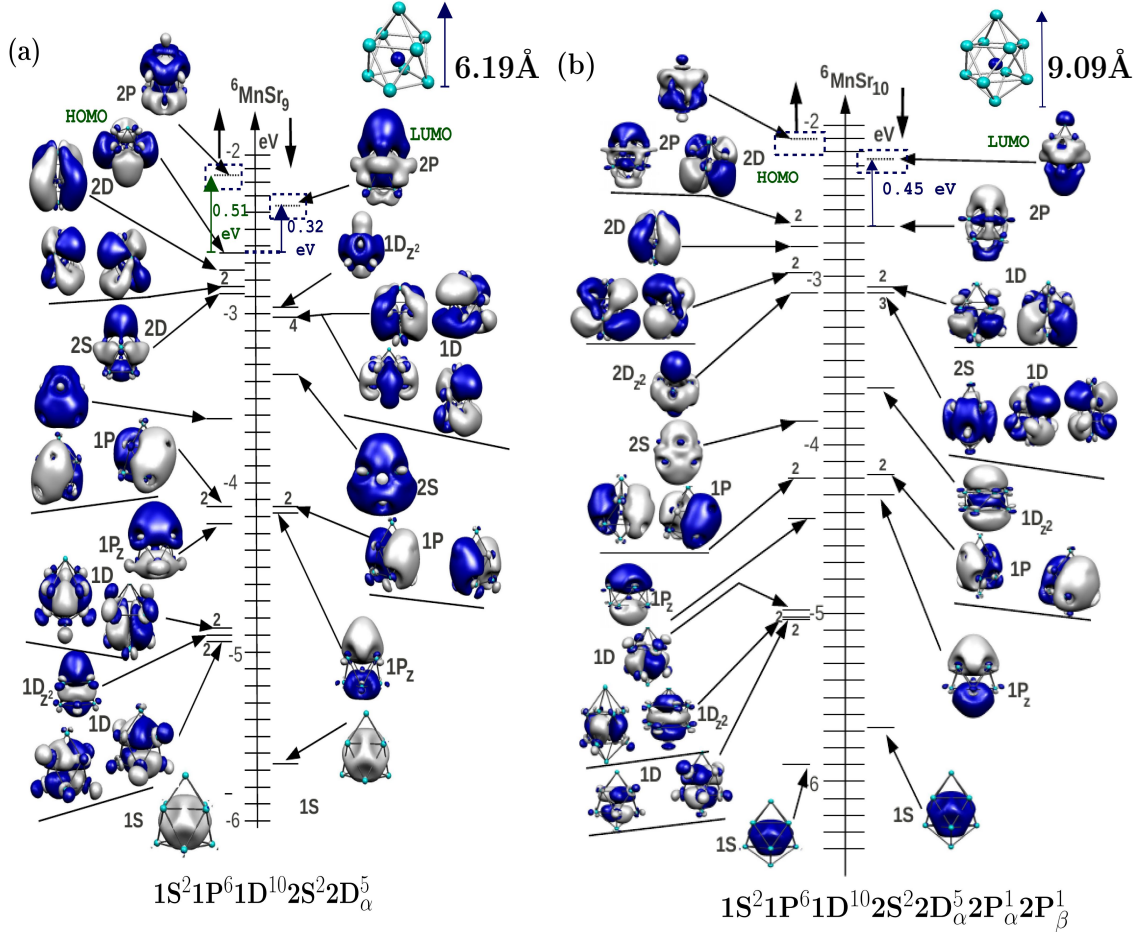


Figure 5.8: MO energy level diagrams and isosurface plots for the (a) ${}^6\text{MnSr}_9$ and (b) ${}^6\text{MnSr}_{10}$ clusters.

Figure 5.8(b) shows the occupied $2P_z$ orbitals in the α and β channels. In the α channel, $2P_z$ orbital becomes degenerate with the highest occupied $2D$ orbital and form the HOMO. Stabilization of the $2P_z$ orbitals leads to sub-shell filling at this size leading to a large HL gap (0.45 eV) and enhanced stability of MnSr_{10} . In addition, a magnetic moment of $5 \mu_B$ in both MnSr_9 and MnSr_{10} clusters arises due to half filled $2D_\alpha$ orbitals.

5.4.4 Magnetic properties of MnSr_N clusters

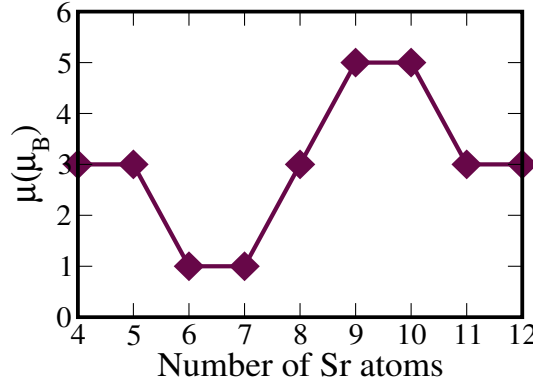


Figure 5.9: Variation of magnetic moment of MnSr_N clusters.

Figure 5.9 shows the variation of the magnetic moments as a function of N in the MnSr_N clusters. It reveals new interesting features. The magnetic moments for size $N=4$ and 5 are found to be $3 \mu_B$, while MnSr_6 and MnSr_7 have magnetic moment of $1 \mu_B$ only. Further addition of successive Sr atoms increases the magnetic moment. MnSr_9 and MnSr_{10} are found to have magnetic moment of $5 \mu_B$. For MnSr_{11} , the magnetic moment is again found to be $3 \mu_B$. Since $3d$ TM elements are shown to polarize the host atoms in the study of TMSr_8 and CrSr_N clusters, we will have a close look at the local moments within the MnSr_N clusters also. Mulliken atomic spins for MnSr_N ($N=4-10$) clusters are given in the Table 5.4. In all the clusters, spin magnetic

Cluster	Mn	Sr ₁	Sr ₂	Sr ₃	Sr ₄	Sr ₅	Sr ₆	Sr ₇	Sr ₈	Sr ₉	Sr ₁₀	Sr ₁₁	Sr ₁₂
⁴ MnSr ₄	4.26	-0.22	-0.40	-0.41	-0.22								
⁴ MnSr ₅	4.27	-0.26	-0.25	-0.25	-0.24	-0.25							
² MnSr ₆	2.64	-0.25	-0.36	-0.19	-0.19	-0.36	-0.25						
² MnSr ₇	3.07	-0.38	-0.06	-0.06	-0.38	-0.38	-0.39	-0.39					
⁴ MnSr ₈	3.46	-0.06	-0.05	-0.05	-0.05	-0.05	-0.05	-0.05	-0.5				
⁶ MnSr ₉	3.74	0.05	0.14	0.05	0.14	0.15	0.43	0.05	0.14	0.05			
⁶ MnSr ₁₀	3.95	0.12	0.07	0.05	0.26	0.05	0.11	0.05	0.05	0.11	0.11		
⁴ MnSr ₁₁	3.66	0.15	-0.07	0.08	-0.21	-0.19	-0.07	-0.05	-0.17	-0.09	-0.18	0.16	
⁴ MnSr ₁₂	3.76	-0.08	0.15	-0.16	-0.16	-0.08	-0.23	0.10	0.10	-0.15	0.15	-0.23	-0.15

Table 5.4: Atomic spins in the MnSr_N clusters obtained by Mulliken population analysis.

moment on Mn is always lower than its atomic value of $5 \mu_B$. Interestingly, moments on the Sr atoms are aligned anti-parallel to the Mn moment in all the clusters except for MnSr_9 and MnSr_{10} . Therefore, it is the anti-ferromagnetic coupling between the moments on Mn and Sr atoms which leads to lower values of magnetic moments of MnSr_N clusters ($N=4-8$). The local spin moment on Mn atom in MnSr_9 and MnSr_{10}

is found to be 3.74 and 3.95 μ_B respectively. From Table 5.4, it is clear that moments on the Sr atoms in these clusters are aligned parallel to the Mn spin. This gives a total magnetic moment of 5 μ_B for these clusters. In case of MnSr_{11} and MnSr_{12} , again anti-ferromagnetic coupling between the moments of Mn and Sr atoms leads to a lower magnetic moment of 3 μ_B .

5.4.5 CrSr_9 and MnSr_{10} clusters as magnetic superatoms

After a detailed study of the TMSr_8 , CrSr_N and MnSr_N clusters, we have identified two clusters which are most likely candidates as magnetic superatoms. These are CrSr_9 and MnSr_{10} which have been shown with enhanced stability and magnetic moment of 4 μ_B and 5 μ_B respectively. To check if these clusters behave as magnetic superatoms, two cluster units are brought close from different directions and in different orientations. Both parallel and anti-parallel alignments of the TM spins are taken in all structures of the dimer studied here. Figure 5.10 shows the optimized structure of the $(\text{CrSr}_9)_2$ dimer. Each unit of CrSr_9 cluster retains its structural

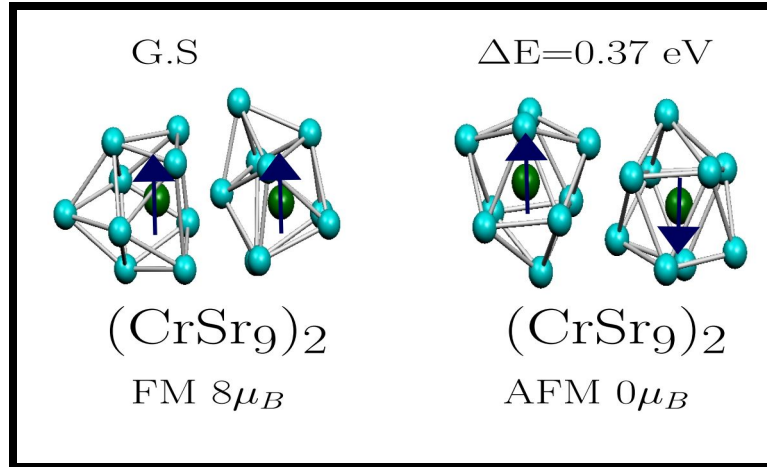


Figure 5.10: Optimized structures for dimers of CrSr_9 with parallel (FM) and anti-parallel (AFM) alignments of the TM spins. ΔE is the energy difference between the two situations.

identity in the ground state of the dimer. Total magnetic moment of the dimer in the ground state is found to be 8 μ_B . Binding energy of the dimer is 2.54 eV relative to two isolated units. An anti-parallel alignment of the Cr spins in the two units is found to be 0.37 eV less stable with respect to the ground state.

Figure 5.11 shows the results for the $(\text{MnSr}_{10})_2$ dimer. In the ground state of $(\text{MnSr}_{10})_2$, each unit of MnSr_{10} retains its structural identity. Again, a parallel arrangement of the spins on the two clusters turns out to be lower in energy with

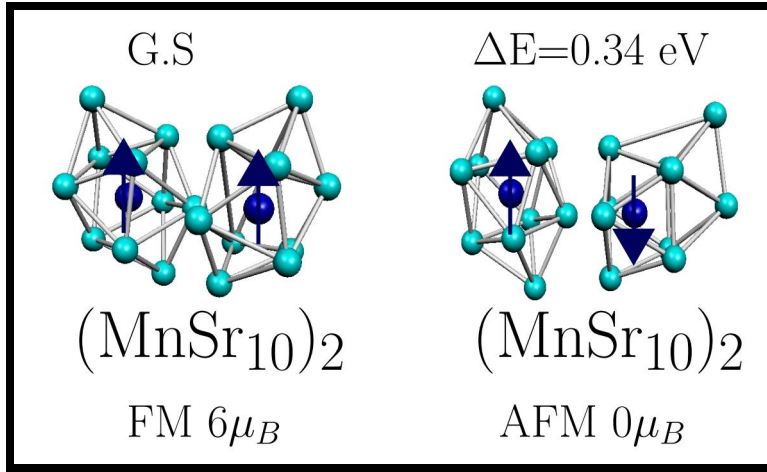


Figure 5.11: Optimized structures for dimer of MnSr_{10} with parallel (FM) and anti-parallel (AFM) alignments of the TM spins.

respect to a dimer with anti-parallel alignment of the Mn spins. The energy difference between these two states is 0.34 eV. The magnetic moment of $(\text{MnSr}_{10})_2$ dimer in the ground state of is found to be $6 \mu_B$. In addition, binding energy of $(\text{MnSr}_{10})_2$ dimer is 2.51 eV against two MnSr_{10} units. Thus both CrSr_9 and MnSr_{10} behave as magnetic superatoms.

5.4.6 Conclusions

We have performed a detailed study of the electronic, magnetic and structural properties of the CrSr_N and MnSr_N clusters. CrSr_9 and MnSr_{10} are found to be stable clusters indicated by their HL gaps, η and $\Delta_2(N)$. Also CrSr_9 and MnSr_{10} have magnetic moment of $4 \mu_B$ and $5 \mu_B$ respectively. We have shown that it is the interplay between crystal field effect and Hund's coupling which stabilizes these clusters. Furthermore two units of stable clusters were found to retain their structural identity when they were brought close to each other from different directions and orientations. Therefore we classified CrSr_9 and MnSr_{10} as magnetic superatoms. Spins of the two cluster units were aligned parallel to each other in the ground state of the dimers providing high magnetic moment.

TM doped aluminium clusters

6.1 Introduction

In the previous chapters, we have shown that an interplay of crystal-field effect and Hund's coupling may lead to sub-shell fillings at unconventional electron counts. FeCa_8 , CrSr_9 and MnSr_{10} with enhanced stability are examples of such an interplay. First two clusters have 24 valence electrons, while MnSr_{10} has 27 valence electrons. Also these clusters have large magnetic moments and are shown to be attractive candidates for magnetic superatoms. It has been observed that crystal-field effects are more pronounced in the Al clusters compared to group-I and II metal clusters because of large effective nuclear charge ($Z_A=3$) [74, 75]. Recently, non-reactive behaviour of CuAl_{22}^- towards O_2 has been explained by the splitting of the 2D shell orbitals due to crystal field effect [14]. Therefore it is interesting to explore whether such interplay between crystal-field effect and Hund's coupling leads to clusters with enhanced stability among TM-Al clusters. Since stable clusters can occur at unconventional electron counts, one has to perform first-principles calculations on a series of clusters to identify them. With this motivation, we have studied the structural, electronic and magnetic properties of Cr, Fe and Mn doped Al clusters. Though we have not been able to identify any possible candidates for magnetic superatoms in these series, FeAl_4 emerges with enhanced stability. Inspired by this finding, we have studied Co and Ni doped Al clusters over a limited size range. We found CoAl_3 to have enhanced stability among the CoAl_N ($N=2-6$) clusters. We will discuss the origin of their stability in terms of electronic and geometric structures. Most importantly, we will show that spherical shell models are not appropriate descriptions for the electronic structures of TM doped aluminum clusters. In fact, we will show

that stability of FeAl_4 , and CoAl_3 can be associated with their aromatic behaviour, revealed by their negative NICS values.

6.2 Computational details

We have used the same formalism for all our first-principles calculations described in the previous chapters. All electrons on the $3d$ TM atoms and Al are treated explicitly using the double- ζ valence plus polarization basis sets optimized for GGA functionals by Calaminici et al. (DZVP-GGA) [163]. The exchange-correlation effects are taken into account using the generalized gradient approximation (GGA) functional proposed by Perdew, Burke and Ernzerhof (PBE) [162]. By using these basis sets and exchange-correlation functional, first and second ionization potentials of Al are found to be 6.05 eV and 18.73 eV respectively. These potentials are in excellent agreement with the experimental values of 5.98 and 18.82 eV respectively [164].

6.3 Study of TM-Al clusters (TM=Cr, Mn and Fe)

6.3.1 Ground state structures

Figure 6.1 shows the optimized ground state structures and spin multiplicities of all the TMAI_N (TM=Cr, Mn, Fe ; $N=2-12$) clusters. From $N=3$ onwards, all the clusters adopt three dimensional structures. In CrAl_N and MnAl_N clusters, Cr and Mn occupy the exterior positions at all sizes. Fe atom starts to get encapsulated in the Al_{10} cage. This can be understood from the fact that early $3d$ TM atoms have atomic radii larger than Fe. For example, the atomic radius of Cr and Mn atoms are 1.30 Å and 1.35 Å respectively, while Fe has an atomic radius of 1.26 Å. Our results are also consistent with the recent experiments of Lang *et al* on Cr-Al clusters [120]. The smallest size at which Cr is encapsulated by an Al cage in the CrAl_N^+ series is at $N=16$. A few higher energy isomers of these clusters are given in the Appendix [D.1, D.2, D.3].

6.3.2 Relative stabilities

We will now discuss the chemical and thermodynamic stability of TM-Al (TM=Cr, Mn and Fe) clusters.

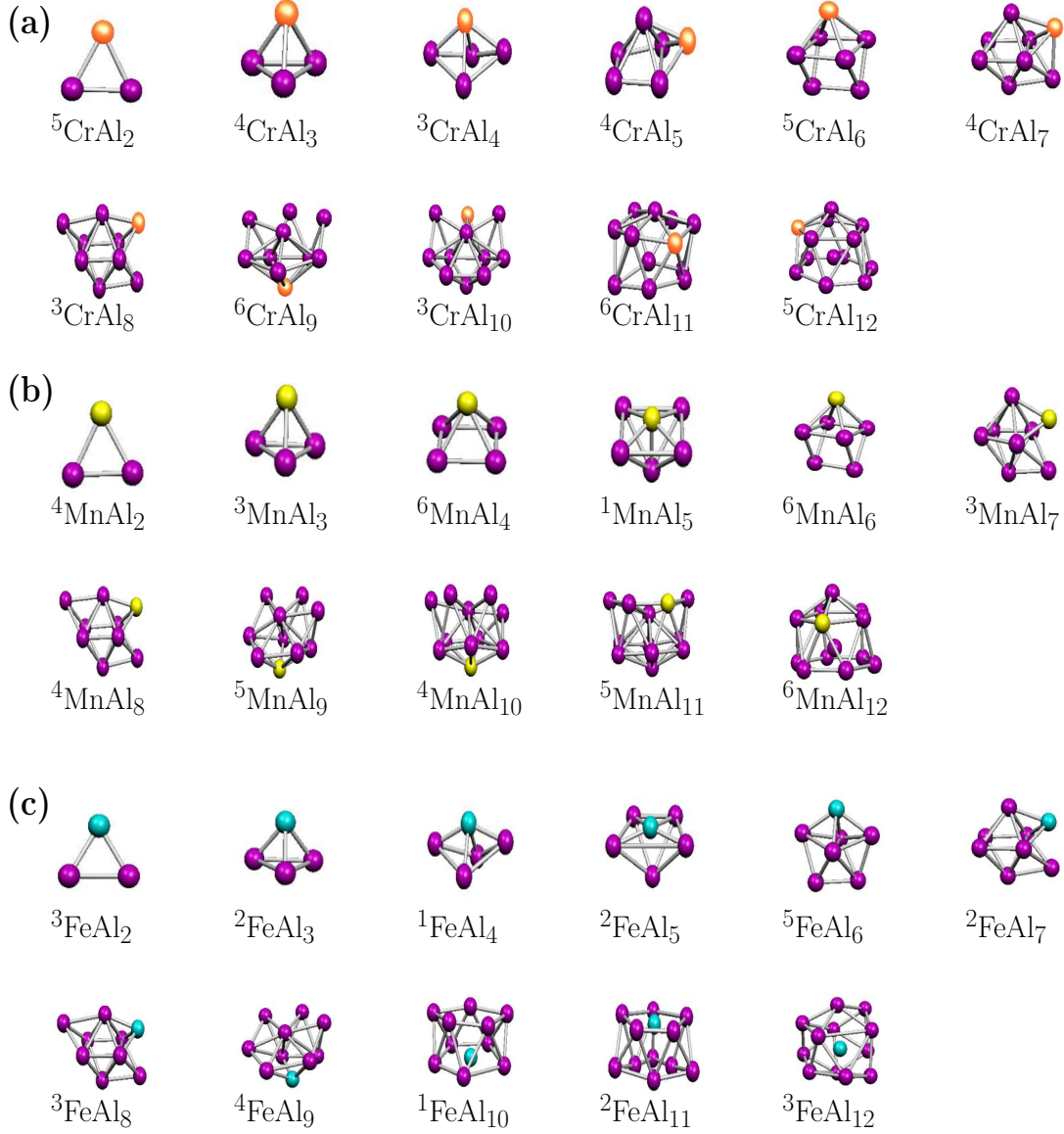


Figure 6.1: Ground state structures and spin multiplicities of Cr-, Mn- and FeAl_N clusters for $N=2-12$.

6.3.2.1 CrAl_N clusters

Figure 6.2(a) shows the evolution of the HL gap and ΔE_{spin} with the number of Al atoms for CrAl_N clusters. In the size range studied here, the HL gap varies from 0.24 eV to 0.92 eV. Two local maxima are observed at $N=4$ and 7 in the HL gap, indicating their chemical stability. However, CrAl₄ and CrAl₇ relatively are less stable against the adiabatic spin excitation. In addition, Figure 6.2(b) shows no

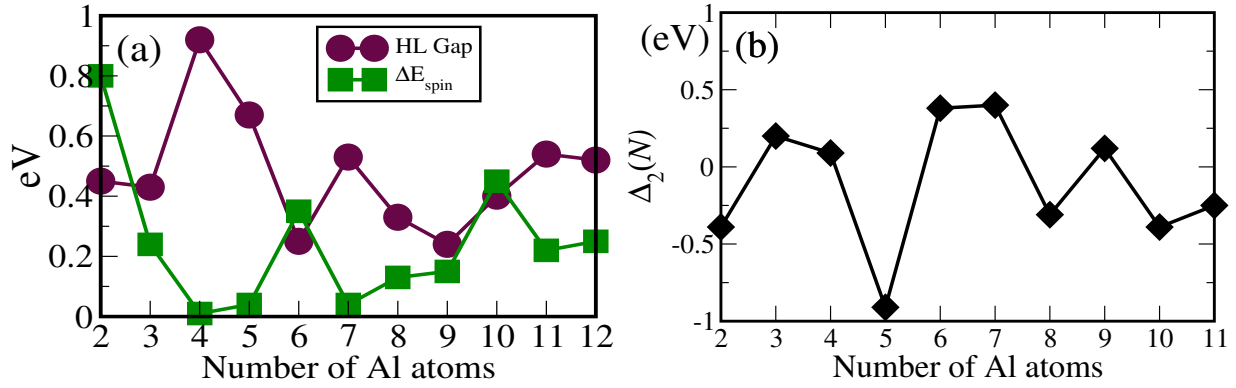


Figure 6.2: (a) HL gap and ΔE_{spin} (b) second order energy difference ($\Delta_2(N)$) of CrAl_N clusters as a function of number of Al atoms.

distinct peaks at $N=4$ and 7 in $\Delta_2(N)$. A small and local maximum in $\Delta_2(N)$ is observed at $N=9$, but there is no corresponding peak in the HL gap. The HL gap, ΔE_{spin} , η and Δ_n^2 values for the CrAl_n clusters are given in Table 6.1. η values are calculated using the ΔSCF method.

Cluster	HL Gap	ΔE_{spin}	η	$\Delta_2(N)$
${}^5\text{CrAl}_2$	0.45	0.80	1.03	-0.39
${}^4\text{CrAl}_3$	0.43	0.24	2.35	0.20
${}^3\text{CrAl}_4$	0.92	0.01	2.45	0.09
${}^4\text{CrAl}_5$	0.67	0.04	2.25	-0.91
${}^5\text{CrAl}_6$	0.25	0.35	2.03	0.38
${}^4\text{CrAl}_7$	0.53	0.04	2.03	0.40
${}^5\text{CrAl}_8$	0.33	0.13	2.00	-0.36
${}^6\text{CrAl}_9$	0.24	0.15	1.81	0.22
${}^5\text{CrAl}_{10}$	0.40	0.45	1.87	-0.32
${}^4\text{CrAl}_{11}$	0.54	0.22	1.80	-0.51
${}^5\text{CrAl}_{12}$	0.52	0.25	1.73	

Table 6.1: HL gap, adiabatic spin excitation (ΔE_{spin}), hardness (η) and $\Delta_2(N)$ of CrAl_N clusters.

6.3.2.2 MnAl_N clusters

Figure 6.3(a) shows the variation of the HL gap and ΔE_{spin} as a function of N for MnAl_N clusters. Local peaks at $N=3, 5, 9$ and 11 are observed in the HL gap. In fact, MnAl_5 has the highest HL gap of 1.18 eV among all the MnAl_N clusters (Table 6.2). This can be understood from the fact that MnAl_5 is a singlet. However, $\Delta_2(N)$ and ΔE_{spin} do not show local peak at $N=5$. Second highest HL

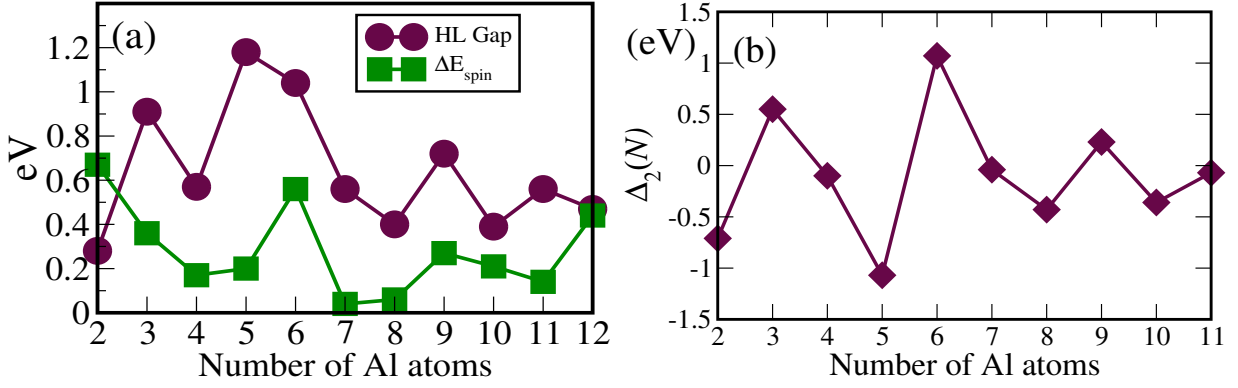


Figure 6.3: (a) HL gap and ΔE_{spin} (b) second order energy difference ($\Delta_2(N)$) of MnAl_N clusters as a function of number of Al atoms.

Cluster	HL Gap	ΔE_{spin}	η	$\Delta_2(N)$
${}^6\text{MnAl}_2$	0.28	0.67	2.26	-0.71
${}^3\text{MnAl}_3$	0.91	0.36	2.52	0.55
${}^6\text{MnAl}_4$	0.57	0.17	2.25	-0.10
${}^1\text{MnAl}_5$	1.18	0.20	2.38	-1.07
${}^6\text{MnAl}_6$	1.04	0.56	2.50	1.07
${}^3\text{MnAl}_7$	0.56	0.04	2.03	-0.04
${}^4\text{MnAl}_8$	0.40	0.06	1.91	-0.43
${}^5\text{MnAl}_9$	0.72	0.27	1.98	0.16
${}^6\text{MnAl}_{10}$	0.39	0.21	1.95	-0.27
${}^3\text{MnAl}_{11}$	0.56	0.14	1.79	-0.38
${}^6\text{MnAl}_{12}$	0.47	0.44	1.81	

Table 6.2: HL gap, adiabatic spin excitation (ΔE_{spin}), hardness (η) and $\Delta_2(N)$ of MnAl_N clusters.

gap is found to be 1.04 eV for MnAl_6 . $\Delta_2(N)$ shows maxima at $N=3, 6$ and 9 in Figure 6.3(b), indicating enhanced thermodynamic stability at these sizes. Therefore MnAl_3 and MnAl_9 are found to have both enhanced chemical and thermodynamic stability. However, MnAl_3 is less stable against adiabatic spin excitation compared to MnAl_2 as shown in Figure 6.3(a). ΔE_{spin} shows local peaks at $N=6$ and 9 only. Magnetic moment of MnAl_3 and MnAl_9 are found to be $2 \mu_B$ and $4 \mu_B$ respectively. Because of small value of magnetic moment, we have not consider MnAl_3 as a suitable candidate for magnetic superatom. In magnetic superatoms, we have seen that a TM is encapsulated inside the cage formed by alkaline earth elements, e.g., FeCa_8 and CrSr_9 . Consequently, their magnetic properties remain intact while making dimers. Al_6 and Al_9 cages are not able to encapsulate a Mn atom. Therefore, it is unlikely that MnAl_6 and MnAl_9 would behave as magnetic superatoms.

6.3.2.3 FeAl_N clusters

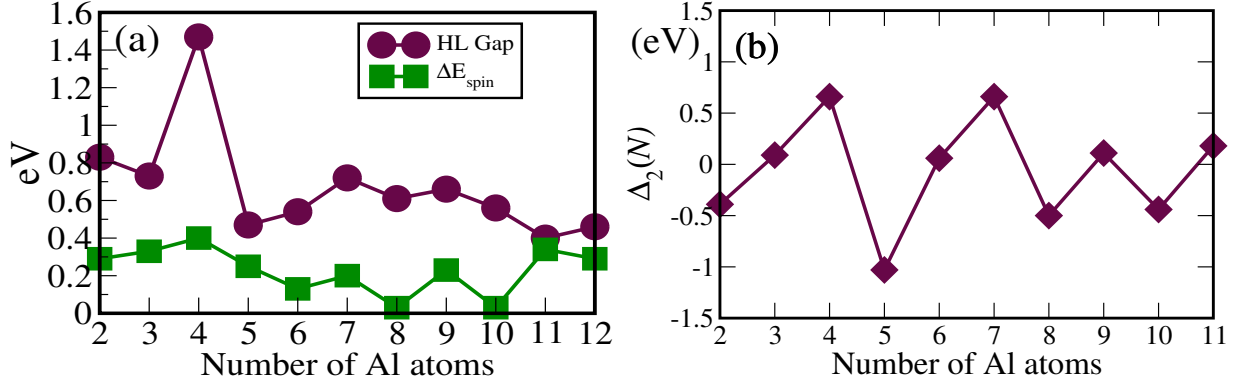


Figure 6.4: (a) HL gap and ΔE_{spin} (b) second order energy difference ($\Delta_2(N)$) of FeAl_N clusters as a function of number of Al atoms.

Cluster	HL Gap	ΔE_{spin}	η	$\Delta_2(N)$
³ FeAl ₂	0.83	0.29	2.85	-0.39
² FeAl ₃	0.73	0.33	2.40	0.09
¹ FeAl ₄	1.47	0.40	2.60	0.66
² FeAl ₅	0.47	0.25	2.11	-1.03
⁵ FeAl ₆	0.54	0.13	2.20	0.06
² FeAl ₇	0.72	0.20	2.16	0.66
³ FeAl ₈	0.61	0.03	1.96	-0.50
⁴ FeAl ₉	0.66	0.23	1.98	0.11
¹ FeAl ₁₀	0.56	0.03	1.89	-0.44
² FeAl ₁₁	0.40	0.34	1.79	-0.07
³ FeAl ₁₂	0.46	0.29	1.73	

Table 6.3: The HL gap, adiabatic spin excitation energy (ΔE_{spin}), hardness (η) and $\Delta_2(N)$ of FeAl_N clusters.

The HL gap and ΔE_{spin} values of FeAl_N clusters are plotted in Figure 6.4(a). FeAl₄ is a singlet in its ground state and has highest HL gap of 1.47 eV among all the FeAl_N clusters. The HL gap of FeAl₄ can be compared to the HL gap (1.87 eV) of Al₁₃⁻ in our calculations. Al₁₃⁻ is known to be a very stable cluster which is resistant to etching by O₂. FeAl₄ also has a local peak in $\Delta_2(N)$ as shown in Figure 6.4(b). In addition, $\Delta_2(N)$ and HL gap show maxima at N=7 and 9, though FeAl₇ and FeAl₉ have small HL gap compared to FeAl₄ (Table 6.3). ΔE_{spin} also reveals the enhanced stability of FeAl₄, FeAl₇ and FeAl₉. Because of small magnetic moment (1 μ_B), FeAl₇ does not qualified for a suitable candidate of magnetic superatom. Although FeAl₉ has a magnetic moment of 3 μ_B , it is not considered as an appropriate candidate for

magnetic superatom because Fe atom is not encapsulated by Al₉ cage in way similar to MnAl₉.

6.4 Study of TMAI₄ and TMAI₃ (TM=Cr-Ni) clusters

While discussing the relative stabilities of the clusters in three series of doped clusters, we find stable clusters with finite magnetic moments, e.g, ⁵MnAl₉ and ⁴FeAl₉. However, these clusters are not considered as possible candidates for magnetic superatoms due to lack of the compact structures. FeAl₄ is found to be a singlet and has relatively greater stability as indicated by various stability descriptors. We will now investigate whether FeAl₄ retains its enhanced stability when TM changes within TMAI₄ clusters. To answer this question, we have performed first-principles calcula-

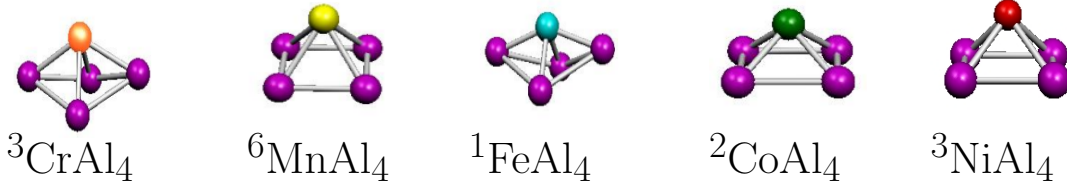
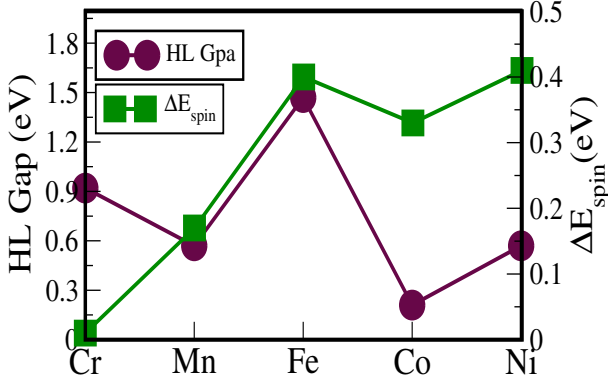


Figure 6.5: Ground state structures and spin multiplicities of TMAI₄ clusters.

tions for TMAI₄ (TM=Cr-Ni) clusters. Figure 6.5 shows the optimized ground state structures and spin multiplicities of the TMAI₄ clusters. MnAl₄, CoAl₄ and NiAl₄ have similar ground state structures in which the TM atoms occupy the square face of the Al₄ unit, while CrAl₄ and FeAl₄ have slightly different structures. To study relative stabilities of the TMAI₄ clusters, we have plotted their HL gap and ΔE_{spin} values in Figure 6.6. Amazingly, both stability descriptors show FeAl₄ as the most stable cluster among the TMAI₄ clusters. Also FeAl₄ has the maximum hardness of 2.60 eV as shown in Table 6.4.

A bare Mn atom has a $3d^54s^2$ electronic configuration, i.e., five unfilled *d* orbitals in the β channel and MnAl₅ emerges as a singlet in its ground state structure, though it does not show an enhanced stability. A close inspection of the geometry of MnAl₅ reveals that the Mn atom is bonded to five Al atoms (Figure 6.1). Maximum Mn-Al distance is found to be 2.23 Å. A bare Fe atom has four unfilled *d* orbitals and four Al



Cluster	HL	η	ΔE_{spin}
${}^3\text{CrAl}_4$	0.92	2.45	0.01
${}^6\text{MnAl}_4$	0.57	2.25	0.17
${}^1\text{FeAl}_4$	1.47	2.60	0.40
${}^2\text{CoAl}_4$	0.21	2.11	0.33
${}^3\text{NiAl}_4$	0.57	2.26	0.41

Table 6.4: The HL gap, hardness (η) and ΔE_{spin} of TMAl_4 clusters. All values are given in eV.

Figure 6.6: The HL gap and ΔE_{spin} of TMAl_4 clusters.

atoms are bonded with Fe atom in the ground state structure of FeAl_4 . Furthermore, FeAl_4 turns out to be a singlet in its ground state and has enhanced chemical and thermodynamic stability. Therefore one obvious question is whether CoAl_3 will also be a singlet in its ground state and have enhanced stability since a Co atom has only three unfilled d orbitals. Similarly, NiAl_2 may show enhanced stability. However, this argument does not apply to CrAl_6 , though Cr has six unfilled orbitals (five $3d$ and one $4s$). The reason is related to its ground state geometry. Out of six Al atoms, only four Al atoms (in square plane) are bonded to Cr atom as shown in Figure 6.1. The distance between the Cr and four Al atoms is $\sim 2.67 \text{ \AA}$, while distance of the Cr to other two Al atoms is 4.36 \AA . As a result, CrAl_6 does not emerge as a singlet in the ground state structure. However, the questions whether CoAl_3 and NiAl_2 will have enhanced stability can be answered only after doing first-principles calculations.

We will first address the question of enhanced stability of CoAl_3 . For this we performed the first-principles calculations for CoAl_N clusters over a limited size range ($N=2-6$). Figure 6.7 shows the optimized ground state structures and spin multiplicities of CoAl_N clusters.

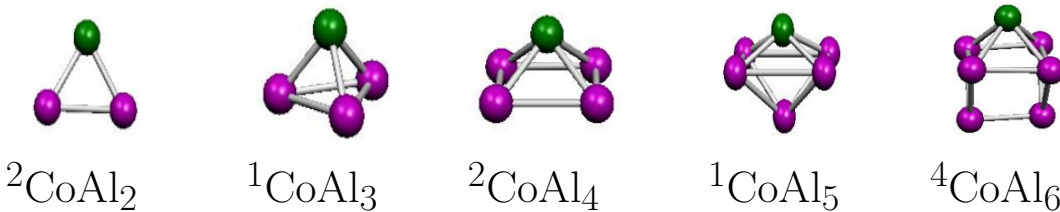


Figure 6.7: Ground state structures and spin multiplicities of CoAl_N ($N=2-6$) clusters.

ities of all the CoAl_N clusters. Structural evolution of these clusters is very similar to that of the MnAl_N clusters. As we anticipated, CoAl_3 turns out to be a singlet in its ground state structure. Also the Co atom is bonded to all three Al atoms in the ground state geometry. To see its relative stability, we plot the HL gap and $\Delta_2(N)$ of the CoAl_N clusters in Figure 6.8(a). Interestingly, both stability descriptors show

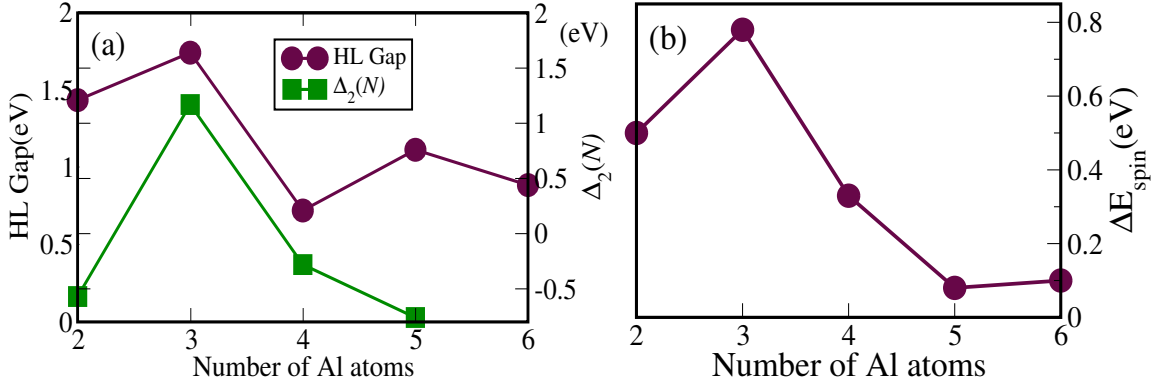


Figure 6.8: (a) The HL gap, $\Delta_2(N)$ and (b) spin excitation energy (ΔE_{spin}) of CoAl_N clusters.

clear peaks for CoAl_3 . In fact, the HL gap of CoAl_3 is found to be 1.64 eV, even higher than that of FeAl_4 . Also CoAl_3 has a large spin excitation energy of 0.78 eV in Figure 6.8(b). Table 6.5 summarizes values of the HL gaps, η , ΔE_{spin} and $\Delta_2(N)$ of the CoAl_N clusters. CoAl_3 is also found to have maximum hardness in the size range $N=2-6$.

Cluster	HL Gap	ΔE_{spin}	η	$\Delta_2(N)$
$^2\text{CoAl}_2$	1.21	0.50	2.77	-0.57
$^1\text{CoAl}_3$	1.64	0.78	2.86	1.17
$^2\text{CoAl}_4$	0.21	0.33	2.11	-0.28
$^1\text{CoAl}_5$	0.76	0.08	2.28	-0.76
$^4\text{CoAl}_6$	0.44	0.10	2.11	-

Table 6.5: The HL gap, adiabatic spin excitation (ΔE_{spin}), hardness (η) and $\Delta_2(N)$ of CoAl_N clusters. All values are given in eV.

Enhanced stability of CoAl_3 is also observed in the study of the TMAI_3 clusters. Figure 6.9 shows the optimized ground state structures and spin multiplicities of all the TMAI_3 (TM=Cr-Ni) clusters. All the 3d TM elements are found to cap the Al_3 triangle. Figure 6.10 shows the HL gap and ΔE_{spin} of the TMAI_3 clusters. CoAl_3 is found to have the highest HL gap. We have given the HL gap, η , and ΔE_{spin} values in Table 6.6. Though, CoAl_3 has the highest HL gap and hardness, its ΔE_{spin}



Figure 6.9: Ground state structures and spin multiplicities of TMA_3 clusters.

value is smaller than that of NiAl_3 which is a doublet. This is surprising but can be understood qualitatively in terms of frozen orbital approximation. This issue is discussed below.

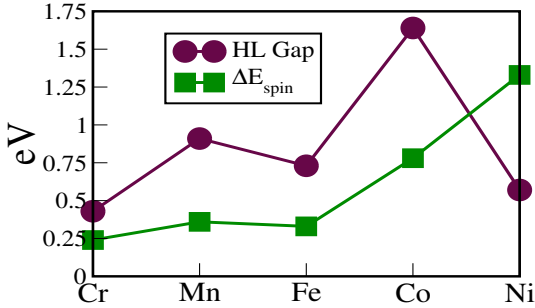


Figure 6.10: The HL gap and ΔE_{spin} of TMA_3 clusters.

Cluster	HL	η	ΔE_{spin}
${}^4\text{CrAl}_3$	0.43	2.35	0.24
${}^3\text{MnAl}_3$	0.91	2.52	0.36
${}^2\text{FeAl}_3$	0.73	2.41	0.33
${}^1\text{CoAl}_3$	1.64	2.86	0.78
${}^2\text{NiAl}_3$	0.57	2.38	1.33

Table 6.6: The HL gap, hardness (η) and ΔE_{spin} of TMA_3 clusters. All values are given in eV.

Motivated by the enhanced stability of FeAl_4 and CoAl_3 , we have studied the NiAl_N ($N=1-6$) clusters via first-principles calculations. Amazingly, NiAl_2 turns out to be a singlet in its ground state structure. Being a singlet, it has relatively a large HL gap of 1.16 eV. However, it is thermodynamically less stable compared to NiAl_3 . This can be understood from the fact that NiAl_3 has a more compact structure than NiAl_2 . Ground state structures of NiAl_N are given in Appendix D.4. Their HL gaps, $\Delta_2(N)$ and ΔE_{spin} are plotted in Appendix D.5, while values are given in Table D.1.

6.5 Shell model and electronic structure of TM-Al clusters

6.5.1 Stability of FeAl_4 and CoAl_3 clusters and shell models

We have shown the FeAl_4 and CoAl_3 are the most stable clusters. Their stability is reflected in various stability descriptors, i.e., $\Delta_2(N)$, η , and the HL gap. If we treat all the $3d$ and $4s$ electrons of Fe as valence electrons and assume that Al acts as a trivalent atom within cluster, there will be 20 valence electrons in FeAl_4 . By a similar argument, CoAl_3 will have 18 electrons. According to shell models, clusters with 20 and 18 valence electrons have closed electronic shells. It is then natural to ask

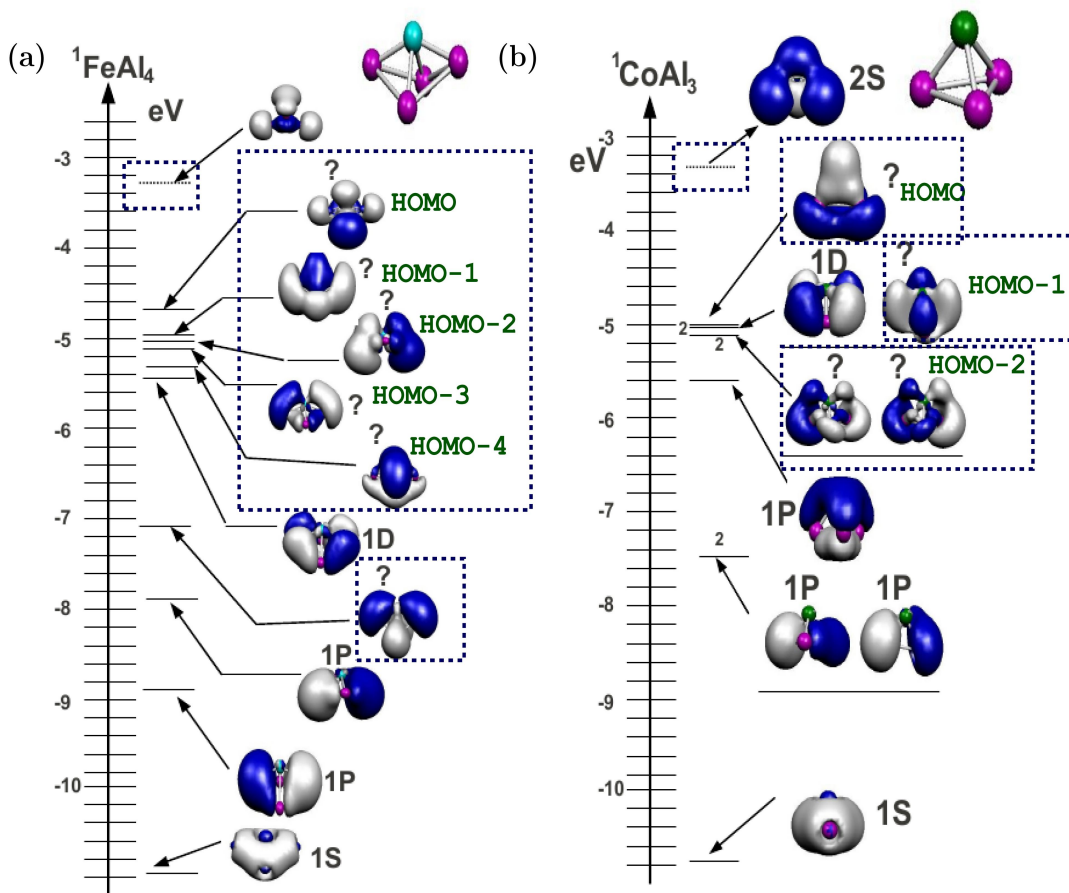


Figure 6.11: MO energy level diagrams and isosurface plots for (a) ${}^1\text{FeAl}_4$ and (b) ${}^1\text{CoAl}_3$.

whether the stability of FeAl_4 and CoAl_3 is due to filled electronic shells within the spherical shell models. If shell model is the underlying mechanism of their stability, electronic configurations of FeAl_4 and CoAl_3 should come out as $1\text{S}^21\text{P}^61\text{D}^{10}2\text{S}^2$ and

$1S^21P^61D^{10}$ respectively. We check this by examining their MO plots in Figure 6.11.

Evidently, most of the MO's in the $FeAl_4$ and $CoAl_3$ clusters cannot be identified with shell orbitals. For example, HOMO and HOMO-1 in $FeAl_4$ do not show correspondence with any shell orbitals of definite angular momentum character. Similar is the case with third orbital above the 1S orbital. In $CoAl_3$, the HOMO, one of the HOMO-1, and HOMO-2 orbitals do not bear any resemblance to shell orbitals. Therefore we conclude that the stability of these clusters cannot be explained in terms of shell filling within shell models.

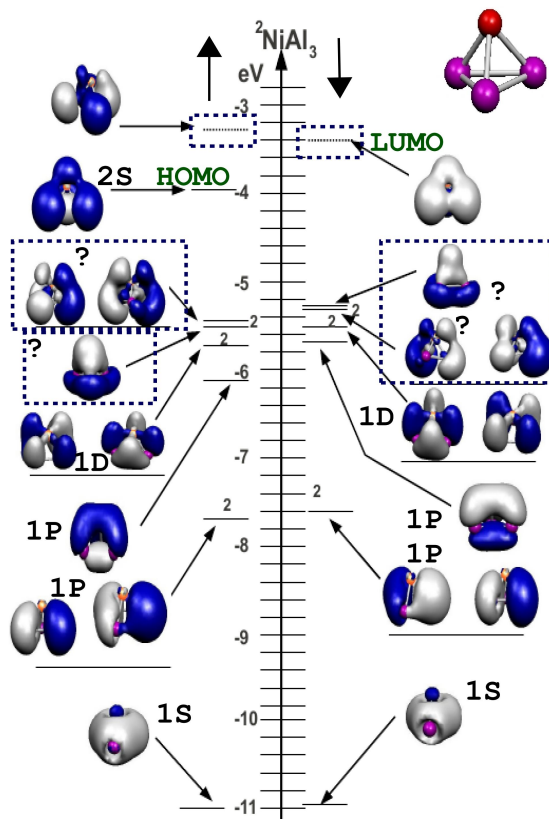


Figure 6.12: MO energy level diagrams and isosurface plots of 2NiAl_3 .

Coming to the question of smaller value of ΔE_{spin} for $CoAl_3$ in $TMAI_3$ series, let us have a close look at the MO plot of $NiAl_3$ in Figure 6.12. $NiAl_3$ is a doublet in its ground state structure. The next higher spin isomer of $NiAl_3$ is a quartet. Within frozen orbital approximation, energy required to excite an electron from the HOMO in the β channel to the LUMO in the α channel is 2.10 eV. On the other hand, energy required to obtain the triplet state of $CoAl_3$ is equal to its HL gap, i.e., 1.64 eV within frozen orbital approximation. As discussed in previous chapters,

these values will change after doing self consistent calculations of the spin excited states of the clusters, but NiAl_3 still has a larger ΔE_{spin} .

6.5.2 Applicability of shell models at larger sizes

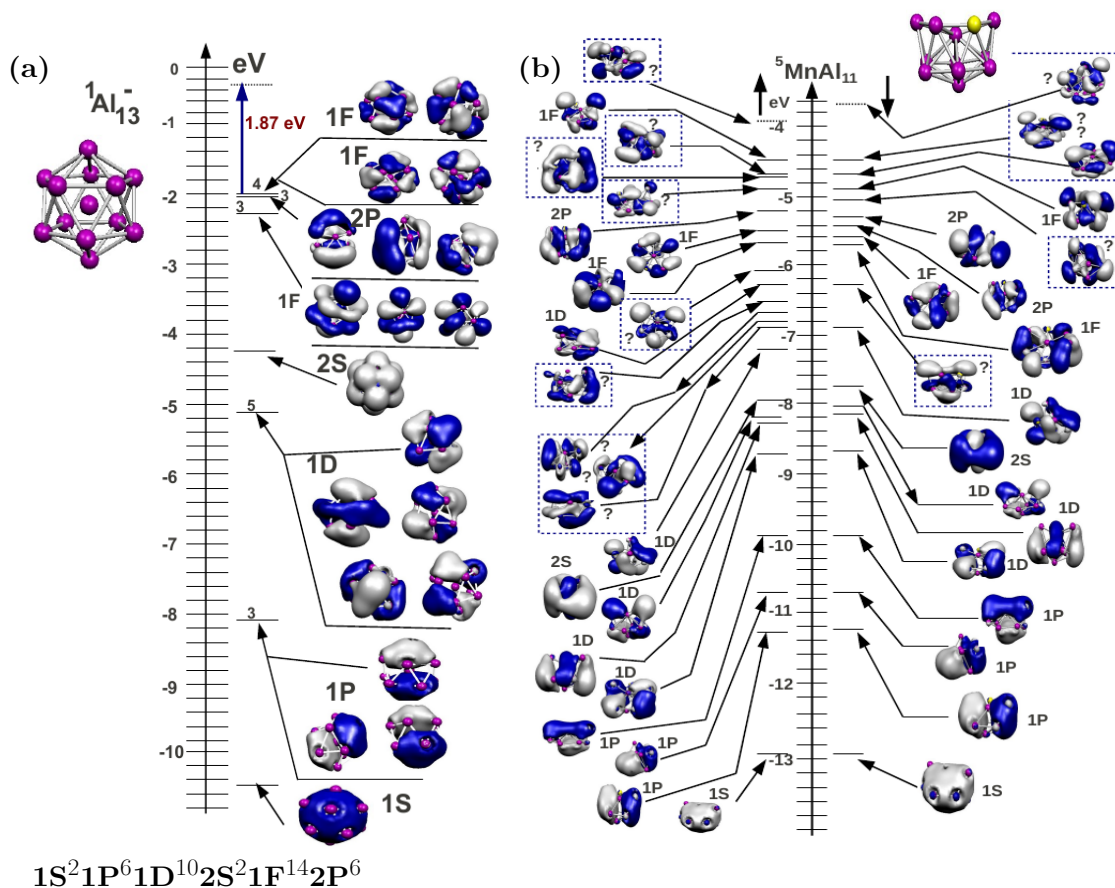


Figure 6.13: MO energy level diagrams and isosurface plots of (a) ${}^1\text{Al}_{13}^-$ and (b) ${}^5\text{MnAl}_{11}$.

It is well known that spherical shell models very nicely explain the electronic properties of the Al_{13} , Al_{13}^- and Al_{14} clusters [8]. For example, Al_{13}^- behaves as an inert gas atom and has a filled shell $1S^2 1P^6 1D^{10} 2S^2 1F^{14} 2P^6$ configuration as shown in Figure 6.13(a). This raises the question whether TMAI_N clusters at larger sizes follow shell models. If shell model emerges at large sizes then we may expect enhanced stability of MnAl_{11} as it has 40 electrons. However, this is not the case as indicated by the HL gap and Δ_n^2 (Figure 6.3). MnAl_{11} is found to be a quintet in its ground state. To illustrate the point more clearly, MO plot of MnAl_{11} is given in Figure 6.13(b). Though deep lying orbitals can be identified with 1S, 1P, 1D and 2S orbitals, frontier

orbitals do not bear any resemblance to shell orbitals. Clearly, even at larger sizes electronic structure of the TMAI_N clusters cannot be described by the spherical shell models unlike pure Al, TM-alkali and TM-alkaline earth clusters.

6.5.3 *s-p* hybridization

In section 1.5, we have given a brief summary of the early studies of pure Al clusters. Many studies reported the absence of features of shell models at smaller sizes in the Al clusters. The underlying reason was claimed to be a lack of *s-p* hybridization. Now we ask whether the absence of shell picture in the TMAI_N clusters is related to a lack of the *s-p* hybridization. We have analyzed the MO's of the TMAI_3 and TMAI_4 clusters. Table 6.7 shows the contributions of TM elements and *sp* atomic orbitals of Al atoms to the frontier MO's of the TMAI_3 clusters. Almost all the frontier orbitals

Cluster	HOMO					LUMO				
	TM(%)	TM _d (%)	Al(%)	Al _s (%)	Al _p (%)	TM(%)	TM _d (%)	Al(%)	Al _s (%)	Al _p (%)
⁴ CrAl ₃	22	85	78	9	89	34	80	66	14	84
³ MnAl ₃	43	94	57	15	80	30	33	70	43	54
² FeAl ₃	49	98	51	20	77	66	98	34	10	90
¹ CoAl ₃	35	71	65	44	51	43	63	57	40	58
² NiAl ₃	31	71	69	39	58	35	69	65	41	57

Table 6.7: Contribution of the TM and Al atomic orbitals to the frontier orbitals in the TMAI_3 clusters. Also contributions of the *d* orbitals of the TM atoms and *sp* atomic orbitals of Al atoms are given.

have contributions from Al *sp* and TM *d* orbitals. For example, the HOMO of CoAl_3 consists of 35% Co and 65% Al orbitals. Out of the Co contribution, 71% comes from the Co *d* orbitals. Of the Al contribution, 44% is *s* and 51% is *p*. Similarly, the HOMO in FeAl_4 has 63% contribution from Fe and 37% contribution from the Al *s* and *p* orbitals. Out of the Al contribution, 39% is *s* and 56% is *p* as shown in Table 6.8. Thus *s-p* hybridization is present in small TMAI clusters just as in pure

Cluster	HOMO					LUMO				
	TM(%)	TM _d (%)	Al(%)	Al _s (%)	Al _p (%)	TM(%)	TM _d (%)	Al(%)	Al _s (%)	Al _p (%)
³ CrAl ₄	41	88	59	22	77	22	85	78	10	89
⁶ MnAl ₄	28	45	72	46	54	50	92	50	19	77
¹ FeAl ₄	63	62	37	39	56	42	75	58	38	59
² CoAl ₄	76	70	59	24	74	40	82	60	24	74
³ NiAl ₄	59	81	77	41	58	35	70	65	40	59

Table 6.8: Contribution of the TM and Al atomic orbitals to the frontier orbitals in the TMAI_4 clusters. Also contributions of the *d* orbitals of the TM atoms and *sp* atomic orbitals of Al atoms are given.

Al clusters. With these results we conclude that overlap of these *sp* hybrids with the TM *d* orbitals gives rise to bonding between the Al_N unit and the TM elements.

6.6 Origin of stability: Aromaticity

So far we have demonstrated the enhanced stability of FeAl_4 and CoAl_3 , and have also argued that this cannot be explained in terms of shell models. We will now try to understand the origin of FeAl_4 and CoAl_3 . In section 1.9, we reported a summary of recent works on Al based binary clusters in which stability was explained in terms of aromaticity. Therefore we ask whether aromaticity plays a role in the stability of FeAl_4 and CoAl_3 also. Originally, the concept of aromaticity was introduced in the context of planar molecules. Now this idea has been extended to include non-planar molecules and clusters. The most widely used measure of aromaticity is the nucleus

TM	TMA ₃		TMA ₄	
	M	NICS(ppm)	M	NICS(ppm)
Cr	4	-17.77	3	-41.11
Mn	3	-10.23	6	-29.66
Fe	2	-41.80	1	-99.36
Co	1	-126.28	2	-12.88
Ni	2	-65.36	3	-22.03

Table 6.9: Multiplicity ($M=2S+1$) and NICS values for TMA₃ and TMA₄ clusters.

independent chemical shift (NICS). Since it is a position dependent quantity, for planar molecules or clusters this quantity is usually calculated at the center of the plane (NICS(0)) or at a certain distance (typically 1 or 2 Å) away from the center of the plane (NICS(1) or NICS(2)). On the other hand, aromaticity for non-planar clusters has been calculated at the unweighted geometric center of structures [172]. Following the same procedure, we have calculated NICS values¹ for some of the FeAl_N and CoAl_N clusters. NICS values at the center of TMA₃ and TMA₄ clusters are given in Table 6.9. While all the values turn out to be negative, CoAl_3 and FeAl_4 turn out to have the most negative values that indicate their aromatic character. NICS values for FeAl_N and CoAl_N clusters are given in Table 6.10. Again, FeAl_4 has a large negative NICS. FeAl_5 has a positive NICS indicating its anti-aromatic character. Among the CoAl_N clusters studied, only CoAl_3 and CoAl_4 have negative

¹We have calculated NICS values using Gaussian03 code. We have used same basis sets and exchange-correlation functional which are taken for structure optimization and self-consistent electronic structure calculations in deMon2k.

Cluster	M	NICS(ppm)	Cluster	M	NICS(ppm)
FeAl ₃	2	-41.8	CoAl ₂	2	36.37
FeAl ₄	1	-99.36	CoAl ₃	1	-126.28
FeAl ₅	2	9.06	CoAl ₄	2	-12.88
FeAl ₆	5	-65.19	CoAl ₅	1	31.54
FeAl ₇	2	-51.11	CoAl ₆	4	-36.62

Table 6.10: Multiplicity ($M=2S+1$) and NICS values for FeAl_N and CoAl_N clusters.

NICS values. CoAl₂ and CoAl₅ have positive NICS indicating that these clusters are anti-aromatic. Thus we conclude that FeAl₄ and CoAl₃ are the most aromatic clusters in the size range studied here.

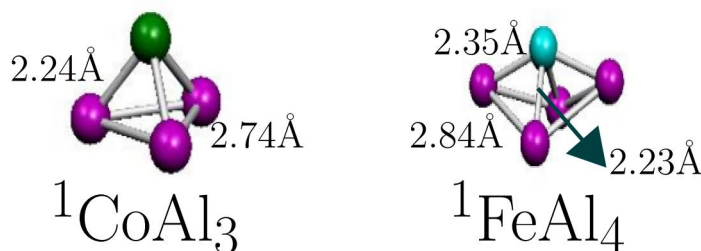


Figure 6.14: Bond lengths in Å of the CoAl₃ and FeAl₄ clusters.

One of the characteristics of aromatic clusters is that they tend to have equal bond lengths [17]. We found that bond lengths are equalized in the FeAl₄ and CoAl₃ clusters. In FeAl₄, all of the Al-Al bond lengths are 2.84 Å as shown in Figure 6.14. Two of the Fe-Al bond lengths are 2.35 Å (to two Al atoms on opposite sides), and the other two are 2.23 Å. In CoAl₃, while the Co-Al bond lengths are all 2.24 Å, all of the Al-Al bond lengths are 2.74 Å. The reactivity measure of aromaticity includes chemical hardness. We have already shown that FeAl₄ and CoAl₃ have the largest chemical hardness.

6.6.1 Conclusions

We have presented a detailed study of TM-doped Al clusters. The stable clusters are identified within the CrAl_N, MnAl_N, FeAl_N series. We do find stable clusters (MnAl₆, MnAl₉, and FeAl₉) with large spin moments among these series. However, we have not identified these as suitable candidates for magnetic superatoms because Mn and Fe are not encapsulated by Al cages. We have also studied CoAl_N, NiAl_N, TMAI₃ and TMAI₄ clusters. FeAl₄ and CoAl₃ are the most stable clusters

as indicated by their large HL gap, $\Delta_2(N)$, and η . The most important result of these studies is that electronic structure of these clusters cannot be described by the shell models. Even at large sizes, electronic structures of the TM-Al clusters do not follow shell models. FeAl_4 and CoAl_3 possess enhanced stability originating from aromaticity. This shows up in NICS values and large chemical hardness.

V doped silver clusters

7.1 Introduction

Studies of V doped Ag clusters are motivated by the photo-fragmentation experiments performed on VAg_N clusters by Janssens *et al* [20]. VAg_N clusters were first produced by a dual-laser vaporization source. In the photo-fragmentation experiments, intense laser light was used to irradiate and highly excite the produced neutral clusters. This resulted in ionization and fragmentation of the clusters. Resulting mass abundance spectrum of the cation clusters showed peaks at VAg_5^+ , VAg_7^+ , and VAg_{14}^+ . Sharp drops in the intensity of mass-spectrum are observed just after these sizes. In order to explain the relative abundance of VAg_7^+ and VAg_{14}^+ , Janssens *et al* proposed that V has valence of 2 and 5 in these clusters. Then VAg_7^+ and VAg_{14}^+ respectively will have 8 and 18 valence electrons. These are magic numbers at which closing of the electronic shells occur within spherical shell models. However, there is no theoretical justification of Janssens *et al*'s proposal from first-principles calculations. Furthermore, origin of the greater stability of VAg_5^+ is not clear. Hence we have performed first-principles calculations for $\text{VAg}_N^{+/0}$ ($N=3-10$) in order to understand the microscopic mechanism which accounts the stability of VAg_5^+ and VAg_7^+ .

7.2 Computational details

Previously described formalism of first-principles electronic structure calculations is adopted for the study of V doped Ag clusters. For the Ag atom, a quasi-relativistic effective core potential (ECP) (with 19 electrons in the core) and basis set combination from Stuttgart-Dresden (QECP19|SD) distributed with deMon2K is used. This

produces the first and second ionization potentials of 8.05 eV and 21.54 eV for a Ag atom, which are in good agreement with experimental values of 7.57 eV and 21.47 eV respectively [164].

7.3 Ground State structures

Figure 7.1 shows the evolution of ground state structures of the VAg_N^+ and VAg_N ($N=3-10$) clusters. From $N=3$ to 5, Ag atoms form a planar framework in both series of clusters. VAg_6^+ has a pentagonal bi-pyramid structure with the V atom occupying an apex position. VAg_6 has a slightly different structure. One Ag atom is removed

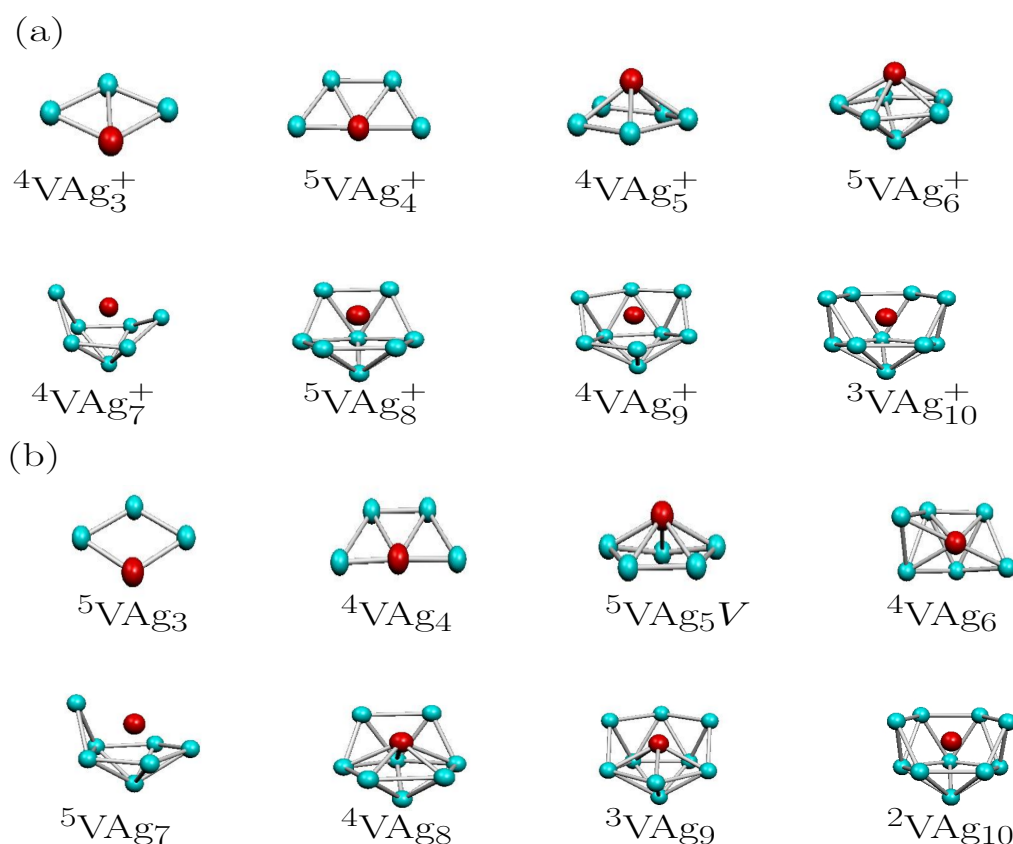


Figure 7.1: Ground state structures and spin multiplicities of (a) VAg_N^+ and (b) VAg_N clusters.

from pentagonal frame of Ag_5 and attached to a triangular face comprised of V and two Ag atoms. Structures of VAg_8^+ , VAg_9^+ , and VAg_{10}^+ are obtained by capping the Ag atom at triangular faces of VAg_6^+ motif. In the ground state structure of

VAg_7^+ , the V atom is above at the center of square frame of Ag atoms. Two out of remaining three Ag atoms are attached to the edges of the Ag_4 unit while the last one is attached to the square face. Ground state structures of the VAg_8 , VAg_9 and VAg_{10} clusters are similar to corresponding cation clusters. A few high energy isomers in both the series are given in the Appendix[E.1,E.2].

7.4 Relative stabilities

Experiments performed by Janssens *et al* revealed the enhanced stability of VAg_5^+ and VAg_7^+ . Therefore it will be interesting to see their energetic stability via various stability descriptors. In this regard, we have first calculated the HL gap and $\Delta_2(N)$. Figure 7.2 shows the HL gap and $\Delta_2(N)$ of both neutral and cationic series. VAg_5^+

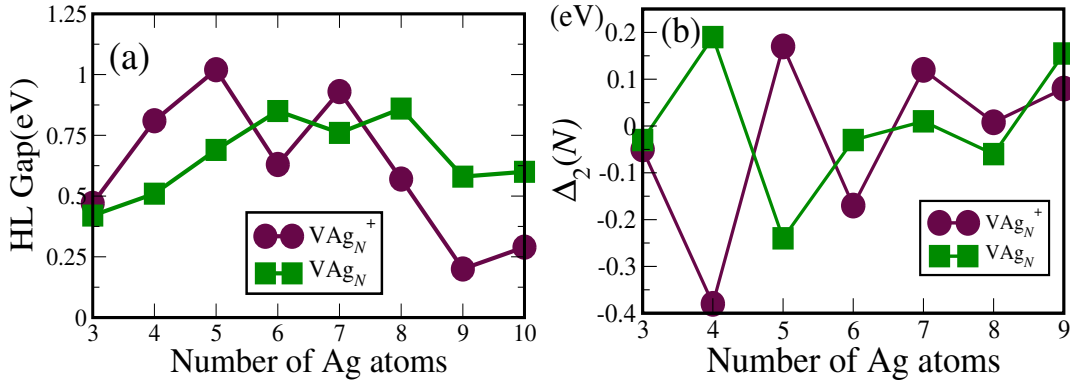


Figure 7.2: (a) The HL gap and (b) $\Delta_2(N)$ of $\text{VAg}_N^{+/0}$ clusters.

and VAg_7^+ are found to have the two largest HL gaps within the size range studied here. Also $\Delta_2(N)$ shows maxima at $N=5$ and 7 in the cation series as shown in Figure 7.2(b). Therefore VAg_5^+ and VAg_7^+ have enhanced chemical and thermodynamic stability relative to their neighbors. For VAg_N clusters, small peaks occur at $N=6$ and 8 in the HL gap, while accompanying peaks are not observed in $\Delta_2(N)$. Interestingly, VAg_4 shows a clear indication of its thermodynamic stability, though it has a HL gap of only 0.51 eV, smaller than most other neutral clusters (Table 7.1). Another stability descriptor is Ag addition energy, i.e., ΔE_{Ag} which is defined as

$$\Delta E_{\text{Ag}} = E(\text{VAg}_{N-1}^{+/0}) + E_{\text{Ag}} - E(\text{VAg}_N^{+/0}) \quad (7.1)$$

where E is the total energy of the indicated species. Figure 7.3 shows the variation of ΔE_{Ag} as a function of size for both series. As we can see VAg_5^+ and VAg_7^+ show maximum energy gain in forming the clusters from the preceding sizes and a decrease in

Cluster	HL Gap	$\Delta_2(N)$	Cluster	HL Gap	$\Delta_2(N)$
${}^4\text{VAg}_3^+$	0.47	-0.05	${}^5\text{VAg}_3$	0.42	-0.03
${}^5\text{VAg}_4^+$	0.81	-0.38	${}^4\text{VAg}_4$	0.51	0.19
${}^4\text{VAg}_5^+$	1.02	0.17	${}^5\text{VAg}_5$	0.69	-0.24
${}^5\text{VAg}_6^+$	0.63	-0.17	${}^4\text{VAg}_6$	0.85	-0.03
${}^4\text{VAg}_7^+$	0.93	0.12	${}^5\text{VAg}_7$	0.76	-0.01
${}^5\text{VAg}_8^+$	0.57	0.008	${}^4\text{VAg}_8$	0.86	-0.06
${}^4\text{VAg}_9^+$	0.20	0.07	${}^3\text{VAg}_9$	0.58	0.15
${}^3\text{VAg}_{10}^+$	0.29		${}^2\text{VAg}_{10}$	0.60	

Table 7.1: The HL gap and $\Delta_2(N)$ values of VAg_N^+ and VAg_N clusters. All the values are given in eV.

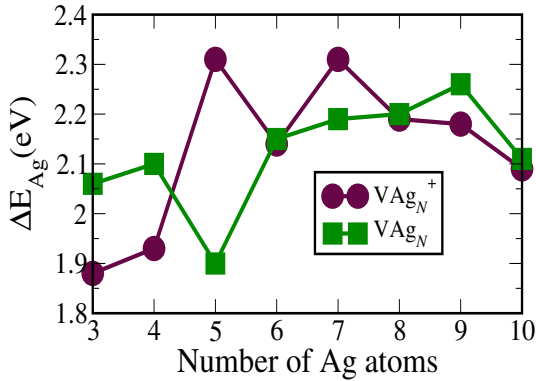


Figure 7.3: ΔE_{Ag} , i.e., Ag addition energy of $\text{VAg}_N^{+/0}$ clusters.

Cluster	ΔE_{Ag}	Cluster	ΔE_{Ag}
${}^4\text{VAg}_3^+$	1.88	${}^5\text{VAg}_3$	2.06
${}^5\text{VAg}_4^+$	1.93	${}^4\text{VAg}_4$	2.10
${}^4\text{VAg}_5^+$	2.31	${}^5\text{VAg}_5$	1.90
${}^5\text{VAg}_6^+$	2.14	${}^4\text{VAg}_6$	2.15
${}^4\text{VAg}_7^+$	2.31	${}^5\text{VAg}_7$	2.19
${}^5\text{VAg}_8^+$	2.19	${}^4\text{VAg}_8$	2.20
${}^4\text{VAg}_9^+$	2.18	${}^3\text{VAg}_9$	2.26
${}^3\text{VAg}_{10}^+$	2.10	${}^2\text{VAg}_{10}$	2.11

Table 7.2: ΔE_{Ag} values of VAg_N^+ and VAg_N clusters. All the values are given in eV.

the energy gain when going to the next size. This is consistent with the experimental observations where drops in the intensity are observed just after $N=5$ and 7 . Two local maxima in ΔE_{Ag} at $N=4$ and 9 are found for VAg_N clusters. It is important to understand the relevance of the two stability descriptors ΔE_{Ag} and $\Delta_2(N)$ to the experiments. Which of these is more relevant for describing stability depends on the experimental conditions. When clusters are produced at their evaporation temperatures and the final step leading to stabilization is evaporation of one or more atoms, $\Delta_2(N)$ will be more relevant to defining stability, for example in a seeded supersonic nozzle source. On the other hand, for cold clusters produced in a gas-aggregation cluster or laser vaporization source, where cluster growth involves single-atom addition at a time, Ag addition energy will be more relevant [1]. Since mass abundance spectrum of the VAg_N^+ clusters was obtained after fragmenting the neutral clusters (produced using a dual-laser vaporization source) by an intense laser light, their stabilities cannot be entirely governed by either $\Delta_2(N)$ or ΔE_{Ag} . However, enhanced

stability of VAg_5^+ and VAg_7^+ is captured by both $\Delta_2(N)$ and ΔE_{Ag} .

Furthermore, to obtain a qualitative idea about the relative abundance of cation clusters, one can calculate the AIP and VIP of the VAg_N clusters. If the energy of laser is equal to or higher than the IP of a neutral cluster in the photofragmentation experiments, the intensity of produced cation clusters depends upon not only on photon flux but also on the absorption cross section. However, in a simple approach we can assume that a lower IP of a neutral cluster will lead to more abundance of the corresponding cation cluster. Variations of the calculated AIP and VIP as a function of size are shown in Figure 7.4. Sharp drops in both AIP and VIP are observed from $N=4$ to 5, and 6 to 7. Lower IP values of VAg_5 and VAg_7 possibly

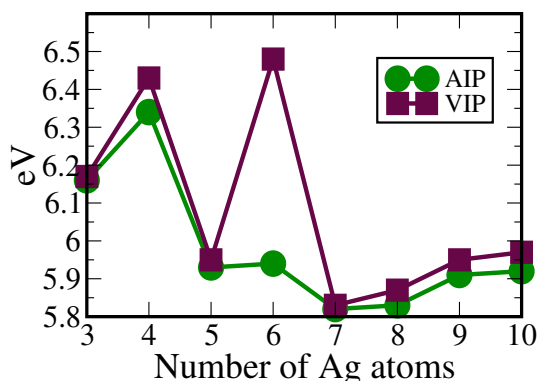


Figure 7.4: Variation of AIP and VIP of VAg_N clusters as a function of number of Ag atoms.

Cluster	AIP	VIP
$^5\text{VAg}_3$	6.16	6.17
$^4\text{VAg}_4$	6.34	6.43
$^5\text{VAg}_5$	5.93	5.95
$^4\text{VAg}_6$	5.94	6.48
$^5\text{VAg}_7$	5.82	5.83
$^4\text{VAg}_8$	5.83	5.87
$^3\text{VAg}_9$	5.91	5.95
$^2\text{VAg}_{10}$	5.91	5.97

Table 7.3: Adiabatic and vertical ionization potential of VAg_N clusters.

lead to large abundance of VAg_5^+ and VAg_7^+ . There is a large difference between the AIP and VIP of VAg_6 . This is because of the fact that the ground state structure of VAg_6^+ is substantially different from that of VAg_6 .

In the photo-fragmentation experiments, large size clusters break up into smaller sizes which are stable against further fragmentation. However, the actual fragmentation paths in these experiments are unknown. There could be various possible initial sizes and fragmentation pathways leading to VAg_5^+ and VAg_7^+ as stable clusters. Calculating such processes are difficult, but we can more easily confirm the stability of VAg_5^+ and VAg_7^+ with respect to further fragmentation. For this we have considered only two fragmentation channels of the VAg_N^+ clusters. One channel corresponds to fragmentation of VAg_N^+ into V^+ and Ag_N , and the second is fragmentation into V and Ag_N^+ . The fragmentation energy (FE) of VAg_N^+ for the two channels are given

by

$$FE^{V^+} = E(V^+) + E(Ag_N) - E(VAg_N^+) \quad (7.2)$$

Or

$$FE^V = E(V) + E(Ag_N^+) - E(VAg_N^+) \quad (7.3)$$

Figure 7.5 shows the fragmentation energy as a function of size for VAg_N^+ . If we consider the first fragmentation channel, there are jumps from $N=4$ to 5 and 6 to 7. Considering this we can rationalize the relative stability of VAg_5^+ and VAg_7^+ in the experiments. However, considering the second fragmentation channel we do not find these features.

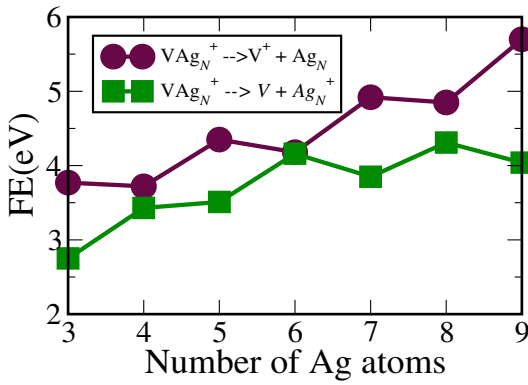


Figure 7.5: Variation of the fragmentation energy of VAg_N^+ clusters.

Cluster	FE^{V^+}	FE^V
${}^4VAg_3^+$	3.77	2.75
${}^5VAg_4^+$	3.72	3.43
${}^4VAg_5^+$	4.35	3.51
${}^5VAg_6^+$	4.18	4.16
${}^4VAg_7^+$	4.92	3.85
${}^5VAg_8^+$	4.85	4.31
${}^4VAg_9^+$	5.70	4.04

Table 7.4: Fragmentation energies of VAg_N^+ clusters. All values are given in eV.

7.5 Origin of the stability of VAg_5^+ and VAg_7^+

Having demonstrated the enhanced stability of VAg_5^+ and VAg_7^+ , we will now discuss the origin of their stability. For this, we examine the MO plots of VAg_5^+ and VAg_7^+ given in Figure 7.6. VAg_5^+ has 9 valence electrons and is a quartet in its ground state structure. VAg_5^+ comprises of the V atom capping a quasi planar frame of Ag_5 atoms in its ground state structure (Figure 7.1(a)). Because of a non-compact structure, interpretation of its electronic structure in terms of shell models become difficult. The lowest energy MOs shown in Figure 7.1(a), i.e., α_1 and β_1 are of 1S character. The orbital α_2 is approximately of d character. MO's α_3 - α_8 all look similar in character, and not all of them can be assigned 1P character. In fact, a closer inspection of these orbitals reveals that all of them have substantial contribution from V 3d orbitals.

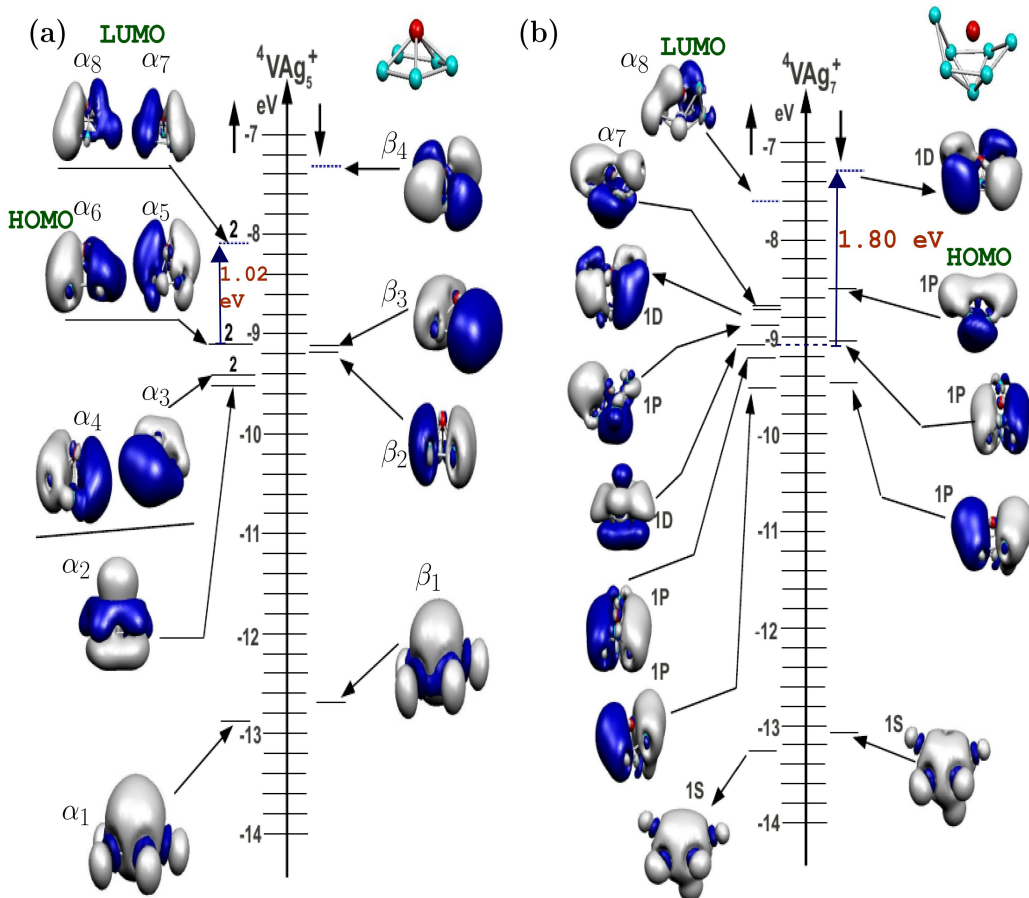


Figure 7.6: MO energy level diagrams and isosurface plot of (a) VAg_5^+ (b) VAg_7^+ clusters. Blue arrow shows exchange splitting in 1D orbitals.

α_3 - α_6 have contributions from the occupied V 3d orbitals, while α_7 and α_8 have major contributions from the unoccupied V 3d orbitals in the α channel. The large gap between the occupied and unoccupied 3d orbitals in the α channel in the bare V atom results in the large HL gap in VAg_5^+ leading to its chemical stability.

V atom has the electronic configuration $3d^34s^2$. In the α channel, three occupied atomic orbitals ($3d_{xy}$, $3d_{yz}$, and $3d_{xz}$) are degenerate in energy¹. Next set of orbitals consists of unoccupied degenerate $3d_{x^2-y^2}$ and $3d_{z^2}$ orbitals. The energy separation between occupied and unoccupied 3d orbitals is found to be 1.69 eV. In our calculations, contribution of the V atom to α_1 and β_1 MO's is only 10%, while 90% contribution is from the Ag atoms. Next two MO's in the β channel, i.e., β_2 and β_3 have $\sim 88\%$ contribution from the Ag atoms. The α_2 MO has almost 85%

¹one electron energy levels and atomic orbitals of a V atom is given in the Appendix E.3

contribution from the V $3d$ states. α_3 and α_4 MO's have $\sim 44\%$ from the V $3d$ states and 56% contribution from the Ag atoms, while the α_5 and α_6 MO's have nearly 44% from the Ag atoms and 56% contribution from the V $3d$ states. Interestingly, unoccupied α_7 and α_8 MO's are found to have significant contributions from the unoccupied $3d_{x^2-y^2}$ and $3d_{z^2}$ orbitals of V atom respectively. For example, the α_7 MO has $\sim 77\%$ contribution from V and 23% from the Ag atoms. Of the V contribution, nearly 60% comes from V $3d_{x^2-y^2}$ orbital. Similarly, V $3d_{z^2}$ orbital gives 47% of the V contribution ($\sim 70\%$) to the α_8 MO. We believe contributions from unoccupied V atom pushes the LUMO to higher energy with respect to the HOMO, leading to a HL gap of 1.02 eV. Addition of one more Ag atom to VAg_5^+ leads to a pentagonal bi-pyramid structure for VAg_6^+ as shown in Figure 7.1(a). The environment of the V atom does not change compared to VAg_5^+ , as it is still bonded to five Ag atoms in the shape of a pentagon. This leads to only minor changes in the structure of the frontier orbitals that have significant contributions from the V atom. Thus the s electron from the sixth Ag atom is accommodated in one of the degenerate orbitals (α_7, α_8) leading to a small HL gap.

Interestingly, the origin of greater stability of VAg_7^+ is found to be different. VAg_7^+ has 11 valence electrons and is a quartet in its ground state structure. Ag₇ cage attempts to enclose the V atom, leading to a more compact structure than VAg_5^+ . As a consequence, correspondence to shell picture is more clearer than VAg_5^+ as shown in Figure 7.6(b). It shows a $1S^21P^6$ closed shell configuration. We found that these shell orbitals have maximum contributions from Ag atoms. The remaining three electrons are accommodated in MO's that have major contributions from V $3d$ states. The states marked 1D have 73% and 67% contribution from the V atom, while α_7 has 35% contribution from V. LUMO (α_8) has 42% contribution from V. The LUMO in the β channel again is of 1D character and has significant contribution from V. Thus the exchange splitting (3.00 eV) in the V atom gets transferred to VAg_7^+ resulting in a large HL gap of 0.93 eV. As the Ag atoms successively are added to form large size clusters, shell model picture emerges even more evidently. For example, VAg_9^+ is found to be a quartet with a $1S^21P^61D_\alpha^41D_\beta^1$ configuration as shown in the Appendix E.4. This is the first time when 1D orbital in the β channel starts to fill.

7.6 Conclusions

$\text{VAg}_N^{+/0}$ ($N=3-10$) clusters are studied via first-principles calculations. Enhanced stability of VAg_5^+ and VAg_7^+ is shown by their large HL gap, $\Delta_2(N)$ and ΔE_{Ag} values. By examining their MO plot, we demonstrate different origin of the enhanced stability of VAg_5^+ and VAg_7^+ . Due to non-compact structure of VAg_5^+ , its enhanced stability cannot be explained in terms of shell models. We showed that the energy gap between the occupied and unoccupied $3d$ orbitals of a bare V atom leads to its greater stability. A closed shell configuration of $1S^21P^6$ is observed VAg_7^+ . However, a closed shell configuration does not account the enhanced stability of VAg_7^+ . We have shown that an effective exchange splitting in $1D$ orbitals plays a very important role in determining its enhanced stability.

Future prospects

8.1 Introduction

So far, we have studied the singly *3d*-TM doped Ca, Sr, and Al clusters, in which possibilities of new magnetic superatoms are discussed. We have explained their electronic and magnetic properties in terms of the shell models. We have also shown the potentials of magnetic superatoms to form CAM's. Furthermore, incapacibilities of shell models to explain the properties of TM doped Al and V doped Ag clusters is also shown. In this chapter, we present the possible future works which can be of great importance to enhance our understanding of these clusters.

8.2 Reactivity with Oxygen

One issue regarding the designing CAM's based on magnetic superatoms is their stability against O₂. Therefore it would be of great interest to examine the stability of magnetic superatoms when exposed to O₂. It has been shown that large HL gap, hardness as well as large spin excitation energy of a cluster also plays a decisive role in its reactivity towards oxygen. For example, pure and hydrogenated Al_{*n*}⁻ having unpaired spins or small singlet-triplet ΔE_{spin} are readily etched away by oxygen, while those having large spin excitation energies are not reactive [168]. Clusters having unpaired spins or small spin excitation energy can easily transfer electrons to the anti-bonding LUMO in the β channel of the O₂ molecule facilitating its dissociation. Clusters that were etched away easily by oxygen were also found to dissociate O₂ without a barrier in DFT calculations. In order to check the stability of magnetic superatoms (FeCa₈, CrSr₉, and MnSr₁₀), one can optimize their ground

state structures with the O_2 approaching the cluster from different orientations and directions. Since magnetic superatoms have unpaired spins, it will also be interesting to see if they also dissociate O_2 without a barrier.

While studying the reactivity of these superatoms against O_2 , one also has to take care of ‘delocalization error’ [173]. Delocalization error occurs because of non cancellation of self-interaction via exchange part of functional. It has been shown that stability of charge-transfer complex is overestimated due to delocalization error. If charge-transfer complex occurs as a transition state (TS) during a reaction between the reactants, then it leads to an underestimation of the reaction barrier [173]. However, delocalization error was shown to be minimize when one use the hybrid functionals such as hybrid B3LYP and BhandHLYP which incorporate 22% and 50% of HF exchange functional respectively. Therefore one can also study the effect of hybrid B3LYP and BhandHLYP on the reactivity of magnetic superatoms.

8.3 Magnetic superatoms at finite temperature

We have shown that $FeCa_8$, $CrSr_9$ and $MnSr_{10}$ are the clusters with greater stability and have finite magnetic moments. Also these clusters demonstrate magnetic superatom characteristics. However, these observations obtained within conventional DFT are valid at zero temperature. Therefore it would be of immense interest to explore the effect of finite temperature on structural, electronic and magnetic properties of these magnetic superatoms. This can be done via ab-initio molecular dynamics simulations.

8.4 Magnetic superatoms on substrates

We have studied assemblies, i.e., dimers of magnetic superatoms in the gas phase. However, it is desirable to have CAM’s either supported on a substrate or in a zeolite cage for practical purpose. Therefore one can study electronic and magnetic properties of magnetic superatoms supported on a substrate. While making the CAM’s, the most challenging task is to find the right substrate because of the following questions:

- (i): While depositing magnetic superatoms on substrate, superatom-substrate interactions should be such that superatoms retain their structural identity.
- (ii): Superatom-substrate interactions should be such that magnetic moments of isolated superatoms remain intact while they keep their structural identities.

(iii): When two or more superatoms deposited on the substrate, intra-cluster interaction should be such that each superatom units maintain their structural identities and magnetic moments.

8.5 Applicability of shell models

In chapter 6, one of the important conclusions is that electronic and magnetic properties of TM doped aluminium clusters cannot be explained in terms of shell models. This observation is particularly interesting because understanding of electronic and magnetic properties of TM doped Al clusters in many studies has been attempted through shell models. For example, Harms *et al* [117] studied the reduced reactivity of NbAl_4^- and VAl_6^- clusters against oxygen. They have argued that closure of electronic shells within shell models can account for their reduced reactivity.

Therefore it is natural to ask whether non-reactive behaviour of NbAl_4^- is really due to closure of an electronic shell with 20 electrons, and why VAl_6^- having 24 electrons is non-reactive. Is there any inherent role of crystal field effect which may provide a sub-shell closing as in FeCa_8 , CrSr_9 and MnSr_{10} ? Most importantly, we have explained the unusual stability of CoAl_3 and FeAl_4 in terms of their aromatic behaviour. Hence one can ask whether the enhanced stability of NbAl_4^- and VAl_6^- can be understood via aromaticity. To answer these interesting questions, one can do first-principles calculations to study the structural and electronic properties of these clusters.

APPENDIX A

TM doped calcium clusters

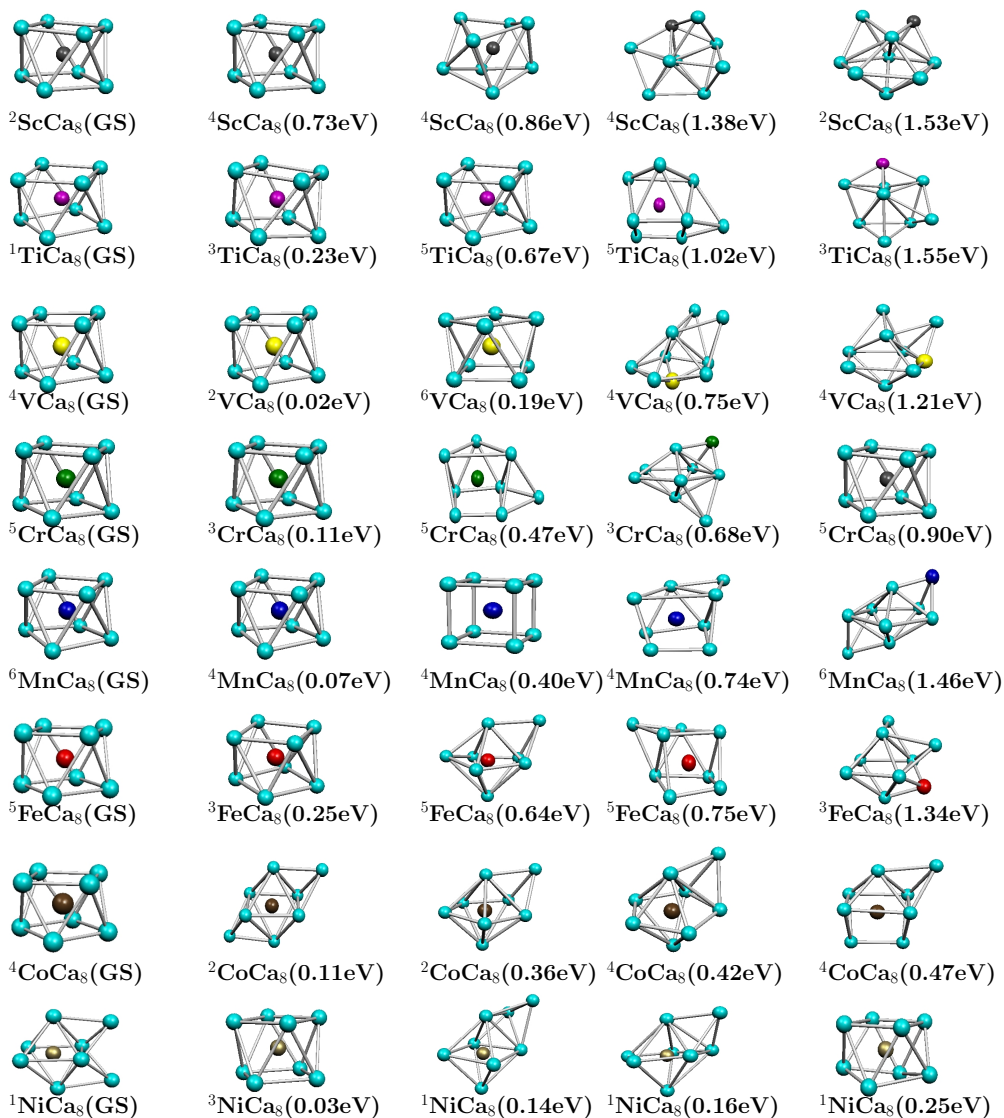


Figure A.1: Higher energy isomers of TMCa_8 clusters.

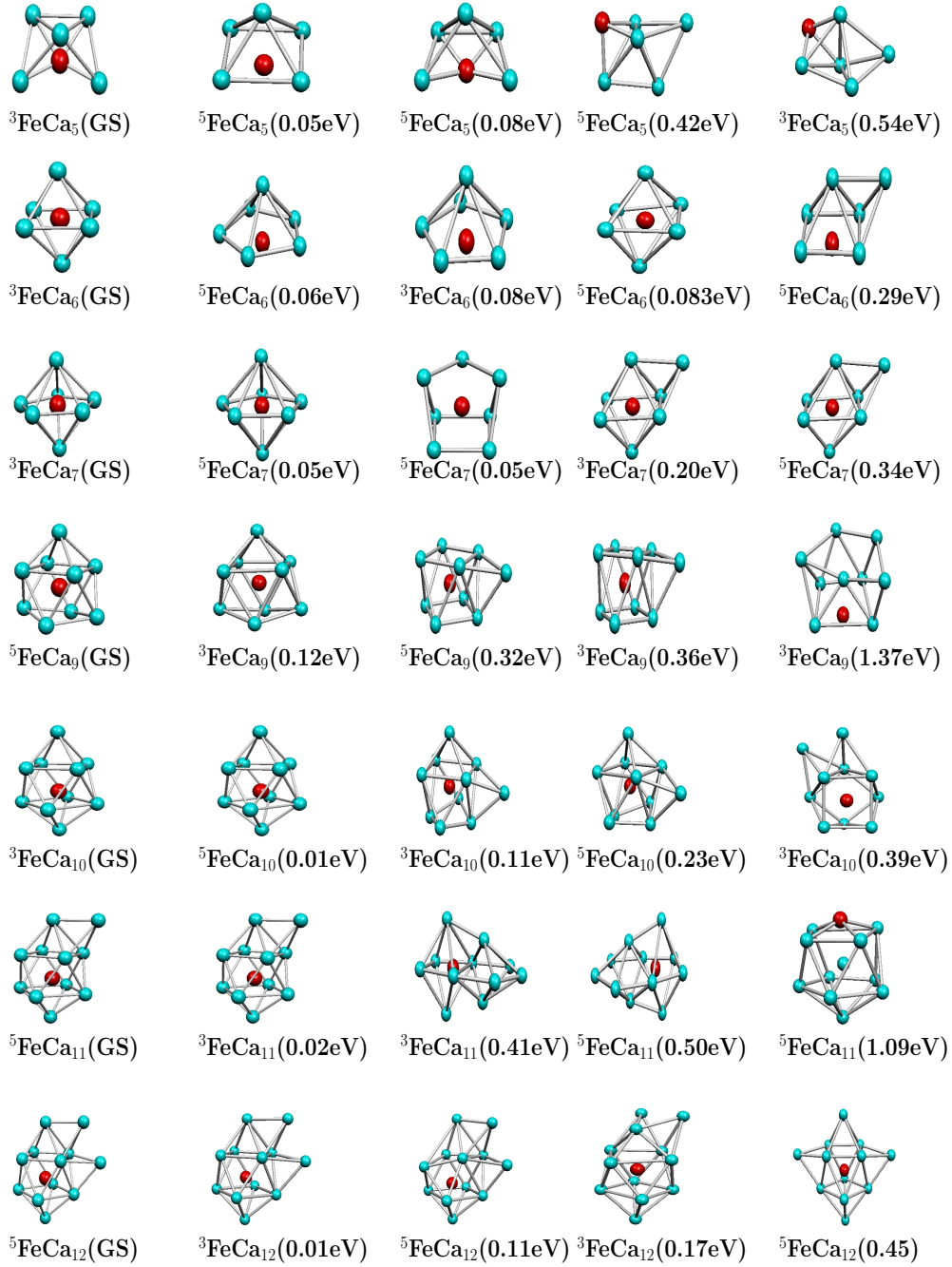


Figure A.2: Higher energy isomers of FeCa_N ($N=5-12$) clusters.

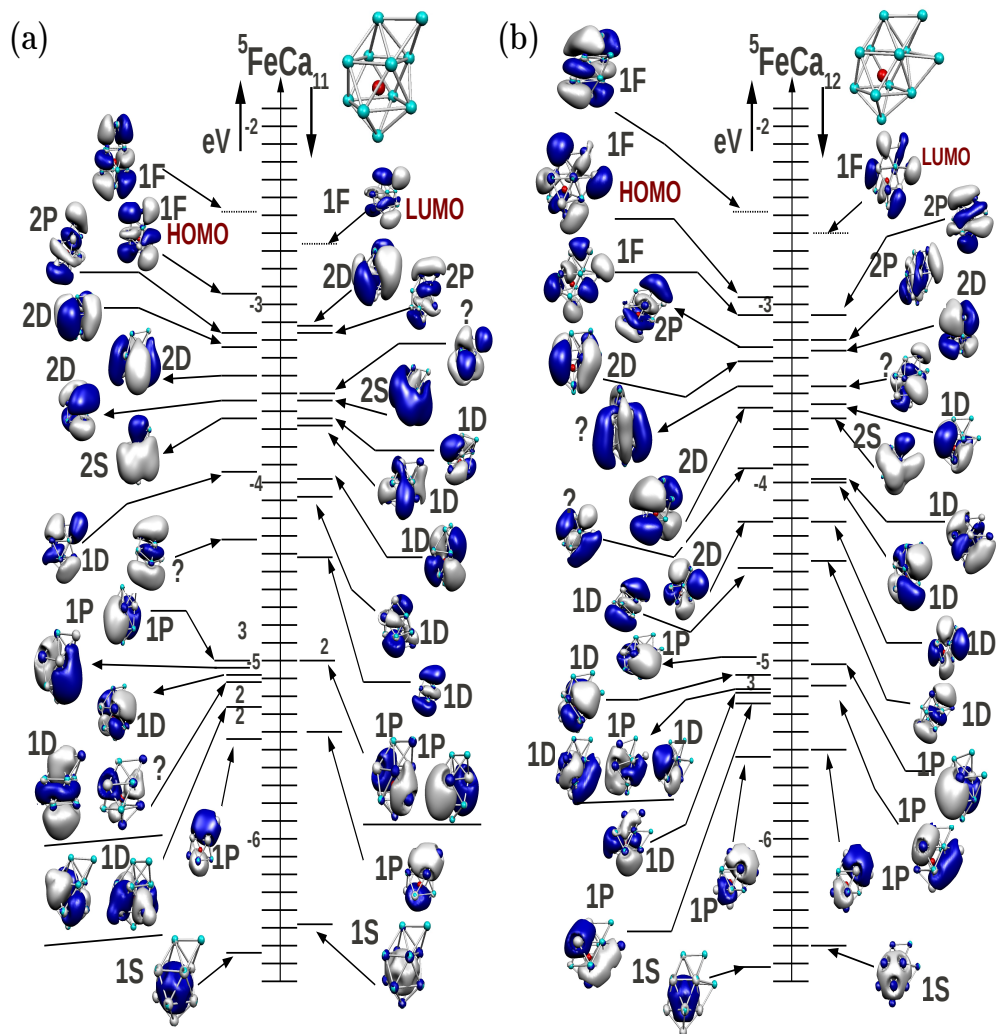


Figure A.3: MO energy level diagrams and isosurface plot of (a) ${}^5\text{FeCa}_{11}$ and (b) ${}^5\text{FeCa}_{12}$.

APPENDIX B

TM doped strontium clusters

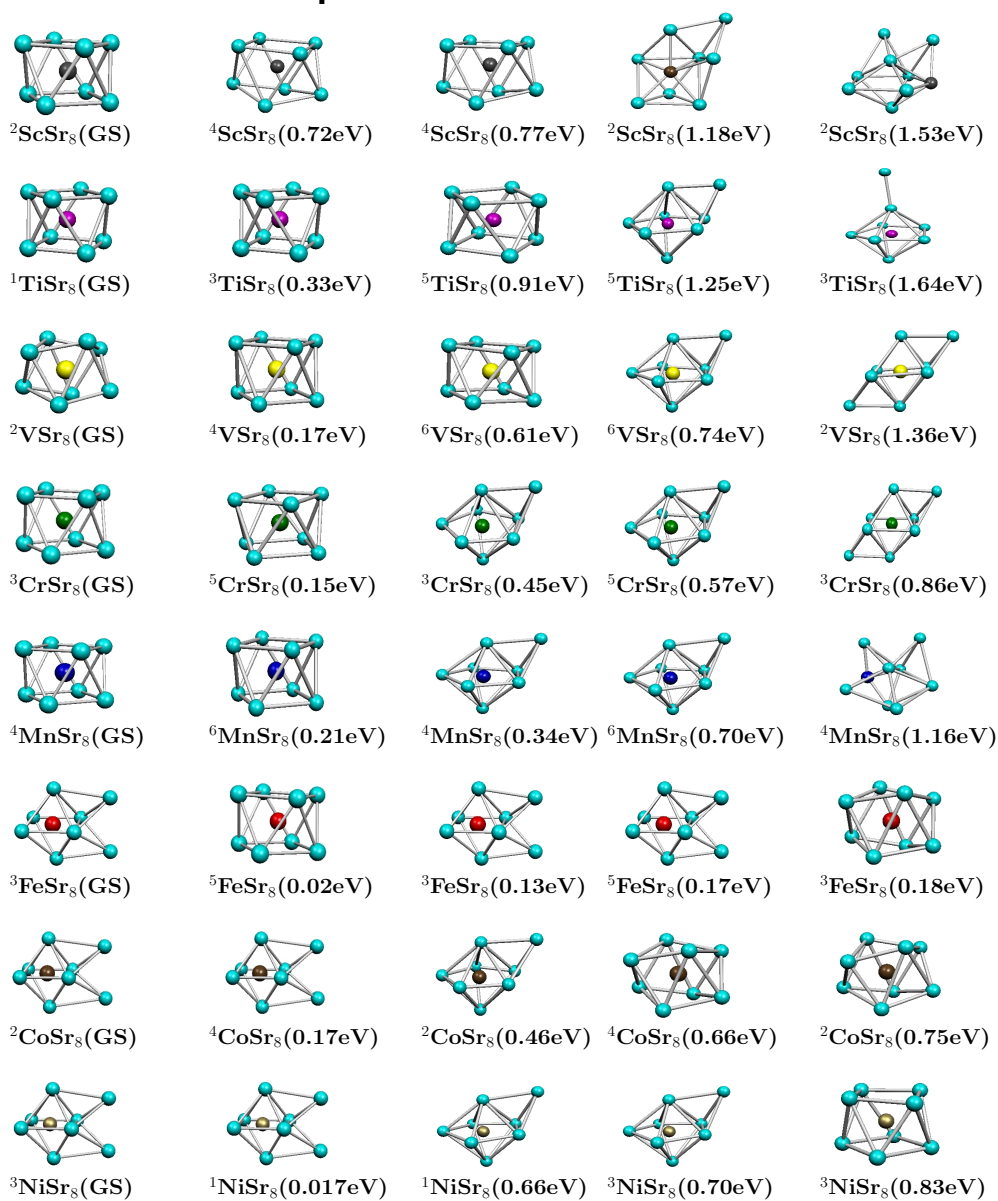


Figure B.1: Higher energy isomers of TMSr_8 clusters.

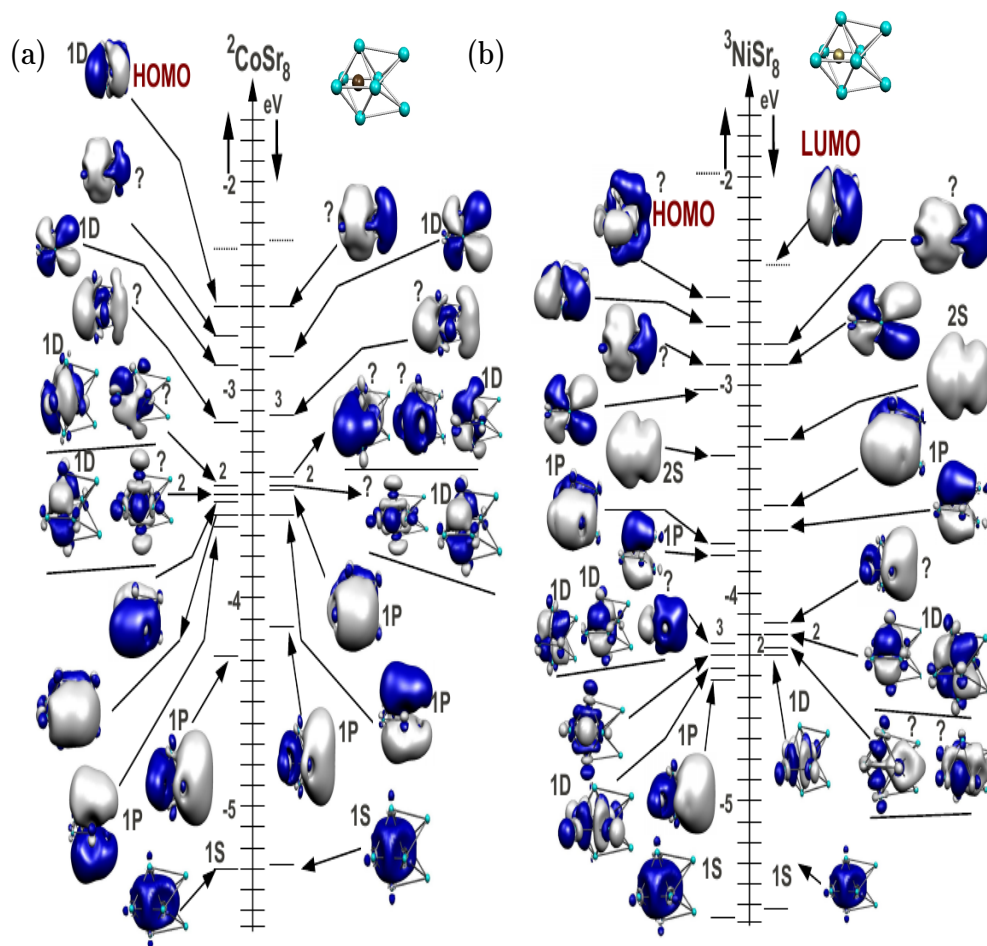


Figure B.2: MO energy level diagrams and isosurface plot of (a) ${}^2\text{CoSr}_8$ and (b) ${}^3\text{NiSr}_8$.

APPENDIX C

Cr and Mn doped strontium clusters

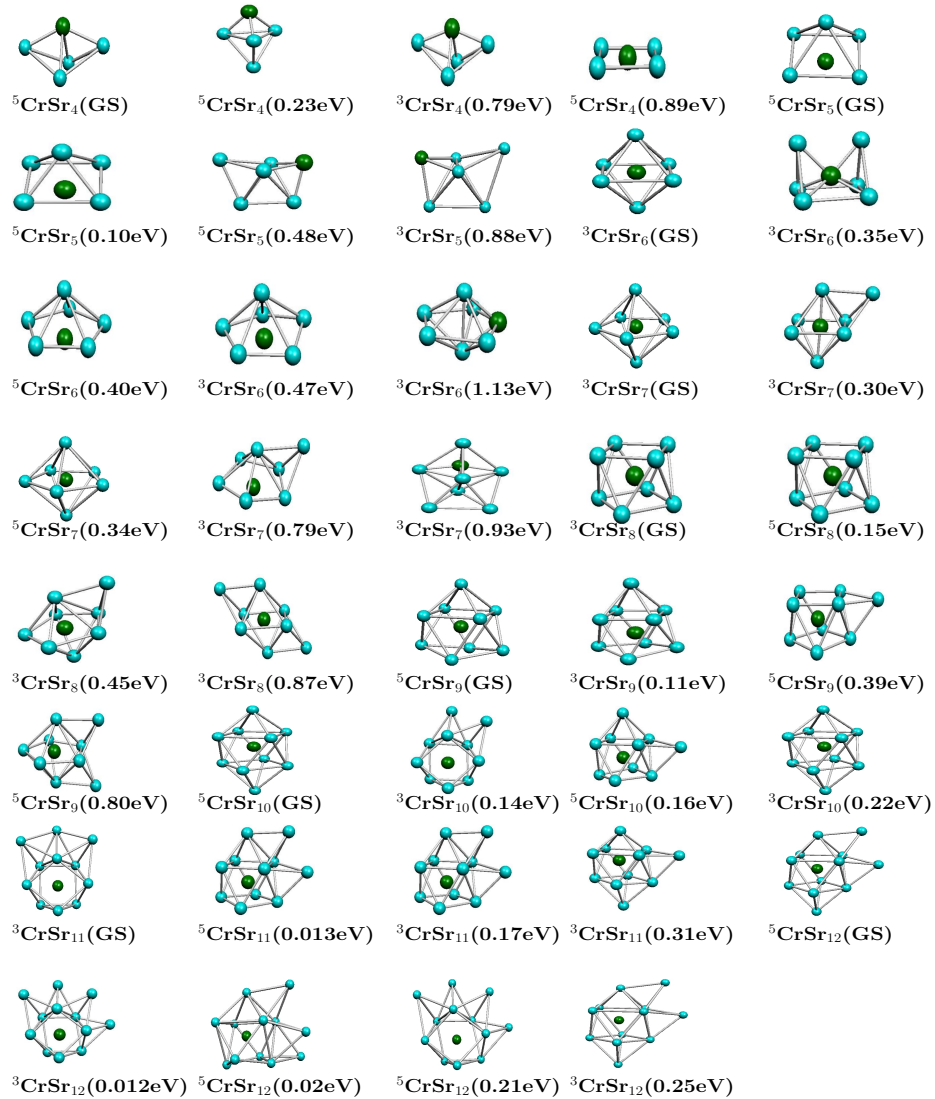


Figure C.1: Higher energy isomers of CrSr_N ($N=4-12$) clusters.

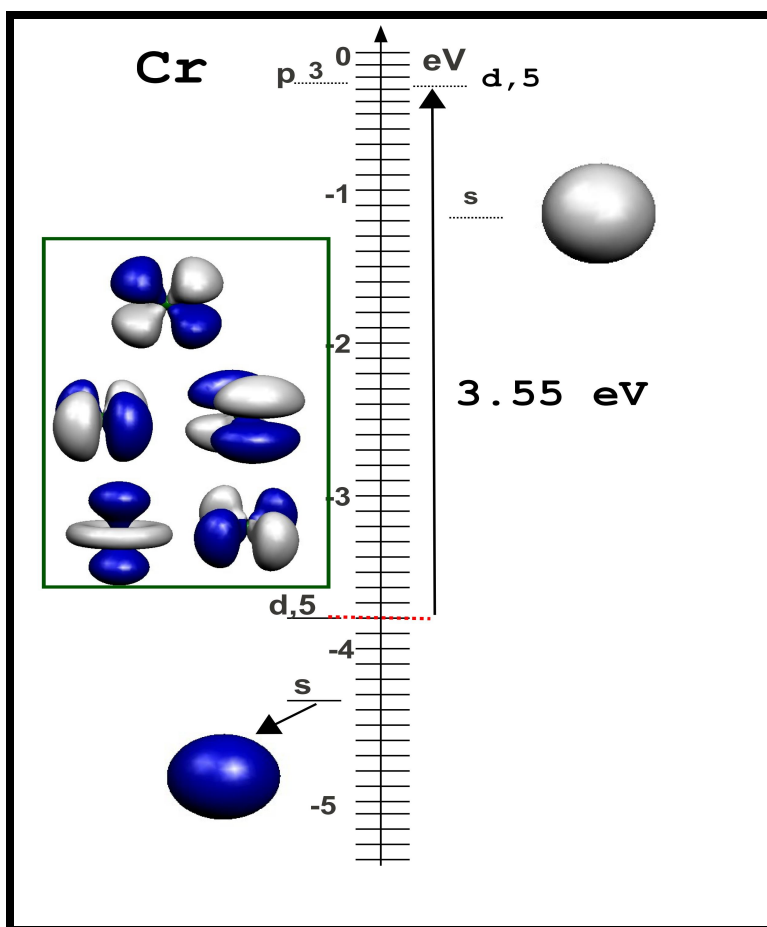


Figure C.2: One electron energy levels and atomic orbitals of Cr atom. Arrow shows the exchange splitting in 3d orbitals of Cr atom.

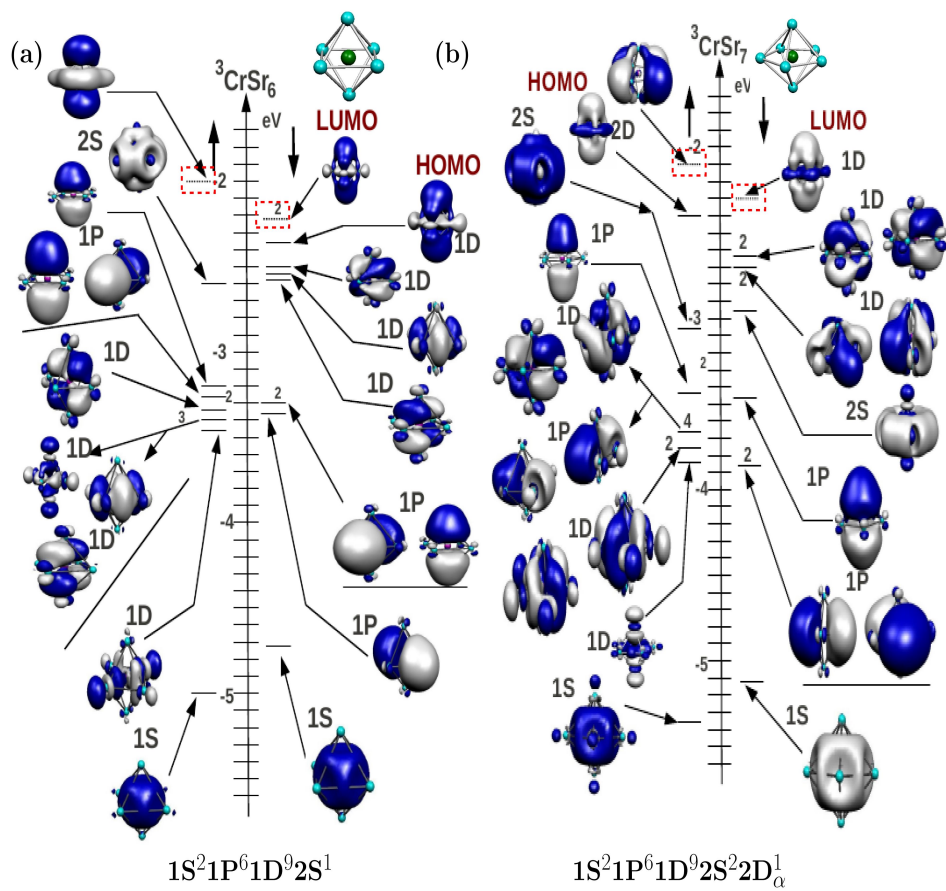


Figure C.3: MO energy level diagrams and isosurface plot of (a) ${}^3\text{CrSr}_6$ (b) ${}^3\text{CrSr}_7$.

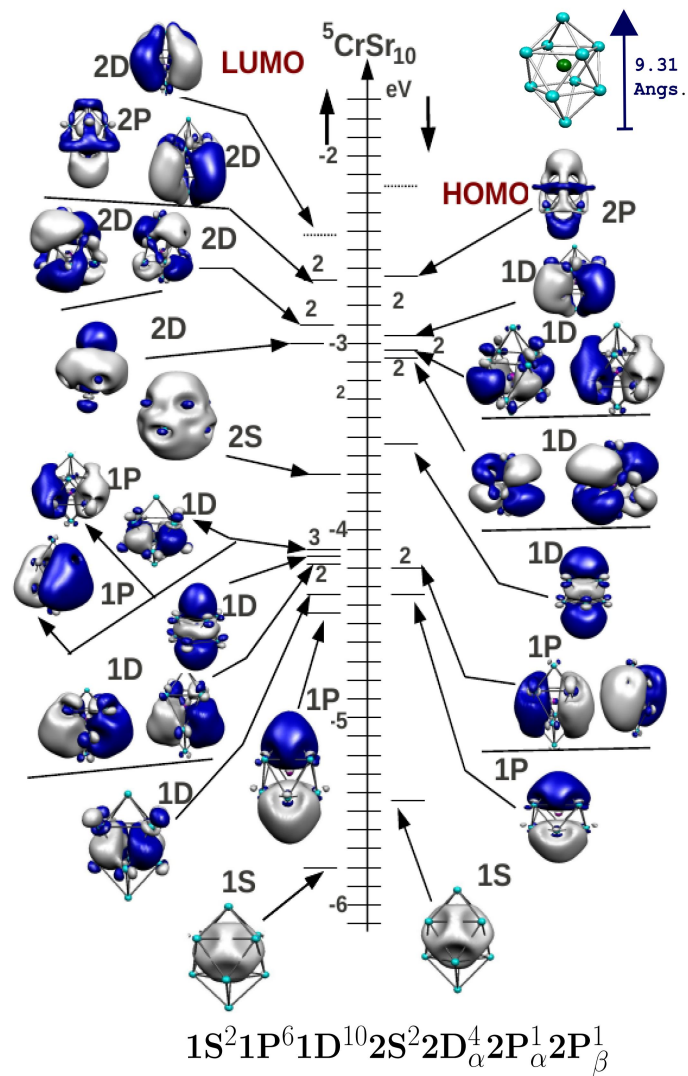


Figure C.4: MO energy level diagrams and isosurface plot of ${}^5\text{CrSr}_{10}$.

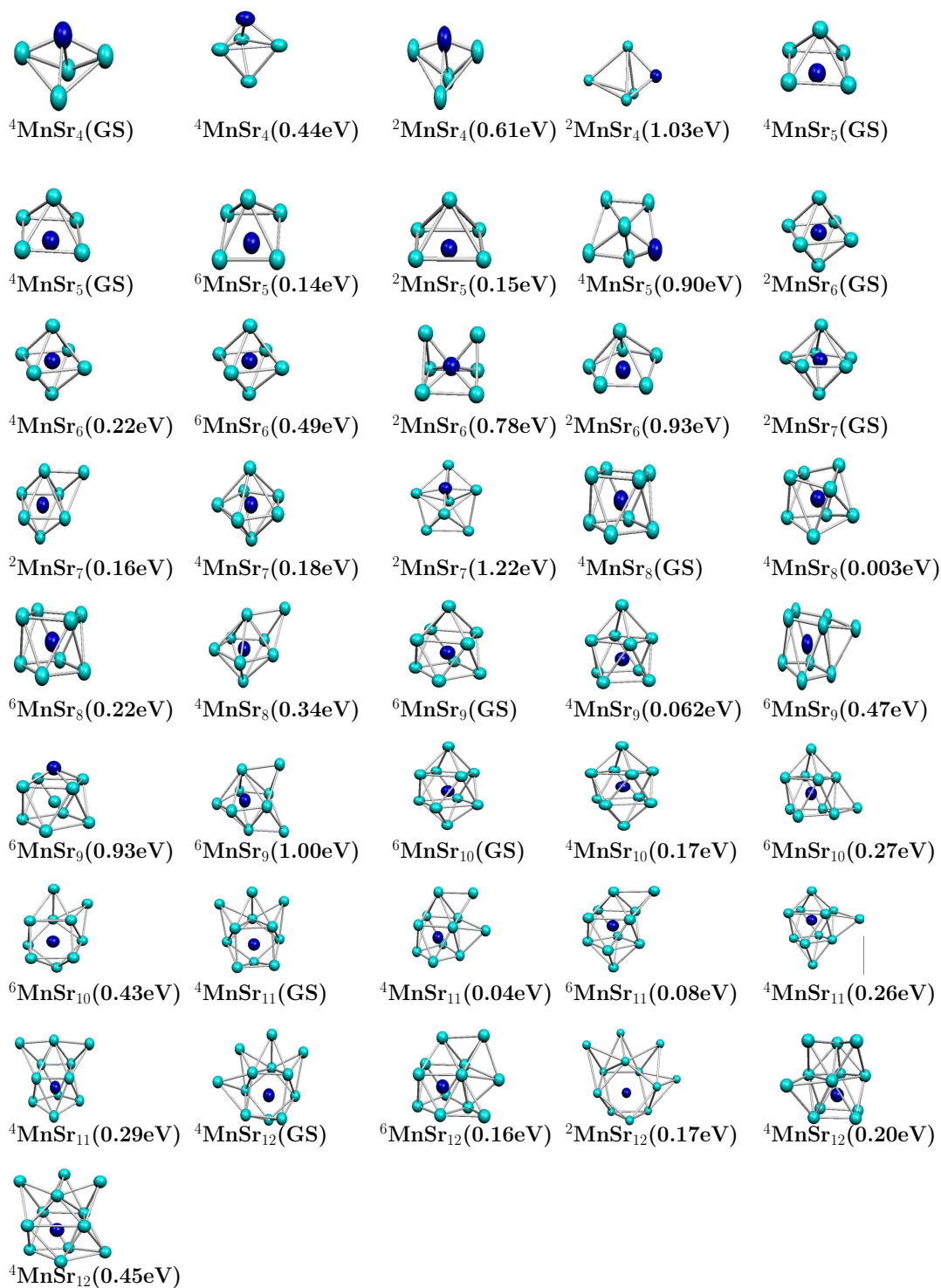


Figure C.5: Higher energy isomers of MnSr_N ($N=4-12$) clusters.

APPENDIX D

TM doped aluminium clusters

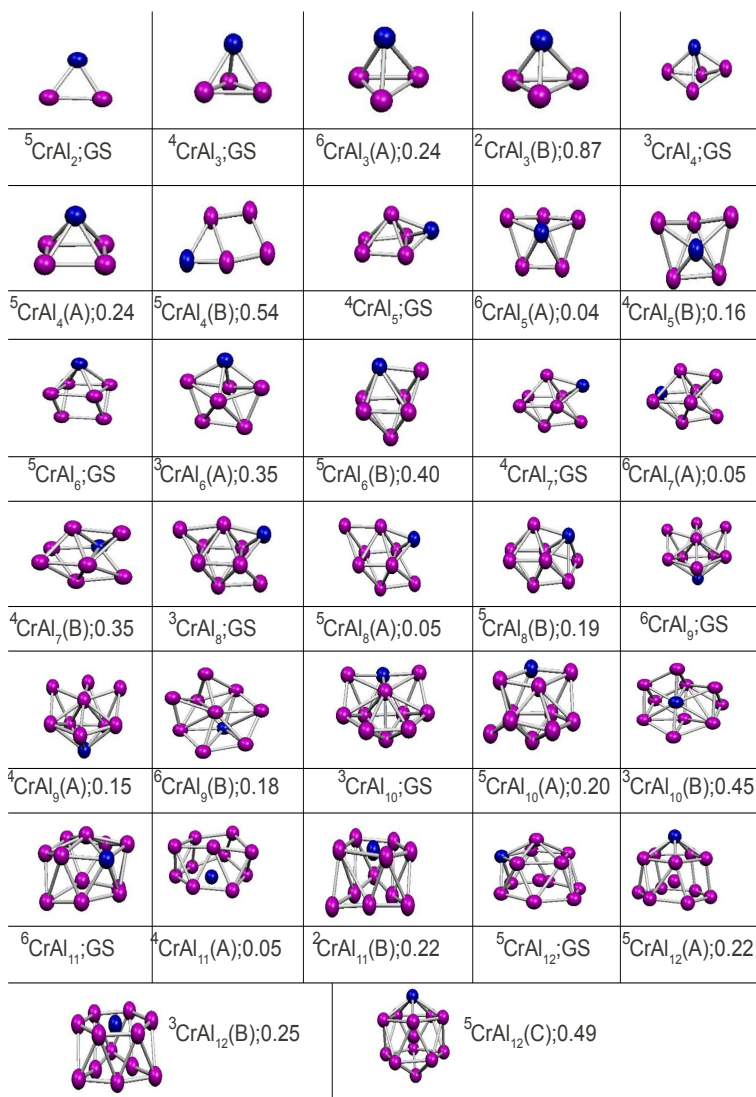


Figure D.1: Higher energy isomers of CrAl_N ($N=2=12$) clusters.

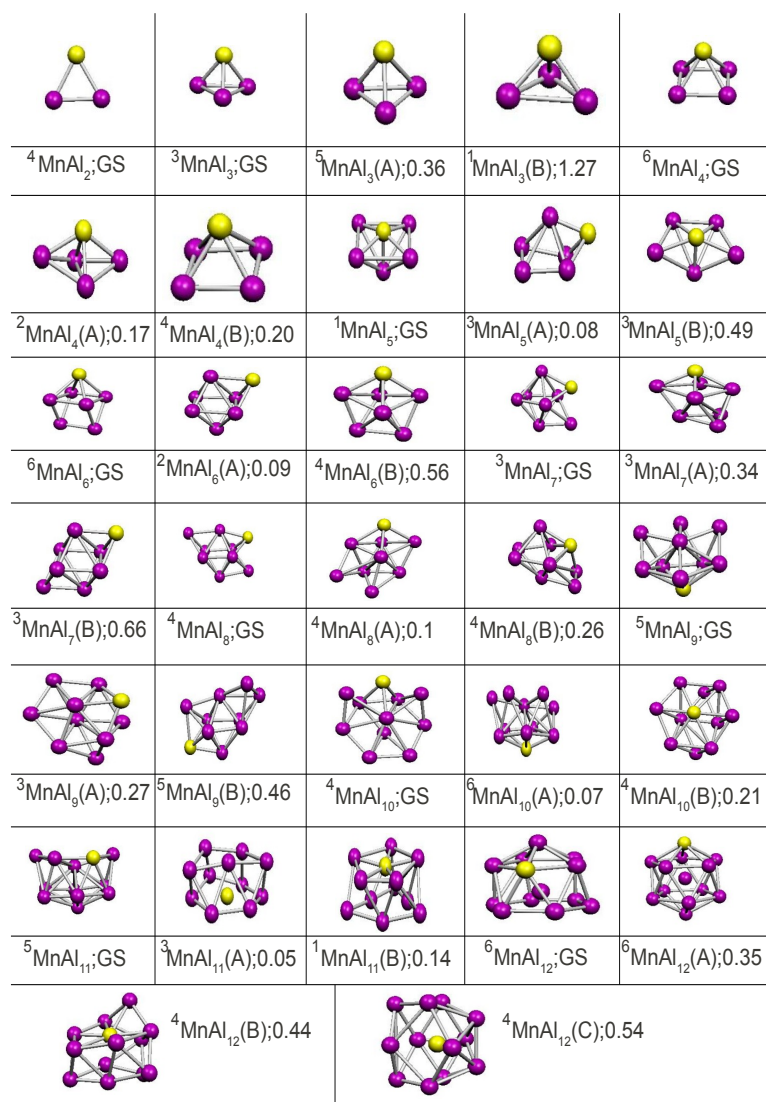


Figure D.2: Higher energy isomers of MnAl_N ($N=2=12$) clusters.

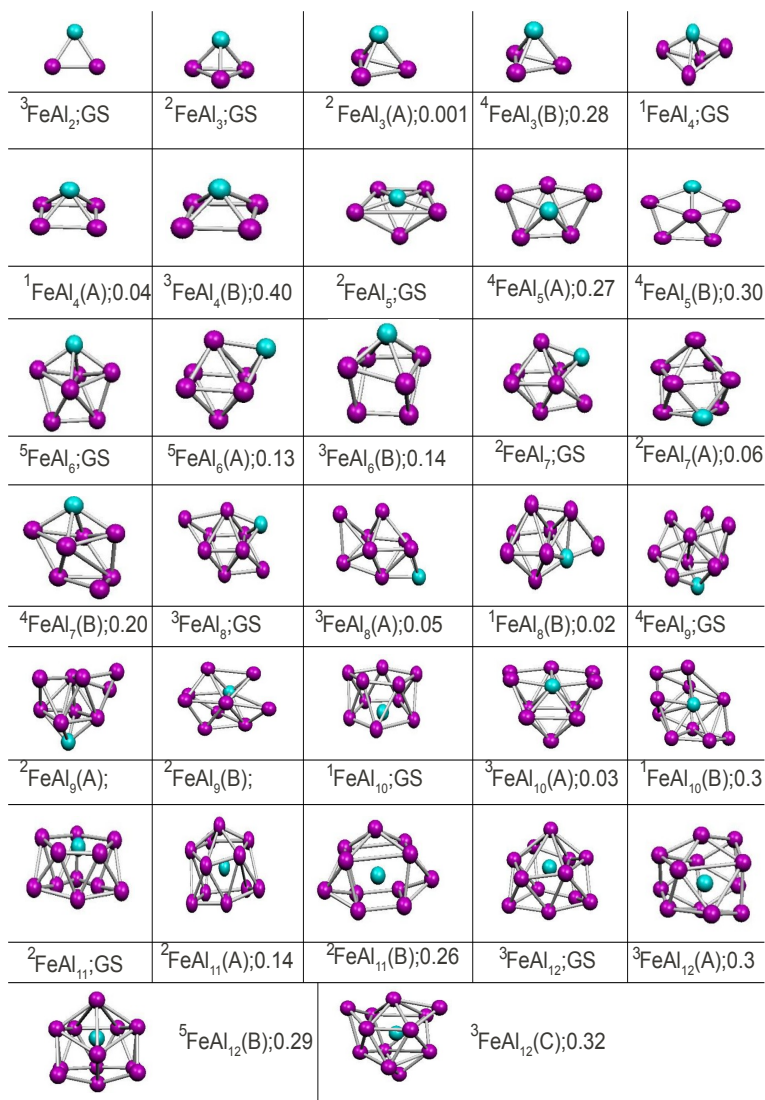


Figure D.3: Higher energy isomers of FeAl_N ($N=2=12$) clusters.



Figure D.4: Higher energy isomers of Co-, and Ni- doped Al_N clusters.

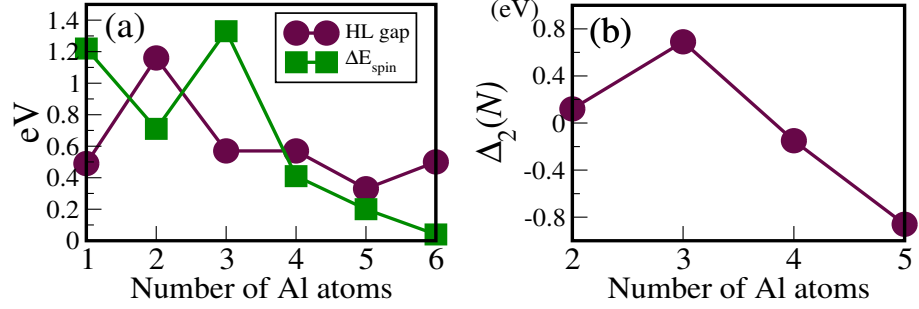


Figure D.5: (a) HL gap, ΔE_{spin} and (b) $\Delta_2(N)$ for NiAl_N clusters.

Cluster	HL Gap	ΔE_{spin}	η	$\Delta_2(N)$
${}^5\text{NiAl}$	0.49	1.22	3.31	
${}^4\text{NiAl}_2$	1.16	0.71	2.94	0.12
${}^3\text{NiAl}_3$	0.57	1.33	2.38	0.69
${}^4\text{NiAl}_4$	0.57	0.41	2.26	-0.15
${}^5\text{NiAl}_5$	0.33	0.20	2.20	-0.86
${}^4\text{NiAl}_6$	0.50	0.04	2.07	

Table D.1: HL gap, Adiabatic spin excitation (ΔE_{spin}), Hardness (η) and $\Delta_2(N)$ of NiAl_N clusters.

APPENDIX E

V doped silver clusters

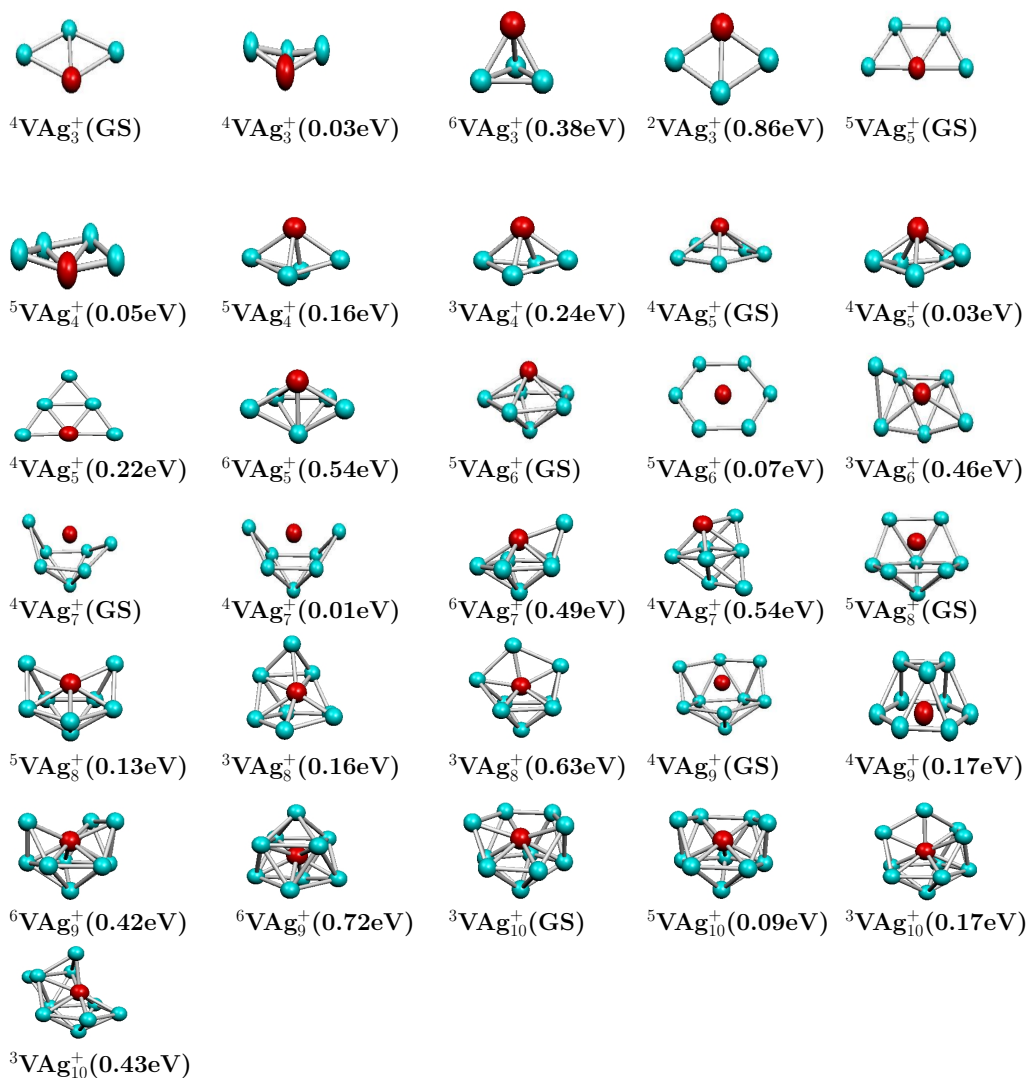


Figure E.1: Higher energy isomers of $\text{VAg}_N^+(N=3-10)$ clusters.

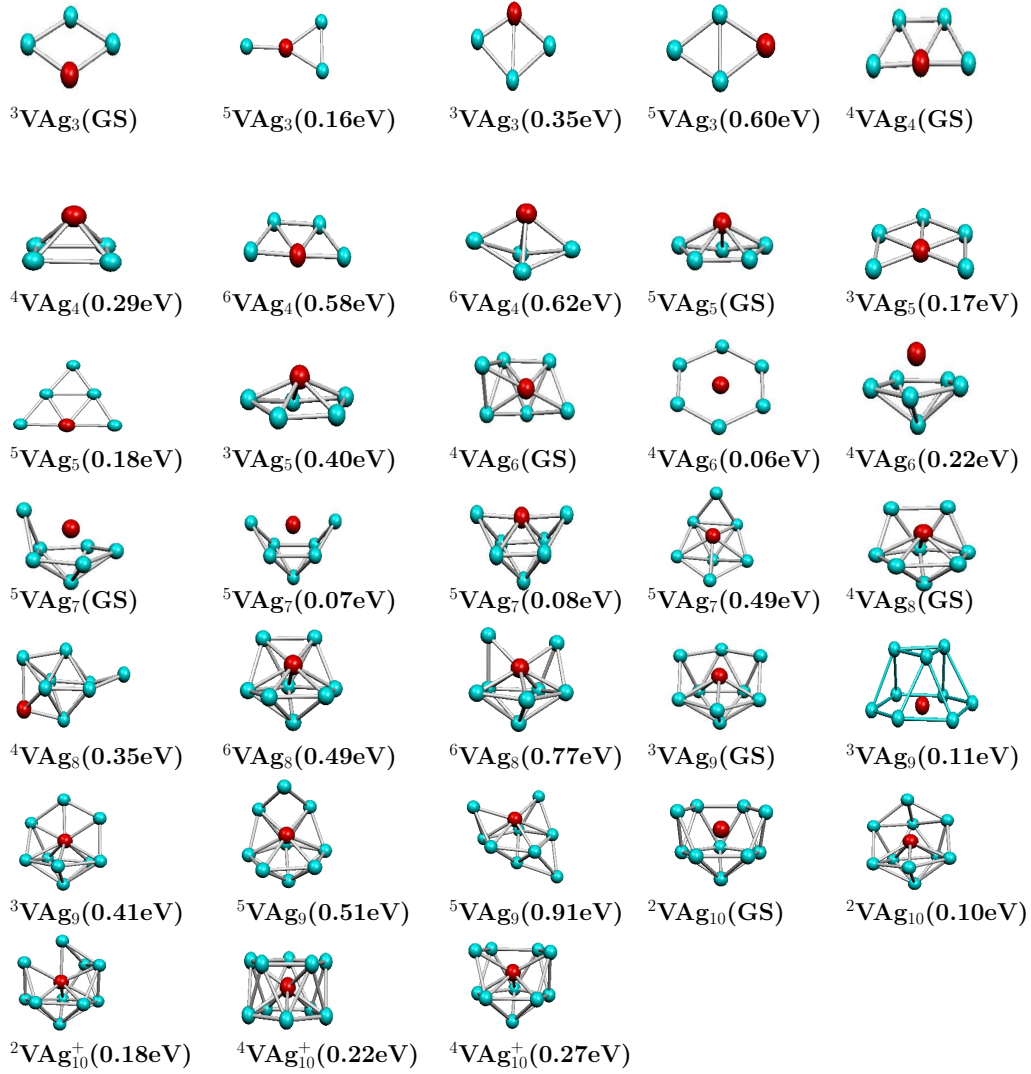


Figure E.2: Higher energy isomers of VAg_N ($N=3-10$) clusters.

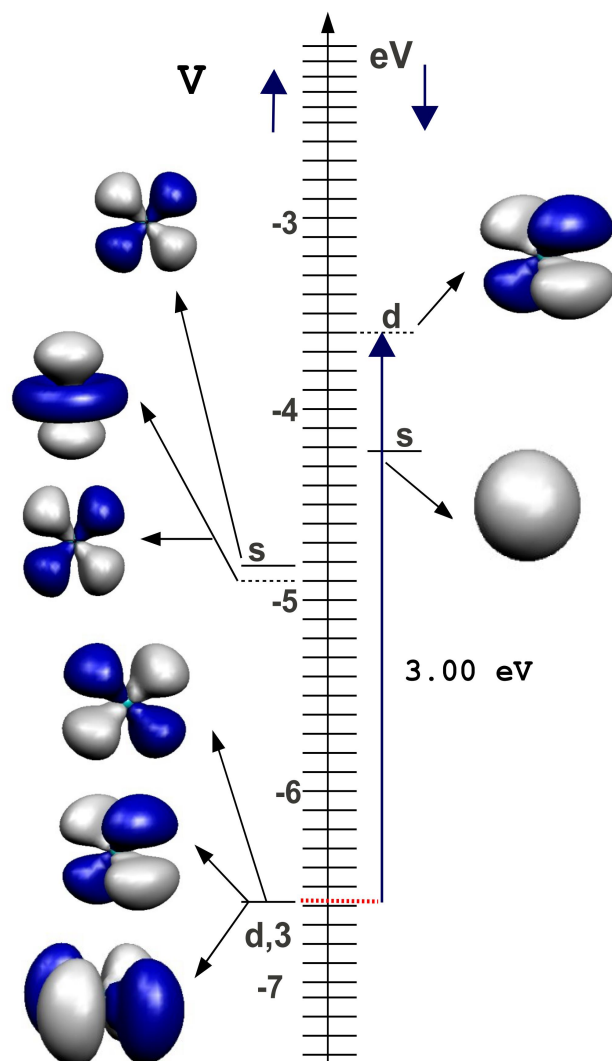


Figure E.3: One electron energy level and atomic orbital plots of V.

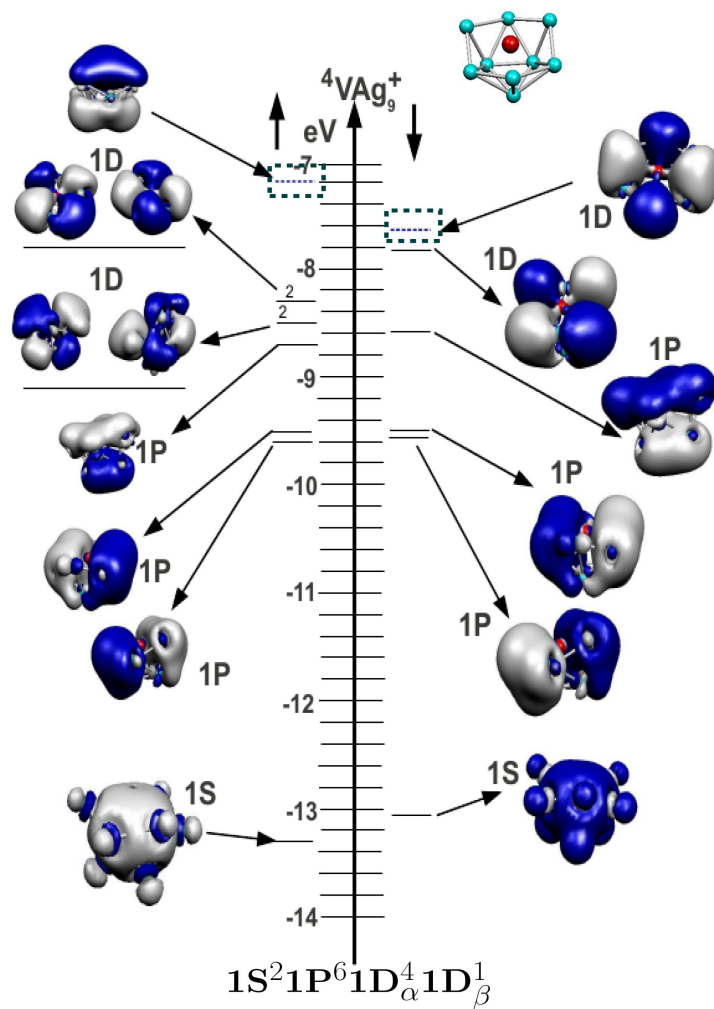


Figure E.4: MO energy level diagrams and isosurface plot of $4VAg_9^+$.

Bibliography

- [1] W. A. de Heer, *Rev. Mod. Phys.* **65**, 611 (1993).
- [2] I. A. Solov'yov, A. V. Solov'yov, and W. Greiner, *Phys. Rev. A* **65**, 053203 (2002).
- [3] A. Lyalin, I. A. Solov'yov, A. V. Solov'yov, and W. Greiner, *Phys. Rev. A* **67**, 063203 (2003).
- [4] W. D. Knight, K. Clemenger, W. A. de Heer, W. A. Saunders, M. Y. Chou, and M. L. Cohen, *Phys. Rev. Lett.* **52**, 2141 (1984).
- [5] K. Clemenger, *Phys. Rev. B* **32**, 1359 (1985).
- [6] P. Sen, Chapter 8, page 137, *Aromaticity and Metal Clusters* (Boca Raton, FL: CRC Press, Taylor and Francis), P. K. Chattaraj (ed) 2001.
- [7] R. E. Leuchtner, A. C. Harms, and A. W. Castleman, Jr., *J. Chem. Phys.* **91**, 2753 (1989).
- [8] A. W. Castleman, Jr., and S. N. Khanna, *J. Phys. Chem. C* **113**, 2664 (2009).
- [9] S. N. Khanna and P. Jena, *Phys. Rev. B* **51**, 13705 (1995).
- [10] S. N. Khanna, P. Jena, *Chem. Phys. Lett.* **219**, 479 (1994).
- [11] D. E. Bergeron, A. W. Castleman, T. Morisato, and S. N. Khanna, *Science* **304**, 84 (2004).
- [12] D. E. Bergeron, P. J. Roach, A. W. Castleman, Jr., N. O. Jones, and S. N. Khanna, *Science* **307**, 231 (2005).

- [13] J. U. Reveles, S. N. Khanna, P. J. Roach, and A. W. Castleman, Jr., Proc. Natl. Acad. Sci. U.S.A. **103**, 18405 (2006).
- [14] P. J. Roach, W. H. Woodward, A. C. Reber, S. N. Khanna, and A. W. Castleman, Jr., Phys. Rev. B **81**, 195404 (2010).
- [15] J. U. Reveles, P. A. Clayborne, A. C. Reber, S. N. Khanna, K. Pradhan, P. Sen, and M. R. Pederson, Nat. Chem. **1**, 310 (2009).
- [16] X. Li, A. E. Kuznetsov, H. -F. Zhang, A. I. Boldyrev, and L. -S. Wang, Science **291**, 859 (2001).
- [17] P. K. Chattaraj (ed) 2001 Aromaticity and Metal Clusters (Boca Raton, FL: CRC Press, Taylor and Francis).
- [18] P. v. R. Schleyer, C. Maerker, A. Dransfeld, H. Jiao, and N. J. R. van Eikema Hommes, J. Am. Chem. Soc. **118**, 6317 (1996).
- [19] J. F. Chen, C. S. Wannere, C. Corminboeuf, R. Puchta, and P. v. R. Schleyer, Chem. Rev. Washington, D. C. **105**, 3842 (2005).
- [20] E. Janssens, S. Neukermans, H. M. T. Nguyen, M. T. Nguyen, and P. Lievens, Phys. Rev. Lett. **94**, 113401 (2005).
- [21] V. Chauhan, V. M. Medel, J. U. Reveles, S. N. Khanna, and P. Sen, Chem. Phys. Lett. **528**, 39 (2012).
- [22] V. Chauhan and P. Sen, Chem. Phys. **417**, 37 (2013).
- [23] V. Chauhan, A. Singh, C. Majumder, and P. Sen, J. Phys.; Condens. Matter **26**, 015006 (2014).
- [24] V. M. Medel, A. C. Reber, V. Chauhan, P. Sen, A. M. Köster, P. Calaminici, and S. N. Khanna, J. Am. Chem. Soc. **136**, 8229 (2014).
- [25] I. Katakuse, T. Ichihara, Y. Fujita, T. Matsuo, T. Sakurai, and H. Matsuda, International Journal of Mass Spectrometry and Ion Processes **67**, 229 (1985).
- [26] M. Itoh, V. Kumar, T. Adschiri, and Y. Kawazoe, J. Phys. Chem. **131**, 174510 (2009).
- [27] C. Massobrio, A. Pasquarello, and R. Car, Chem. Phys. Lett. **238**, 215 (1995).

- [28] I. M. L. Billas, A. Châtelain, and W. A. de Heer, *Science* **265**, 1682 (1994).
- [29] L. F. Mondolfo (ed.), *Aluminum alloys : structure and properties*, (Butterworths, London, 1976).
- [30] M. Y. Chou, A. Cleland, and M. L. Cohen, *Solid State Commun.* **52**, 645 (1984).
- [31] W. Ekardt and Z. Penzar, *Phys. Rev. B* **38**, 4273 (1988).
- [32] Z. Penzar and W. Ekardt, *Z. Phys. D* **17**, 69 (1990).
- [33] W. D. Knight, W. A. de Heer, K. Clemenger, and W. A. Saunders, *Solid State Commun.* **53**, 445 (1985).
- [34] H. Göhlich, T. Lange, T. Bergmann, and T. P. Martin, *Phys. Rev. Lett.* **65**, 748 (1990).
- [35] C. Yannouleas and U. Landman, *Phys. Rev. B* **51**, 1902 (1995).
- [36] P. Dugourd, D. Rayane, P. Labastie, B. Vezin, J. Chevaleyre, and M. Broyer, *Chem. Phys. Lett.* **197**, 434 (1992).
- [37] G. Alameddin, J. Hunter, D. Cameron, and M. M. Kappes, *Chem. Phys. Lett.* **192**, 122 (1992).
- [38] M. B. Knickelbein, *Chem. Phys. Lett.* **192**, 129 (1992).
- [39] T. A. Koopmans, *Physica*, **1** 104 (1933).
- [40] J. G. Eaton, L. H. Kidder, H. W. Sarkas, K. M. McHugh, and K. H. Bowen *Photoelectron Spectroscopy of Alkali Metal Cluster Anions*.
- [41] C. L. Pettiette, S. H. Yang, M. J. Craycraft, J. Conceiaco, R. T. Laaksonen, O. Cheshnovsky, and R. E. Smalley, *J. Chem. Phys.* **88**, 5377 (1988).
- [42] G. Ganteför, M. Gaussa, K. H. Meiwes-Broer, and H. O. Lutz, *Faraday Discuss. Chem. Soc.* **86**, 197 (1988).
- [43] G. Ganteför, M. Gaussa, K. H. Meiwes-Broer, and H. O. Lutz, *Z. Phys. D* **9**, 253 (1988).
- [44] T. Diederich, T. Döppner, J. Braune, J. Tiggesbäumker, and K. -H. Meiwes-Broer, *Phys. Rev. Lett.* **86**, 4807 (2001).

- [45] O. C. Thomas, W. Zheng, S. Xu, and K. H. Bowen, Phys. Rev. Lett. **89**, 213403 (2002).
- [46] T. J. Lee, A. P. Rendell, and P. R. Taylor, J. Chem. Phys. **93**, 6636 (1990).
- [47] W. Klopper and J. Almlöf, J. Chem. Phys. **99**, 5167 (1993).
- [48] C. W. Bauschlicher, Jr. and H. Partridge, Chem. Phys. Lett. **300**, 364 (1999).
- [49] F. Reuse, S. N. Khanna, V. de Coulon, and J. Buttet, Phys. Rev. B **39**, 12911 (1989).
- [50] F. Reuse, S. N. Khanna, V. de Coulon, and J. Buttet, Phys. Rev. B **41**, 11743 (1990).
- [51] P. H. Acioli and J. Jellinek, Phys. Rev. Lett. **89**, 213402 (2002).
- [52] J. Jellinek and P. H. Acioli, J. Phys. Chem. A **106**, 10919 (2002); **107**, 1670 (2003).
- [53] V. Kumar and R. Car, Phys. Rev. B **44**, 8243 (1991).
- [54] P. Delaly, P. Ballone, and J. Buttet, Phys. Rev. B **45**, 3838 (1992).
- [55] J. Akola, K. Rytkönen, and M. Manninen, Eur. Phys. J. D **16**, 21 (2001).
- [56] L. Serra, P. -G. Reinhard, and E. Suraud, Eur. Phys. J. D **18**, 327 (2002).
- [57] A. Kohn, F. Weigend and R. Ahlrichs, Phys. Chem. Chem. Phys. **3**, 711 (2001).
- [58] A. Lyalin, I. A. Solov'yov, A. V. Solov'yov, and W. Greiner, Phys. Rev. A **67**, 063203 (2003).
- [59] T. P. Martin U. Näher, T. Bergmann, H. Göhlich, and T. Lange, Chem. Phys. Lett. **183**, 119 (1991).
- [60] T. P. Martin, Phys. Rep. **273**, 199 (1996).
- [61] E. Hearn and R. L. Johnston, J. Chem. Phys. **107**, 4674 (1997).
- [62] J. W. Mirick, C. -Hang Chien, and E. Blaisten-Barojas, Phys. Rev. A **63**, 023202, (2001).
- [63] Y. Dai and E. Blaisten-Barojas, J. Phys. Chem. A **112**, 11052 (2008).

- [64] G. Pacchioni and J. Koutecky, *Chem. Phys.* **71**, 181 (1982).
- [65] X. Dong, G. M. Wang, and E. Blaisten-Barojas, *Phys. Rev. B* **70**, 205409 (2004).
- [66] E. Blaisten-Barojas, C. -Hong Chien, M. R. Pederson, and J. W. Mirick, *Chem. Phys. Lett.* **395**, 109 (2004).
- [67] P. Dugourd, J. Chevalerey, C. Bordas, and M. Broyer, *Chem. Phys. Lett.* **193**, 539 (1992).
- [68] C. Bréchnac, P. Cahuzac, N. Kébaili, J. Leygnier, and H. Yoshida, *Phys. Rev. B* **61**, 7280 (2000).
- [69] D. Rayane, P. Melinon, B. Cabaud, A. Hoareau, B. Tribollet, and M. Broyer, *Phys. Rev. A* **39**, 6056 (1989).
- [70] G. M. Wang, E. Blaisten-Barojas, and A. E. Roitberg, *J. Chem. Phys.* **115**, 3640 (2001).
- [71] V. Kumar and Y. Kawazoe, *Phys. Rev. B* **63**, 075410 (2001).
- [72] Y. Wang, H. -Jurgen Flad, and M. Dolg, *J. Phys. Chem. A* **104**, 5558 (2004).
- [73] A. Lyalin, I. A. Solov'yov, A. V. Solov'yov, and W. Greiner, *Phys. Rev. A* **75**, 053201 (2007).
- [74] K. E. Schriver, J. L. Persson, E. C. Honea, and R. L. Whetten, *Phys. Rev. Lett.* **64**, 2539 (1990).
- [75] T. H. Upton, *Phys. Rev. Lett.* **56**, 2168 (1986).
- [76] C. E. Moore, in *Atomic Energy Levels*, Natl. Bur. Stand. (U.S.) Circ. (U.S. GPO, Washington, D.C., 1971), Vol. I
- [77] G. Ganteför and W. Eberhardt, *Chem. Phys. Lett.* **217**, 600 (1994).
- [78] C. Y. Cha, G. Ganteför, and W. Eberhardt, *J. Chem. Phys.* **100**, 995 (1994).
- [79] X. Li, H. Wu, X. -B. Wang, and L. -S. Wang, *Phys. Rev. Lett.* **81**, 1909 (1998).
- [80] B. K. Rao and P. Jena *J. Chem. Phys.* **111**, 1890 (1999).
- [81] J. Akola, H. Hfökkien and M. Manninen, *Phys. Rev. B* **58**, 3601 (1998).

- [82] J. J. Melko and A. W. Castleman, Jr., *Phys. Chem. Chem. Phys.* **15**, 3173 (2013).
- [83] C. Bartels, C. Hock, J. Huwer, R. Kuhnen, J. Schwöbel, and B. von Issendorff, *Science* **323**, 1323 (2009).
- [84] H. Bethe, in *Handbuch der Physik*, H. Geiger, K. Scheel, Eds. (Springer, Berlin, 1933), chap. **3**, pp. 475.
- [85] J. Cooper, R. N. Zare, *J. Chem. Phys.* **48**, 942 (1968).
- [86] M. Manninen, J. Mansikka-aho, S. N. Khanna, and P. Jena, *Solid State Commun.* **85**, 11 (1993).
- [87] F. Liu, M. Mostoller, T. Kaplan, S. N. Khanna, and P. Jena, *Chem. Phys. Lett.* **248**, 213 (1996).
- [88] C. Ashman, S. N. Khanna, F. Liu, P. Jena, T. Kaplan, and M. Mostoller, *Phys. Rev. B* **55**, 15868 (1997).
- [89] A. W. Castleman, Jr., S. N. Khanna, A. Sen, A. C. Reber, M. Qian, K. M. Davis, S. J. Peppernick, A. Ugrinov, and M. D. Merrit, *Nano Lett.* **7**, 2734 (2007).
- [90] A. W. Castleman, Jr., and S. N. Khanna, *J. Phys. Chem. C* **113**, 2664 (2009).
- [91] A. C. Reber, A. Ugrinov, A. Sen, M. Qian, and S. N. Khanna, *Chem. Phys. Lett.* **473**, 305 (2009).
- [92] M. Qian, A. C. Reber, A. Ugrinov, N. K. Chaki, S. Mandal, H. M. Saavedra, S. N. Khanna, A. Sen, and P. S. Weiss, *ACS Nano* **4**, 235 (2010).
- [93] S. N. Khanna and P. Jena, *Chem. Phys. Lett.* **219**, 479 (1994).
- [94] S. N. Khanna and P. Jena, *Phys. Rev. Lett.* **69**, 1664 (1992).
- [95] S. Neukermans, E. Janssens, H. Tanaka, R. E. Silverans, and P. Lievens, *Phys. Rev. Lett.* **90**, 033401 (2003).
- [96] E. Janssens, H. Tanaka, S. Neukermans, R. E. Silverans, and P. Lievens, *New J. Phys.* **5**, 46 (2003).
- [97] E. Janssens, H. Tanaka, S. Neukermans, R. E. Silverans, and P. Lievens, *Phys. Rev. B* **69**, 085402 (2004).

- [98] X. Li, B. Kiran, L. F. Cui, and L. S. Wang, Phys. Rev. Lett. **95**, 253401 (2005).
- [99] M. B. Torres, E. M. Fernández, and L. C. Balbás, Phys. Rev. B **71**, 155412 (2005).
- [100] K. Pradhan, P. Sen, J. U. Reveles, and S. N. Khanna, Phys. Rev. B **77**, 045408 (2008).
- [101] K. Pradhan, P. Sen, J. U. Reveles, and S. N. Khanna, J. Phys.: Condens. Matter **20**, 255243 (2008).
- [102] J. U. Reveles, P. Sen, K. Pradhan, D. R. Roy, and S. N. Khanna, J. Phys. Chem. C **114**, 10739 (2010).
- [103] K. Pradhan, J. U. Reveles, P. Sen, and S. N. Khanna, J. Chem. Phys. **132**, 124302 (2010).
- [104] X. Zhang, Y. Wang, H. Wang, A. Lim, G. Ganteföer, K. H. Bowen, J. U. Reveles, and S. N. Khanna J. Am. Chem. Soc. **135**, 4856 (2013).
- [105] V. M. Medel, J. U. Reveles, S. N. Khanna, V. Chauhan, P. Sen, and A. W. Castleman, Jr., Proc. Natl. Acad. Sci. U.S.A. **108**, 10062 (2011).
- [106] D. J. Henry, A. Varano, and I. Yarovsky, J. Phys. Chem. A **113**, 5832 (2009).
- [107] A. Dhavale, D. G. Kanhere, S. A. Blundell, and R. R. Zope, Phys. Rev. B **65**, 085402 (2002).
- [108] A. Datta and K. P. Swapan, J. Phys. Chem. A **108**, 9527 (2004).
- [109] V. Shah, D. G. Kanhere, C. Majumder, G. P. Das, J. Phys: Condens. Matter **9**, 2165 (1997).
- [110] V. Kumar, Phys. Rev. B **57**, 8827 (1998).
- [111] Q. L. Lu, A. F. Jalbout, Q. Q. Luo, J. G. Wan, and G. H. J. Wang, J. Chem. Phys. **128**, 224707 (2008).
- [112] S. N. Khanna, C. Ashman, B. K. Rao, and P. Jena, J. Chem. Phys. **114**, 9792 (2001).
- [113] W. -J. Zheng, O. C. Thomas, T. P. Lippa, S. -J. Xu, and K. H. Bowen, Jr., J. Chem. Phys. **124**, 144304 (2006).

- [114] O. C. Thomas, W. J. Zheng, T. P. Lippa, S. -J. Xu, S. A. Lyapustina, and K. H. Bowen, Jr., *J. Chem. Phys.* **114**, 9895 (2001).
- [115] O. C. Thomas, W. J. Zheng, and K. H. Bowen, Jr., *J. Chem. Phys.* **114**, 5514 (2001).
- [116] S. N. Khanna and P. Jena, *Phys. Rev. B* **51**, 13705 (1995).
- [117] A. C. Harms, R. E. Leuchtner, S. W. Sigsworth, and A. W. Castleman, Jr., *J. Am. Chem. Soc.* **112**, 5673 (1990).
- [118] W. J. C. Menezes and M. B. Knickelbein, *Z. Phys. D* **26**, 322 (1993).
- [119] A. Pramann A, A. Nakajima, and K. Kaya, *J. Chem. Phys.* **115**, 5404 (2001).
- [120] S. M. Lang, P. Claes, S. Neukermans, and E. Janssens, *J. Am. Soc. Mass Spectrom.* **22**, 1508 (2011).
- [121] X. G. Gong and V. Kumar, *Phys. Rev. B* **50**, 17701 (1994).
- [122] M. Wang, X. Huang, Z. Du, and Y. Li, *Chem. Phys. Lett.* **480**, 258 (2009).
- [123] A. I. Boldyrev and L. -S. Wang, *Chem. Rev.* **105**, 3716 (2005).
- [124] X. Li, A. Grubisic, S. T. Stokes, J. Cordes, G. F. Ganteför, K. H. Bowen, B. Kiran, M. Willis, P. Jena, R. Burgert, and H. Schnöckel, *Science* **315**, 356 (2007).
- [125] K. Wade, *Adv. Inorg. Chem. Radiochem*, **18**, 1 (1976).
- [126] P. Bultinck, S. Fias, M. Mandado, and R. Ponec, *Aromaticity and Metal Clusters* ed P. K. Chattaraj (Boca Raton, FL: CRC Press, Taylor and Francis) p 245 (2001).
- [127] X. Li, H. F. Zhang, L. -S. Wang, A. E. Kuznetsov, N. A. Cannon, and A. I. Boldyrev, *Angew. Chem. Int. Ed.* **40**, 1867 (2001).
- [128] C. E. Jones, Jr., P. A. Clayborne, J. U. Reveles, U. Gupta, J. J. Melko, A. W. Castleman, Jr., and S. N. Khanna, *J. Phys. Chem. A* **112**, 13316 (2008).
- [129] J. J. Melko, P. A. Clayborne, C. E. Jones, Jr., J. U. Reveles, U. Gupta, S. N. Khanna, and A. W. Castleman, Jr., *J. Phys. Chem. A* **114**, 2045 (2010).

- [130] D. Y. Zubarev, B. B. Averkiev, H. -J. Zhai, L. -S. Wang, and A. I. Boldyrev, *Phys. Chem. Chem. Phys.* **10**, 257 (2008).
- [131] P. A. Clayborne, U. Gupta, A. C. Reber, J. J. Melko, S. N. Khanna, and A. W. Castleman, Jr., *J. Chem. Phys.* **133**, 134302 (2010).
- [132] J. J. Melko, S. V. Ong, U. Gupta, J. U. Reveles, J. D. Emidio, S. N. Khanna, and A. W. Castleman, Jr., *Chem. Phys. Lett.* **500**, 196 (2010).
- [133] P. Hohenberg and W. Kohn, *Phys. Rev.* **136**, B864 (1964).
- [134] W. Kohn and L. J. Sham, *Phys. Rev.* **140**, A1133 (1965).
- [135] D. M. Cepreley and B. J. Alder, *Phys. Rev. Lett.* **45**, 566 (1980).
- [136] S. J. Vosko, L. Wilk, and M. Nusair, *Can. J. Phys.* **58**, 1200 (1980).
- [137] J. P. Perdew and A. Zunger, *Phys. Rev. B* **23**, 5048 (1981).
- [138] W. M. C. Foulkes, L. Mitas, R. J. Needs and G. Rajagopal, *Rev. Mod. Phys.* **73**, 33 (2001).
- [139] S. Baroni, S. de Gironcoli, A. D. Corso, and P. Giannozzi, *Rev. Mod. Phys.* **73**, 515 (2001).
- [140] J. P. Perdew, J. A. Chevary, S. H. Vosko, K. A. Jackson, M. R. Pederson, D. J. Singh, and C. Fiolhais, *Phys. Rev. B* **46**, 6671 (1992).
- [141] J. P. Perdew, K. Burke, M. Ernzerhof, *Phys. Rev. Lett.* **77**, 3865 (1996); *ibid.* **78**, 1396(E) (1997).
- [142] W. Kohn, *Rev. Mod. Phys.* **71**, 1253 (1999).
- [143] A. Szabo and N. S. Ostlund, *Modern Quantum chemistry*, Dover Publications, Inc. Mineola, New York.
- [144] C. J Cramer, *Essentials of Computational Chemistry, Theories and Models*, John Wiley & Sons Ltd.
- [145] B. I. Dunlap, J. W. D. Connolly, and J. R. Sabin, *J. Chem. Phys.* **71**, 4993 (1979).
- [146] J. W. Mintmire, and B. I. Dunlap, *Phys. Rev. A* **25**, 88 (1982).

- [147] José Ulises Reveles Ramírez, “Geometry Optimization in LCGTO-DFT Methods with Auxiliary Functions.” Ph. D Thesis, Chemistry Science.
- [148] P. Calaminici, V. -D. Domínguez-Soria, R. Flores-Moreno, G. U. Gamboa-Martínez, G. Geudtner, A. Goursot, D. R. Salahub, A. M. Köster, Auxiliary Density Functional Theory: From Molecules to Nanostructures, Ch-16, pp. 575, J. Leszczynski (ed.), Handbook of Computational Chemistry, Springer Science+Business Media B. V. (2012). Centre For Research and Advanced Studies of the National Politechnic Institute, Mañico D. F. (2004).
- [149] J. R. Chelikowsky, *J. Phys. D: Appl. Phys.* **33**, 33 (2000).
- [150] P. Schwerdtfeger, *Chem. Phys. Chem.* **12**, 3143 (2011).
- [151] P. J. Hay and W. R. Wadt, *J. Chem. Phys.* **82**, 270 (1985).
- [152] Y. S. Lee, W. C. Ermler, and K. S. Pitzer, *J. Chem. Phys.* **67**, 5861 (1977).
- [153] G. Kresse and J. Hafner, *Phys. Rev. B* **47**, 558 (1993), G. Kresse and J. Hafner, *Phys. Rev. B* **49**, 14251 (1994), G. Kresse and J. Furthmüller, *Comput. Mater. Sci.* **6**, 15 (1996), G. Kresse and J. Furthmüller, *Phys. Rev. B* **54** 11169 (1996), G. Kresse Thesis Technische Universität Wien (1993).
- [154] P. E. Blöchl, *Phys. Rev. B* **50**, 17953 (1994).
- [155] M. C. Payne, M. P. Teter, D. C. Allan, T. A. Arias and J. D. Joannopoulos, *Rev. Mod. Phys.* **64**, 1045 (1992).
- [156] P. J. H. Denteneer “The pseudopotential-density-functional method applied to semiconductor crystals”, Ph. D Thesis, Technische Universiteit Eindhoven (1987).
- [157] R. P. Feynman, *Phys. Rev.* **56**, 340 (1939).
- [158] A. R. Oganov and C. W. Glass, *J. Chem. Phys.* **124**, 244704 (2006).
- [159] C. W. Glass, A. R. Oganov and N. Hansen, *Comput. Phys. Commun.* **175**, 713 (2006).
- [160] S. N. Khanna, B. K. Rao, P. Jena, and J. L. Martins, Jahn-Teller distortion, Hund’s coupling and metastability in alkali tetramers, in: P. Jena, B. K. Rao, S. N. Khanna (Eds.), *Physics and Chemistry of Small Clusters*, Plenum Press, New York, pp. 435-438 (1987).

- [161] A. M. Köster, P. Calaminici, M. E. Casida, R. Flores-Moreno, G. Geudtner, A. Goursot, T. Heine, A. Ipatov, F. Janetzko, J. M. del Campo, S. Patchkovskii, J. U. Reveles, D. R. Salahub, and A. Vela, deMon2k, V. 2.3.6, The deMon Developers Community: Cinvestav, Mexico, 2006; available at [jwww.deMon-software.com](http://www.deMon-software.com).
- [162] J. P. Perdew, K. Burke and M. Ernzerhof, *Phys. Rev. Lett.* **77**, 3865 (1996).
- [163] P. Calaminici, F. Janetzko, A. M. Köster, R. Mejia-Olvera, and B. J. Zniga-Gutierrez *J. Chem. Phys.* **126**, 044108 (2007).
- [164] <http://webbook.nist.gov/chemistry/>
- [165] J. U. Reveles, and A. M. Köster, *J. Comp. Chem.* **25**, 1109 (2004).
- [166] R. G. Parr, W. Yang, *Density Functional Theory of Atoms and Molecules*, Oxford University Press, New York, (1989).
- [167] P. K. Chattaraj, U. Sarkar, and D. R. Roy, *Chem. Rev.* **106**, 2065 (2006), R. G. Parr, P. K. Chattaraj, *J. Am. Chem. Soc.* **113**, 1854 (1991).
- [168] A. C. Reber, S. N. Khanna, P. J. Roach, W. H. Woodward, and A. W. Castleman, Jr., *J. Am. Chem. Soc.* **129**, 16098 (2007).
- [169] D. C. Douglass, J. P. Bucher, and L. A. Bloomfield, *Phys. Rev. B* **45**, 6341 (1992).
- [170] N. Boutassetta, A. R. Allouche, and M. A. -Frécon, *Phys. Rev. A* **53**, 3845 (1996).
- [171] E. Chamorro, P. K. Chattaraj, and P. Fuentelba, *J. Phys. Chem. A* **107**, 7068 (2003), P. K. Chattaraj and S. Giri, *J. Phys. Chem. A* **111**, 11116 (2007), R. Parthasarathi, M. Elango, V. Subramanian, and P. K. Chattaraj, *Theo. Chem. Acc.* **113**, 257 (2005).
- [172] X. X. Chi, *Proc. Comput. Sci.* **9**, 348 (2012).
- [173] Y. Zhang and W. Yang, *J. Chem. Phys.* **109**, 2604 (1998).